Dean Vortex-Driven Flow Manipulation and Performance Enhancement in Micro-Hydrocyclones for Biomedical Microfluidic Applications

by

Yeganeh Saffar

A thesis submitted in partial fulfillment of the requirements for the degree of

Doctor of Philosophy

Department of Mechanical Engineering
University of Alberta

Abstract

This dissertation is an experimental investigation of the flow organization and performance enhancement of the micro-hydrocyclone by the means of Dean vortices. Micro-hydrocyclones are compact, passive microfluidic devices designed for the continuous separation of particles. While they hold strong potential for high-throughput applications, their internal flow organization and overall performance remain poorly characterized. Miniaturization can lead to fundamental changes in the flow regime. Yet, the nature of these changes has not been experimentally explored. On the performance side, most prior investigations rely on simplified test cases involving two particles or cell sizes evaluated at a small number of flow rates, offering only a narrow view of device capabilities. As a result, the flow behavior and device performance remain largely unknown. Dean vortices are known as secondary flow form in both macro and micro-curved channels which has significant role in conventional microfluidic devices employing micro-curved channel for particle separation and mixing. In this dissertation it is hypothesized that inducing Dean vortices at the inlet of the micro-hydrocyclone can enhance the performance of the device.

Dean vortices play an important role in particle lateral migration separation techniques but have often been discussed in literature without consistency. A thorough review revealed that the Dean number, a dimensionless parameter used to characterize the onset and strength of Dean vortices, was defined inconsistently across studies, with variations in geometric parameters and reference velocities. This lack of standardization has led to inconsistencies in reported thresholds and made it difficult to develop generalized design criteria. To resolve this, a comprehensive analysis of existing definitions was conducted, and a unified and physically consistent definition of the Dean number, for the microscale flow, was formulated. This new formulation provides a

baseline for comparing results and guiding future microfluidic designs involving curved geometries.

To validate the presence and behavior of Dean vortices in microscale geometries, a series of experiments were conducted using curved microchannels. The goal was to directly observe the formation of secondary flows and assess their influence on larger, deformable objects. Through a combination three-dimensional scanning Particle Image Velocimetry (PIV), and two-phase flow studies, it was experimentally confirmed that Dean vortices consistently form in the curved microchannel geometry when the Reynolds number is high enough. Moreover, these vortices were shown to interact with suspended deformable structures, affecting their shape and trajectory. These findings established a physical basis for manipulating flow fields within a micro-hydrocyclone by integrating a curved inlet geometry.

To investigate whether the flow within a micro-hydrocyclone can be effectively visualized and measured under realistic operating conditions, optical diagnostics were applied to capture both the structure and dynamics of the internal flow. Using planar PIV and Particle Tracking Velocimetry (PTV), flow field was measured in configurations with and without Dean vortex induction. Experiments were also conducted with and without the presence of cell clusters to assess the influence of them on flow organization and measurement feasibility. Additionally, stereoscopic microscopy was employed to resolve the three-component velocity field at the midplane of the micro-hydrocyclone, providing deeper insight into the three-dimensional nature of the flow structures. These techniques together enabled clear visualization and flow measurement of swirling motion and vortex asymmetries inside the device, demonstrating that the internal flow can be captured even in complex, multiphase scenarios. This multi-modal approach established

the feasibility of using optical diagnostics to evaluate and compare the flow organization without the existence of the cell clusters.

Building on the flow characterization, the performance of the micro-hydrocyclone was evaluated across a wide range of operating conditions using both particles and biological cell clusters. To support this extensive analysis, a dedicated software tool was developed to automate image processing, particle detection, size classification, and statistical quantification. This enabled high-throughput assessment of separation efficiency and repeatability. The results showed that Dean vortex induction significantly improved separation performance. In experiments using cell clusters, it was demonstrated that the modified configuration maintained the clusters intact while still enhancing separation efficiency. This confirmed that inducing secondary flows through geometric design not only boosts performance but also allows for gentler operation suitable for biological applications.

Preface

This thesis is based on the original research conducted by Yeganeh Saffar. The experimental work and methodologies outlined in this document were developed and carried out in the Optical Diagnostics Group laboratory, under the supervision of Dr. Reza Sabbagh and Prof. David S. Nobes. This work was funded by Natural Sciences and Engineering Research Council of Canada (NSERC). A significant portion of the research findings presented in this thesis has been published in peer-reviewed journals and conferences, as detailed in the following paragraphs.

Chapter 2 investigates the formation of Dean vortices and the effective parameters in curved microchannels and examines how the Dean number is defined in different works in the literature to find and define a unique definition. The research presented in this chapter has been published in *Micromachines* (2023) under the title "The physics and manipulation of dean vortices in single- and two-phase flow in curved microchannels: a review".

Chapter 3 presents experimental findings on the formation of Dean vortices in curved microchannels. Experiments were performed using 3D scanning PTV to visualize the formation of Dean vortices in a curved micro-channel. The findings from this chapter are based on the paper presented in *20th International Symposium on Applications of Laser and Imaging Techniques to Fluid Mechanics* (2022), in Lisbon, Portugal, under the title "Investigating the flow structure of Dean vortices in a curved microchannel, implementing 3D-μPTV using FVM and near wall data refinement".

Chapter 4 shows the effect of formed Dean vortices in the previous chapter on the deformation and trajectory of deformable droplets acting as circulating tumor cells (CTC) clusters. Lack of breakage or high deformation in this investigation confirms the possibility of employing

this configuration in the modified geometry with actual cell clusters. This chapter was published in *Journal of industrial and engineering chemistry research* (2022), under the title “Experimental investigation of the deformation and migration of microdroplets in curved microchannels” presented at *CSME* 2022, in Edmonton, Canada, under the title of "Experimental analyzes of capsules’ behavior in a curved microchannel" and in *26th International Conference on Miniaturized Systems for Chemistry and Life Sciences* ,virtually (2022) under the title of “ Experimental investigation of the deformation and migration of microcapsules in curved vessels”.

Chapter 5 looks into the feasibility of the application of PIV and PTV for investigating the flow organization micro-hydrocyclone in single- and two-phase flow configurations. This chapter was published in *Chemical Engineering Journal* (2025) under the title “Simultaneous circulating tumor cells (CTCs) tracking and flow field characterization through integrated single camera imaging in a micro-hydrocyclone”. Part of this chapter also was presented at the *21st International Symposium on Applications of Laser and Imaging Techniques to Fluid Mechanics* in Lisbon, Portugal under the title of "Integrated single camera μPTV and florescence imaging for cell tracking and flow investigation in centrifugal microfluidic devices".

Chapter 6 looks into the physics of the flow within micro-hydrocyclones with induced Dean flow and without Dean flow using stereo PIV. Introducing the use of stereoscopic imaging in resolving the three-component 2D velocity fields in complex microdevice as a first time implementation for such confined geometries. Part of this chapter has been presented at the *6th International Conference on Experimental Fluid Mechanics*, in Niagara-on-the-Lake, Canada under the title “Exploring passive flow structure manipulation in micro-hydrocyclone through particle image velocimetry”. This chapter is also prepared to be published as a journal paper.

Chapter 7 explores the performance of the micro-hydrocyclone and its application for the separation of circulating tumor cells with and without inducing Dean vortices. Part of this chapter has been presented at the *6th International Conference on Experimental Fluid Mechanics*, in Niagara-on-the-Lake, Canada under the title "Exploring passive flow structure manipulation in micro-hydrocyclone through particle image velocimetry". This chapter is also prepared to be published as a journal paper.

.

Acknowledgment

I would like to sincerely thank my supervisor, Dr. Reza Sabbagh and Dr. David S. Nobes, for their support, guidance, and knowledge throughout my PhD. Their patience and thoughtful advice have been invaluable, both in shaping the direction of my research and helping me navigate the many challenges along the way. I am grateful for the opportunity to learn from them and for their continued encouragement. I would also like to thank Dr. Mariana Kulka for her generous support, collaborative spirit, and valuable contributions to this research and consistent kindness throughout our work together.

I also extend my thanks to my thesis committee member, Dr. Alexandra Komrakova for her helpful feedback, insightful suggestions, and constructive critique.

A big thank you goes to my lab mates and friends for their collaboration and support over the years. In particular, I would like to acknowledge Dr. Sina Kashanj, Dr. Lisa Kinsale, Dr. Guillermo Bessa and Dr. Shadi Ansari for their advice and assistance during my studies.

I want to express my heartfelt gratitude to my beloved husband, Sina, for his support and patience. A special thanks goes to my family. My parents, Frida and Rahim, have always believed in me and encouraged me to pursue my goals. Their love and guidance have been invaluable throughout my life. Finally, I want to express my heartfelt gratitude to my brother Ali and his wife, Nasim, my sister-in-law Sarina and my best friend of 20 years, Rezvan for supporting me and believing in me all along.

Table of Contents

List of Figures

List of Tables

Chapter 1: Introduction

1.1 Motivation

Particle separation at the microscale is a critical component of many lab-on-a-chip and biomedical applications, e.g., for isolating particles [1], biological cells [2], and droplets from complex fluids [3]. Microfluidic devices offer control over fluid dynamics and are increasingly used for continuous separation based on size, density, deformability, or dielectric properties [4][5]. Among the common designs, spiral microchannels have attracted significant attention due to their ability to leverage inertial and Dean forces to focus and separate particles [6]. In these channels, secondary flows i.e. Dean vortices, drive particles to equilibrium positions depending on their physical properties, enabling effective sorting [7]. Notable studies include Di Carlo *et al.* (2007) [8] who demonstrated size-based separation in spiral inertial microfluidics, using lateral displacement and inertial lift forces in curved channels. Despite these advances, a limitation in these systems is their low throughput, which is inadequate for large-scale applications such as clinical diagnostics or industrial bioprocessing. Other limitations include clogging risks, fabrication complexity, and limited flexibility in processing diverse particle types simultaneously.

To overcome such challenges, micro-hydrocyclones have been introduced as an alternative platform [9]. Hydrocyclones, widely used in the mining and chemical industries, rely on centrifugal forces generated by swirling flows in a conical chamber to separate particles based on size and density [10]. Inspired by this principle, micro-hydrocyclones have been miniaturized and adapted for biological and medical applications, offering the potential for higher throughput and continuous operation [11]. Although there are few studies showing the potential of the micro-hydrocyclone there are many questions need to be answered [12]. First, the internal flow physics

of micro-hydrocyclones remains poorly understood. Most available studies are derived from numerical simulations under idealized conditions and experimental validation is missing [13]. Without detailed flow characterization, it is difficult to design and optimize devices for specific separation tasks. Second, most of the studies focus on binary separation of particles with large size differences [14], which does not reflect real-world scenarios involving overlapping size distributions, deformable cells, or complex suspensions [15]. There is a lack of experimental data on separation performance, particularly for bio-relevant particles. This gap significantly limits the applicability of micro-hydrocyclones in high-throughput, high-fidelity biomedical separation tasks. Therefore, further research is needed to uncover the detailed fluid dynamics within these devices and to experimentally assess their efficiency across a wider range of particle types and biological samples.

1.2 Hypothesis

This work hypothesizes that Dean vortices could be induced to the inlet of micro-hydrocyclone to enhance the performance of this device by making it operational at lower flow velocities which make the use of this device feasible for bio applications. To evaluate this hypothesis several key studies have been carried out which have been reported in each chapter.

1.3 Thesis scope

Following this chapter (Chapter 1: Introduction), in Chapter 2, a comprehensive review of Dean flow behavior in curved microchannels is presented. A unit-consistent definition of the Dean number is proposed, and the role of geometrical parameters in vortex formation is analyzed. This foundational understanding informs the subsequent development of microfluidic configurations that actively harness Dean vortices.

In Chapter 3, Experimental evidence is presented on how curved geometries at the inlet region of the micro-hydrocyclone can induce secondary flows, modifying internal vortex structures and enhancing control over particle trajectories.

In Chapter 4, the influence of Dean vortices on the behavior of deformable droplets is experimentally investigated to assess their behavior as analogs for cell clusters. The study evaluates droplet deformation, trajectory, and lateral migration in curved microchannels under varying flow conditions. The absence of rupture and the predictable deformation patterns support the feasibility of using this configuration in subsequent biological experiments involving actual cell clusters. These findings serve as a critical validation step before transitioning to bio-relevant flow systems in later chapters.

In Chapter 5, a novel imaging and analysis platform is developed to enable simultaneous tracking of circulating tumor cells (CTCs) and flow field mapping within a micro-hydrocyclone. Using integrated image acquisition and segmentation algorithms, the behavior of both tracer particles and biological samples is assessed in real time.

In Chapter 6, the three velocity components of the velocity are measured at the mid-plane of the micro-hydrocyclone using microscopic stereo PIV. This velocity measurement provides information about the evolution of a key indicator of separation performance known as the locus of zero vertical velocity (LZVV). A comparative analysis between spiral and conventional inlets has been carried out.

In Chapter 7, the performance of the modified device i.e. with induced Dean vortices is evaluated over a large dataset using a custom-developed software platform. This tool automates particle detection, size classification, and statistical analysis, allowing a systematic

characterization of device efficiency across different flow regimes and particle populations. The comparison of the performance of the micro-hydrocyclone with and without induced Dean vortices has been undertaken for both particles and circulating tumor cells (CTCs).

1.4 Thesis structure

This thesis was prepared in a paper-based format. Thus, every chapter has either been published or is being prepared for publication as a journal article. Each chapter starts with an abstract description of the main purpose of the chapter and a graphical abstract, relevant to that specific chapter. The references are inclusive to each chapter for convenience. Based on this layout of the thesis, some overlap between the introduction and references can be observed.

References

[1] A. Dalili, A. Sattati, N. Tasnim, M. Hoorfar, Sheath-assisted focusing of microparticles on lab-on-a-chip platforms, Electrophoresis 41 (2020) 2188–2196. https://doi.org/10.1002/elps.202000247.

[2] A. Casciati, M. Tanori, R. Manczak, S. Saada, B. Tanno, P. Giardullo, E. Porcù, E. Rampazzo, L. Persano, G. Viola, C. Dalmay, F. Lalloué, A. Pothier, C. Merla, M. Mancuso, Human medulloblastoma cell lines: Investigating on cancer stem cell-like phenotype, Cancers (Basel). 12 (2020) 1–14. https://doi.org/10.3390/cancers12010226.

[3] M. Bartunik, M. Fleischer, W. Haselmayr, J. Kirchner, Advanced Characterisation of a Sensor System for Droplet-Based Microfluidics, Proc. IEEE Sensors 2020-October (2020) 2–5. https://doi.org/10.1109/SENSORS47125.2020.9278806.

[4] G. Park, D. Han, G. Kim, S. Shin, K. Kim, J.-K. Park, Y. Park, Visualization and label-free quantification of microfluidic mixing using quantitative phase imaging, Appl. Opt. 56 (2017) 6341. https://doi.org/10.1364/ao.56.006341.

[5] M.R. Doostabadi, E. Mangoli, L.D. Marvast, F. Dehghanpour, B. Maleki, H. Torkashvand, A.R. Talebi, Microfluidic devices employing chemo- and thermotaxis for sperm selection can improve sperm parameters and function in patients with high DNA fragmentation, Andrologia 54 (2022) 1–15. https://doi.org/10.1111/and.14623.

[6] A. Khodayari, S. Ebrahimi, S.M.H.R. Demneh, M. Topaheidari, E. Ayani, A. Shamloo, Square-based spiral microchannel for the separation of circulating tumor cells using surrogate optimization based on the inertial method, Phys. Fluids 37 (2025). https://doi.org/10.1063/5.0252985.

[7] N. Nivedita, P. Ligrani, I. Papautsky, Dean flow dynamics in low-aspect ratio spiral microchannels, Sci. Rep. 7 (2017) 1–10. https://doi.org/10.1038/srep44072.

[8] D. Di Carlo, D. Irimia, R.G. Tompkins, M. Toner, Continuous inertial focusing, ordering, and separation of particles in microchannels, Proc. Natl. Acad. Sci. U. S. A. 104 (2007) 18892–18897. https://doi.org/10.1073/pnas.0704958104.

[9] M.S. Syed, C. Marquis, R. Taylor, M.E. Warkiani, A two-step microengineered system for high-density cell retention from bioreactors, Sep. Purif. Technol. 254 (2021) 117610. https://doi.org/10.1016/j.seppur.2020.117610.

[10] Z. shan Bai, H. lin Wang, S.T. Tu, Experimental study of flow patterns in deoiling hydrocyclone, Miner. Eng. 22 (2009) 319–323. https://doi.org/10.1016/j.mineng.2008.09.003.

[11] J.Y. Han, B. Krasniqi, J. Kim, M. Keckley, D.L. DeVoe, Miniaturization of Hydrocyclones by High-Resolution 3D Printing for Rapid Microparticle Separation, Adv. Mater. Technol. 5 (2020) 1–11. https://doi.org/10.1002/admt.201901105.

[12] F. Li, P. Liu, X. Yang, Y. Zhang, Numerical simulation on the effects of different inlet pipe structures on the flow field and seperation performance in a hydrocyclone, Powder Technol. 373 (2020) 254–266. https://doi.org/10.1016/j.powtec.2020.06.066.

[13] Y. Fan, J. Li, Q. Wei, Z. Xiong, Y. Ji, H. Ma, B. Liu, Y. Huang, W. Lv, H. Wang, Study on the law of turbulent flow and self-rotation and revolution of particles in micro-hydrocyclone, Powder Technol. 415 (2023) 118200. https://doi.org/10.1016/j.powtec.2022.118200.

[14] M.S. Syed, F. Mirakhorli, C. Marquis, R.A. Taylor, M.E. Warkiani, Particle movement and fluid behavior visualization using an optically transparent 3D-printed micro-hydrocyclone, Biomicrofluidics 14 (2020). https://doi.org/10.1063/5.0025391.

[15] C. Zhang, D. Wei, B. Cui, T. Li, N. Luo, Effects of curvature radius on separation behaviors of the hydrocyclone with a tangent-circle inlet, Powder Technol. 305 (2017) 156–165. https://doi.org/10.1016/j.powtec.2016.10.002.

Chapter 2: Dean Vortex in Curved Microchannels

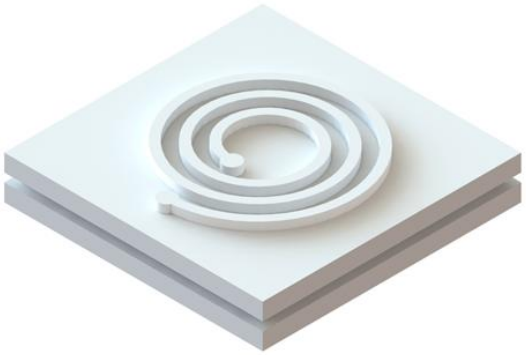

Graphical Abstract: a perspective view of a spiral micro-channel

This chapter provides a comprehensive review of Dean vortices in curved microchannels, focusing on their formation, dynamics, and potential applications in microfluidic devices designed for particle and cell separation. This review establishes the theoretical foundation for inducing Dean vortices to enhance flow control at low velocities. A critical evaluation of existing definitions of the Dean number is conducted, leading to a proposed unified formulation that ensures consistency in describing vortex behavior. Differences between Dean flow in simple curved channels and spiral geometries are examined, along with the effects of channel shape on both single-phase and multiphase flows. This chapter sets the foundation for subsequent chapters by clarifying the parameters required to generate and manipulate Dean vortices within practical microfluidic systems.

This chapter is based on the following paper:

Saffar, Y., Kashanj, S. Nobes, D. S.; Sabbagh, R., "The Physics and Manipulation of Dean Vortices in Single- and Two-Phase Flow in Curved Microchannels: A Review", *Micromachines* 2023, 14, 2202. https://doi.org/10.3390/mi14122202

2.1 Introduction

Microfluidic devices have been continuously developed since the invention of the first laboratory-on-chip (LOC) in 1979 [1,2]. They have been evolved to manipulate and control the flow and its containing materials and features such as cells, capsules, and particles [3–6]. Employment of these manipulation devices is mostly preferred in comparison to others such as flow cytometry, centrifuge, and membrane-based filtering schemes due to the simple structure of the channels and high throughput [7–10]. This method requires less solution sample and is cost effective with a higher efficiency[7–10]. Many microfluidic devices have been invented for a wide range of applications, since bio-cells, particles, and capsules behave differently based on their physical properties during the manipulation [11]. Detecting malaria infected blood cells [12], circulating tumor cells (CTCs) [13], and measuring glucose concentration by various bio fluids [14,15] are instances for diagnostic applications. Controlled chemical reactions [16], protein expression [17], and organic and non-organic compound synthesis [18,19] are among the chemical applications of microfluidic devices. There are also several other applications in cosmetics [20–22], food [23–26], agriculture [27–29], and pharmaceutical [30–32] industries manipulating the flow and its contents at the micro scale.

Based on the implementation of an external source of energy, manipulation methods in microfluidics can be passive or active [33–35]. Geometrical manipulation is a passive method that utilizes the microchannel geometric properties to control the flow [36,37]. For example, channels with grooves form stream wise vortices which can be employed for mixing enhancement [38–41]. T-junction channels generate monodisperse droplets which is a method for cell and particle encapsulation [42][43]. Curved microchannels are other examples of passive manipulation devices that can be used for particle separation [44], cell sorting [45], and mixing purposes [46]. The

asymmetric shape of a curved microchannel wall induces a form of secondary flow, counter rotating vortices, termed Dean vortices and such a flow is called Dean flow or secondary flow [47]. In mixing devices, these vortices increase the mixing efficiency and manipulate the behavior of particles and droplets by changing their equivalent positions and affecting their topology [48][49].

Considering the ongoing research interest on the manipulation of microscale flow behavior, several review papers have been published in this area, discussing the Dean flow [50]. Zhang *et al.* [11] presented a review paper that discusses the fundamental kinematics of particles and a comprehensive review of recent developments in inertial microfluidics. They briefly introduce Dean vortices in a spiral channel and the particle sorting application benefiting from this geometry. Zhao *et al.* [12]reviewed the application of the secondary flow generated by different single layer and multilayer geometrical designs, e.g., microchannels with obstructions, spirals, serpentines and double layered with groove array. In their paper, applications of Dean flow as a type of secondary flow is reviewed as well. Afsaneh and Mohammadi presented a review on the manipulation of cells and particles [52]. They have discussed Dean flow briefly in a curved channel as a fluid based manipulation method [52]. Recently, Mishra *et al.* [53] briefly reviewed the physics of the Dean flow with a main focus on biomedical applications. There are also some papers extensively reviewing the effect of the Dean flow and curved microdevices on sorting and manipulation of particles [11,54] which is not discussed in this work.

There are many works investigating Dean flow in microchannels to provide a better understanding of the physics of the phenomena, effect of the geometrical properties on the vortices, and the interactions between Dean vortices and capsules. Although Dean flow has been mentioned briefly in some of the review papers, there is no literature review concentrating on this

phenomenon specifically at the micro-scale. The lack of sufficient information about the Dean flow at the micro-scale, precludes researchers from performing a physics-based design and optimization of the geometry. Understanding the physics of Dean flow in different operating conditions at the micro-scale provides the knowledge required to optimize the working window of a microfluidic device based on the physics.

This review is focused on three substantial areas that are influenced by Dean vortices which forms the organization of this work as shown in Figure 2-1. The Dean vortices phenomena and its flow structure are reviewed first. Secondly, the relationship between the generated Dean vortices and the geometric properties of a curved microchannel such as cross section, aspect ratio, cross section shape, and potential 3D path of the channel is discussed. Finally, the interaction between Dean vortices and capsules in curved microchannels is investigated. The deformation and trajectories of the capsules, and the topology of the capsules internal flow affected by Dean vortices is reviewed in this section as well.

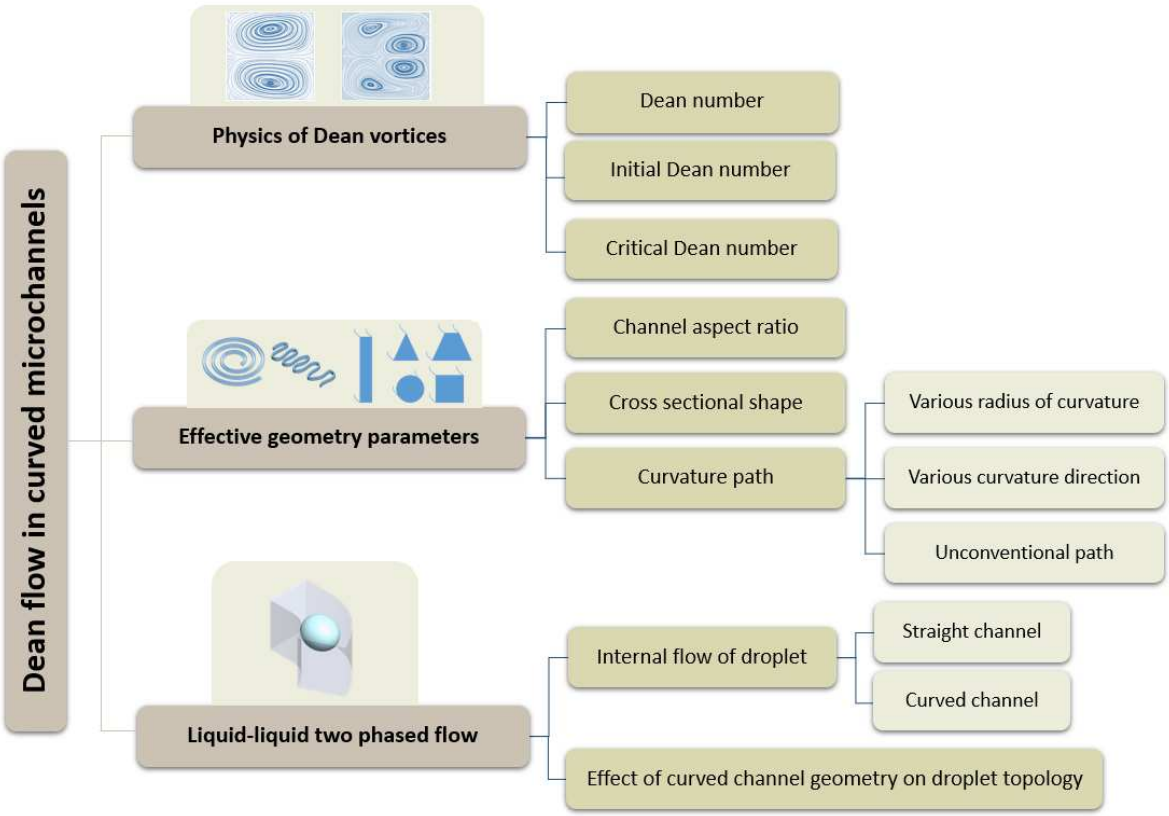

Figure 2-1 Schematic diagram of the paper indicating the layout of the discussions.

2.2 The physics of flow in a curved channel

The velocity profile and flow structure of the Poiseuille flow in a channel with a circular cross section and with an initial radius of curvature, $R_c = \infty$ (straight channel) is shown in Figure 2-2(a) [55,56]. In the straight section , the velocity profile is axisymmetric and the maximum velocity point is on the centerline of the channel [57,58]. Circular constant velocity contours in a channel with circular cross section are concentric with the channel cross section as shown in Figure 2-2(b) [57,58]. The symmetrical shape of the channel walls and cross section balances the velocity and pressure gradients and generates the symmetrical flow diagram [57,58].

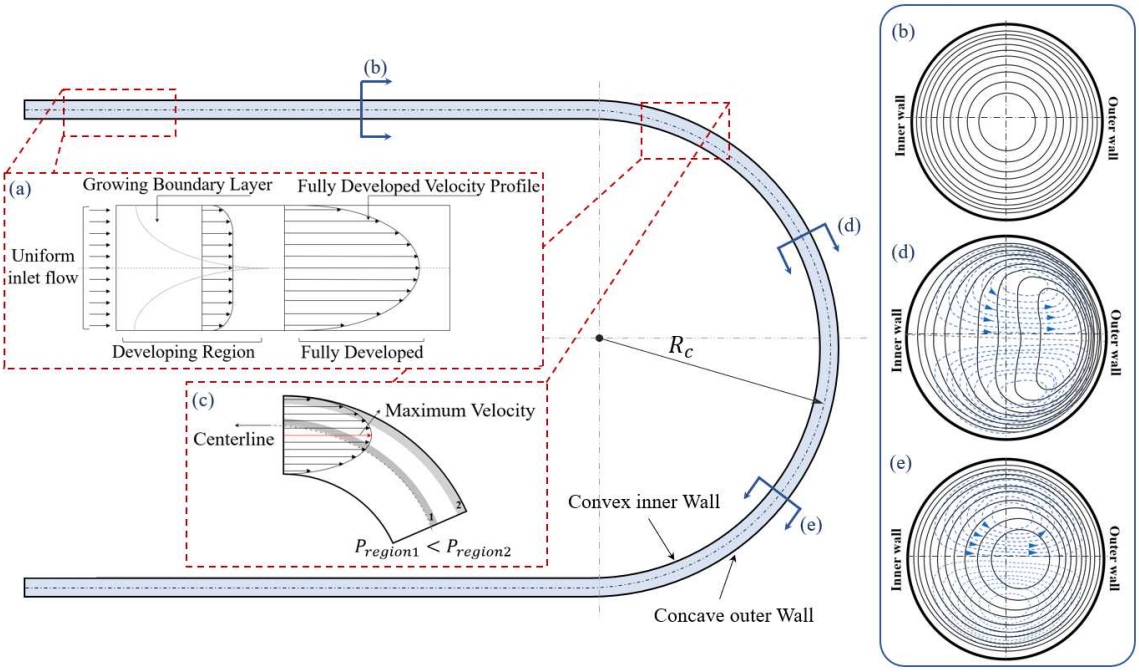

Figure 2-2 Flow in a curved channel (a) velocity profile of the developing and developed flow in straight channel far from the curved section (b), constant velocity lines of the flow in the straight section of the channel (c) unsymmetrical velocity profile of Dean flow entering the curved section of the channel, (d) constant velocity lines of the flow in the entrance of the curved section, (e) further into the curved section where the center of the vortices are shifted more toward the concave wall.

Berger *et al.* [59] highlighted that investigations into the physics of the flow inside curved channels began in the early 1900's. In 1902, an experimental observation in a curved pipe determined that the location of the maximum velocity moves toward the concave outer wall [60]. Later, Eustice (1910, 1911) injected ink into water passing through a pipe and used the streamline motion to demonstrate the existence of the secondary flow [61][62]. In 1928, for the first time, Dean [47,63] realized that in a pressure driven system, flow rate slightly decreases with increasing the channel curvature's radius. For low velocity flows in a curved channel with the Reynolds number $Re = \rho U d/\mu < 2000$ where ρ is fluid density, U is the uniform velocity, d is the

hydraulic diameter of the channel, and μ is the dynamic viscosity, it was proposed that radius of curvature is proportional to variations in the flow rate through the parameter, K, defined as:

$$K = {2Re^2 d}/{R_c} \quad (1)$$

In this equation d is the hydraulic diameter of the channel and R_c is the average of the radius of the curvature of the walls as indicated in Figure 2-2 [47].

A fully developed flow entering a channel with a curved path develops a centrifugal force in an asymmetrical geometry since the inner and outer wall has a different radius of curvature [64]. Such an asymmetricity affects the parabolic velocity profile and causes a shift in the location of the maximum velocity compared to a straight microchannel [65]. Therefore, the maximum velocity shifts from the centerline toward the concave outer wall and forms an asymmetric velocity profile [59], [66] as depicted in Figure 2-2 (c). This velocity profile induces a high pressure difference between the location of maximum velocity and the concave wall as $P_{region2} > P_{region1}$ [67][56]. This induced pressure gradient results in a transverse flow motion on the channel centerline. As a result of this transverse motion, a secondary flow is formed in the flow field [56][65][67]. The secondary flow causes an energy loss from the main flow stream in the curved channel which increases the required pressure difference for a certain flow rate compared to a straight channel with the same cross-sectional area. As a result, with a constant pressure difference between the inlet and outlet of a channel, the flow rate in the curved channel will be less than that of the straight channel [47][65][67][56].

In sub-sections (d) and (e) of the curved channel of Figure 2-2, flow streamlines and constant velocity contours in the cross section of the curved channel are shown [68][69]. With an increase in the velocity, the constant velocity contour lines shown by solid lines in Figure 2-2 (b), start to

deform from circles into bended ovals leaning towards the concave outer wall. Flow streamlines show that the secondary flow pattern forms as two symmetrical and counter-rotating vortices on the top and bottom of the channel [68][69]. These vortices are known as the primary Dean vortices [68][69]. It is shown in the figure that for the higher velocity region in the cross-section, the pressure gradient between the low-pressure zone close to the concave outer wall, and the high-pressure zone close to the convex inner wall, is higher [47][68][69]. Consequently, as the velocity increases the center of the vortices shifts towards the concave outer wall [69].

Considering the scale, the principles of Dean flow remain the same for micro and macroscales. However, the specific details and considerations may differ. At the microscale, such as in microfluidics, the channels typically have dimensions in the order of tens to hundreds of micrometers [70]. At such a scale, the flow characteristics in the microchannel may exhibit unique behaviors due to the dominance of viscous forces over inertial forces [49]. Consequently, the Reynolds number (the ratio of inertial forces to viscous forces) defining the formation of the secondary flow may be much lower for microchannels [65]. At the macroscale, such as in larger channels or pipes, the Dean flow is still present. However, the relative importance of inertial forces increases compared to the viscous forces. Thus, the Reynolds number is typically higher at the macroscale, and inertial effects play a more significant role in the dynamics of the flow [49].

2.2.1 The Dean number

The non-dimensional parameter, K in Eq. (1) was introduced by Dean [47] to investigate the effect of channel curvature on the flow. This parameter was later named after its founder as the Dean number, De [59]. This dimensionless number indicates the relationship between the channel geometry and the reduction of flow rate in curved channels [59]. In addition to the Dean's

definition in Eq. (1), there are several other variations of this equation developed by other researchers. Table 2-1 shows the various equations for Dean number that have been used in experimental studies and reported in the literature.

Theoretical investigations typically deploy either the mean velocity of the channel or pressure gradient as the driving factor to calculate the Dean number. In experimental studies, using the mean velocity is more common since it is more convenient to measure velocity than the pressure gradient considering the fact that in complex flow geometries, the pressure gradient changes in different directions. However, for a fully developed flow, the differences between calculations based on mean axial velocity and pressure gradient are minor [71]. Therefore, in numerical studies, pressure gradient is usually used instead of the mean velocity estimation to reduce the uncertainty of the calculations [72].

The inconsistency in the definition of the geometrical parameters such as the measure of the radius of curvature based on the convex wall, concave wall, or centerline of the channel is another reason that causes the various definitions of *De*. This is always important to identify the equation that each study has used to calculate the De since in a similar case using a different definition can cause disagreement between the results. Comparing the results from different studies without considering the calculation references can lead to incorrect conclusions. As a result, it is mandatory to study the definitions of *De* and their differences based on their applications

Most of these equations use similar parameters such as the Reynolds number, Re, based on hydraulic diameter of the channel and inlet velocity, R_c radius of curvature and d the width of channel in their definitions. But they are slightly different with an additional constant coefficient or constant power. The equation introduced by Dean will be referred to as K and the other equations will be compared with K as the basic equation.

In Table 2-1, equation (2), is the extended form of (1), K, represented in [63]. In (3) the inlet and outlet mass fluxes are used as defining parameters to calculate the Dean number. The calculated Dean number in this case has an inverse relation with d which results in a different trend in cases where the channel width changes from the basic equation. (4) is proposed for a constant radius pipe, so d is assumed to be constant that results in $De_2 = (K/2)^{\frac{1}{2}}$. (5) is the square root of the K multiplied by $\sqrt{2}$ ($De = \sqrt{2K}$). (6) is used in a case with high radius of curvature that the convex wall radius of curvature, r_i, and concave wall radius of curvature, r_o, are assumed to be equal ($^{r_i}/_{r_o} \cong 1$) in this scenario instead of the radius of curvature of the centerline the convex wall radius of curvature is used. (7) is similar to (5) $De_1 = (2K)^{\frac{1}{2}}/2$ but instead of the centerline radius of curvature, the convex wall radius of curvature is applied. (8) is observed to be the most common equation in experimental investigations which is related to K with $De = \left(^{K}/_{4}\right)^{1/4}$.

Table 2-2 contains some of the Dean number definitions mostly obtained from numerical studies that use the pressure gradient as a part of their definitions. In these equations, G is the pressure gradient defined as $G = \partial P/(R\partial\theta)$, where θ is the angular direction in cylindrical coordinates, and $C = {Gd^2}/{(\mu W_0)}$ is a dimensionless constant. Similar to the equations defined for experimental studies, these equations can be derived from each other. As an example, modifying (11) considering a constant pipe radius and pressure gradient leads to the simplification shown in (10) [68]. In fully developed flow cases where pressure gradient can be assumed constant throughout the channel, Dean number is less sensitive to the application of mean velocity or pressure gradient. In such cases using both categories would provide a similar result.

Table 2-1 Equations based on mean axial velocity used for Dean number calculations in experimental investigations. In these equations, d represents the hydraulic diameter of the channel, R_c is the radius of curvature of the channel, ν is the kinematic viscosity of the fluid, W_0 is the mean axial velocity, δ is the curvature ratio which is defined as the ratio of hydraulic diameter, d, to the radius of curvature, R_c and Q_c, Q_s are also the fluxes for curved and straight pipe respectively.

		Equations	Author(s)	Description
Velocity based	(2)	$K = 2\left(\frac{d}{R_c}\right)\left(\frac{dW_0}{\nu}\right)^2 = \left(\frac{2{W_0}^2 d^3}{\nu^2 R_c}\right)$	Dean (1928)	Study the relationship between mass flux and geometry [47]
	(3)	$De_1 = \left(\frac{1}{2}K\right)^{1/2} \times \frac{Q_c}{Q_s} = 2^{5/2}\frac{Re}{\sqrt{dR_c}}$	Dyke (1978)	Dean's series for steady fully developed laminar flow through a toroidal pipe of small curvature ratio [73]
	(4)	$De_2 = \frac{Re}{\sqrt{d/R_c}}$	Bara *et al.* (1992)	Laminar Newtonian flow inside a square duct with non-symmetrical geometries [66]
	(5)	$De_3 = 2\delta^{1/2}Re = \left(\frac{d}{R_c}\right)^{1/2}\left(\frac{2d\overline{W_0}}{\nu}\right)$	Berger & Talbot (1988)	Study the characteristics of the flow in the curved channel [68]
	(6)	$De_4 = \frac{W_0 d}{\nu\sqrt{d/r_i}}$	Ligrani & Niver (1988)	Curved channels with a high radius of curvature $r_i/r_o \cong 1$ [74]
	(7)	$De_5 = Re\sqrt{\frac{d}{R_c}}$	Kim & Lee (2009)	3-D velocity field inside a circular microtube, d is the inner diameter of the microtube [75]
	(8)	$De_6 = Re\sqrt{\frac{d}{2R_c}}$	Nivedita *et al.* (2017) Seo *et al.* (2012)	Investigate Dean vortices inside a low aspect ratio spiral [65,68,76]

Table 2-2 Some of the proposed Dean number definitions based on the pressure gradient mainly used in numerical investigations. In these equations, d represents the hydraulic diameter of the channel, R_c is the radius of curvature of the channel, ν is the kinematic viscosity of the fluid, μ is the dynamic viscosity of the fluid, W_0 is the mean axial velocity, G is the pressure gradient defined as $G = \partial P/(R\partial\theta)$, and c is the dimensionless constant which is defined as $Gd^2/(\mu W_0)$.

		Equation	Author(s)	Description
Pressure based	(9)	$De_7 = \left(\frac{2d^3}{\nu^2 R_c}\right)^{1/2} \frac{Gd^2}{\mu} = 4\left(\frac{2d}{R_c}\right)^{1/2} \frac{Gd^3}{4\mu\nu}$	McConalogue & Srivastava (1968)	Study the motion of the flow in curved tube assuming that $\frac{Gd^2}{\mu W_0} = const.$ [69]
	(10)	$De_8 = \frac{2d^3}{\nu^2 R_c}\left(\frac{Gd^2}{4\mu}\right)^2 = 2\left(\frac{d}{R_c}\right)\left(\frac{Gd^3}{4\mu\nu}\right)^2 = \frac{G^2 d^7}{8\mu^2\nu^2 R_c}$	Burger & Talbot (1988)	Study the flow characteristics in the curved channel with constant fully developed flow [68]
	(11)	$De_9 = \frac{2d^3}{\nu^2 R_c}\left(\frac{Gd^2}{\mu C}\right)^2$	Burger & Talbot (1988)	Study characteristics of the flow in the curved channel [68]
	(12)	$De_{10} = \frac{Gd^3}{16\mu\nu}\left(\frac{d}{R_c}\right)^{1/2}$	Norouzi & Biglari (2003)	Analytical solution for the flow in the curved channel for low Dean numbers [77]
	(13)	$De_{11} = \frac{Gd^3}{\mu\nu}\left[\frac{2d}{R_c}\right]^{\frac{1}{2}}$	Howell *et al.* (2004)	Experimental study of the Dean vortices in a micromixer. G is the pressure gradient on the channel centerline [78]

2.2.1 Dean number thresholds

Various dominant or temporary configurations of Dean vortices can form by changing the flow or geometric parameters. The appearance of these configurations can be characterized by the Dean number [66][79]. Increasing the Dean number from 0, the first configuration of Dean vortices, a pair of counter-rotating vortices, appears and are called the primary Dean vortices. An example of these is shown in Figure 2-3(a) [64][65] in a radial cross-section view of a curved channel with a rectangular cross-section. The first Dean number threshold in which the vortices appear for the first time is termed the initial Dean number, De_i. Increasing the Dean number where $De_i < De$ leads to an increase in the transverse velocity of the flow and the strength of the vortices generated. This can be achieved by increasing the flow rate where the maximum velocity location moves further toward the concave wall as is depicted in Figure 2-3(b). As a result, the core of Dean vortices shifts to the concave wall [64][65]. With further increase of the Dean number, two secondary Dean vortices detach from the main vortices. These secondary vortices are smaller than the main/primary vortices. Figure 2-3(b) shows a flow configuration including the primary and secondary Dean vortices. The Dean number at which the secondary Dean vortices start to form is termed the critical Dean number, De_c [65][80] [81].

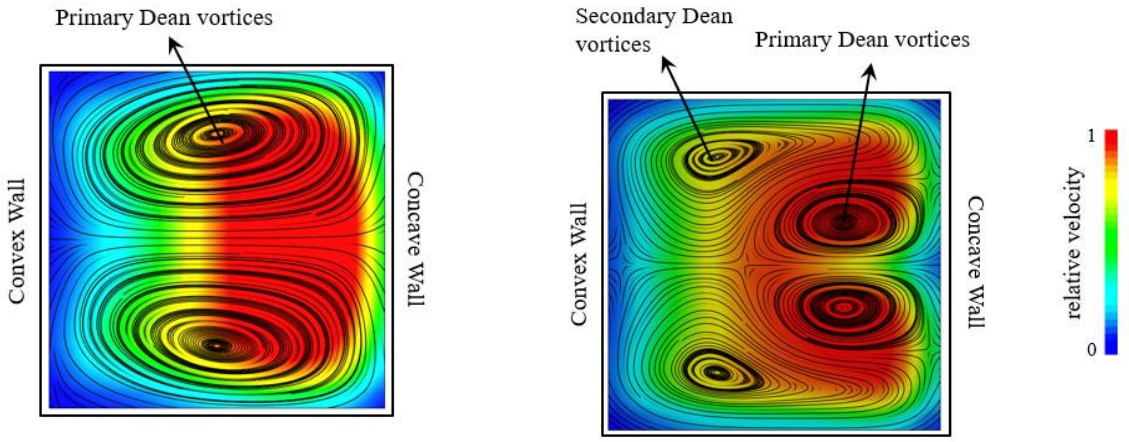

(a) (b)

Figure 2-3 Visualization of the out of plane velocity contour on the back ground and Dean vortices inside a rectangular channel shown by the streamline. (a) Formation of the primary Dean vortices. (b) Formation of the secondary Dean vortices.

The values of initial and critical Dean numbers depend on various factors such as aspect ratio (d/h) which is defined as the ratio of channel width or diameter, d, to height, h, and radius of curvature, R_c [65][79]. Being a function of several parameters makes it difficult to predict the flow configuration in a geometry at a given flow state without numerical or experimental investigations. Values of the Dean numbers which are all recalculated based on (8) and channel cross-sectional aspect ratios for different curve and spiral microchannel geometries have been derived from the literature and presented in Table 2-3. These values are used to generate a phase map shown in Figure 2-4 that compares *De* against channel aspect ratio, d/h. The color variance in the map differentiates the regions of appearance of different Dean vortices. It can be determined from this figure that in a single curve geometry with various channel widths or radius of curvatures shown in Figure 2-4 the initial Dean number is in the range $0 < De_i < 25$, while the critical Dean number is in the range of $100 < De_c < 140$. For spiral microchannels the range are significantly different

for initial and critical *De* than the single curve channel case. Both the initial and critical Dean numbers for spiral cases are close to each other in the range of $20 < De_i < 50$.

Table 2-3 Single curve and spiral microchannels information used to study the initial and critical Dean number relation to the revolution number [55,65,77,80,82–88].

Case	*AR*	*d*	*h*	R_c	De_i	De_c	cross section	channel	Ref
1	1.60	250	150	Various	28.5	30.5	rectangle	spiral	[52]
2	2.5	250	100	Various	34.5	37	rectangle	spiral	[52]
3	5	500	100	Various	31.5	40	rectangle	spiral	[63]
4	2.5	250	100	Various	NA	45	rectangle	spiral	[71]
5	3.3	200	60	2000		23	rectangle	spiral	[75]
6	0.25	NA	NA	NA	NA	72.5	rectangle	curved	[77]
7	0.5	NA	NA	NA	NA	70	rectangle	curved	[78]
8	1	NA	NA	NA	NA	67.5	rectangle	curved	[79]
9	2	NA	NA	NA	NA	60	rectangle	curved	[80]
10	4	NA	NA	NA	NA	52.5	rectangle	curved	[81]
11	2	NA	NA	NA	NA	100	rectangle	curved	[82]
12	1	NA	NA	NA	NA	45	rectangle	curved	[52]
13	0.5	NA	NA	NA	NA	65	rectangle	curved	[52]
14	0.3	NA	NA	NA	NA	80	rectangle	curved	[63]
15	0.25	NA	NA	NA	NA	95	rectangle	curved	[71]
16	0.2	NA	NA	NA	NA	70	rectangle	curved	[75]
17	0.17	NA	NA	NA	NA	57.5	rectangle	curved	[77]
18	0.14	NA	NA	NA	NA	50	rectangle	curved	[78]
19	0.125	NA	NA	NA	NA	42.5	rectangle	curved	[79]
20	0.1	NA	NA	NA	NA	40	rectangle	curved	[80]
21	0.08	NA	NA	NA	NA	40	rectangle	curved	[81]
22	1	NA	NA	NA	NA	72.5	rectangle	curved	[82]
23	1.25	NA	NA	NA	NA	95	rectangle	curved	[52]
24	1	NA	NA	NA	NA	87.5	rectangle	curved	[52]
25	0.8	NA	NA	NA	NA	87.5	rectangle	curved	[63]
26	0.7	NA	NA	NA	NA	92.5	rectangle	curved	[71]
27	0.55	NA	NA	NA	NA	95	rectangle	curved	[75]
28	0.5	NA	NA	NA	NA	204	rectangle	curved	[77]
29	0.3	NA	NA	NA	NA	135	rectangle	curved	[78]
30	0.2	NA	NA	NA	NA	137.5	rectangle	curved	[79]
31	1.7	250	150	2000	17	206	rectangle	curved	[80]
32	2	30	15	400	20	NA	rectangle	curved	[81]
33	1	150	150	4000	6.8	100	rectangle	curved	[82]
34	1	200	200	5000	10	NA	rectangle	curved	[82]
35	1	200	200	2500	0.316	NA	rectangle	curved	[82]

It is shown in Figure 2-4 that critical and initial Dean number (using the same Dean number definitions for all data sets) for a spiral geometry is located in a very small range in the low Dean number area which indicates the small window of the appearance of two primary Dean vortices. The initial Dean number of a single curve is in the same area and about half of the initial Dean number of a spiral. This means that the Dean vortices can be generate at lower velocities in a single curve. The critical Dean number for a single curve is found to be in the high Dean number area and almost three times bigger than the initial Dean number for the same geometry.

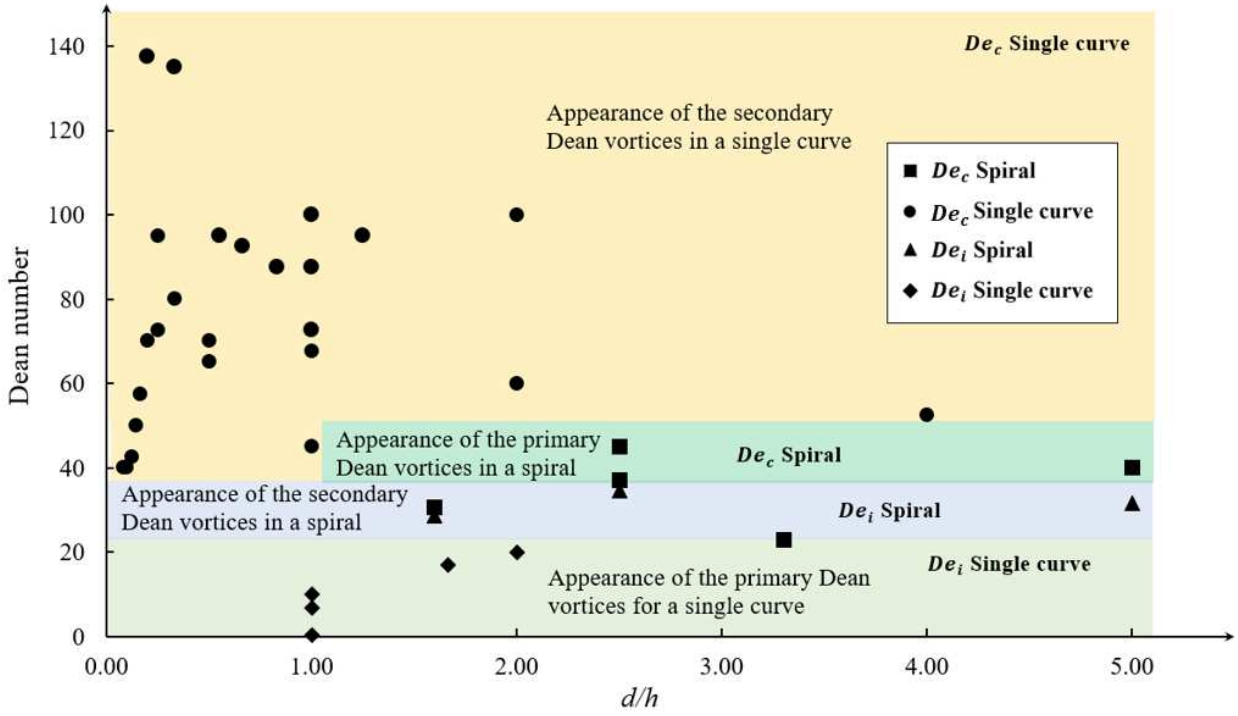

Figure 2-4 Critical and initial Dean number in single and multiple curved geometries showing the effect of channel shape in addition to other geometrical properties. [55,65,77,80,82–88]

Reviewing the variables included in the Dean number for definitions outlined in Table 2-1 and Table 2-2, it is observed that channel shape parameters are not considered as defining parameters. This is despite the fact that changing the channel shape has a significant effect on

critical and initial Dean number as shown in Figure 2-4. Hence, it can be understood that in addition to the basic geometric parameters, parameters related to the shape of the curved channel are also important and affect the formation of Dean vortices. This is an important outcome and highlights the need for further investigations into the effect of geometry and the incapability of the available correlations in predicting the flow behavior in curved microchannels and the formation of secondary Dean vortices. The following section extensively investigates the literature for the effect of geometry on Dean flow.

2.3 The effect of geometry on the Dean flow structure

The formation and topology of Dean vortices are related to both flow properties, such as flow velocity and fluid viscosity, as well as channel geometry. In addition to the curvature ratio, d/R_c that directly affects the Dean number, there are other factors that can affect the velocity field in Dean flows [77,79]. Geometry features such as the channel cross-sectional shape, aspect ratio, and the curvature path that is the shape of the channel centerline showing the layout of the channel are of those factors. These factors affect the formation of Dean vortices by increasing the initial or critical Dean number, changing the shape of vortices and changing the direction of the rotation [39,46,89–91]. Manipulating the specifications of the Dean vortices with geometry can lead to the design of more efficient microchannels for various applications [83]. There are a few studies investigating the flow properties directly [38], [92]. Studies on applications such as mixing and encapsulating, assist understanding the effect of the channel's geometry on the formation and properties of the Dean vortices. This section discusses research results that help to understand the effect of the channel cross-section shape, aspect ratio of the cross-section, and curvature path on the Dean vortices.

2.3.1 Effect of channel aspect ratio

Rectangle and square are the most conventional cross-sectional shapes that have been used in microchannels [74,77][79]. The aspect-ratio of the rectangle is a geometric factor that affects the lateral flow velocity, Dean vortices and their topology [77]. Several studies have focused on the effect of aspect ratio on the Dean vortices and the performance of micro-devices [11]. Norouzi and Biglari [77] investigated the effect of the aspect ratio of a rectangular curved duct on the Dean vortices by applying an analytical perturbation solution. Results showing the effect of this ratio in Figure 2-5(a) for d/h = 1/3 to 5 [77]. Their analytical solution showed that increasing the aspect ratio, changes the shape of Dean vortices and the distance between the core of vortices [77]. Decreasing the aspect ratio leads to a decrease in the lateral velocity of the flow. This implies that by decreasing the aspect ratio and moving from a square cross-section to a high aspect ratio, the mixing efficiency will be increased [80].

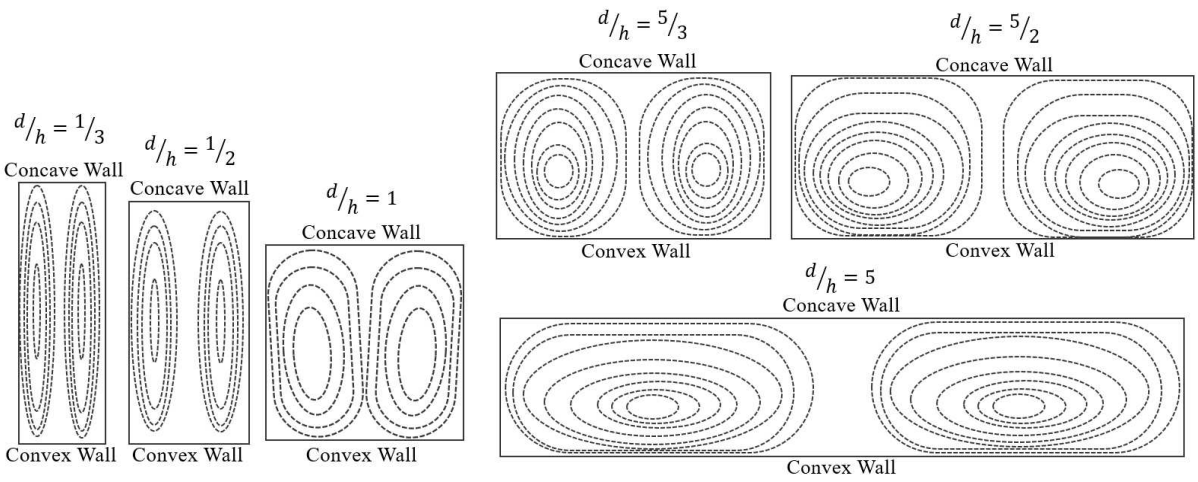

(a)

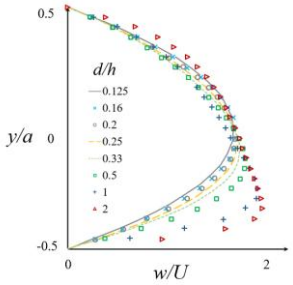

(b)

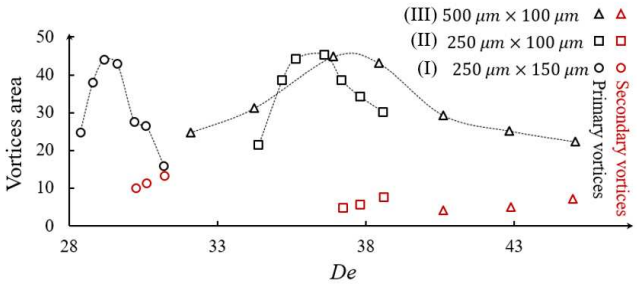

(c)

Figure 2-5 (a) Evaluation of the Dean vortices with aspect ratio, d/h =[1/3, 1/2,1, 5/3, 5/2, 5] *after* [77]; (b) axial velocity profiles for aspect ratios in the range of $0.125 \leq d/h \leq 2$ with non-dimensional channel width [79]. (c) The evaluation of Dean vortices area as a percentage of channel cross-sectional area with Dean number, *De*, for different aspect ratios: (I) d/h = 5/3, (II) d/h= 5/2, and (III) d/h= 5 [65]; Red dots represent the secondary Dean vortices.

In a similar work, Fellouah *et al.* [79] numerically determined the non-dimensional axial velocity profile over the non-dimensional channel width as shown in Figure 2-5(b). For aspect ratios in the range of $0.125 \leq d/h \leq 2$, increasing the aspect ratio of the microchannel forces the maximum velocity location to move toward the concave wall of the channel [79]. Also, the maximum velocity value is increasing by increasing the aspect ratio of the channel cross-section.

Another way to study the development of vortices in different aspect ratios is using the projected area occupied by the Dean vortices. This method is mostly used in experimental mixing studies where one of the streams is visualized with a dye. Figure 2-5(c) represents the evaluation of the projected cross-sectional area of Dean vortices as a percentage of channel cross-sectional area with the associated Dean numbers in different aspect ratios of d/h=5/3, 5/2, and 5 [65]. In Figure 2-5(c)-(I) where the aspect ratio is d/h =5/3, it can be seen that the projected area of the Dean vortices is less than 45% for most Dean numbers except for De = 29. By increasing the aspect ratio to d/h =5/2 as shown in Figure 2-5(c)-(II), the projected area increases for most Dean numbers. By increasing the aspect to d/h =5 as is shown in Figure 2-5(c)-(III), the range of high values of Dean number becomes smaller and the curve shape changes in comparison to the lower aspect ratios [65]. In Figure 2-5(c), the red dots represent the secondary Dean vortices that appear after the critical Dean number, De_c. In the cases shown in Figure 2-5(c), the critical Dean number is changing from 30 to 36 and then 40 by increasing the aspect ratio, d/h from 5/3 to 5/2, and 5 respectively. From Figure 2-5(c)-(II) to (III) it can also be observed that the projected area of the secondary vortices becomes larger with increasing aspect ratio [65].

Although increasing the aspect ratio leads to an increase in the strength of the vortices such as what shown in Figure 2-5(a), other numerical and experimental studies show that for extremely high aspect ratios, 8 <d/h< 40 the primary counter-rotating Dean vortices are converted to multiple pairs of counter-rotating vortices [79][74]. The number of these counter-rotating vortices depends on the Dean number, *De* and aspect ratio, d/h [74,79]. For a very high aspect ratio, d/h= 40 in a curved channel as shown in Figure 2-6 where $De_1 < De_2$ [74] it can be observed that multiple Dean vortices are formed beside each other. The formation of these vortices starts with the appearance of multiple mushroom shapes [74].

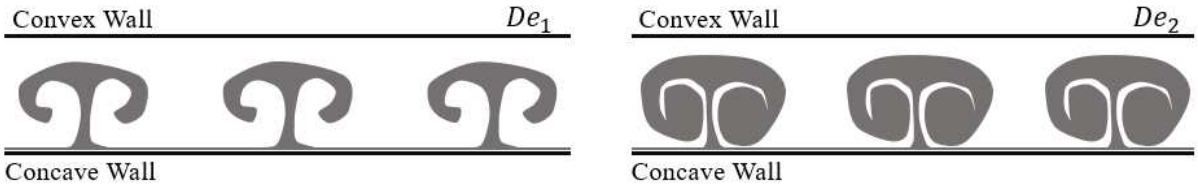

Figure 2-6 Dean vortices structures in a channel with a high aspect ratio, d/h of 40 *after* [74].

The aspect ratio of microchannels also influences the formation of secondary Dean vortices and their behavior [14]. Figure 2-7 shows the evolution of the critical Dean number, De_c with changing the aspect ratio, d/h. In this figure, the effect of the curvature ratio is obtained from different numerical and experimental works which sit in the range of 2.71 $\leq R_c/d \leq$ 20 [43,55,79,93–95]. From this figure and for R_c/d =10, it can be observed that for the aspect ratios within the range of 1/12 $\leq d/h <$ 0.125, the critical Dean number, De_c is almost constant. With increasing the aspect ratio in the range of 0.125 $\leq d/h <$ 0.25, the De_c increases from the local minimum to its maximum and by aspect ratio 1 it reaches its local minimum. By further increasing the aspect ratio to 1 $\leq d/h <$2, the De_c shows a slight increase. The same trend can be seen for d/R_c =12.5 and 7. For $d/R_c <$ 7 and $d/R_c >$12.5, it can be seen that the critical Dean number increases to its maximum and then reduces. This shows the variation in De with the aspect ratio changes without a clear correlation.

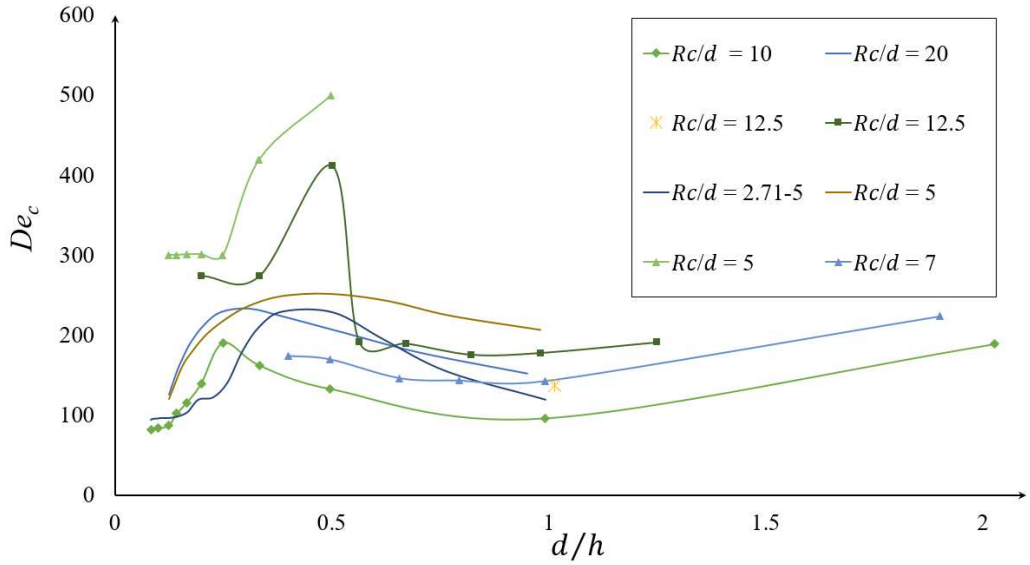

Figure 2-7 Evaluation of the critical Dean number De_c with the aspect ratio of the channel d/h for various curvature ratios, d/R_c [79].

2.3.2 The effect of cross-section shape

Several cross-section shapes such as circular [75,96–102], triangular [103,104] elliptical [83], and trapezoidal [13,105] have been studied, in addition to rectangular curved channels, to understand the effect of the cross-section shape on the properties of the Dean flow. For these cross-section shapes, the effect of the shape has been investigated regarding their applications in a microchannel such as particle sorting [76,106,107], micro-mixing [82,89,108], and heat transfer [93,95]. Table 2-4 includes a list of different cross-sectional shapes (of curved microchannels) and the range of De number investigated for each case. These cross-sections are used to study the flow behavior and the effect of geometry on the efficiency of the application.

Table 2-4 Different cross-section shapes studied in curved microchannel investigations.

Shape		Investigator(s)	Operational De
Square	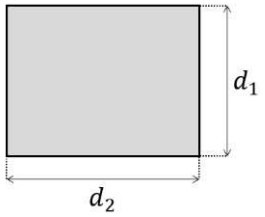	H. Fellouah *et al.* (2006) [79]	$10 < De < 400$
Circle	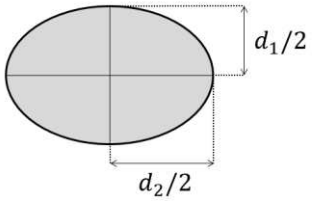	J. Siggers and S. Waters (2005) [64]	$10 < De < 15000$
Triangle	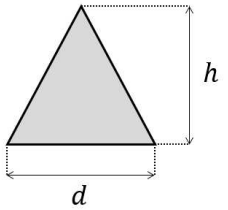	R. Filimonov and J. Sorvari (2017)[103]	$17 < De < 142$
Trapezoid	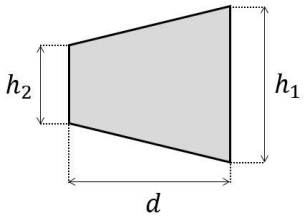	L. Wu *et al.* (2012) [105]	$2.64 < De < 21.12$

The literature review shows that the cross-section can affect the Dean vortices. For a channel with a square cross-section, the general shape of vortices is similar to the ones for circular cross-section as seen in Figure 2-8(a)-(I&II). This figure shows the pattern of vortices inside a circular channel for a low and a high De number [64]. In this scenario, the flow topology contains two counter-rotating vortices for $De<De_c$ shown in Figure 2-8(a)-(I) and a combination of two counter-rotating vortices and two secondary vortices are observed for $De > De_c$ depicted in Figure 2-8(a)-(II). For a circular cross-section, Siggers and Waters [64] used a numerical approach and showed that the critical Dean number, De_c is between 5 to 10 times larger than that for a square cross-

section channel under similar operating conditions. Chen *et al.* [109] used the helical membrane contractor channel with circular cross sections shown in Figure 2-8(a)-(III). It can be seen that Dean vortices are smaller and closer to the walls in comparison to a basic channel without membrane. In these type of channels Dean vortices are continuously renewing the boundary layer which leads to a consistent mixing of solutes throughout the liquid within the channel. By counteracting concentration polarization, this refreshed boundary layer significantly enhances the overall effectiveness of the liquid-liquid extraction process.

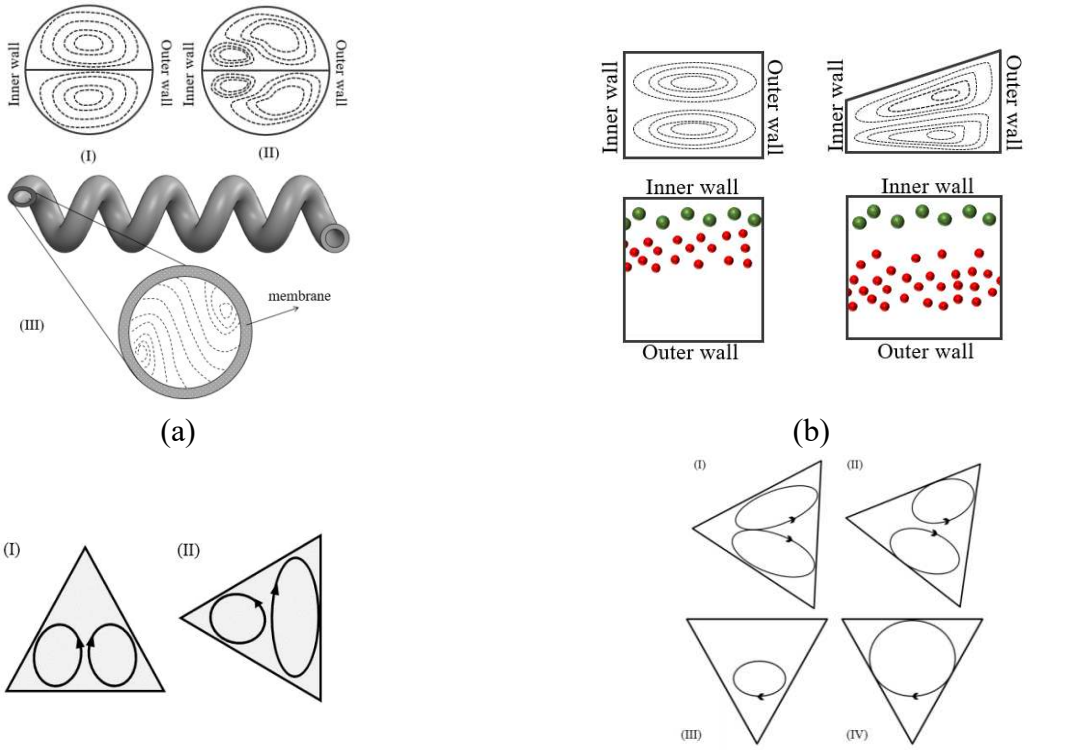

Figure 2-8 (a) Dean vortices in a circular cross-section: (I) for $De < De_c$, (II) for $De > De_c$ [64] and (III) in a helical membrane contractor; [109] (b) Dean vortices and particle separation equilibrium position in rectangular cross-section in comparison with a trapezoidal cross-section channel with different dimensions [105]. (c) Differences between Dean vortices in Top-Ward and Left-Ward cross-sections (d) Dean vortices in four twisted cross-sections *after* [103].

The ability to manipulate Dean vortices is an important factor that is limited in symmetrical cross-sections [110]. With a trapezoidal cross-section, Dean vortices can be controlled without active intervention [105]. In such cross-sections, either the convex wall or concave wall can serve as the smaller side and this choice will have distinct effects on the flow behavior. Wu *et al.* [105] conducted an experiment that showed that for $2<De<22$, changing the cross-section from a rectangle to a trapezoid by increasing the size of the concave wall makes the center of the Dean vortices move toward the concave wall as shown in Figure 2-8(b). For a particle sorting application, this leads to an increase in the space between the settling position of particles in the channel, making it a better choice for this application [104] [105].

The triangular cross-section is another shape that has been investigated, in a limited number of studies. Filimonov and Sorvari [103] investigated Dean vortices inside a serpentine microchannel with a triangular cross-section, by performing numerical simulations. For Dean numbers of, $De = 38$, 76 and 114 they showed that two symmetrical counter-rotating vortices form as is shown in Figure 2-8(c) part (I) [103]. With a 90° rotation of the cross-section, as can be seen in Figure 2-8(c) part (II), the two symmetric counter-rotating Dean vortices become asymmetric for the same range of Dean numbers [103]. It was shown that the leftward cross-section enhances the heat transfer in comparison to the upward cross-section [103]. This enhancement in the heat transfer can be accounted for by the better mixing due to the more powerful vortices observed in the channel [103]. Also twisting the cross-section along the channel leads to the formation of different patterns of Dean vortices as can be seen in Figure 2-8(d). Although these different Dean vortices patterns enhances the mixing, the enhancement is not significant [103].

In addition to the microchannels with usual cross-sections, microchannels with uncommon cross-section shapes have also been employed and studied [43][111]. Mixing in a microchannel

with an incomplete rectangular cross-section has been experimentally investigated for three Reynolds numbers of 1, 20, and 100 [111]. This microchannel is designed to enhance the mixing efficiency in the different units of the serpentine and compared with standard serpentine microchannels as shown in Figure 2-9(a). The comparison of the image intensities for the two geometries under different flow rates is shown in Figure 2-9(b). It indicates that mixing is almost accomplished from the second unit in the notched rectangular cross-section. However, in the conventional rectangular cross-section it is not expected until the final unit [111][112]. The sudden increase in the mixing index after the first unit is shown in Figure 2-9(b) for the notched rectangular cross-section. It indicates that the chaotic behavior of the flow inside this cross-section may contain extra flow structures in addition to the Dean vortices [113][111]. The additional flow structures that are generated in the flow pattern due to the interaction between the flow and geometry are known as secondary vortices which should not be mistaken with the secondary Dean vortices [51].

Figure 2-9(c) shows the flow visualization in three sections of a serpentine microchannel with changing rectangular cross-section using grooves as shown in Figure 2-9(d). The visualized planes on Figure 2-9(c) are shown in the microchannel diagram, including the normal section (plane 3), the section with a groove on one side in unit 4 (plane 1), and unit 5 (plane 2). Comparing plane 3 with plane 1 and 2, it can be realized that the Dean vortices become larger similar to what occurs in the rectangular cross-section with a higher aspect ratio [99]. A noticeable difference is in the stagnation area which is again not occupied by the Dean vortices [99].

A variable unconventional cross section can be also introduced by adding micropillar arrays in curved microchannels as shown in Figure 2-9(e). Micropillar arrays in general alter the organization of the flow by enhancing its complexity [114]. Particularly, the uneven splitting of laminar streamlines around the micropillar arrays result in size dependent, and predictable

trajectories for particles [114]. These structures demonstrate an enhanced particle manipulation through asymmetric bifurcation of laminar streamlines around micropillar arrays [114]. The advantages include enhanced separation efficiency and a substantial reduction in the required sample volume in the inner channel [115]. Despite these discernible benefits, investigations into their specific interaction with Dean vortices remain limited [115]. Figure 2-9(f) shows schematics of multi-vortex structures generated in an ultra-low aspect ratio spiral with fins. The generated flow structure contains helical vortices at the corner of the fins in addition to the Dean vortices [116]. This multi-vortex flow structure can be adjusted to variety of applications [116].

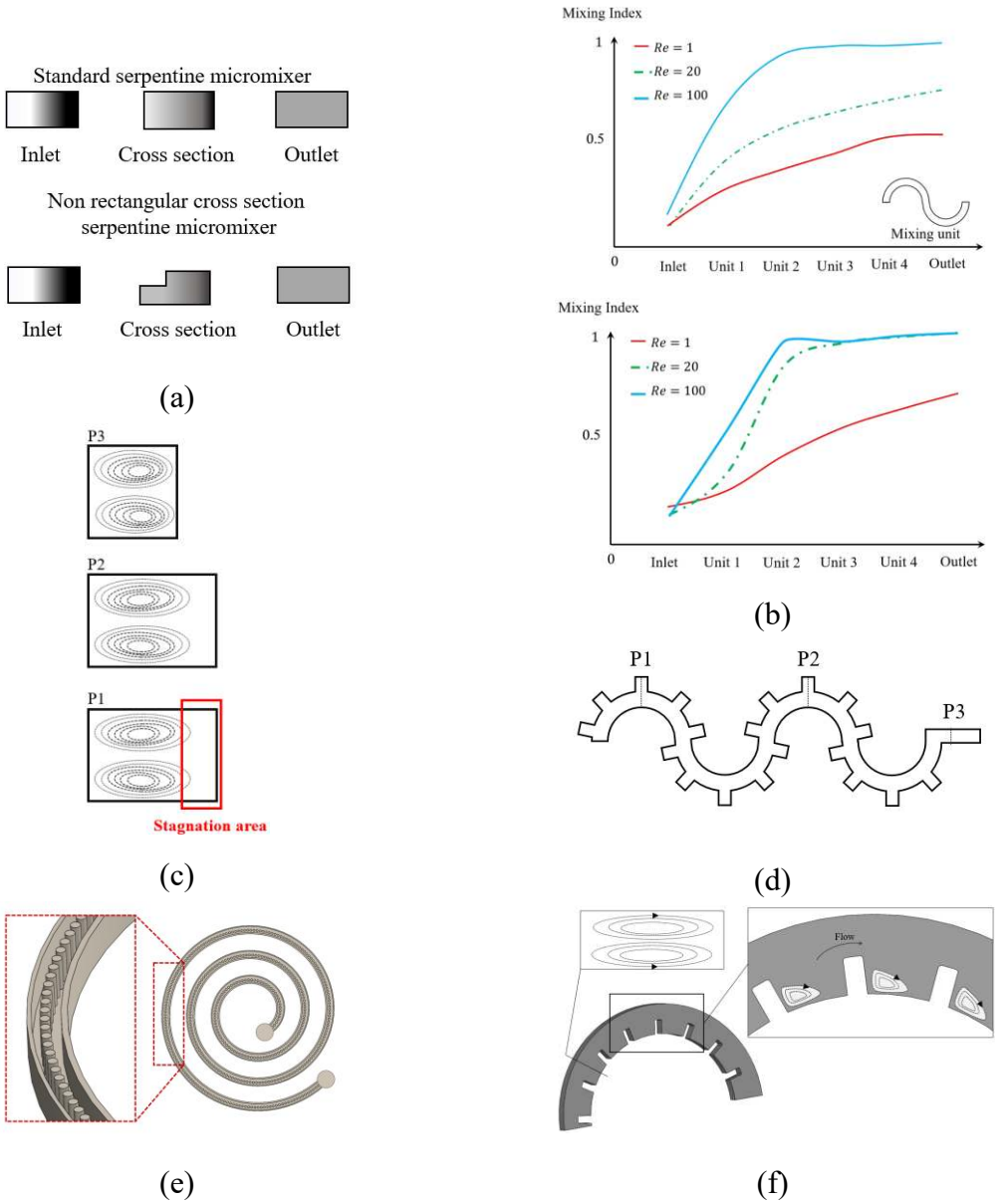

Figure 2-9 Uncommon cross-sections in curved microchannels. (a) Mixing comparison in serpentine with a rectangular and multi-rectangular cross-section in $Re = 100$ *after* [111] (b)The growth of mixing performance in different sections for $Re = (1, 20, 100)$ [111] (c) The effect of changing cross-section on the vortices in a serpentine channel with grooves *after* [99]. (d) The geometry of a serpentine channel with grooves added to enhance the mixing efficiency *after* [99] (e) Curved microchannels with micropillar structures *after* [116] (f) Ultra-low aspect ratio indented spiral generating multi-vortex *after* [114].

2.3.3 The effect of cross-section shape

Microchannel geometries are made from different combinations of a curved channel which is the basic structure of a curved microfluidic device [104]. The centerline of the segments generates a path which is referred to as the curvature path line [104]. The curvature path is important since it can increase or decrease the strength of Dean vortices [13,91,117], and also it can generate more complex flow structures [39]. The radius or direction of the curvature for each of the base segments dictates the flow behavior [104]. Most common path lines have either varying radius of curvature such as a spiral or changing curvature directions such as a serpentine [87][118]. Geometries excluding these categories are considered to have an unconventional path line [97].

A microchannel with a variation of radius of curvature of the channel path, a spiral microchannel, has been used to improve particle sorting and mixing performance [91][119]. In a spiral microchannel, flow enters from one of the ports either at the center of the spiral or on the outer revolution [91,107]. When flow enters the spiral microchannel from the center port, the flow moves toward the outer revolution where a general increase in the radius of curvature leads to a decrease in the Dean number [65]. As a result, the strength of generated Dean vortices decreases as the fluid moves towards the outer revolution [65]. When the flow enters the spiral from the port on the outer revolution, the radius of curvature decreases [91]. In this scenario the strength of Dean vortices will increase by moving towards the center of the spiral microchannel [91]. By increasing the Dean number towards the center of the microchannel, there is a possibility of reaching De_c indicating the generation of four Dean vortices [91].

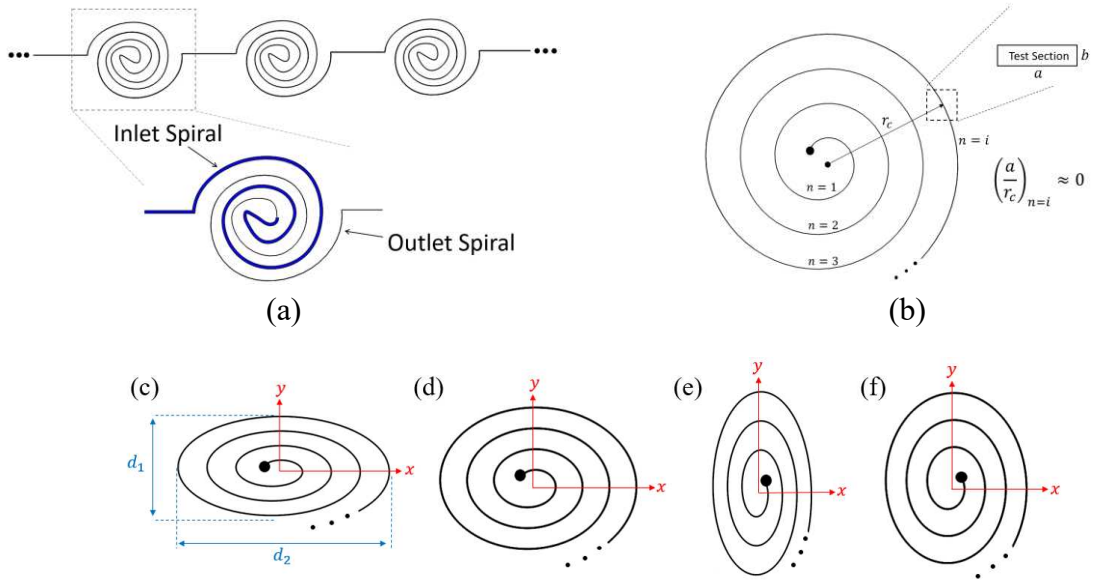

Figure 2-10 (a) Multi-stage spiral microchannel showing three stage microchannel and inlet and outlet spiral part of a single channel [91]. (b) The radius of curvature varies in spirals based on the number of the revolutions from one to infinity. The high radius of the curvature of the larger revolutions decreases the local Dean number [120]. (c)-(f) Elliptical spirals with different aspect ratios.

For spiral microchannels, by increasing the number of revolutions, the radius of curvature and the curvature ratio increases. As a result, for a high number of revolutions, the formation of Dean vortices will be suppressed due to the high curvature ratio [120]. In this scenario, to prevent a significant decrease in the Dean vortices power, a combination of several successive spiral microchannels with a fewer number of revolutions, Figure 2-10(a) can be used [91]. Considering the same length of the channel, using the multistage spiral microchannel results in more powerful Dean vortices in comparison to a single spiral with a higher number of revolutions [91]. Additionally, in a multiple spiral system multiple inlets can be added to each stage in order to inject a new phase, e.g. droplets and particles to the system at each stage [121]. This can be used in many applications such as generating a linear concentration gradient to enhance the drug performance prediction [121].

The aspect ratio of the whole spiral channel is another factor affecting the Dean vortices and flow structures [120]. The aspect ratio of the spiral channel is defined as d_2/d_1 where d_1 and d_2 are defined based on the spiral shape and orientation in Figure 2-10(c). Four different spirals with different aspect ratios of 3/2, 11/9, 9/11, and 2/3 can be seen in Figure 2-10(c)-(f), respectively. Despite the aspect ratio of the conventional spirals being equal to 1 (non-elliptical spiral), the radius of curvature in these cases varies frequently in each revolution [120]. This variation leads to frequent changes in the strength of the Dean vortices and the lateral velocity in the microchannel [120]. For cases with a high aspect ratio the difference between the velocity vectors and Dean vortices of the two sections is significant due to the high change in radius of curvature [120]. However, in the cases with the aspect ratio the differences in velocity vectors in the flow field are not noticeable [120]. These four spiral microchannels were designed for particle separation purposes [120]. The results of their studies show that the purest particle separation was obtained for Figure 2-10(c) where the lateral migration velocity is most significant compared to the other cases [120].

For serpentine microchannels, unlike the spiral, the radius of curvature is constant. However, the direction of the radius changes for each revolution. This means that the concave wall and convex wall frequently interchange and the pattern of Dean vortices evolve according to the direction of the curvature [89]. Multiple studies have investigated the benefits of flow patterns inside a serpentine channel as shown in Figure 2-11(a) for applications such as mixing [111][117][112], particle sorting [122][106] and encapsulation [123][124]. Figure 2-11(a) shows two sections from two revolutions of a serpentine with different curvature directions. The concave wall and convex wall change place in two sections as can be observed in the zoomed views and the Dean vortices are appeared in the same locations with respect to the convex wall [89]. The

maximum velocity moves laterally to a point closer to the concave wall. As a result of changes in the direction, the maximum velocity location changes after the transient section to the next curvature and the core of the Dean vortices relocates [89]. The idea for using this types of channels is that the transient section in addition to the Dean vortices provides a good mixing opportunity [80]. This can be inferred from the results of Figure 2-11(b) which shows the average mixing intensity as an indicator of mixing efficiency for a straight channel, square wave, and a 3-D serpentine. For Reynolds numbers in the range of $0 < Re < 80$, it can be seen that the average intensity is more than 80% which is higher than other investigated geometries [112].

Four sections of a serpentine segment are shown in Figure 2-11(c) with different view angles [117]. On the first velocity field, at $\theta = 0$ the pattern of vortices is completely different from what can be seen at $\theta = {}^{\pi}/_{2}$. This indicates that a transient section exists in the first quarter of this revolution [117]. From the other sections in Figure 2-11(c), it can be understood that as the flow moves further inside the revolution the Dean vortices form [117]. Figure 2-11(d) also shows the configuration of vortices on each of these sections. Although mixing performance in geometries with curvature direction variation is studied in many works, the evolution of Dean vortices that effect the mixing performance in this geometry has not been investigated to the knowledge of the authors.

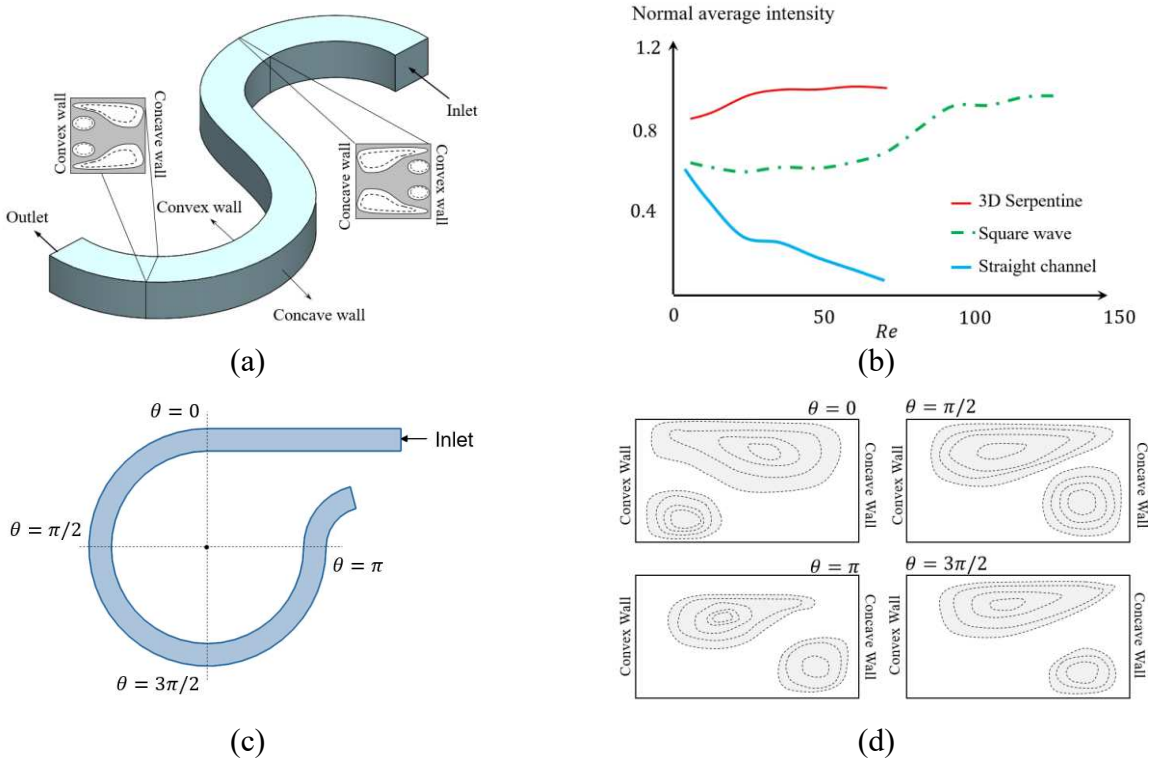

Figure 2-11 (a) Comparing Dean vortices topology in two sections from two opposite bends of a serpentine *after* [89]. (b) Comparison between the mixing intensity of three different types of microchannel: Serpentine, wavy square, and straight [89]. (c), (d) Dean vortices schematics in different sections in a unit of the serpentine *after* [117].

The channel centerline shape can affect the strength of Dean vortices or change the pattern of flow inside the channel to make new phenomena or even generate chaos [111]. Adding a divider or joint to the channel can easily disturb the flow pattern [111]. Therefore, unconventional geometries are sometimes used to enhance the performance of the microchannels through changing the microchannel centerline shape [97].

Figure 2-12(a) shows a microchannel geometry along with the Dean vortices, velocity vectors at different sections of the microchannel obtained in a numerical research undertaken for such an unconventional path with multiple bends [97]. The two flow streams are introduced to the channel Mixing has been studied for Reynolds numbers in the range of $0.5 < Re < 50$. Different directions,

sizes, and power for Dean vortices have been observed at different cross-sections of this channel [97]. Dean vortices split and their recombination enhanced the performance of the micromixer significantly [97]. It can be seen in Figure 2-12(a) that after joining two different flow streams from different curvatures the direction of rotation changes to follow the curvature of the channel. For different sections from a to i, with different channel dimensions the curvature of the channel determines the direction of the rotation not the maximum velocity or flow rate of the upstream flow. For instance, looking at the vortices before and after section h shown in Figure 2-12(a), it can be seen that direction of the Dean vortices changes from g to h, but remains constant from h to i. This behavior was considered to be related to the unconventional path of the flow [97].

Figure 2-12(b) shows the effect of the complex geometry on the mixing interfaces for the geometry shown in Figure 2-12(a). By changing the geometry the shape of interfacial lines between two fluids in a micromixer changes [97]. The pattern of the interfacial lines is associated to the existence and number of Dean vortices. At lower Reynolds numbers the Dean vortices are not observable. For $Re = 25$ in Figure 2-12(b) the interface line separates near the wall and this can be explained with the existence of Dean vortices. At higher Reynolds numbers such as 50 the interfacial line deformation indicates the existence of two secondary Dean vortices. Figure 2-12(c) also shows another unconventional path that generates additional flow structures in curved microchannels used for mixing [39].

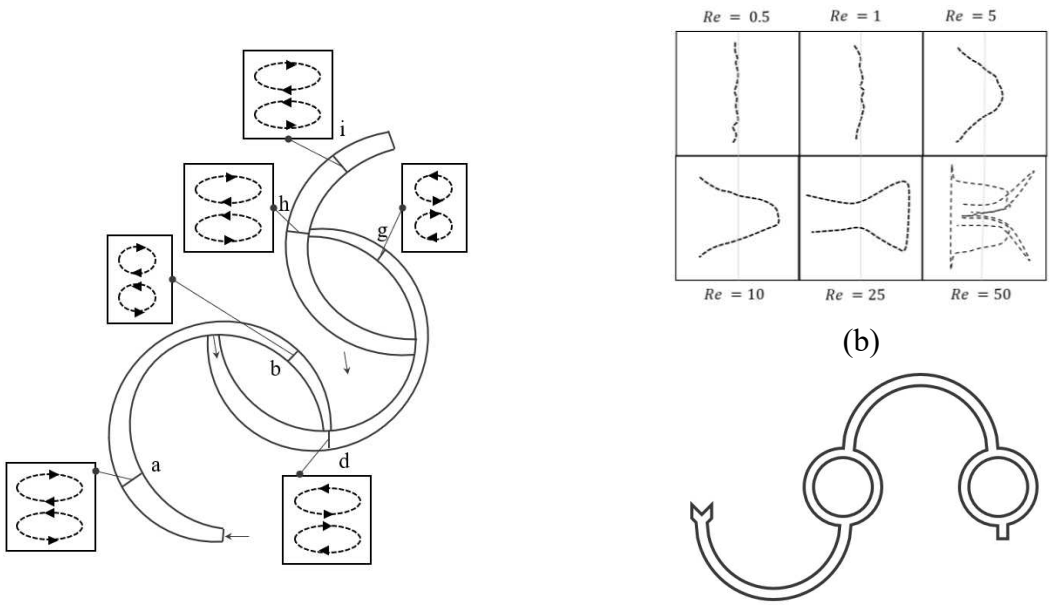

(a) (b) (c)

Figure 2-12 (a) An unconventional 3-D path designed for micromixers to use the power of Dean vortices [97] (b) The comparison of the interfacial lines for a single curved micromixer and a complex geometry a for *Re* numbers of 1, 5, 10, 25, and 50 *after* [97]. (c) Instances have been reported where the channel's design has induced the emergence of additional secondary flow patterns, alongside the typical Dean vortices. (c) shows an unconventional curved channel containing loops between the sections. In this case, entering the loops, the flow will experience a stagnation point *after* [39]. The complexity of the flow structure increases the mixing efficiency. The axis of vortices generating in this channel is normal to the axis of the longitudinal Dean vortices *after* [39].

2.4 The liquid-liquid two phased flow in curved channels

Droplet-based microfluidics is attracting extensive attention due to its high potential in research and medical applications. A common type for such devices are microfluidic systems that contain two immiscible fluids [125]. This system contains a main fluid flow in a microchannel known as the continuous phase and a second phase forming capsules inside it known as the dispersed phase [126–128]. There are many applications in areas such as medicine, biology and material science employing the potential of a two-phase flow in microfluidic devices.

Using such devices, a well-defined environment can be provided for investigation of an isolated cell. Biochemical reactions can be contained in a droplet to reduce the heat emission or processing time of the reaction and to fabricate materials with special properties. A droplet flowing in a curved channel is also one of the most common passive techniques used to enhance mixing inside the droplet [118]. In applications such as encapsulation of cells and drug delivery, the shear stresses formed due to the vortices inside the droplets can damage the living cells in some conditions [24]. The deformation of the capsule and its internal flow topology affect the performance of microfluidic devices or the procedures. For this purpose, several studies have investigated the effect of geometry on the topology of droplets and bubbles [129–136] and are reviewed in this section.

2.4.1 The effect of cross-section shape

To better understand the effect of Dean vortices on the droplet in a curved channel, it is important to briefly overview the internal flow topology of a droplet in a straight channel. Figure 2-13(a) represents the schematic of a droplet moving in the channel direction in a microchannel where the droplet size is in the order of the channel width [137]. The purple areas on the 3-D schematic of the droplet in Figure 2-13(a) indicate the contact surfaces between the channel wall and the droplet. I is assumed that the channel is rectangular, as a result, the droplet has a higher contact area at the top and bottom and a lower contact area at the sidewalls [137]. On the contact area, the droplet is subjected to stress from the walls. This stress is a resistance to the droplet movement against the flow direction. In addition to the contact area stress, the continuous phase applies stress to the droplet [137].

The flow topology schematic of the cross-section at the middle plane of the droplet is shown in Figure 2-13(b). The superposition of these two stresses forms four different eddies inside the droplet. On each half of the droplet, there are two pairs of counter-rotating vortices, V1-V3 and V2-V4. The rotation direction of each vortex is shown with blue arrows in Figure 2-13(b) [137].

Under the effect of these stresses in lower flow rates (0.5 μl/min), four vortices exist inside the droplet which is shown in Figure 2-13(c) through the contours of the flow streamlines. By ten times increasing the flow rate (5 μl/min), vortices on the back side of the droplet start to move forward and toward the edges of the droplet shown in Figure 2-13(d) [137]. As it is seen in Figure 2-13(e), the growth of the front side vortices leads to the elimination of the two counter-rotating vortices at the left-hand side [138–140] at the higher flow rate (20 μl/min). The change in the velocity distribution is perhaps the reason for the change in the number and shape of the flow vortices [137].

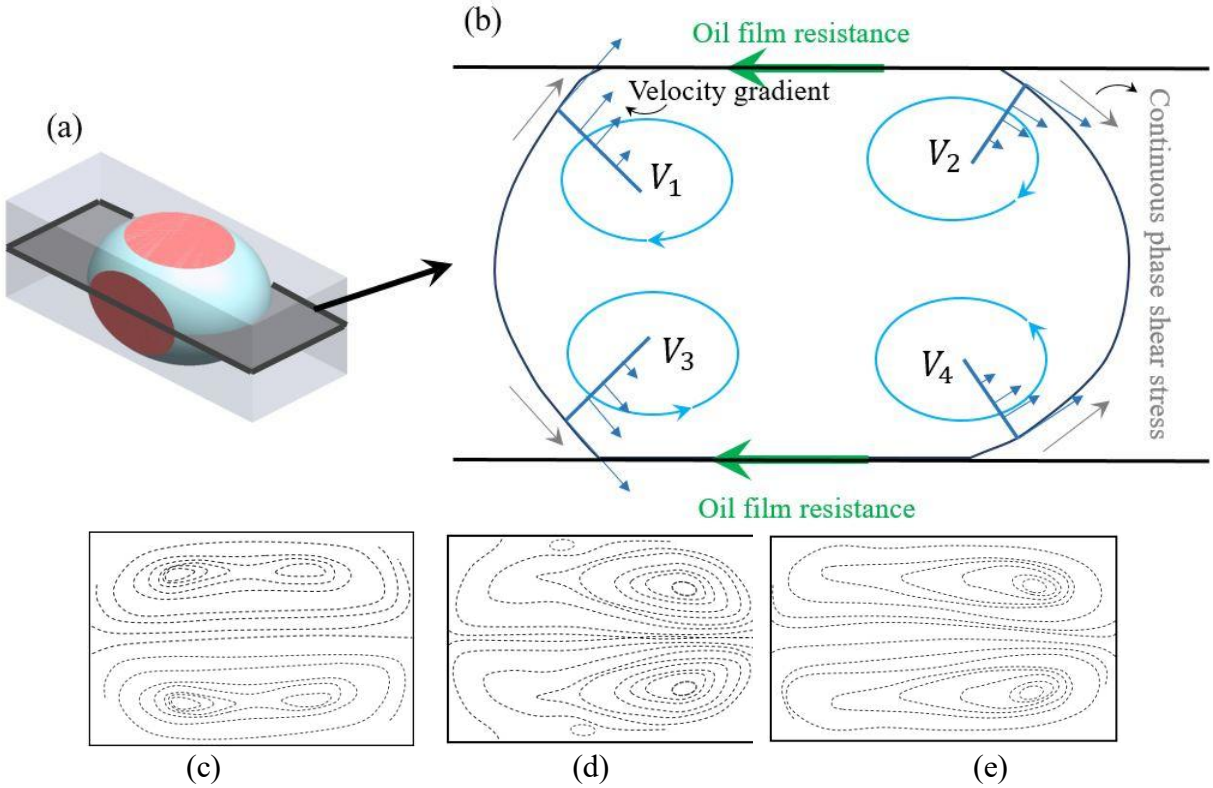

Figure 2-13 (a) Schematic of a droplet flowing in a straight channel. (b) Schematic of the flow structure inside the droplet on a cross-section shown with the blue plane ploted from *after* [137]. Streamlines of the flow inside the droplet at the center plane with the flow rate of (c) 0.5 µl/min, (d) 5µl/min and (e) 20 µl/min *after* [137] obtained experimentally.

2.4.2 Physics of flow inside the droplet in curved microchannels

The flow topology of a droplet inside both a straight channel and in a curved channel is compared using the experimental results shown in Figure 2-14, [141]. The internal flow velocity vectors and magnitude in the straight section of the microchannel is shown in Figure 2-14(a). These are representing the same physics as Figure 2-13 (e) with a pair of counter rotating vortices. The flow structure of the droplet entering the curved channel can be seen in Figure 2-14(b). When the droplet enters a single curved attached to the straight channel, the configuration of the vortices changes due to the asymmetric velocity gradient [141]. The higher velocity near the concave wall causes a shift in the vortices location toward the sides and the wall [141]. Close to the convex wall

the two vortices proceed to the middle and become larger with lower velocity [141]. It is worth noting that the number of vortices also increases to four similar to what is seen for the droplet inside a low flow rate of the continuous phase. However, with multiple curves or longer curves, the topology of the droplet significantly changes and the vortices are not symmetrical with respect to the centerline of the channel [141]. The maximum velocity position moves toward the concave wall due to the curvature effect. Thus, the relocated maximum velocity affects the symmetry of the flow inside a droplet and changes the configuration of vortices [141].

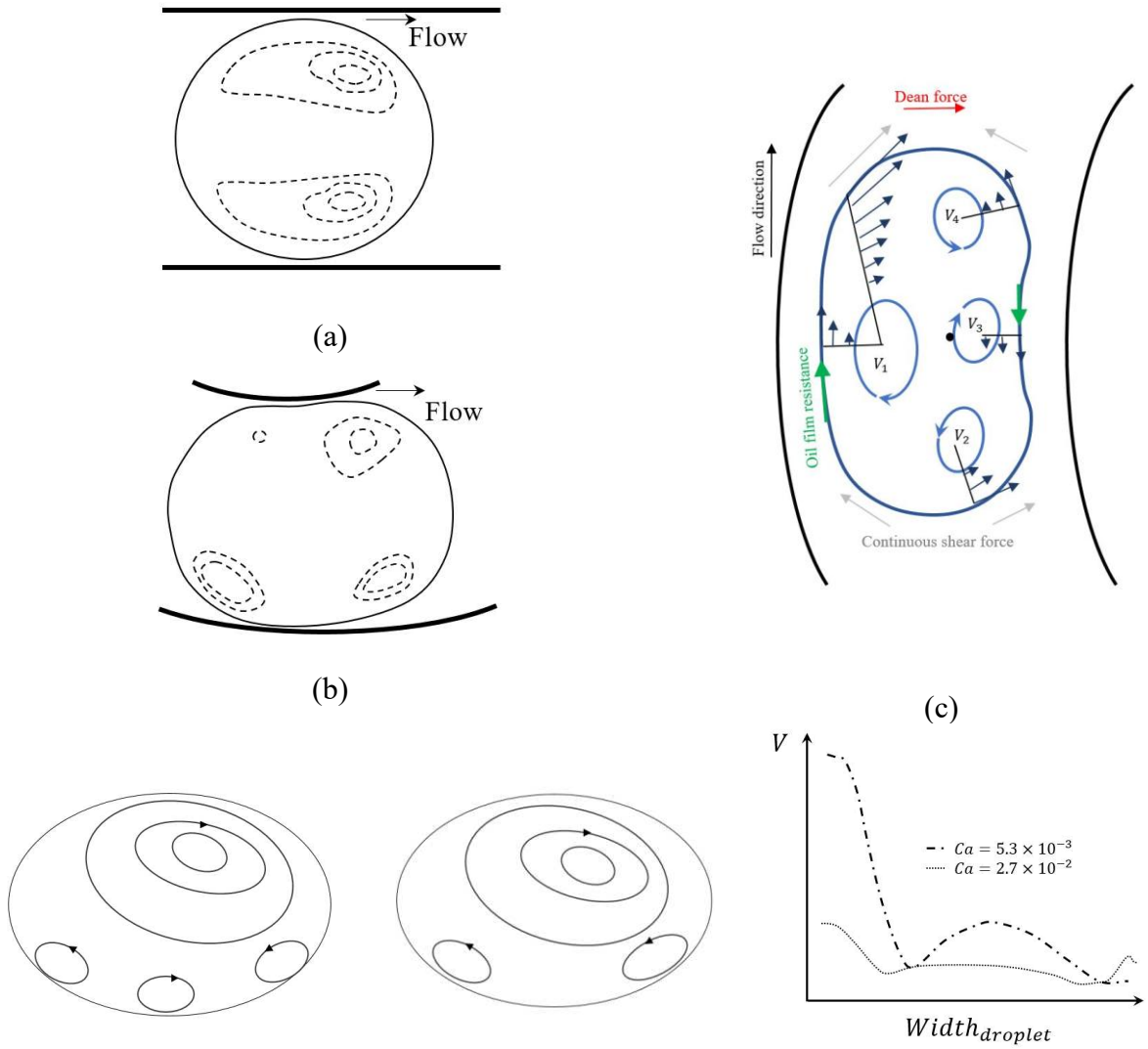

Figure 2-14 (a) Schematics of the flow inside a droplet in a straight microchannel. (b) Schematics of the flow inside a droplet entering a curved microchannel *after* [141]. (c) Schematic diagram of the forces in the middle plane of the droplet in a curved microchannel *after* [142]. Vortices inside the droplet in a curved microchannel with (d) $Ca = 5.3 \times 10^{-3}$, and (e) 2.7×10^{-2}. (f) Variation of the velocity magnitude along the width of the droplet *after* [143].

Figure 2-14 (c) shows the schematic of a droplet moving inside a curved channel. In this figure, comparable to Figure 2-14(b), the diagram of the vorticesin the droplet is illustrated as well as the velocity profiles inside the droplet. As is shown in this figure, near the concave wall a clockwise vortex (V1) forms which is larger than the others. This vortex is shaped in the higher

velocity area of the channel. Near the convex wall, three vortices appear in the curve, two counterclockwise (V2 and V3) on the sides and a clockwise vortex on the middle (V4). Similar to the droplet in the straight channel, the topology of the eddies will change by increasing the continuous phase velocity [142]. The clockwise vortex, V4 from Figure 2-14(c), disappears at high velocities while the other two vortices on the side that are moving counter-clockwise, i.e. V2 and V3 become larger [142].

Interfacial tension between continuous and dispersed phase is an important factor influencing the physics of flow in curved microchannel. This factor can be investigated using capillary number, $Ca = \frac{V\mu^2}{\sigma\mu'}$ where V is continuous phase velocity, μ is continuous phase dynamic viscosity, μ' is dispersed phase dynamic viscosity and σ is interfacial tension between continuous and dispersed phase. Figure 2-14(d)-(f) shows the results of an experiment conducted by Liu *et al.* [143] showing the effect of capillary number, Ca on the internal flow of a droplet in a curved channel. where the capillary number was changed by changing the velocity. Figure 2-14(d) shows the formation of four vortices at a low velocity of the continuous phase similar to what was illustrated in Figure 2-14(c). The three small vortices at the bottom of the droplet turn into two larger vortices by increasing the velocity which is shown in Figure 2-14(e). Though the size of the top vortices is the same for both capillary numbers, the vorticity of the one with a higher capillary number is more powerful than the one with a lower capillary number [143]. This can be further verified through Figure 2-14(f) showing the magnitude of the velocity on the vertical axis of the droplet.

2.4.3 Effect of microchannel geometry on the droplet topology

A circular capillary cross-section will distribute the stresses and forces uniformly on the droplet [137]. This uniformity leads to a simple and symmetrical flow pattern inside the droplet. Including the effect of curvature geometry to the discussion, such a pattern may no longer remain symmetrical. In rectangular cross-sections, due to the existence of corners and corner flow streams, the topology inside the droplet will change to a more complex shape [137].

Capillary number typically affects the deformability of the droplet [144]. With small Ca about less than 0.1 the droplet is stiff. The stiffness of the droplet maintains its spherical shape and reduces the effect of Dean vortices on the internal flow [144][145]. Without the changes in the shape of the droplet, the change of the velocity vectors on the boundary is the only parameter that affects the internal flow. Increasing the Ca increases the deformability of the droplet [144–146]. A more deformable droplet has a more complex internal flow structure due to the consistent motion of the boundary. Figure 2-15 shows the effect of Ca and Re on small and large droplets [143]. It can be seen from the figure that increasing the Ca leads to a completely deformed droplet where in smaller Ca both small and large droplets remain spherical. This figure shows the deformation for a large droplet and a small droplet [147] at different Reynolds numbers. The schematics of the droplets are shown for their top views in a straight channel after an experimental study [147].

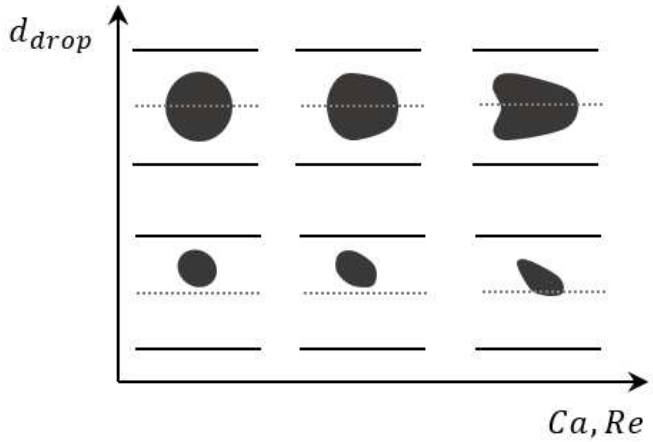

Figure 2-15 Deformability of capsules in a straight channel with lateral flow inlet *after* [147]**.**

In addition to the channel cross-section shape and capillary number, the droplet size ratio which can be defined as the ratio of droplet length to the width of the channel can significantly affect the topology of vortices inside the droplet [128][137]. A non-dimensional ratio of length to width of the droplet, β, which starts from 1 for spherical droplets [137] is used to identify droplet shape. To study the effect of β on the flow topology, an important principle is to keep the capillary number constant [143]. For β =1 in a straight channel, two counter-rotating vortices exist inside the droplet as is shown in Figure 2-16(a). By increasing β to 1.2, the droplet contains four vortices shown in Figure 2-16(b). Two powerful vortices are generated at the front which is in touch with the continuous phase and the other two form at the back of the droplet [137] [143].

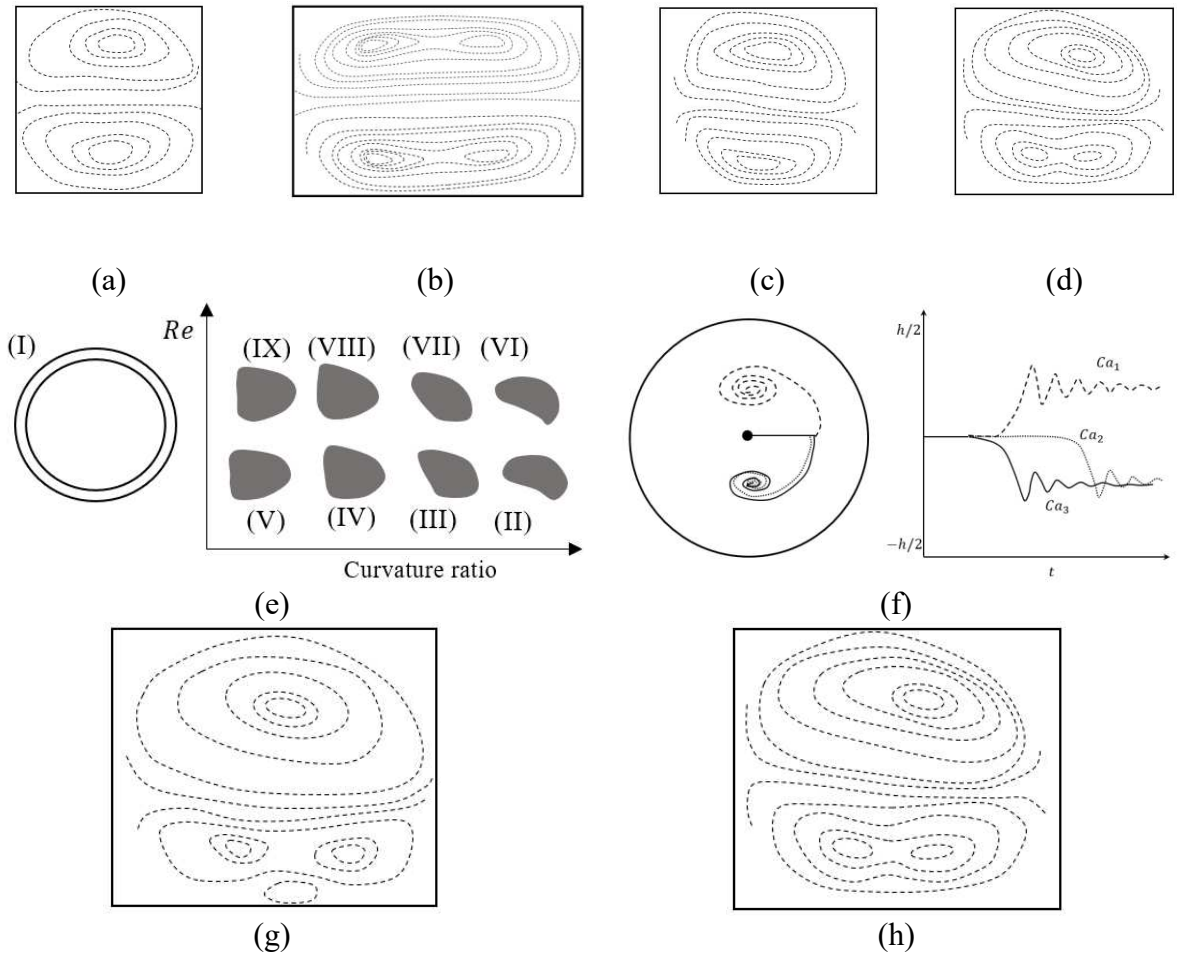

Figure 2-16 Schematics of the flow inside the droplet moving in a straight channel. (a) β = 1 *after* [143], (b) β = 1.2 [137]. Vortices inside the droplet with (c) β=1 and (d) β=1.1 at the same radius of curvature *after* [142]. (e) Droplet shape with different curvature ratios in a donut shape channel and for curvature ratios of (0.05,0.5,0.9) and *Re* of 0.04 and 10 (f) the trajectory of the droplets with size ratio less than 0.3 on the cross section of a curved channel (on the left) and among the channel length (on the right) [145]. Vortices inside the droplet with (g) *R* = 2.2 mm and (h) *R* = 6.2 mm at the same β = 1.1 *after* [142].

For a curved channel, when β is equal to 1 a similar topology to the straight channel can be observed [143][137]. However, the vortex which is closer to the concave wall occupies more than half of the area [137]. The vortices of the Dean flow are also stronger near the concave wall [137]shown in Figure 2-16(c). Such stronger vortices, which can be seen in both the continuous phase and the droplet is possibly based on the velocity difference between the concave and convex

wall. As is shown in Figure 2-16(d), by increasing the droplet size, the vortex closer to the convex wall breaks into two smaller vortices [143]. It is important to note that both droplets shown in Figure 2-16(c)-(d) have the same capillary number.

Reducing the droplet size to less than 1/2 of the channel provides the ability to study the deformability of the droplet. It can replicate the blood cells in a curved vessel [148] or the internal shear rate [149] and flow behavior inside the droplet which affects the cells in encapsulation [43,150]. Size ratio, ε can be defined as the ratio of droplet diameter, a to the channel diameter, d. For droplets with $0.3 < \varepsilon < 0.6$ droplet starts to form a cone shape moving forward through the channel as it is shown in Figure 2-16(e). Decreasing the curvature ratio less than 0.3 changes the spherical shape of the droplet to a bean shape [145] shown in Figure 2-16(IV,V,VIII,IX). Increasing the *Re* number and decreasing the *Ca* number also increases the droplet deformability [145].

The small size ratio also affects the trajectory of the droplets in a curved channel [145,146]. Figure 2-16(f) shows the trajectory of droplets released on the symmetry plane of the channel where $Re = 20$. Droplets follow a spiral trajectory to its equilibrium position which is at the center of the Dean vortex. The Ca number of the droplet determines whether the droplet moves toward the upper or lower vortex. In lower capillary numbers where the droplet is more deformable, it moves through the upper spiral to the center of the upper vortex. However, for a higher Ca number where the droplet is stiffer, the motion is toward the lower vortex with the lower spiral. With increasing the Capillary number to higher values droplet remains longer on the center axis and starts to follow the spiral trajectory further into the channel [145].

The radius of curvature is another important parameter affecting the flow pattern in the curved channel and strength of the generated Dean vortices [142]. This parameter also affects the flow

topology inside the droplet [142]. Figure 2-16(g)-(h) shows the flow pattern inside a droplet in two different radii of curvatures. In both cases β is equal to 1.1. As it can be seen from the figure, the number of vortices and their location are the same as the droplet passing through the curved channel with a lower radius. However, the single vortex near the concave wall vanishes in Figure 2-16(h). With decreasing the radius of curvature, the vortex near the concave wall becomes stronger, and its area increases which is similar to increasing the vortices power in the continuous phase. Stronger vortices create a stronger shear rate and increase the rotating velocity inside the droplet. Figure 2-16(g) shows a droplet with $\beta = 1.1$ in a channel with a radius of curvature equals 2.2 mm. Inside the droplet four vortices are formed on strong large vortex near the concave wall. Two vortices near the concave wall close to the trailing edge and leading edge of the droplet and one vortex close to the convex wall [142].

2.5 Conclusion

This chapter aims to build a fundamental understanding of the Dean flow phenomenon in curved microchannels as a basis for intentional geometric modifications that can induce and control vortices in microfluidic systems. The physics of Dean flow and the formation of Dean vortices in curved channels are examined, followed by an investigation into the relationship between the Dean number and vortex configuration. Several equations have been introduced in the literature for calculating the Dean number. The variation in these formulations, despite referring to the same physical phenomenon, introduces inconsistencies in interpretation and limits the comparability of results across studies. To address this, the most common versions of the Dean number equation are compiled and presented. These formulations are grouped into numerical and experimental categories based on their prevalent usage in computational or experimental studies, highlighting the different assumptions embedded in each approach.

The effect of geometrical properties on the formation and characteristics of Dean vortices is analyzed to identify structural features that can be used to manipulate flow behavior. Channel cross-sectional shapes, including circular, triangular, square, rectangular, and trapezoidal, are reviewed in the context of single-phase and multiphase flows. In rectangular geometries, a range of aspect ratios is evaluated, and the conditions under which multiple vortex pairs emerge are discussed. Modifications in channel curvature and the implementation of non-planar three-dimensional paths are also assessed. These parameters are recognized as passive design elements for controlling vortex formation. Serpentine channels are primarily used to enhance mixing, while spiral geometries are typically employed for inertial separation as a distinction that informs the inlet design modifications evaluated in subsequent chapters.

Droplet behavior in curved flow environments is also reviewed, with attention to internal vortex structures and deformation patterns. Droplets in curved channels have been shown to contain four internal vortices rather than the two typically seen in straight channels. The influence of droplet stiffness, Capillary number, size, and curvature radius on internal flow structure and deformation is discussed in detail. Stiffer droplets respond less to the external flow, and those with lower Capillary numbers exhibit reduced deformability. These properties not only affect internal dynamics but also influence migration trajectories, with a transition in the settling path from the upper to the lower channel half observed as the Capillary number increases.

Although significant progress has been made in characterizing Dean vortices and their applications, predictive understanding of their behavior and interactions with suspended phases remains limited. This lack of clarity represents a challenge for rational microfluidic design involving curved geometries. By consolidating prior knowledge and identifying key geometric and flow parameters, this review provides the analytical basis for later experimental investigations, in

which Dean vortices are intentionally introduced into micro-hydrocyclone inlets to enhance performance at lower flow rates.

References

[1] G. M. Whitesides, “What comes next?,” Lab on a Chip, vol. 11, no. 2, pp. 191–193, 2011, doi: 10.1039/c0lc90101f.

[2] J. B. Angell, S. C. Terry, and P. W. Barth, “Silicon micromechanical devices,” Micromechanics and MEMS: Classic and Seminal Papers to 1990, vol. 248, no. 4, pp. 38–49, 1997, doi: 10.1109/9780470545263.sect1.

[3] T. Luo, L. Fan, R. Zhu, and D. Sun, “Microfluidic single-cell manipulation and analysis: Methods and applications,” Micromachines, vol. 10, no. 2, pp. 1–31, 2019, doi: 10.3390/mi10020104.

[4] Q. Feng, J. Sun, and X. Jiang, “Microfluidics-mediated assembly of functional nanoparticles for cancer-related pharmaceutical applications,” Nanoscale, vol. 8, no. 25, pp. 12430–12443, 2016, doi: 10.1039/c5nr07964k.

[5] G. Luo, L. Du, Y. Wang, and K. Wang, “Recent developments in microfluidic device-based preparation, functionalization, and manipulation of nano- and micro-materials,” Particuology, vol. 45, pp. 1–19, 2019, doi: 10.1016/j.partic.2018.10.001.

[6] S. Zhang, Y. Wang, P. Onck, and J. den Toonder, “A concise review of microfluidic particle manipulation methods,” Microfluidics and Nanofluidics, vol. 24, no. 4, pp. 1–20, 2020, doi: 10.1007/s10404-020-2328-5.

[7] A. A. S. Bhagat, H. Bow, H. W. Hou, S. J. Tan, J. Han, and C. T. Lim, “Microfluidics for cell separation,” Medical and Biological Engineering and Computing, vol. 48, no. 10, pp. 999–1014, 2010, doi: 10.1007/s11517-010-0611-4.

[8] C. D. Chin, V. Linder, and S. K. Sia, “Lab-on-a-chip devices for global health: Past studies and future opportunities,” Lab on a Chip, vol. 7, no. 1, pp. 41–57, 2007, doi: 10.1039/b611455e.

[9] S. A. Soper et al., “Point-of-care biosensor systems for cancer diagnostics/prognostics,” Biosensors and Bioelectronics, vol. 21, no. 10, pp. 1932–1942, 2006, doi: 10.1016/j.bios.2006.01.006.

[10] A. J. Tüdos, G. A. J. Besselink, and R. B. M. Schasfoort, “Trends in miniaturized total analysis systems for point-of-care testing in clinical chemistry,” Lab on a Chip, vol. 1, no. 2, pp. 83–95, 2001, doi: 10.1039/b106958f.

[11] J. Zhang et al., “Fundamentals and applications of inertial microfluidics: A review,” Lab on a Chip, vol. 16, no. 1, pp. 10–34, 2016, doi: 10.1039/c5lc01159k.

[12] H. Bow, I. V. Pivkin, M. Diez-Silva, S. J. Goldfless, and M. Dao, “A microfabricated deformability-based flow cytometer with application to malaria,” Lab on a Chip, vol. 11, no. 6, pp. 1065–1073, 2011, doi: 10.1039/c0lc00472c.

[13] A. Al-Halhouli, W. Al-Faqheri, B. Alhamarneh, L. Hecht, and A. Dietzel, “Spiral microchannels with trapezoidal cross section fabricated by femtosecond laser ablation in glass for

the inertial separation of microparticles," Micromachines, vol. 9, no. 4, 2018, doi: 10.3390/mi9040171.

[14] V. Srinivasan, V. K. Pamula, and R. B. Fair, "An integrated digital microfluidic lab-on-a-chip for clinical diagnostics on human physiological fluids," Lab on a Chip, vol. 4, no. 4, pp. 310–315, 2004, doi: 10.1039/b403341h.

[15] V. Srinivasan, V. K. Pamula, and R. B. Fair, "Droplet-based microfluidic lab-on-a-chip for glucose detection," Analytica Chimica Acta, vol. 507, no. 1, pp. 145–150, 2004, doi: 10.1016/j.aca.2003.12.030.

[16] Z. Mao and C. Yang, "Micro-mixing in chemical reactors: A perspective," Chinese Journal of Chemical Engineering, vol. 25, no. 4, pp. 381–390, 2017, doi: 10.1016/j.cjche.2016.09.012.

[17] A. Huebner et al., "Quantitative detection of protein expression in single cells using droplet microfluidics," Chemical Communications, vol. 2, no. 12, pp. 1218–1220, 2007, doi: 10.1039/b618570c.

[18] X. Yu et al., "The Importance of Dean Flow in Microfluidic Nanoparticle Synthesis: A ZIF-8 Case Study," Small Methods, vol. 2300603, pp. 1–9, 2023, doi: 10.1002/smtd.202300603.

[19] D. M. Ratner, E. R. Murphy, M. Jhunjhunwala, D. A. Snyder, K. F. Jensen, and P. H. Seeberger, "Microreactor-based reaction optimization in organic chemistry - Glycosylation as a challenge," Chemical Communications, no. 5, pp. 578–580, 2005, doi: 10.1039/b414503h.

[20] S. Chen et al., "Preparation of Coenzyme Q10 nanostructured lipid carriers for epidermal targeting with high-pressure microfluidics technique," Drug Development and Industrial Pharmacy, vol. 39, no. 1, pp. 20–28, 2013, doi: 10.3109/03639045.2011.650648.

[21] C. T. Lo, A. Jahn, L. E. Locascio, and W. N. Vreeland, "Controlled self-assembly of monodisperse niosomes by microfluidic hydrodynamic focusing," Langmuir, vol. 26, no. 11, pp. 8559–8566, 2010, doi: 10.1021/la904616s.

[22] E. Sutterby, P. Thurgood, S. Baratchi, K. Khoshmanesh, and E. Pirogova, "Microfluidic Skin-on-a-Chip Models: Toward Biomimetic Artificial Skin," Small, vol. 16, no. 39, pp. 1–17, 2020, doi: 10.1002/smll.202002515.

[23] H.-H. Jeong, S. H. Jin, B. J. Lee, T. Kim, and C.-S. Lee, "Microfluidic static droplet array for analyzing microbial communication on a population gradient," Lab on a Chip, vol. 2019-Novem, pp. 1–10, 2012, doi: 10.1039/x0xx00000x.

[24] S. Neethirajan, I. Kobayashi, M. Nakajima, D. Wu, S. Nandagopal, and F. Lin, "Microfluidics for food, agriculture and biosystems industries," Lab on a Chip, vol. 11, no. 9, pp. 1574–1586, 2011, doi: 10.1039/c0lc00230e.

[25] B. Deng and J. De Ruiter, "Application of Microfluidics in the Production and," 2019.

[26] K. Schroen et al., "Droplet microfluidics for food and nutrition applications," Micromachines, vol. 12, no. 8, 2021, doi: 10.3390/mi12080863.

[27] R. N. Pudake, N. Chauhan, and C. Kole, Nanoscience for sustainable agriculture. 2019. doi: 10.1007/978-3-319-97852-9.

[28] J. Luecha, A. Hsiao, S. Brodsky, G. L. Liu, and J. L. Kokini, "Green microfluidic devices made of corn proteins," Lab on a Chip, vol. 11, no. 20, pp. 3419–3425, 2011, doi: 10.1039/c1lc20726a.

[29] Y. J. Juang and J. S. Chang, "Applications of microfluidics in microalgae biotechnology: A review," Biotechnology Journal, vol. 11, no. 3, pp. 327–335, 2016, doi: 10.1002/biot.201500278.

[30] M. Maeki, Microfluidics for pharmaceutical applications. Elsevier Inc., 2018. doi: 10.1016/B978-0-12-812659-2.00004-1.

[31] R. Ran, Q. Sun, T. Baby, D. Wibowo, A. P. J. Middelberg, and C. X. Zhao, "Multiphase microfluidic synthesis of micro- and nanostructures for pharmaceutical applications," Chemical Engineering Science, vol. 169, pp. 78–96, 2017, doi: 10.1016/j.ces.2017.01.008.

[32] S. I. Hamdallah et al., "Microfluidics for pharmaceutical nanoparticle fabrication: The truth and the myth," International Journal of Pharmaceutics, vol. 584, no. January, 2020, doi: 10.1016/j.ijpharm.2020.119408.

[33] C. Chen et al., "Passive mixing inside microdroplets," Micromachines, vol. 9, no. 4, pp. 1–16, 2018, doi: 10.3390/mi9040160.

[34] P. Sajeesh and A. K. Sen, "Particle separation and sorting in microfluidic devices: A review," Microfluidics and Nanofluidics, vol. 17, no. 1, pp. 1–52, 2014, doi: 10.1007/s10404-013-1291-9.

[35] A. C. Hatch, A. Patel, N. R. Beer, and A. P. Lee, "Passive droplet sorting using viscoelastic flow focusing," Lab on a Chip, vol. 13, no. 7, pp. 1308–1315, 2013, doi: 10.1039/c2lc41160a.

[36] M. Bayareh, "An updated review on particle separation in passive microfluidic devices," Chemical Engineering and Processing - Process Intensification, vol. 153, no. June, p. 107984, 2020, doi: 10.1016/j.cep.2020.107984.

[37] V. Narayanamurthy et al., "Advances in passively driven microfluidics and lab-on-chip devices: A comprehensive literature review and patent analysis," RSC Advances, vol. 10, no. 20, pp. 11652–11680, 2020, doi: 10.1039/d0ra00263a.

[38] H. Yasutaka et al., "A Micromixer Using the Chaos of Secondary Flow: Rotation Effect of Channel on the Chaos of Secondary Flow," Open Journal of Fluid Dynamics, vol. 2012, no. 04, pp. 195–201, Dec. 2012, doi: 10.4236/OJFD.2012.24A021.

[39] A. A. Mouza, C. M. Patsa, and F. Schönfeld, "Mixing performance of a chaotic micro-mixer," Chemical Engineering Research and Design, vol. 86, no. 10, pp. 1128–1134, 2008, doi: 10.1016/j.cherd.2008.04.009.

[40] D. Bothe, C. Stemich, and H. J. Warnecke, "Fluid mixing in a T-shaped micro-mixer," Chemical Engineering Science, vol. 61, no. 9, pp. 2950–2958, 2006, doi: 10.1016/j.ces.2005.10.060.

[41] Y. K. Suh and S. Kang, “A review on mixing in microfluidics,” Micromachines, vol. 1, no. 3, pp. 82–111, 2010, doi: 10.3390/mi1030082.

[42] Y. Chen and Z. Deng, “Hydrodynamics of a droplet passing through a microfluidic T-junction,” Journal of Fluid Mechanics, vol. 819, pp. 401–434, 2017, doi: 10.1017/jfm.2017.181.

[43] S. J. S. Lee et al., “Hydrodynamics of a droplet passing through a microfluidic T-junction,” Lab on a Chip, vol. 9, no. 3, pp. 1–13, 2009, doi: 10.1038/srep44072.

[44] A. Russom, A. K. Gupta, S. Nagrath, D. Di Carlo, J. F. Edd, and M. Toner, “Differential inertial focusing of particles in curved low-aspect-ratio microchannels,” New Journal of Physics, vol. 11, pp. 0–9, 2009, doi: 10.1088/1367-2630/11/7/075025.

[45] A. Volpe, C. Gaudiuso, and A. Ancona, “Sorting of particles using inertial focusing and laminar vortex technology: A review,” Micromachines, vol. 10, no. 9, 2019, doi: 10.3390/mi10090594.

[46] V. Kumar, M. Aggarwal, and K. D. P. Nigam, “Mixing in curved tubes,” Chemical Engineering Science, vol. 61, no. 17, pp. 5742–5753, 2006, doi: 10.1016/j.ces.2006.04.040.

[47] W. R. Dean, “The stream-line motion of fluid in a curved pipe,” The London, Edinburgh, and Dublin Philosophical Magazine and Journal of Science, vol. 5, no. 30, pp. 673–695, 1928, doi: 10.1080/14786440408564513.

[48] H. Amini, W. Lee, and D. Di Carlo, “Inertial microfluidic physics,” Lab on a Chip, vol. 14, no. 15, pp. 2739–2761, 2014, doi: 10.1039/c4lc00128a.

[49] D. Di Carlo, “Inertial microfluidics,” Lab on a Chip, vol. 9, no. 21, pp. 3038–3046, 2009, doi: 10.1039/b912547g.

[50] H. Tang, J. Niu, H. Jin, S. Lin, and D. Cui, “Geometric structure design of passive label-free microfluidic systems for biological micro-object separation,” Microsystems and Nanoengineering, vol. 8, no. 1, 2022, doi: 10.1038/s41378-022-00386-y.

[51] Q. Zhao, D. Yuan, J. Zhang, and W. Li, “A review of secondary flow in inertial microfluidics,” Micromachines, vol. 11, no. 5, pp. 1–23, 2020, doi: 10.3390/MI11050461.

[52] H. Afsaneh and R. Mohammadi, “Microfluidic platforms for the manipulation of cells and particles,” Talanta Open, vol. 5, p. 100092, 2022, doi: 10.1016/j.talo.2022.100092.

[53] S. Mishra, J. Mukherjee, D. Chaturvedi, R. Jain, and P. Dandekar, The mechanisms and properties of inertial microfluidics: from fundamental models to biomedical applications, vol. 27, no. 12. Springer Berlin Heidelberg, 2023. doi: 10.1007/s10404-023-02692-x.

[54] D. Jiang, S. Liu, and W. Tang, “Fabrication and Manipulation of Non-Spherical Particles in Microfluidic Channels: A Review,” Micromachines, vol. 13, no. 10, 2022, doi: 10.3390/mi13101659.

[55] K. C. Cheng and R. C. Lin, “Fully Developed Laminar Flow in Curved Rectangular Channels.,” Journal of Fluids Engineering, no. (1976), 1976.

[56] K. C. Cheng and M. Akiyama, “Laminar forced convection heat transfer in curved rectangular channels,” International Journal of Heat and Mass Transfer, vol. 13, no. 3, pp. 471–490, 1970, doi: 10.1016/0017-9310(70)90144-4.

[57] S. W. Churchill, “Comprehensive Correlating Equations for Heat, Mass and Momentum Transfer in Fully Developed Flow in Smooth Tubes,” Industrial and Engineering Chemistry Fundamentals, vol. 16, no. 1, pp. 109–116, 1977, doi: 10.1021/i160061a021.

[58] G. M. Corcos and J. R. Sellars, “On the stability of fully developed flow in a pipe,” Journal of Fluid Mechanics, no. Leite 1959, 1968.

[59] S. A. Berger, L. Talbot, and L.-S. Yao, “Flow in curved pipes,” 1983.

[60] G. S. Williams, C. W. Hubbell, and G. H. Fenkell, “Experiments at Detroit, Mich., on the effect of curvature upon the flow of water in pipes.,” Transactions of the American Society of Civil Engineers, vol. 1, no. 47, pp. 1-196., 1902, doi: 10.1126/science.1.3.84.

[61] J. Eustice, “Flow of Water in Curved Pipes,” Proceedings of the Royal Society of London. Series A, pp. 107–118, 1910.

[62] J. Eustice, “Experiments on stream-line motion in curved pipes,” Proceedings of the Royal Society of London. Series A, Containing Papers of a Mathematical and Physical Character, vol. 85, no. 576, pp. 119–131, 1911, doi: 10.1098/rspa.1911.0026.

[63] W. R. Dean, “ LXXII. The stream-line motion of fluid in a curved pipe (Second paper) ,” The London, Edinburgh, and Dublin Philosophical Magazine and Journal of Science, vol. 5, no. 30, pp. 673–695, 1928, doi: 10.1080/14786440408564513.

[64] J. H. Siggers and S. L. Waters, “Steady flows in pipes with finite curvature,” Physics of Fluids, vol. 17, no. 7, pp. 1–18, 2005, doi: 10.1063/1.1955547.

[65] N. Nivedita, P. Ligrani, and I. Papautsky, “Dean flow dynamics in low-aspect ratio spiral microchannels,” Scientific Reports, vol. 7, no. October 2016, pp. 1–10, 2017, doi: 10.1038/srep44072.

[66] B. Bara and J. H. Masliyah, “An experimental and numerical study of the Dean problem: Flow development towards two-dimensional multiple solutions,” Journal of Fluid Mechanics, vol. 244, pp. 339–376, 1992, doi: 10.1017/S0022112092003100.

[67] O. O. Mojola, “on Secondary Flow in Streamwise Corners.,” Journal de mecanique appliquee, vol. 4, no. 2, pp. 177–196, 1980.

[68] S. A. Berger and L. Talbot, “Flow in curved pipes.,” Annual Review of Fluid Mechanics, vol. 4, no. 15, p. 262, 1983.

[69] R. S. Srivastava and D. J. McConalogue, “Motion of a fluid in a curved tube,” Proceedings of the Royal Society of London. Series A. Mathematical and Physical Sciences, vol. 307, no. 1488, pp. 37–53, 1968, doi: 10.1098/rspa.1968.0173.

[70] T. Harirchian and S. V Garimella, “A systematic investigation of the effects of microchannel width, depth, and aspect ratio on convective boiling heat transfer and flow regimes in parallel microchannels,” Heat Transfer Summer Conference, vol. 43567, pp. 1–10, 2009.

[71] S. A. Berger and L. Talbot, “Flow in curved pipes.,” Annual review of fluid mechanics, vol. 4, no. 15, p. 262, 1983, doi: 10.1146/annurev.fl.15.010183.002333.

[72] E. J, “Flow of water in curved pipes.,” Proceedings of the Royal Society of London., vol. xxiii, pp. 113–117, 1910.

[73] M. Van Dyke, “Extended Stokes series: Laminar flow through a loosely coiled pipe,” Journal of Fluid Mechanics, vol. 86, no. 1, pp. 129–145, 1978, doi: 10.1017/S0022112078001032.

[74] P. M. Ligrani and R. D. Niver, “Flow visualization of Dean vortices in a curved channel with 40 to 1 aspect ratio.,” Physics of Fluids, vol. 31, no. 12, Dec. 1988, pp. 3605–3617, 1988, doi: 10.1063/1.866877.

[75] S. Kim and S. J. Lee, “Measurement of Dean flow in a curved micro-tube using micro digital holographic particle tracking velocimetry,” Experiments in Fluids, vol. 46, no. 2, pp. 255–264, 2009, doi: 10.1007/s00348-008-0555-8.

[76] K. W. Seo, Y. S. Choi, and S. J. Lee, “Dean-coupled inertial migration and transient focusing of particles in a curved microscale pipe flow,” Experiments in Fluids, vol. 53, no. 6, pp. 1867–1877, 2012, doi: 10.1007/s00348-012-1403-4.

[77] M. Norouzi and N. Biglari, “An analytical solution for Dean flow in curved ducts with rectangular cross section,” Physics of Fluids, vol. 25, no. 5, 2013, doi: 10.1063/1.4803556.

[78] P. B. Howell, D. R. Mott, J. P. Golden, and F. S. Ligler, “Design and evaluation of a Dean vortex-based micromixer,” Lab on a Chip, vol. 4, no. 6, pp. 663–669, 2004, doi: 10.1039/b407170k.

[79] B. Bara and J. H. Masliyah, “An experimental and numerical study of the Dean problem: Flow development towards two-dimensional multiple solutions,” Journal of Fluid Mechanics, vol. 244, pp. 339–376, 1992, doi: 10.1017/S0022112092003100.

[80] H. Fellouah, C. Castelain, A. Ould El Moctar, and H. Peerhossaini, “A criterion for detection of the onset of Dean instability in Newtonian fluids,” European Journal of Mechanics, B/Fluids, vol. 25, no. 4, pp. 505–531, 2006, doi: 10.1016/j.euromechflu.2005.11.002.

[81] V. S. Duryodhan, R. Chatterjee, S. Govind Singh, and A. Agrawal, “Mixing in planar spiral microchannel,” Experimental Thermal and Fluid Science, vol. 89, no. August, pp. 119–127, 2017, doi: 10.1016/j.expthermflusci.2017.07.024.

[82] S. Baheri Islami and M. Khezerloo, “Enhancement of mixing performance of non-newtonian fluids using curving and grooving of microchannels,” Journal of Applied Fluid Mechanics, vol. 10, no. 1, pp. 127–141, 2017, doi: 10.18869/acadpub.jafm.73.238.26374.

[83] D. Ma, Y. Zhang, and Y. Chen, “Effects of microchannel cross-section shape on particle focusing,” 2019 IEEE International Conference on Manipulation, Manufacturing and Measurement on the Nanoscale, 3M-NANO 2019 - Proceedings, pp. 237–240, 2019, doi: 10.1109/3M-NANO46308.2019.8947374.

[84] R. Altay, A. A. Yetisgin, K. Erdem, and A. Koşar, “The effect of varying radius of curvature on mixing in elliptical spiral microchannels,” Chemical Engineering and Processing - Process Intensification, vol. 164, no. April, 2021, doi: 10.1016/j.cep.2021.108401.

[85] S. Ookawara, D. Street, and K. Ogawa, “Numerical study on development of particle concentration profiles in a curved microchannel,” Chemical Engineering Science, vol. 61, no. 11, pp. 3714–3724, 2006, doi: 10.1016/j.ces.2006.01.016.

[86] I. D. Johnston, M. B. McDonnell, C. K. L. Tan, D. K. McCluskey, M. J. Davies, and M. C. Tracey, “Dean flow focusing and separation of small microspheres within a narrow size range,” Microfluidics and Nanofluidics, vol. 17, no. 3, pp. 509–518, 2014, doi: 10.1007/s10404-013-1322-6.

[87] K. Yong Chung, M. E. Brewster, and G. Belfort, “Dean Vortices with Wall Flux in a Curved Channel Membrane System: 2. The velocity field,” AIChE Journal, vol. 42, no. 2, pp. 347–358, 1996, doi: 10.1252/jcej.31.683.

[88] F. Schönfeld and S. Hardt, “Simulation of Helical Flows in Microchannels,” AIChE Journal, vol. 50, no. 4, pp. 771–778, 2004, doi: 10.1002/aic.10071.

[89] S. Kim and S. J. Lee, “Micro holographic PTV measurements of Dean flows in a curved micro-tube,” Proceedings of the 12th Asian Congress of Fluid Mechanics, 18–21 August 2008, Daejeon, Korea, no. August, pp. 689–690, 2008.

[90] F. Jiang, K. S. Drese, S. Hardt, M. Küpper, and F. Schönfeld, “Helical flows and chaotic mixing in curved micro channels,” AIChE Journal, vol. 50, no. 9, pp. 2297–2305, 2004, doi: 10.1002/aic.10188.

[91] M. Jarrahi, C. Castelain, and H. Peerhossaini, “Secondary flow patterns and mixing in laminar pulsating flow through a curved pipe,” Experiments in Fluids, vol. 50, no. 6, pp. 1539–1558, 2011, doi: 10.1007/s00348-010-1012-z.

[92] A. P. Sudarsan and V. M. Ugaz, “Fluid mixing in planar spiral microchannels,” Lab on a Chip, vol. 6, no. 1, pp. 74–82, 2006, doi: 10.1039/b511524h.

[93] L. Li, P. Wu, and Z. Luo, “Dean flow assisted single cell and bead encapsulation for high performance single cell expression profiling,” ACS Sensors, vol. 4, no. 5, pp. 1299–1305, 2019, doi: 10.1021/acssensors.9b00171.

[94] T. T. Chandratilleke and A. Nursubyakto, “Numerical prediction of secondary flow and convective heat transfer in externally heated curved rectangular ducts,” International Journal of Thermal Sciences, vol. 42, no. 2, pp. 187–198, 2003, doi: 10.1016/S1290-0729(02)00018-2.

[95] S. Thangam and N. Hur, “Laminar secondary flows in curved rectangular ducts,” Journal of Fluid Mechanics, vol. 217, pp. 421–440, 1990, doi: 10.1017/S0022112090000787.

[96] Y. Komiyama, F. Mikami, K. Okui, and T. Hori, “Laminar faced convection heat transfer in curved channels of rectangular cross section,” Heat transfer. Japanese research, vol. 13.3, pp. 68–91, 1984.

[97] J. K. Chen, W. J. Luo, and R. J. Yang, “Electroosmotic flow driven by DC and AC electric fields in curved microchannels,” Japanese Journal of Applied Physics, vol. 45, no. 10 A, pp. 7983–7990, 2006, doi: 10.1143/JJAP.45.7983.

[98] T. S. Sheu, S. J. Chen, and J. J. Chen, “Mixing of a split and recombine micromixer with tapered curved microchannels,” Chemical Engineering Science, vol. 71, pp. 321–332, 2012, doi: 10.1016/j.ces.2011.12.042.

[99] J. C. Chu, J. T. Teng, and R. Greif, “Experimental and numerical study on the flow characteristics in curved rectangular microchannels,” Applied Thermal Engineering, vol. 30, no. 13, pp. 1558–1566, 2010, doi: 10.1016/j.applthermaleng.2010.03.008.

[100] A. Alam and K. Y. Kim, “Analysis of mixing in a curved microchannel with rectangular grooves,” Chemical Engineering Journal, vol. 181–182, no. May 2019, pp. 708–716, 2012, doi: 10.1016/j.cej.2011.12.076.

[101] V. Dore, D. Tsaoulidis, and P. Angeli, “Mixing patterns in water plugs during water/ionic liquid segmented flow in microchannels,” Chemical Engineering Science, vol. 80, pp. 334–341, 2012, doi: 10.1016/j.ces.2012.06.030.

[102] N. Xiang, Q. Dai, Y. Han, and Z. Ni, “Circular-channel particle focuser utilizing viscoelastic focusing,” Microfluidics and Nanofluidics, vol. 23, no. 2, pp. 1–10, 2019, doi: 10.1007/s10404-018-2184-8.

[103] Y. Agrawal, L. Talbot, and K. Gong, “Laser anemometer study of flow development in curved circular pipes,” Journal of Fluid Mechanics, vol. 85, no. 3, pp. 497–518, 1978, doi: 10.1017/S0022112078000762.

[104] R. Filimonov and J. Sorvari, “Numerical study on the effect of cross-section orientation on fluid flow and heat transfer in a periodic serpentine triangular microchannel,” Applied Thermal Engineering, vol. 125, pp. 366–376, 2017, doi: 10.1016/j.applthermaleng.2017.07.027.

[105] M. A. Raoufi et al., “Fabrication of unconventional inertial microfluidic channels using wax 3D printing,” Soft Matter, no. 16, pp. 2448–2459, 2020.

[106] L. Wu, G. Guan, H. W. Hou, A. A. S. Bhagat, and J. Han, “Separation of leukocytes from blood using spiral channel with trapezoid cross-section,” Analytical Chemistry, vol. 84, no. 21, pp. 9324–9331, 2012, doi: 10.1021/ac302085y.

[107] S. S. Kuntaegowdanahalli, A. A. S. Bhagat, G. Kumar, and I. Papautsky, “Inertial microfluidics for continuous particle separation in spiral microchannels,” Lab on a Chip, vol. 9, no. 20, pp. 2973–2980, 2009, doi: 10.1039/b908271a.

[108] I. D. Johnston, M. B. Mcdonnell, C. K. L. Tan, D. K. Mccluskey, M. J. Davies, and M. C. Tracey, “Dean flow focusing and separation of small microspheres within a narrow size range,” Microfluidics and Nanofluidics, vol. 17, pp. 509–518, 2014, doi: 10.1007/s10404-013-1322-6.

[109] S. W. Lee and S. S. Lee, “Rotation effect in split and recombination micromixing,” Sensors and Actuators, B: Chemical, vol. 129, no. 1, pp. 364–371, 2008, doi: 10.1016/j.snb.2007.08.038.

[110] J. Chen, C. Zhou, B. Xie, and J. Zhang, “Simulation of the enhancement of Dean flow on the liquid–liquid extraction in membrane contactors,” Separation and Purification Technology, vol. 285, no. November 2021, p. 120384, 2022, doi: 10.1016/j.seppur.2021.120384.

[111] M. Rafeie, S. Hosseinzadeh, R. A. Taylor, and M. E. Warkiani, “New insights into the physics of inertial microfluidics in curved microchannels. I. Relaxing the fixed inflection point assumption,” Biomicrofluidics, vol. 13, no. 3, pp. 1–15, 2019, doi: 10.1063/1.5109004.

[112] J. Clark, M. Kaufman, and P. S. Fodor, “Mixing enhancement in serpentine micromixers with a non-rectangular cross-section,” Micromachines, vol. 9, no. 3, 2018, doi: 10.3390/mi9030107.

[113] R. H. Liu et al., “Passive mixing in a three-dimensional serpentine microchannel,” Journal of Microelectromechanical Systems, vol. 9, no. 2, pp. 190–197, 2000, doi: 10.1109/84.846699.

[114] A. D. Stroock et al., “Chaotic Mixer for microchannels,” American Association for the Advancement of Science, vol. 295, no. 5555, pp. 647–651, 2016.

[115] Z. Geng, Y. Ju, W. Wang, and Z. Li, “Continuous blood separation utilizing spiral filtration microchannel with gradually varied width and micro-pillar array,” Sensors and Actuators, B: Chemical, vol. 180, pp. 122–129, 2013, doi: 10.1016/j.snb.2012.06.064.

[116] Z. Geng, Y. Ju, Q. Wang, W. Wang, and Z. Li, “Multi-component continuous separation chip composed of micropillar arrays in a split-level spiral channel,” RSC Advances, vol. 3, no. 34, pp. 14798–14806, 2013, doi: 10.1039/c3ra41906a.

[117] S. Shen, X. Wang, and Y. Niu, “Multi-vortex regulation for efficient fluid and particle manipulation in ultra-low aspect ratio curved microchannels,” Micromachines, vol. 12, no. 7, 2021, doi: 10.3390/mi12070758.

[118] A. Shamloo, P. Vatankhah, and A. Akbari, “Analyzing mixing quality in a curved centrifugal micromixer through numerical simulation,” Chemical Engineering and Processing - Process Intensification, vol. 116, pp. 9–16, 2017, doi: 10.1016/j.cep.2017.03.008.

[119] A. P. Sudarsan and V. M. Ugaz, “Fluid mixing in planar spiral microchannels,” Lab on a Chip, vol. 6, no. 1, pp. 74–82, 2006, doi: 10.1039/b511524h.

[120] M. Madadelahi and A. Shamloo, “Droplet-based flows in serpentine microchannels: Chemical reactions and secondary flows,” International Journal of Multiphase Flow, vol. 97, pp. 186–196, 2017, doi: 10.1016/j.ijmultiphaseflow.2017.08.010.

[121] A. A. S. Bhagat, S. S. Kuntaegowdanahalli, and I. Papautsky, “Continuous particle separation in spiral microchannels using dean flows and differential migration,” Lab on a Chip, vol. 8, no. 11, pp. 1906–1914, 2008, doi: 10.1039/b807107a.

[122] K. Erdem, V. E. Ahmadi, A. Kosar, and L. Kuddusi, “Differential sorting of microparticles using spiral microchannels with elliptic configurations,” Micromachines, vol. 11, no. 4, 2020, doi: 10.3390/MI11040412.

[123] S. Shen et al., “Construction of multiple concentration gradients for single-cell level drug screening,” Microsystems and Nanoengineering, vol. 9, no. 1, 2023, doi: 10.1038/s41378-023-00516-0.

[124] J. Zhang, W. Li, M. Li, G. Alici, and N. T. Nguyen, “Particle inertial focusing and its mechanism in a serpentine microchannel,” Microfluidics and Nanofluidics, vol. 17, no. 2, pp. 305–316, 2014, doi: 10.1007/s10404-013-1306-6.

[125] G. D. Nicodemus and S. J. Bryant, “Cell encapsulation in biodegradable hydrogels for tissue engineering applications,” Tissue Engineering - Part B: Reviews, vol. 14, no. 2, pp. 149–165, 2008, doi: 10.1089/ten.teb.2007.0332.

[126] C. Kantak, Q. Zhu, S. Beyer, T. Bansal, and D. Trau, “utilizing microfluidics to synthesize polyethylene glycol microbeads for forster resonance enery transfer based glucose sensing,” vol. 6, no. 2, 2012.

[127] M. P. Boruah, A. Sarker, P. R. Randive, S. Pati, and K. C. Sahu, “Tuning of regimes during two-phase flow through a cross-junction,” Physics of Fluids, vol. 33, no. 12, 2021, doi: 10.1063/5.0071743.

[128] S. Y. Teh, R. Lin, L. H. Hung, and A. P. Lee, “Droplet microfluidics,” Lab on a Chip, vol. 8, no. 2, pp. 198–220, 2008, doi: 10.1039/b715524g.

[129] X. Casadevall i Solvas and A. De Mello, “Droplet microfluidics: Recent developments and future applications,” Chemical Communications, vol. 47, no. 7, pp. 1936–1942, 2011, doi: 10.1039/c0cc02474k.

[130] R. Seemann, M. Brinkmann, T. Pfohl, and S. Herminghaus, “Droplet based microfluidics,” Reports on Progress in Physics, vol. 75, no. 1, 2012, doi: 10.1088/0034-4885/75/1/016601.

[131] R. Azadi, J. Wong, and D. S. Nobes, “Determination of fluid flow adjacent to a gas/liquid interface using particle tracking velocimetry (PTV) and a high-quality tessellation approach,” Experiments in Fluids, vol. 62, no. 3, pp. 1–20, 2021, doi: 10.1007/s00348-020-03103-5.

[132] S. Ansari, Y. Yusuf, R. Sabbagh, and D. S. Nobes, “Determining the pressure distribution of a multi-phase flow through a pore space using velocity measurement and shape analysis,” Measurement Science and Technology, vol. 30, no. 5, p. 054004, Apr. 2019, doi: 10.1088/1361-6501/AB0AFC.

[133] R. Azadi and D. S. Nobes, “Local flow dynamics in the motion of slug bubbles in a flowing mini square channel,” International Journal of Heat and Mass Transfer, vol. 178, p. 121588, Oct. 2021, doi: 10.1016/J.IJHEATMASSTRANSFER.2021.121588.

[134] R. Azadi, J. Wong, and David. S. Nobes, “Experimental and analytical investigation of meso-scale slug bubble dynamics in a square capillary channel,” Physics of Fluids, vol. 32, no. 8, p. 083304, Aug. 2020, doi: 10.1063/5.0016241.

[135] R. Azadi and David. S. Nobes, “On the three-dimensional features of a confined slug bubble in a flowing square capillary,” Physics of Fluids, vol. 33, no. 3, p. 033327, Mar. 2021, doi: 10.1063/5.0043508.

[136] J. Raffel, S. Ansari, and D. S. Nobes, “An Experimental Investigation of Flow Phenomena in a Multi-Stage Micro Tesla Valve,” Journal of Fluids Engineering, no. c, 2021, doi: 10.1115/1.4051401.

[137] S. Ansari, M. Bayans, F. Rasimarzabadi, and D. S. Nobes, “Flow visualization of the Newtonian and non- Newtonian behavior of fluids in a Tesla-diode valve,” 5th International Conference on Experimental Fluid Mechanics – ICEFM 2018 Munich, Munich, Germany, July 2-4, 2018, 2018.

[138] Y. Saffar, D. S. Nobes, and R. Sabbagh, “Experimental Investigation of the Motion and Deformation of Droplets in Curved Microchannel,” 2023, doi: 10.1021/acs.iecr.3c01623.

[139] C. Yan, “Flow topology and its transformation inside droplets traveling in rectangular microchannels,” Physics of Fluids, vol. 32, no. 5, p. 052009, 2020, doi: 10.1063/5.0004549.

[140] S. R. Hodges, O. E. Jensen, and J. M. Rallison, “The motion of a viscous drop through a cylindrical tube,” Journal of Fluid Mechanics, vol. 501, no. 501, pp. 279–301, 2004, doi: 10.1017/S0022112003007213.

[141] M. Oishi, H. Kinoshita, T. Fujii, and M. Oshima, “Simultaneous measurement of internal and surrounding flows of a moving droplet using multicolour confocal micro-particle image velocimetry (micro-PIV),” Measurement Science and Technology, vol. 22, no. 10, 2011, doi: 10.1088/0957-0233/22/10/105401.

[142] H. Kinoshita, S. Kaneda, T. Fujii, and M. Oshima, “Three-dimensional measurement and visualization of internal flow of a moving droplet using confocal micro-PIV,” Lab on a Chip, vol. 7, no. 3, pp. 338–346, 2007, doi: 10.1039/b617391h.

[143] D. Malsch et al., “μPIV-Analysis of Taylor flow in micro channels,” Chemical Engineering Journal, vol. 135, no. SUPPL. 1, pp. 166–172, 2008, doi: 10.1016/j.cej.2007.07.065.

[144] Z. Liu, M. Li, Y. Pang, L. Zhang, Y. Ren, and J. Wang, “Flow characteristics inside droplets moving in a curved microchannel with rectangular section,” Physics of Fluids, vol. 31, no. 2, 2019, doi: 10.1063/1.5080373.

[145] Z. Liu, L. Zhang, Y. Pang, X. Wang, and M.-P. investigation of the internal flow transitions inside droplets traveling in a rectangular microchannel Li, “Micro-PIV investigation of the internal flow transitions inside droplets traveling in a rectangular microchannel,” Microfluidics and Nanofluidics, vol. 21, no. 12, pp. 1–8, 2017, doi: 10.1007/s10404-017-2019-z.

[146] L. Zhu and L. Brandt, “The motion of a deforming capsule through a corner,” Journal of Fluid Mechanics, vol. 770, pp. 374–397, 2015, doi: 10.1017/jfm.2015.157.

[147] A. Lafzi et al., “Inertial migration of deformable droplets in a microchannel,” Physics of Fluids, vol. 26, no. 11, pp. 7–10, 2020, doi: 10.1063/1.4901884.

[148] S. Ebrahimi, P. Balogh, and P. Bagchi, “Motion of a capsule in a curved tube,” Journal of Fluid Mechanics, vol. 908, no. A28, 2020, doi: 10.1017/jfm.2020.831.

[149] X. Chen, C. Xue, L. Zhang, G. Hu, X. Jiang, and J. Sun, “Inertial migration of deformable droplets in a microchannel,” Physics of Fluids, vol. 26, no. 11, 2014, doi: 10.1063/1.4901884.

[150] R. Seemann, M. Brinkmann, T. Pfohl, and S. Herminghaus, “Droplet based microfluidics,” Reports on Progress in Physics, vol. 75, no. 1, 2012, doi: 10.1088/0034-4885/75/1/016601.

[151] T. Ye, N. Phan-Thien, C. T. Lim, and Y. Li, “Red blood cell motion and deformation in a curved microvessel,” Journal of Biomechanics, vol. 65, pp. 12–22, 2017, doi: 10.1016/j.jbiomech.2017.09.027.

[152] C. D. Xue, X. D. Chen, C. Liu, and G. Q. Hu, “Lateral migration of dual droplet trains in a double spiral microchannel,” Science China: Physics, Mechanics and Astronomy, vol. 59, no. 7, pp. 1–10, 2016, doi: 10.1007/s11433-016-0115-1.

[153] N. Wen et al., “Development of droplet microfluidics enabling high-throughput single-cell analysis,” Molecules, vol. 21, no. 7, pp. 1–13, 2016, doi: 10.3390/molecules21070881.

.

Chapter 3: Experimental Evidence in Formation of Dean Vortices in Curved Microchannel

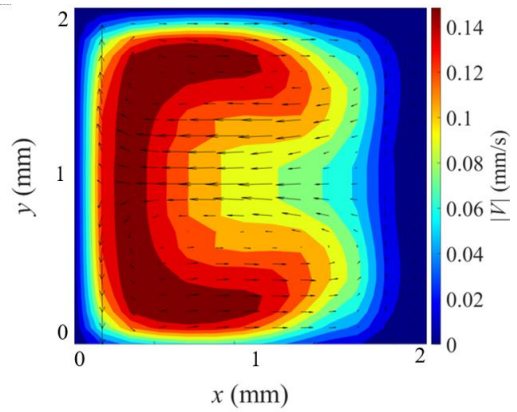

Graphical Abstract: The measured flow with Dean vorticities

This chapter presents an experimental investigation of flow behavior in a single curved microchannel using scanning microscopic particle tracking velocimetry (μPTV). The objective is to determine whether Dean vortices form under the selected operating conditions, as their presence would imply that a similar spiral geometry, later used in the device design, would also generate such vortices. A method for calculating out-of-plane velocity components is developed and implemented to reconstruct the three-dimensional velocity field within the channel. The results confirm the presence of Dean vortices in the single-curve geometry.

This chapter is based on the following paper:

Saffar, Yeganeh, David Nobes, and Reza Sabbagh.” Investigating the Flow Structure of Dean Vortices in a Curved Microchannel, implementing 3D-μPTV Using FVM and Near Wall Data Refinement”; *20th International Symposium on Applications of Laser and Imaging Techniques to Fluid Mechanics Lisbon, Portugal, July 11 - 14, 2022*.

3.1 Introduction

Microfluidic devices are used in different applications for particle sorting [1], encapsulation [2], and micro-mixing [3]. Among different geometries, curved channels are employed in the design of most microfluidic devices [4]. The geometry and flow conditions, such as the curvature radius and Reynolds number within these curved channels can produce two or more counter-rotating vortices due to the generated centrifugal force in the bend. These so-called Dean vortices [5] can affect the performance of the microfluidic devices, for instance, by changing the equilibrium position of the particles and enhancing the mixing index [5][6]. For every application, there is an optimum working window that depends on the properties of the Dean vortices [6]. Understanding the flow structure and properties of the Dean vortices provides important information for determining the optimum working window to improve the performance of microfluidic devices [6].

In order to determine the flow structure and calculate the velocity field of a flow domain in a three-dimensional flow geometry, there are several 3D optical velocimetry methods such as defocused particle image/tracking velocimetry (PIV/PTV) [7], tomographic PIV/PTV [8] and scanning PIV/PTV [9][10]. There are few experiments on 3D visualization of the flow structures in a curved microchannel by applying optical methods and these include holographic PTV [11] and confocal microscopy [6]. However, they do not provide enough three-dimensional quantitative information about the flow domain to study the Dean vortices [6][11].

The aim of this work is to apply an enhanced 3D micro-shadowgraph particle tracking velocimetry (3D-μSPTV) to study the 3D flow structures inside a curved microchannel. Different planes in the channel depth are scanned to determine the in-plane velocity field. Using a

tessellation approach, the calculated sparse velocity vectors from μPTV obtained in each plane are mapped to a high-resolution triangular mesh. This refines the velocity data near the curved edges of the channel. The resultant velocity field is used to calculate the out-of-plane velocity component by applying the continuity equation and solving it leading to the determination of the 3 components of the flow velocity.

3.2 Experimental setup

A schematic of the experimental setup used to apply 3D-μPTV to investigate Dean vortices at the microscale is shown in Figure 3-1(a). A high-speed camera is used to capture the seeding particles in the curved region of a microchannel flow. This camera is mounted on a micro-stage with the minimum displacement of 10 μm and moves in the z direction to scan the depth of the channel. A compact high intensity LED light (SL191, Advanced Illumination) is utilized as the backlight illuminator to visualize the motion of particles in a shadowgraph configuration. Tracer particles used for this purpose are 2 μm polymer beads. A programmable syringe pump (PHD4400, Harvard Apparatus) is used to set the flow rate using water as the working fluid.

The microfluidic chip shown in Figure 3-1(b) is designed and built using an additive manufacturing technique. The channel has a square cross section with the width d = 2 mm and radius of curvature, R_c = 3 mm. Inlet and outlet channels are considered to be long enough (greater than 10 × d) to eliminate the effect of inlet and outlet joints. The test cell is fabricated in 3 different layers including the top window (optical window layer), a seal and the main flow channel. The optical window layer is built using a laser cutter out of an acrylic sheet with a thickness of 6.35 mm. A silicone sheet with Shore A hardness of 60±5 and thickness of t = 0.5 mm is implemented as the sealing layer between the optical window and the main flow channel. The main

flow channel which contains support connections to the optical table, connections to the flow source via a printed Luer connection and the flow channel, is printed using an SLA 3D printer (Form 3, FormLab Inc.) with the semi-transparent resin. To improve the surface finish, the main device is printed at the highest resolution setting, 25 μm printing layer thickness. The field of view captured by the camera is also shown and highlighted by light blue in Figure 3-1(b).

(a)

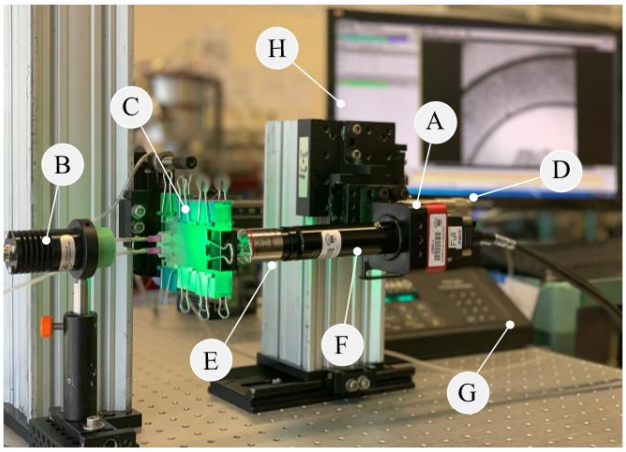

A	CMOS Camera
B	High Intensity LED
C	Microfluidic Device
D	Micro Stage
E	Objective Lens
F	Extension Tube
G	Syringe Pump
H	Computer

(b)

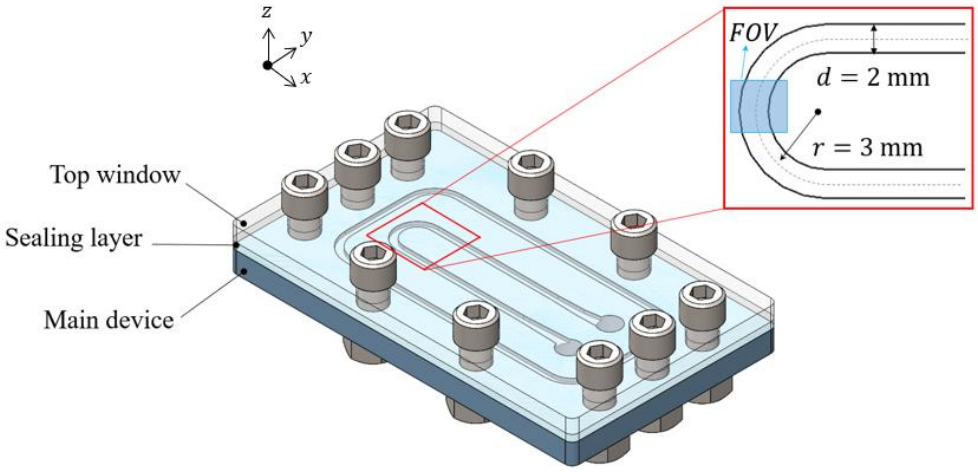

Figure 3-1 (a) Experimental setup applying shadowgraph technique, (b) fabricated microchip designed to study the Dean vortices.

3.3 In-plane velocity

A raw image of the middle section of the curved channel is shown in Figure 3-2(a). The flow is investigated using PTV at each measuring plane. A tessellation approach [13] is applied to calculate the velocity vectors in missing regions where there are not enough particles to obtain the velocity components. To generate the mesh for the tessellation approach, the boundaries of the channel need to be detected. To detect the channel walls, unwanted shadow regions are eliminated from the raw images and velocity calculations. A raw data image shown in Figure 3-2(a) shows the geometry of the channel with seeding particles and other extra shadows around the channel.

(a) (b) (c)

Figure 3-2 Image processing steps to obtain the wall boundaries of the geometry, (a) a raw image showing the initial domain, (b) the masked generated by image processing of the intensity standard deviation of 1000 images, (c) a masked image with seeding particles.

Since uncommon geometries, as in Figure 3-2(a), are challenging to be masked using mathematical approaches, raw images of the flow field are alternative sources that can be used in the masking process. To overcome the masking problem, 1000 frames containing flow and tracer particles are used to calculate the standard deviation of the image's intensity. With the high contrast apparent between the channel and the background in the intensity standard deviation of the raw images, the edge of the channel walls is detected using an in-house developed image processing

algorithm in MATLAB. Figure 3-2 (b) shows the final binarized mask of the geometry generated from the raw images. Applying such a mask to the images allows isolation of only the region containing the seed particles as shown in Figure 3-2(c). These data images are used to define the region-of-interest where the velocity field is calculated.

A commercial software (DaVis V8.4 LaVision GmbH) was used for time resolved PTV calculation. Particles with a shadow diameter of smaller than 6 pixels were tracked. PTV algorithm calculates the velocity vector for each detected particle which leads to a dispersed velocity field. To apply the continuity law and calculate the out-of-plane velocity component the obtained dispersed velocity field should be distributed on a discretized domain. In curved geometries the near wall result of the velocity calculations from PTV on the structured grid is not reliable. This is due to the structure of the grid not well representing the curved geometry of this flow.

3.4 Scanning

To generate a full 3D flow vector field, PTV can be applied over multiple imaging planes through the channel depth (z-axis). The distance between the planes was chosen based on the channel geometry and optical access. A higher number of scanning planes provides more information for the full 3C3D (3components 3 dimensional) velocity field reconstruction, but there is a limit for the minimum achievable depth of focus. The depth of focus of the lens is ~100 μm, and considering that the depth of the channel is 2 mm, a configuration of 20 evenly distributed scanning planes on the z-axis was selected for the experiment. Since it is known that the Dean flow is a steady flow under a constant geometry and certain flow conditions [12], the average of the velocity field for a number of frames can be used in further calculations.

The sequence of imaging and scanning shown in Figure 3-3(a) depends on the time scale of particle movements in the flow field and changes in the flow structure. This figure shows the volumetric scanning schematics. S_{1-n} that represents the series of scanning of each plane used for velocimetry and Δt is the time step between each two frames. The relation between the camera shifts and signals is shown in Figure 3-3(b). Scanning starts from the plane at $z_1 = 0$ and after recording the frames for that plane the camera shifts to plane z_2. The first camera signal has dt delay after which the camera shifts to a new plane. This provides the required time for the system to become stable before imaging. Following the first signal, 2000 frames capture particle motion with time step Δt.

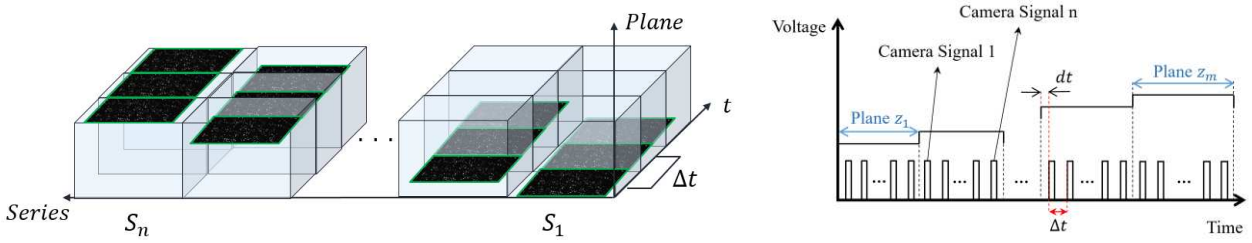

(a) (b)

Figure 3-3 (a) The diagram of the scanning imaging along the depth of the channel, (b) schematic of the timing diagram that is applied to synchronize the scanning signal with camera signal using a double frame approach.

3.5 Tessellation

Distributing the dispersed PTV velocity field from each individual plane on a discretized domain and reconstructing the 3D velocity field, allows the calculation of flow properties such as the pressure distribution [13]. A structured/rectangular grid reduces the calculation expense. However, it is typically applied to simple geometries where the geometry does not reduce the grid quality [13]. For cases with curvature, moving boundaries or complex geometries such as a curved channel in a microfluidic device, producing a high-quality mesh is more challenging. To overcome

this issue, a tessellation approach can be used. This approach maps the dispersed PTV velocity data onto an optimized high quality triangular node structure [13][14].

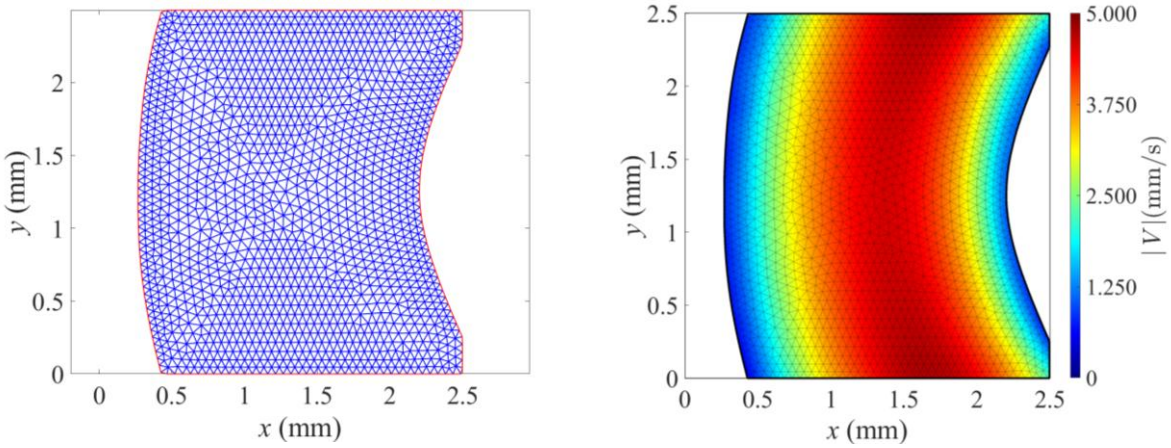

(a) (b)

Figure 3-4 (a) The triangular mesh generated using the tessellation approach, (b) velocity field of the middle plane of the channel distributed on the rectangular mesh.

To map the velocities, the boundaries of the domain are identified first and nodes are distributed along these boundaries. A triangular high-quality mesh is generated based on the node distribution on the boundaries. Maximum and minimum sizes of each single grid shown in Figure 3-4(a) are chosen in a way that $h_{max} \leq 2 \times h_{min}$. The mesh size and the node distribution depend on the geometry of the channel and flow conditions [13]. The Delaunay triangulation algorithm [13] used in this approach adjusts itself to the proper position in order to make a high quality mesh. This adjustment produces a mesh which can be easily matched to the boundaries of the domain. Consequently, refined, near wall data shown in Figure 3-4(b) can be determined using the proper mesh size and PTV velocity results. Figure 3-5(b) shows the effect of distribution mesh on the velocity field. As the generated rectangular grid shown in Figure 3-5(a) does not match the curved and oblique boundaries, the resultant velocity field contains missing data in the near wall area. Figure 3-5(b) represents the uniformly distributed velocity contour mapped to the triangular mesh

obtained from the tessellation approach. Since this unstructured mesh is well adjusted to the boundaries of the channel, the near wall data is refined to cover all the channel.

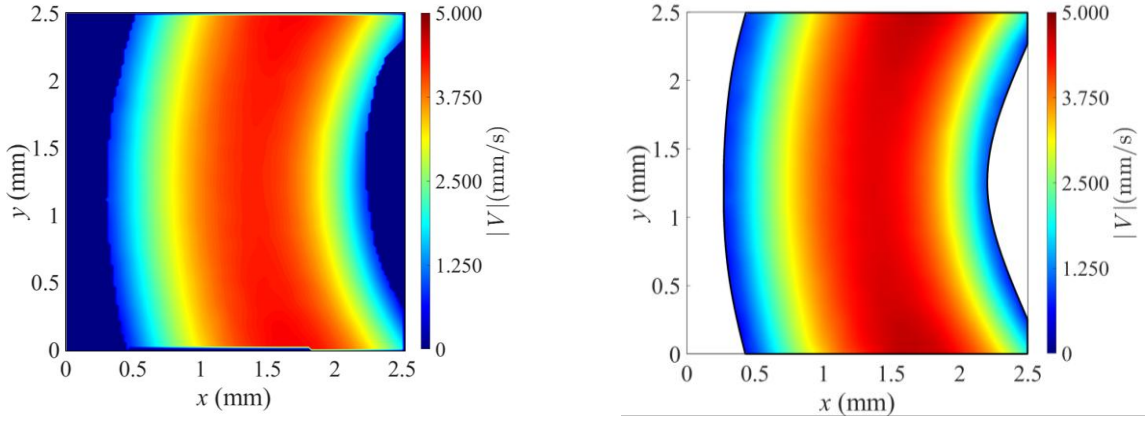

(a) (b)

Figure 3-5 Near wall data refinement using the tessellation approach; (a) PTV velocity field mapped to a structure grid with low resolution near wall data and (b) velocity field on a triangular mesh with smooth boundaries and high resolution, near wall data.

3.6 Out-of-plane velocity calculation

The 2D velocity fields resulting from the scanning process over the channel depth provides u and v, components of velocity on each plane (each z position). The 2D velocity fields are used to calculate the out-of-plane velocity, w, using the continuity equation (14) in a control volume (cell). By applying the non-slip boundary condition ($u_{wall} = v_{wall} = w_{wall} = 0$), the out-of-plane velocity component of each cell can be calculated on a structured mesh.

$$\frac{\partial u}{\partial x} + \frac{\partial v}{\partial y} + \frac{\partial w}{\partial z} = 0 \tag{14}$$

$$\left(\frac{\partial V_x}{\partial x}\right)_{i.j.k} = \frac{V_{x\,i+1.j.k} - V_{x\,i.j.k}}{\Delta x} \tag{15}$$

$$\left(\frac{\partial V_y}{\partial y}\right)_{i.j.k} = \frac{V_{y_{i.j+1.k}} - V_{y_{i.j.k}}}{\Delta y} \tag{16}$$

$$\left(\frac{\partial V_z}{\partial z}\right)_{i.j.k} = \frac{V_{z_{i.j.k+1}} - V_{z_{i.j.k}}}{\Delta z} \tag{17}$$

First order discretized continuity (equations (15)-(17)) is employed to calculate the out of plane velocity as the first step. In order to validate the out of plane calculation, flow in the curved channel is simulated (flow simulation tool, SOLIDWORKS). A similar channel geometry with the width $d = 2$ mm and radius of curvature, $R_c = 3$ mm is used in the simulation. The in-plane velocity data of the simulation is used to calculate the out-of-plane component of the velocity. Figure 3-6 represents the result of these calculations. Figure 3-6(a) shows the velocity contour and vector field on the channel cross section from the simulation. Figure 3-6(b) shows the velocity field calculated using the continuity equation and 2D velocity components. Two counter rotating Dean vortices are visible in both figures and it can be seen that the resultant velocity field is similar to the simulations.

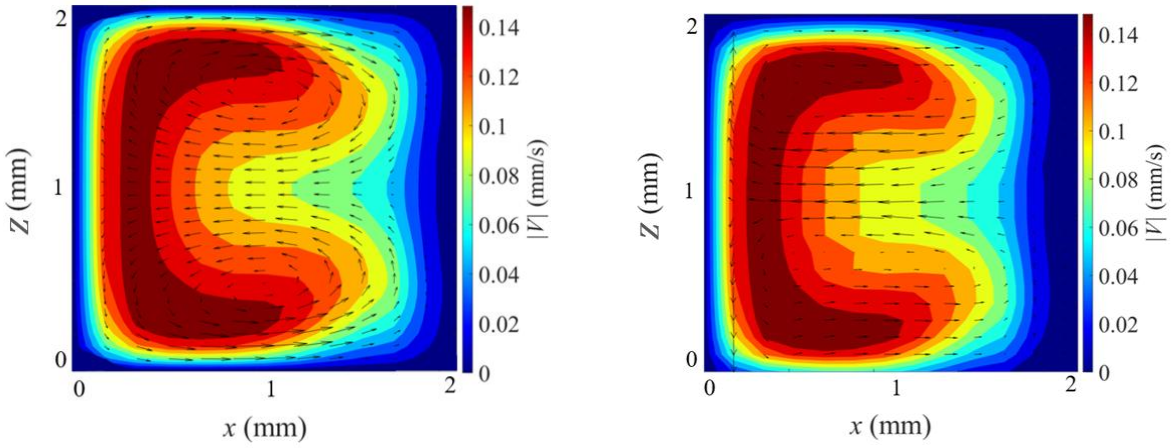

(a) (b)

Figure 3-6 Velocity contour and velocity vector in the cross section of a curved channel (a) velocity results from simulation, (b) velocity results from continuity equation and 2D velocity components.

The velocity contours and vector fields in scanning planes among the channel depth are shown in Figure 3-7. This figure also represents the maximum velocity magnitude in each scanning plane. It can be seen that the parabolic velocity diagram is captured well at the low flow rates in the microchannel. Velocity contour and vector fields for planes 2, 4, 6, 8 show experimental results among the depth of channel. Flow velocity near the wall is well refined and adjusted to the edges of the curved channel using the tessellation approach.

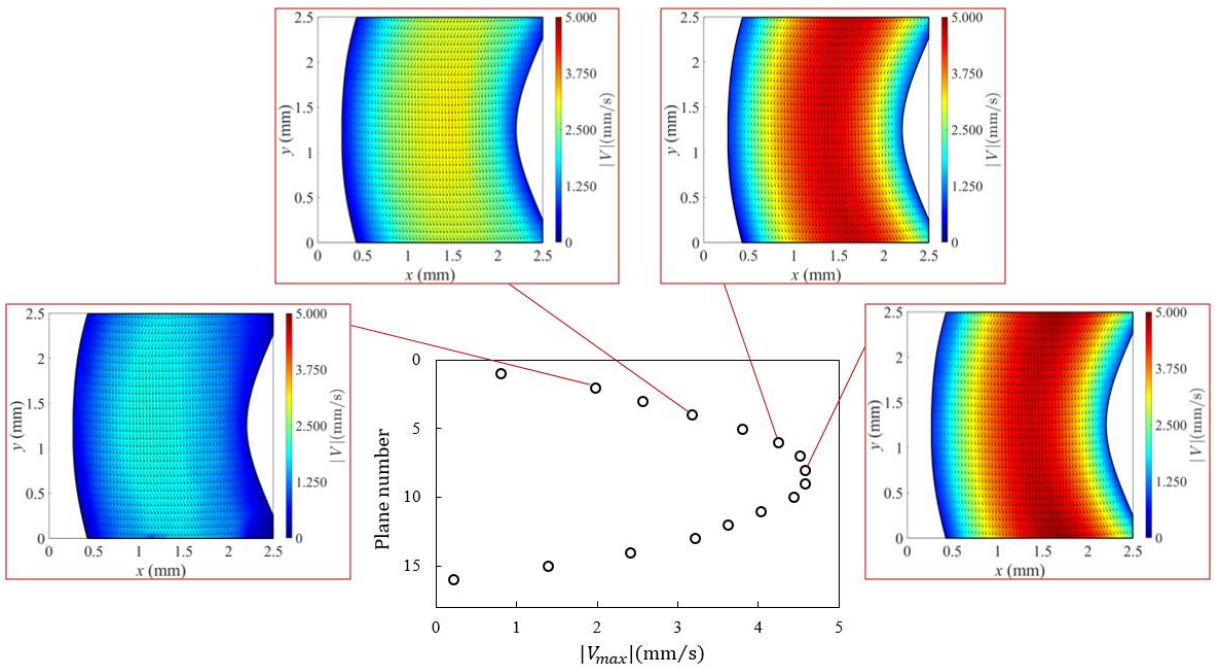

Figure 3-7 Maximum velocity magnitude for each plane among the depth of channel indicating the parabolic velocity diagram, the velocity contours and velocity vector field for planes 2,4,6,8 in curved channel with flow rate 35 ml/h.

In low flow rates where there is no secondary flow motion, the pressure near the outer wall is higher than the inner wall [15]. As a result, the maximum velocity location shifts towards the inner wall [15]. As a result, the maximum velocity location shifts towards the inner wall (Jing-lei, 2008).

Figure 3-8 shows the same trend in a microchannel. The velocity diagram in this figure shows the location of the maximum velocity point. The deviation between the maximum velocity point and the centerline of the channel indicates the lateral movement of the high velocity region toward the inner wall. Using the tessellated velocity field, it can be seen that flow velocity near the wall is well captured.

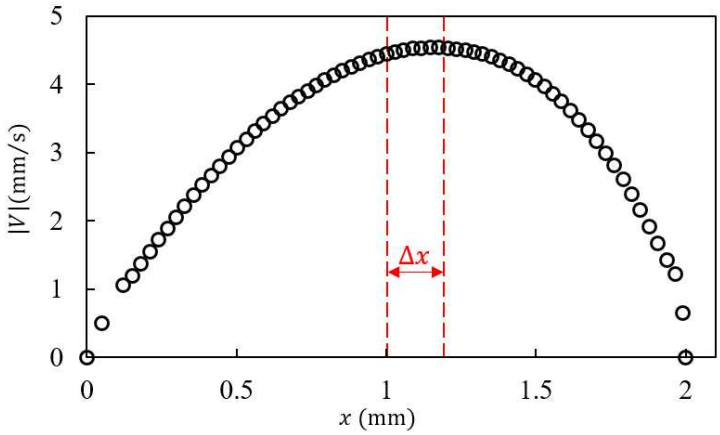

Figure 3-8 Deviation of the maximum velocity point location from the channel center in the velocity diagram of the middle scanning plane for flow rate 35 ml/h.

3.7 Conclusion

This chapter presents the application of scanning microscopic particle tracking velocimetry (μPTV) for three-dimensional flow characterization in a curved microchannel, with the goal of confirming the presence of Dean vortices under the selected flow conditions. A multi-step experimental approach was implemented to resolve the in-plane velocity field at multiple depths using a high-speed camera mounted on a precision-controlled stage. Custom image processing was employed to generate high-contrast binary masks from raw shadowgraph images, allowing accurate definition of the channel boundaries. To improve near-wall resolution, a tessellation approach was used to distribute the sparse PTV velocity vectors onto an unstructured triangular mesh that conforms to the channel curvature.

The measured in-plane velocities across scanning planes were used to reconstruct the full three-component velocity field by solving the discretized continuity equation. The calculated out-of-plane velocities were validated against numerical simulations of the same geometry. The comparison confirmed the presence of two counter-rotating Dean vortices, consistent with theoretical expectations for flow in curved channels. The deviation of the maximum velocity point from the channel centerline further confirmed inertial effects associated with secondary flow.

By demonstrating the formation of Dean vortices in a single-curve geometry under experimentally controlled conditions, this chapter supports the assumption that similar vortex structures would form in a spiral microchannel of equivalent curvature. This validation is critical to the broader hypothesis of this thesis, which proposes that inducing Dean vortices at the inlet of a micro-hydrocyclone can enhance its performance at low flow velocities. The methods and results presented here provide direct experimental evidence for the feasibility of this design approach and establish a velocity field reconstruction technique applicable to further studies in more complex geometries.

References

[1] P. Sajeesh and A. K. Sen, “Particle separation and sorting in microfluidic devices: A review,” Microfluid Nanofluidics, vol. 17, no. 1, pp. 1–52, 2014, doi: 10.1007/s10404-013-1291-9.

[2] L. Li, P. Wu, and Z. Luo, “Dean flow assisted single cell and bead encapsulation for high performance single cell expression profiling,” ACS Sens, vol. 4, no. 5, pp. 1299–1305, 2019, doi: 10.1021/acssensors.9b00171.

[3] O. Der and V. Bertola, “An experimental investigation of oil-water flow in a serpentine channel,” International Journal of Multiphase Flow, vol. 129, p. 103327, Aug. 2020, doi: 10.1016/j.ijmultiphaseflow.2020.103327.

[4] V. Kumar, M. Aggarwal, and K. D. P. Nigam, “Mixing in curved tubes,” Chemical Engineering Science, vol. 61, no. 17, pp. 5742–5753, 2006, doi: 10.1016/j.ces.2006.04.040.

[5] W. R. Dean, “The stream-line motion of fluid in a curved pipe,” The London, Edinburgh, and Dublin Philosophical Magazine and Journal of Science, vol. 5, no. 30, pp. 673–695, 1928, doi: 10.1080/14786440408564513.

[6] N. Nivedita, P. Ligrani, and I. Papautsky, “Dean flow dynamics in low-aspect ratio spiral microchannels,” Sci Rep, vol. 7, no. October 2016, pp. 1–10, 2017, doi: 10.1038/srep44072.

[7] F. Pereira and F. Pereira, “Defocusing digital particle image velocimetry: a 3-component 3-dimensional DPIV measurement technique. Application to bubbly flows,” Experiments in Fluids, no. 29.1, pp. 78–84, 2000.

[8] C. Atkinson, S. Coudert, J. M. Foucaut, M. Stanislas, and J. Soria, “The accuracy of tomographic particle image velocimetry for measurements of a turbulent boundary layer,” Experiments in Fluids, vol. 50, no. 4, pp. 1031–1056, 2011, doi: 10.1007/s00348-010-1004-z.

[9] R. Sabbagh, M. A. Kazemi, H. Soltani, and D. S. Nobes, “Micro- and macro-scale measurement of flow velocity in porous media: a shadow imaging approach for 2D and 3D,” Optics, vol. 1, no. 1, pp. 71–87, 2020, doi: 10.3390/opt1010006.

[10] S. Kashanj and D. Nobes, “Application of simultaneous time-resolved 3-D PTV and two colour LIF in studying Rayleigh-Benard convection,” 14th International Symposium on Particle Image Velocimetry, vol. 1, no. 1, 2021, doi: 10.18409/ispiv.v1i1.164.

[11] S. Kim and S. J. Lee, “Micro holographic PTV measurements of Dean flows in a curved micro-tube,” Proceedings of the 12th Asian Congress of Fluid Mechanics, 18–21 August 2008, Daejeon, Korea, no. August, pp. 689–690, 2008.

[12] S. A. Berger, L. Talbot, and L.-S. Yao, “Flow in curved pipes,” 1983.

[13] R. Azadi, J. Wong, and D. S. Nobes, “Determination of fluid flow adjacent to a gas/liquid interface using particle tracking velocimetry (PTV) and a high-quality tessellation approach,” Exp Fluids, vol. 62, no. 3, pp. 1–20, 2021, doi: 10.1007/s00348-020-03103-5.

[14] Y. Saffar, S. Ansari, R. Azadi, J. Raffel, D. Nobes, and R. Sabbagh, “Determination of the near wall flow of a multi-stage Tesla diode using PIV and PTV,” 14th International Symposium on Particle Image Velocimetry, vol. 1, no. 1, 2021, doi: 10.18409/ispiv.v1i1.169.

[15] X. U. Jing-lei, “Nonlinear turbulence models for predicting strong curvature effects,” Applied Mathematics and Mechanics (English Edition), vol. 29, no. April, pp. 31–42, 2008, doi: 10.1007/s10483-008-0105-z.

-

Chapter 4: Influence of Microchannel Curvature on Synthetic Cell Clusters Mimicking by Deformable Droplets

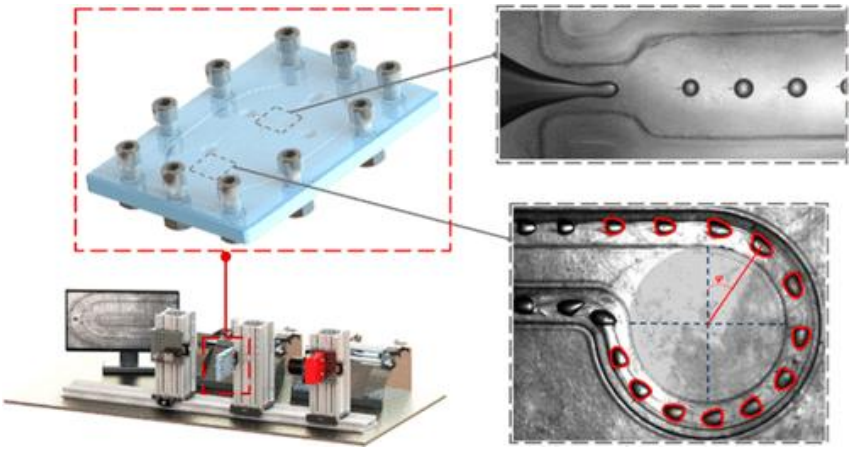

Graphical Abstract: a schematic of the droplet detection experiment

This chapter investigates the behavior of deformable droplets introduced into a curved microchannel as analogs for bio cell clusters. The study aims to assess whether exposure to Dean vortices and channel curvature results in significant deformation, trajectory deviation, or structural breakup of the secondary phase. By evaluating the motion and deformation of droplets under controlled conditions, the work provides insight into how actual cell clusters may behave in the modified geometry proposed for the micro-hydrocyclone. This analysis is critical for ensuring that the design modification intended to enhance device performance at lower flow rates does not compromise the structural integrity or separation predictability of the biological components. *(Disclaimer: In this experiment different boxes of canola oil have been used)*

This chapter is based on the following paper:

Saffar, Y., Nobes, D. S. & Sabbagh, R., “Experimental Investigation of The Deformation and Migration of Microdroplets in curved microchannels”, *Journal of Industrial and Engineering Chemistry Research* 62.42 (2023): 17275-17286. https://doi.org/10.1021/acs.iecr.3c01623

4.1 Introduction

The manipulation and control of droplets within microfluidic systems is referred to as droplet microfluidics. These distinct droplets, known as the disperse phase, consist of immiscible fluids usually containing samples, reagents, or biological entities. Droplet microfluidics has gained extensive attention due to the variety of its applications. These applications encompass diagnostics for circulating tumor cells [1], malaria-infected red blood cells detection [2], targeted drug delivery [3,4], chemical reactions [5–7], and applications in cosmetics and food industry [8]. Given its potential to advance various fields and address numerous scientific challenges, droplet microfluidics is a rapidly growing research area.

Curved microchannels are one of the most intriguing geometries in microfluidic device design due to their capability to passively manipulate the flow [9]. Curved microchannels such as serpentines and spirals have been used in many microfluidic devices for mixing and particle sorting purposes [10]. In the domain of droplet microfluidics, serpentine channels are usually used for purposes such as chemical reactions in a controlled volume which is the disperse phase [11]. Spiral microchannels are typically employed to control the path of the disperse phase for sorting applications [12].

The disperse phase typically comprises a soft membrane containing fluid which can be deformed from a perfect spherical shape due to its interaction with the continuous phase [13]. This deformation becomes more pronounced within curved channels due to the complexity of the continuous phase flow topology in comparison to straight channels. The curvature of the channel can also influence the equilibrium position of the disperse phase and consequently the sorting performance [14].

In many biotechnology applications, the disperse phase usually contains living cells interacting with the internal flow dynamics of the disperse phase [15]. The variation of the droplet deformation along the channel leads to variation in the boundary conditions of the disperse phase affecting the flow structure inside the droplet that is interacting with the living cells [16]. This variation of the flow topology inside the disperse phase is crucial in other applications such as mixing, which is attributed to this inner flow [17].

Beyond the aspect of deformation, another factor to consider is the potential lag between the flow of the disperse phase and that of the continuous phase. This discrepancy hinges on parameters such as the shape of the disperse phase, its dimensions, and its lateral positioning within the channel. All these parameters collectively influence the flow dynamics within the disperse phase, consequently impacting the sorting performance and overall behavior.

Interaction between the droplets and the fluid structures has been extensively studied in straight channels and capillaries both experimentally and numerically [18–25]. The effect of the curvature of the microchannel on droplet-based microfluidics has recently been the focus of research interests. The role of the curvature of the channel on the droplet properties in U-shape and perfect torus shape microchannels has been studied numerically [26] for a Reynolds number of the continuous phase in the range of $0.1 \leq Re \leq 50$. For the torus microchannel, the study found that there is an equilibrium position at very low Reynolds numbers, i.e., non-inertial flow. However, for higher Reynolds numbers where the flow is inertial, a stable equilibrium position was not observed. They attributed this instability to the formation of the secondary flow known as Dean vortices within the curved channel [27]. They introduced the capillary number and Reynolds number of the channel as the two parameters influencing the equilibrium location of the droplets. For the U-shape microchannel, it was found that the curvature ratio of the channel, r/d, where r

is the radius of the channel and d is the diameter of the channel, influences the lateral migration of the droplets. They showed the lateral migration of the droplets toward the outer and inner wall for low and high curvature ratios, respectively. In another numerical investigation in a corner-shape microchannel [28], the capillary number was found to influence the deformability of the droplets. However, it was shown that capillary number does not have a significant effect on the lateral migration of the droplets in this geometry.

Despite the substantial interest in comprehending the influence of microchannel curvature on the behavior of the disperse phase in droplet microfluidics, the available literature predominantly features numerical simulations as the primary method used to explore this area of research [26,28,29]. Hence, there are many simplification assumptions that affect the results. For example, in all of these research studies in literature, the immiscible droplets have similar fluid properties, e.g., viscosity and density, to the continuous phase. However, in real applications it is almost impossible to have an immiscible disperse phase with similar properties to the continuous phase. Geometrical assumptions in numerical works can also affect the results. The torus shape microchannel which cannot be used in real scenarios is an example of this type of assumption.

Moreover, reviewing the literature, it becomes evident that there are only a limited number of numerical investigations on the effect of the curvature of the microchannel on the disperse phase in droplet microfluidics. Hence, there are many questions remaining unanswered in this field. The objective of this research is to experimentally examine the impact of curvature on deformation and migration of immiscible droplets in curved microchannels. To achieve this goal, two microchannels were designed, each featuring different curvature lengths while maintaining an identical curvature ratio representing simplified droplet based microfluid chips or curved vessels. The continuous and dispersed phase working fluids are chosen to have different properties. A

custom image processing algorithm was developed and employed to capture the droplet topology and extract its features. Using this information, the effect of Reynolds number, surface tension, and the droplet size have been investigated on the trajectory and topology of the droplets.

4.2 Characteristics of the flow

Lateral migration in microchannels is highly influenced by the presence of inertia [30]. In a straight channel with low Reynolds number, where inertia is negligible, the lateral migration only occurs for particles which are deformable such as elastic particles, cells, liquid capsules and droplets. The effect of channel walls or shear gradient causes particle deformation [31]. A velocity component perpendicular to the flow stream compels the particle to migrate laterally to eliminate any asymmetry [9]. In this context, deformable particles tend to migrate from walls towards the low shear gradient area. As a consequence, a mild separation between the deformable and stiff particles can occur leading to reducing the uniformity of the cells/droplet distribution inside a curved channel such as a microdevice or vessel [32].

In the presence of inertia at higher Reynolds numbers, both rigid and deformable particles are subject to the wall induced lift force and shear induced lift force [33]. Rigid particles tend to migrate away from the center of the channel towards the channel walls settling at an equilibrium position [33]. In a circular cross section, particles are randomly distributed on a cylindrical surface with the same axis as the channel itself with a radius equating to 60% of the channel radius [9,14]. Conversely, in a square cross section, the equilibrium zone minimizes to a single location close to each wall [9]. With increasing aspect ratio to form a rectangular cross section, two unstable points emerge nearer to the shorter walls, and the equilibrium positions reduce to two points situated at a distance of ~ 20% from the channel height, close to the larger walls [34,35]. In this scenario, particles are randomly distributed between the equilibrium positions while their properties do not

exert an influence on the sorting outcome. In the case of deformable particles, all of the earlier mentioned mechanisms will occur simultaneously which affect both the location of the equilibrium position and the shape of the deformable particles [35].

In a curved microchannel, flow structure displays a more complex behavior in comparison to the Poiseuille flow in a straight channel due to the asymmetric channel geometry [36]. An instability in the pressure gradient leads to a lateral flow movement and generation of a pair of counter rotating Dean vortices [37]. Where the inertial lift is dominant, the sorting process does not occur in the channel. However, the domination of Dean drag, results in particles mixing [33].

The lateral migration of rigid particles is mostly observed and reported with the existence of inertia. In the presence of finite inertia, for a rigid particle, the pair of equilibrium positions in the rectangular straight channel shift towards the inner wall and merge into a single equilibrium position in curved channels [38]. This position, however, can be manipulated by changing the ratio of lift to drag forces and cross section shape of the channel. By optimizing the lift to drag ratio, this system can effectively sort the sample based on particle sizes [39].

Deformable particles, however, appear to be affected whether inertia is present or not. In the absence of inertia, where channel and droplet Reynolds numbers are low, deformable particles are under the effect of the wall, forcing the particle to migrate away. This leads to an equilibrium position between the location of maximum velocity and the inner wall where the wall has a higher curvature [40]. In inertial microfluidics, the equilibrium position of deformable particles is affected by the deformation of the particle, Dean flow, the effect of the channel curvature and inertial lift. The equilibrium position in this state can be affected by capillary number and Reynolds number as well [40].

4.3 Experiment

The flow cell presented in Figure 4-1 was fabricated using a semitransparent resin in an SLA 3D printer (Formlab 3, FormLab Inc.) with a 25 μm resolution. The microchip's back face surface finish was sanded to improve optical access to the channel. The optical window attached to the top of the flow channels was made from an acrylic sheet with a thickness of 6.35 mm using a laser cutter. A silicone membrane sheet with a thickness of 0.5 mm and Shore A hardness of 60±5 was utilized between the flow channel and optical window to seal the flow cell.

To investigate the effect of curvature on droplet deformation, two microchannels were designed with 180° (Channel A) and 270° (Channel B) curved geometries, respectively as shown Figure 4-1. Each channel consisted of a droplet generator, two settling channels, and a curved section with a radius of curvature of r = 3.5 mm and a channel width of w = 1 mm. Droplets of different sizes, with an equivalent diameter, d_{eq}, 95 μm $\leq$ d_{eq} $\leq$ 600 μm, were generated using a flow focusing droplet generator. The droplet generator was designed using a web-based tool [41],, DAFD, which employs machine learning algorithms to automate the design process of flow-focusing droplet generators. The generated droplets are characterized using a real-time imaging system, and the main parameters of the droplet generator are defined. In order to investigate the droplet behavior, canola oil was used as the continuous phase, while a 2-propanol-water mixture with concentration, c of $20\% \leq c \leq 80\%$ was employed as the dispersed phase, to generate monodisperse droplets in both dripping and jetting regimes. Both phases are chosen in a way to generate immiscible droplets. By increasing the concentration of 2-propane in the dispersed phase mixture, the capillary number, $Ca = \mu_c U_\infty a/\sigma w$ increases. Here μ_c is the continuous phase dynamic viscosity, U_∞ is the mean axial velocity, a is droplet diameter, σ is the surface tension

and w is the width of the channel [42]. Increasing the capillary number is expected to increase the deformability of the droplets [29].

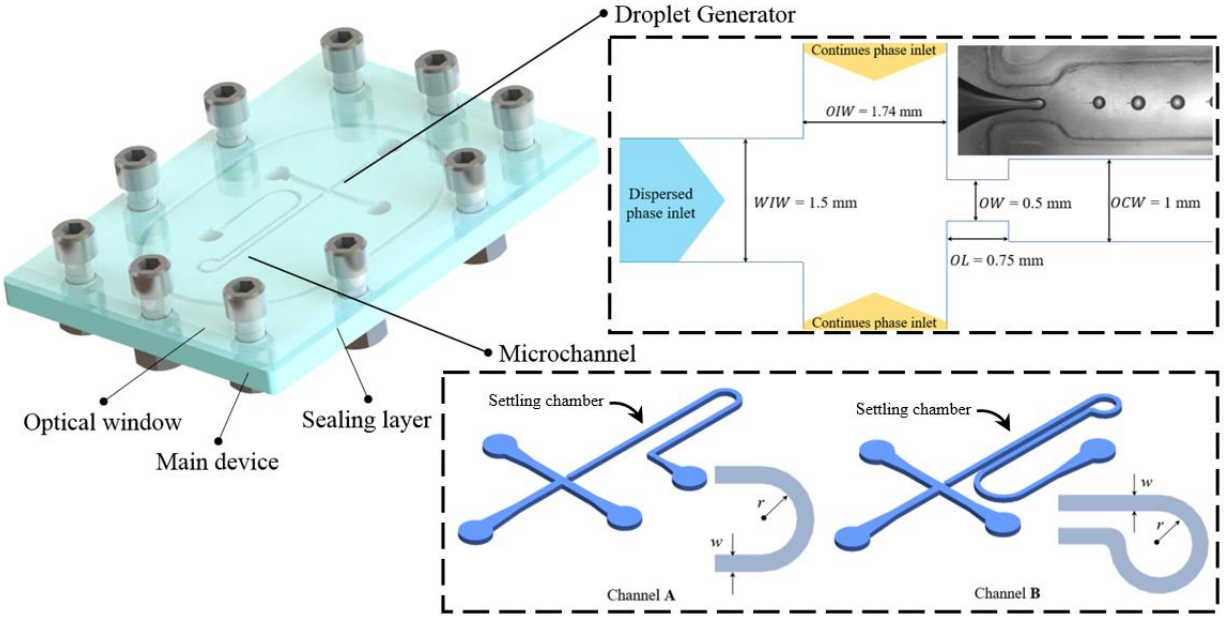

Figure 4-1 A schematic of the microchip device containing microchannels and three layers, highlighting droplet generator section and the layout of channels A and B.

A schematic representation of the experimental setup utilized for imaging the dynamics of the droplets is shown in Figure 4-2. The setup contains an optical imaging and a fluid system. In the optical imaging system, a compact high intensity spot LED light (SL191, Advanced Illumination Inc.) is employed as a backlight illuminator. Droplets are captured by a high frame rate camera (acA2000, BASLER Inc.) with a frame rate of 200 fps. The midplane of the channel is focused using a macro lens in a 6.5 mm × 9 mm field of view. The fluid system contains two programmable syringe pumps (PHD4400, Harvard Apparatus) and a fabricated microchip. Syringe pumps are utilized for controlling the flow rate of the 2-propane-water mixture as the dispersed phase and canola oil as the continuous phase.

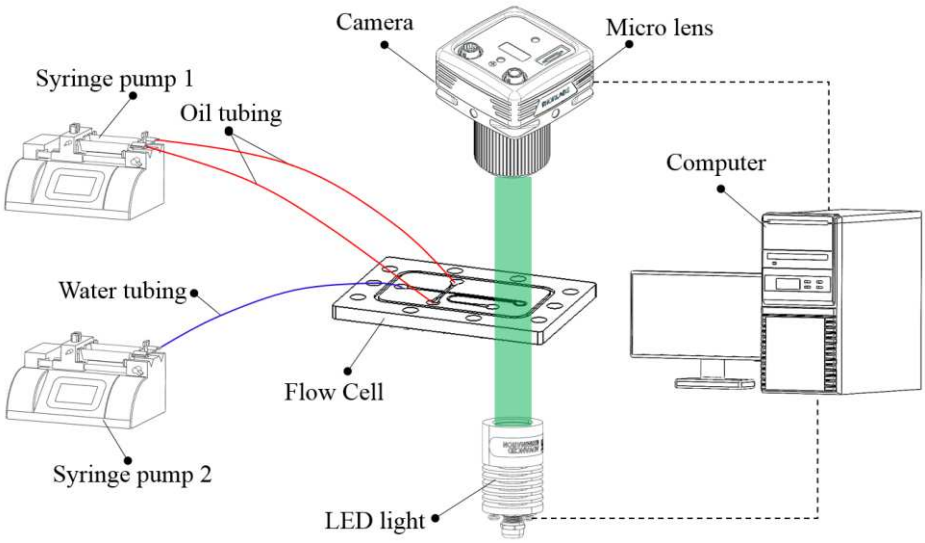

Figure 4-2 A schematic of the experimental setup.

4.4 Data processing

The process of analyzing the droplet behavior within a channel involves several essential stages. The main steps are image acquisition, coordinate mapping, droplet wall delimitation and droplet detection. The initial phase involves capturing raw images of droplets within the microchannel and converting them into grayscale to simplify the subsequent image processing. The grayscale conversion reduces the color variations, which could potentially interfere with the detection of the droplet edges. Subsequently, the origin of the images is aligned with the default origin location using a correction vector, which ensures that the images are correctly aligned, and enabling precise droplet tracking. Contrast dark stretching enhancement is applied on aligned images to improve image visibility. This technique is used to amplify the dark regions of an image and increase the contrast between the droplet and its surroundings. By enhancing the contrast in the image, it becomes easier to delineate the droplet edges and accurately track its movement within the channel. Following these steps and binarizing the images, the droplet edges can be clearly delineated as shown with red boundaries in Figure 4-3.

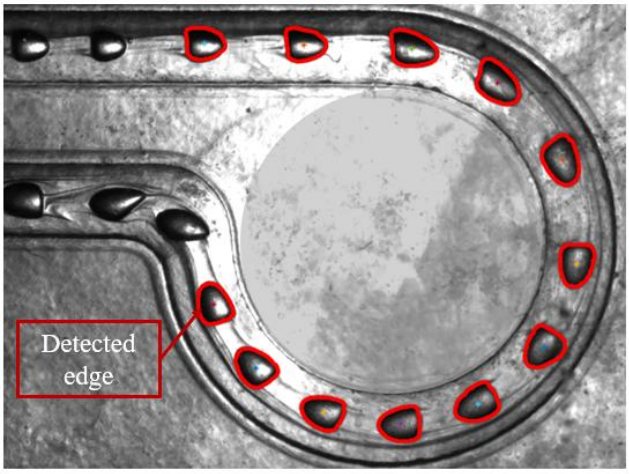

Figure 4-3 Detected droplet boundaries mapped onto the raw image.

Droplet features such as its centroid, size and location can be extracted from the data obtained through image processing and utilized to investigate droplet topology and trajectory. The longest, L_{max} and shortest, L_{min} distances of a boundary to the centroid are key measurements, as depicted in Figure 4-4(a). Additionally, the angular position of the droplet with respect to the starting point of the curvature, θ and radial position of the droplet with respect to the connection line between the centroid and channel center, r_d are shown in Channel A and B in Figure 4-4(b). Additional information regarding the image processing procedures is presented in the Appendix 1: Droplet detection image processing scheme.

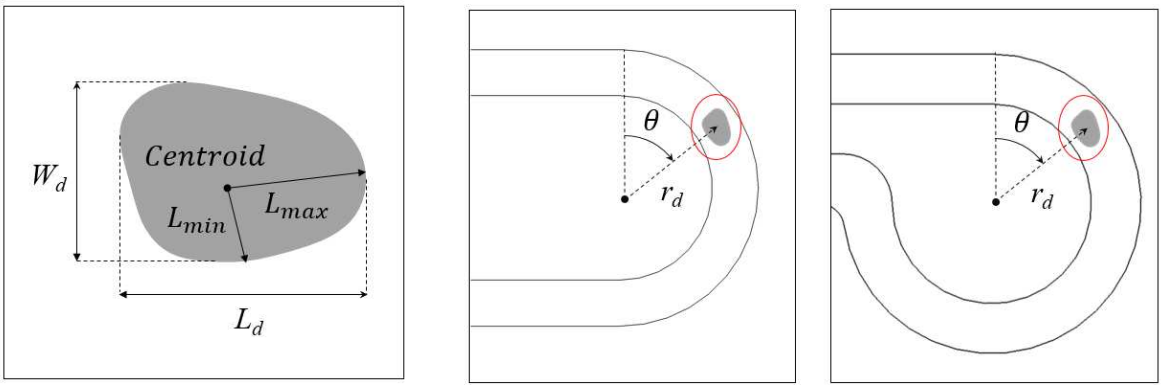

(a) (b)

Figure 4-4 (a) Droplet features extracted from the detected region, (b) Trajectory of the droplet using angular, θ and radial position, r_d.

4.5 Results and discussion

In this research, droplet behavior is studied under the effect of channel Reynolds number, Re, capillary number, Ca and the droplet size. This analysis offers valuable insights on the effect of these parameters on the droplet characteristics such as the tangential velocity of the droplet, deformation of the droplets, and the lateral migration of the droplet.

4.5.1. The effect of droplet size

The tangential velocity of droplets flowing in the channel for different droplet sizes is shown in Figure 4-5 for Channel A and Channel B. The nondimensional tangential velocity of the droplet, u_θ/U_∞, is plotted against the angular position of the droplet, θ. Here, the tangential velocity of the droplet is defined as $u_\theta = d\theta/dt$ and U_∞ is the mean axial velocity of the continuous phase as the flow enters the curved region. In this case, channel Reynolds number, Re is held constant and capillary number, Ca is increasing in proportion with equivalent diameter while other parameters are kept constant. Figure 4-5(a) shows the tangential velocity of the droplets for Channel A for different cases with equivalent diameter varying in the range of 240 μm $\leq d_{eq} \leq$

400 μm and $1.2 \leq Ca \leq 2$. It can be seen in this figure that when the equivalent diameter, $d_{eq} = 240$ μm, tangential velocity reaches its maximum value, nearing 80% of the mean axial velocity, U_{∞}. This is observed near to the mid-point of the curved region of the channel, $\theta \approx 90°$. Either side of this maximum the velocity has a similar trend with the beginning and end of the curve having quite similar values, indicating $u_{\theta,\theta=0} \approx u_{\theta,\theta=180°}$.

To investigate the effect of droplet size on the tangential velocity of the droplets in a channel with higher length of curvature, this velocity component has been measured in Channel B as well. Figure 4-5 shows the results for different cases with equivalent diameter varying in the range of $310 \text{ μm} \leq d_{eq} \leq 610$ μm and capillary number spanning the interval of $1.5 \leq Ca \leq 3$. Similar to the trend observed in Channel A, a corresponding pattern is evident in the results shown in Figure 4-5(a). Across all droplet size cases, $d_{eq} = 310$ μm to $d_{eq} = 610$ μm, it can be seen that the maximum tangential velocity of the droplet is occurring near the middle of the curved section, $\theta \approx 90°$. This means that in Channel B, the maximum droplet tangential velocity shifts to the entrance of the curved section in contrast to Channel A where the maximum tangential velocities are observed at $\theta \approx 90°$.

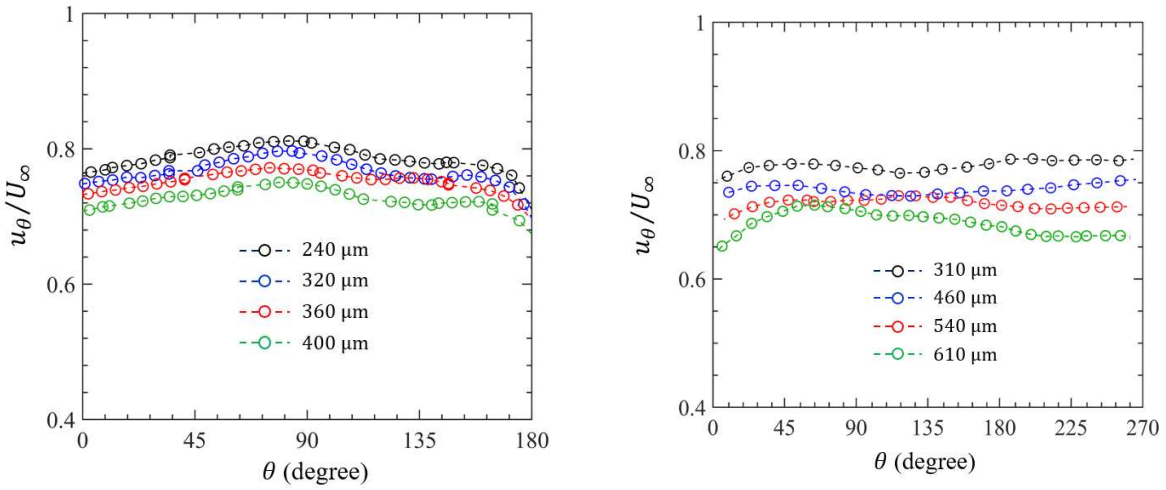

(a) (b)

Figure 4-5 Nondimensional tangential velocity of droplets, u_θ/U_∞ as a function of different droplet size against angular position, θ. Data is represented for $Re = 3.5$ (a) in Channel A with a 180° curved section, and (b) in Channel B with a 270° curved section.

The deformation of a single droplet from its original circular projected shape is studied using a deformation index defined as, $DI = (L_{max} - L_{min})/(L_{max} + L_{min})$. The deformation index, DI of the droplet under the effect of different droplet sizes for Channel A and B is presented in Figure 4-6. In this figure, channel Reynolds number, Re is constant for all droplets with different sizes.

Figure 4-6(a) shows the deformation index, DI against angular position, θ for different cases with equivalent diameter varying in the range of 95 µm $\leq d_{eq} \leq$ 400 µm and capillary number spans from $0.45 \leq Ca \leq 2$ for Channel A. It can be seen that the deformation of the droplet increases with increasing the droplet size from $d_{eq} = 95$ µm to $d_{eq} = 400$ µm. Across all cases, the maximum DI is observed at the entrance of the curved section around $\theta \approx 0°$. The minimum value is seen to be near to the center of the channel, $\theta \approx 90°$. Figure 4-6(b) presents the deformation index for Channel B for cases with equivalent diameter varying in the range of 310 µm $\leq d_{eq} \leq$ 610 µm. A similar trend to Channel A is observed in Figure 4-6(a) where

deformation of a droplet increases with increasing the droplet size. However, for larger droplets two local maximums can be seen at $\theta \sim 100°$ and $\theta \sim 150°$.

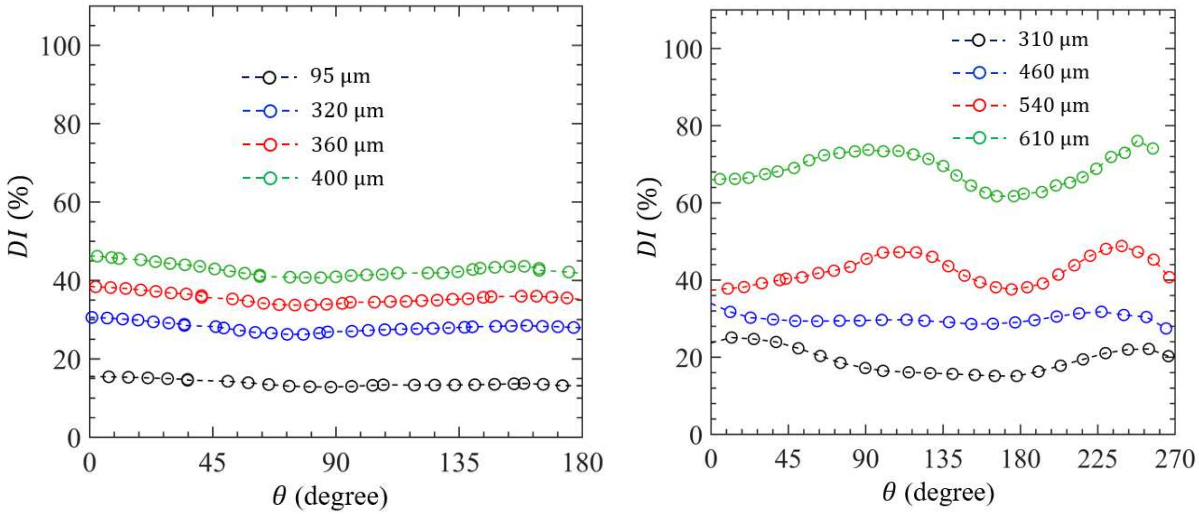

(a) (b)

Figure 4-6 Deformation index, DI as a function of droplet size, d_{eq} against angular position, θ. Data is represented for $Re = 3.5$, (a) in Channel A with a 180° curved section, and (b) in Channel B with a 270° curved section.

Radial migration of a droplet in a curved microfluidic channel refers to the movement of the droplet towards or away from the channel walls. This behavior arises due to the combined effects of centrifugal forces, viscous drag, and surface tension. Understanding radial migration is important for the development of microfluidic devices and for improving our understanding of how droplets behave in complex fluidic environments. The lateral migration of different droplets with different equivalent diameters for Channel A and Channel B are shown in Figure 4-7. The radial position, r_d of the centroid of the droplet is nondimensionalized using the radius of the channel centerline, r_c and channel width, w. In this case channel Reynolds number, Re is held constant.

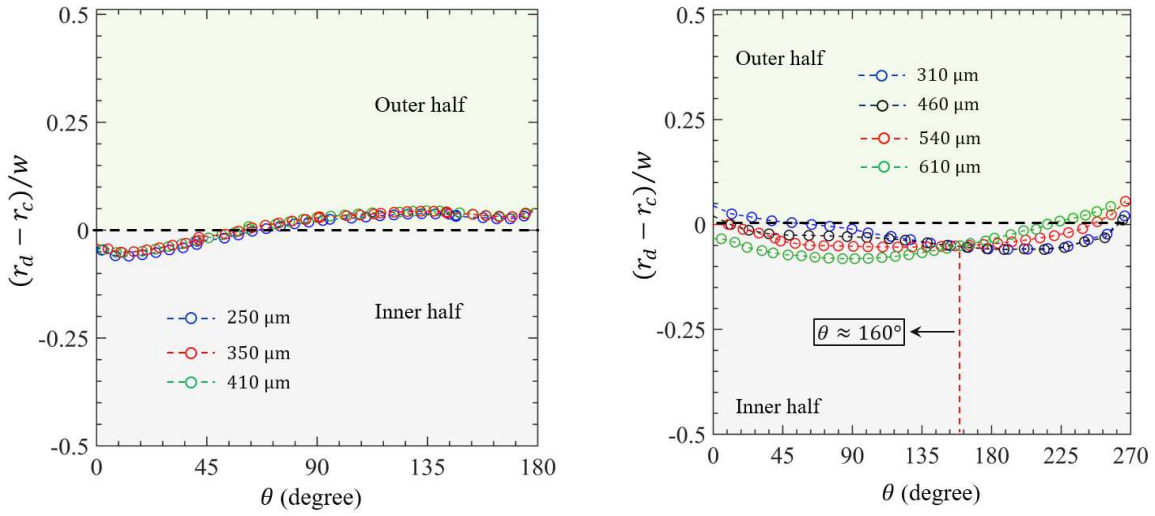

Figure 4-7 Lateral migration of droplets as a function of droplet size, d_{eq} against angular position, θ. Data is represented for $Re = 3.5$,(a) in Channel A with a 180° curved section, and (b) in Channel B with a 270° curved section.

Figure 4-7(a) shows the trajectory of different droplets with equivalent diameter in the range of $250\ \mu m \leq d_{eq} \leq 410\ \mu m$ and capillary number intervals spanning from $1.25 \leq Ca \leq 2$ for Channel A. It is noticeable that droplets generally enter the curved section at $\theta = 0°$ in the inner half of the channel where their radius, $r_d < r_c$. Moving into the curved region of the channel they shift toward the outer half of the channel. All cases follow the same trajectory in Channel A and differences between their trajectories are negligible in comparison to the deviation itself. Figure 4-7(b) shows the trajectory of different droplets with equivalent diameter in the range of $310\ \mu m \leq d_{eq} \leq 610\ \mu m$ for Channel B. It is observable in this figure that droplets entering the curved section at $\theta = 0°$, positioned in proximity to the centerline of the channel. Here, smaller droplets are more deviated towards the outer wall and larger droplets deviate more towards the inner wall. All trajectories converge at around $\theta \approx 160°$ and divert in a reverse trend where smaller droplet shift closer to the inner wall and larger droplets move toward the outer wall.

The trajectory of a droplet centroid passing through a curved channel in comparison to the centerline of the channel is shown in Figure 4-8(a) for a droplet with equivalent diameter, $d_{eq} =$ 450 µm. The zoomed image of the droplet for $\theta = 45°$ is shown in Figure 4-8(b) in which the centroid of the droplet is slightly moving towards the outer wall. However, progressing further along the channel to the droplet located at zoomed area for $\theta = 210°$ shown in Figure 4-8(c), it becomes apparent that the droplet centroid is shifted toward the inner wall. Along with the droplet centroid, the leading edge (LE) of the droplet is also shown to deviate towards the channel walls in each highlighted image for Figure 4-8(b) and (c).

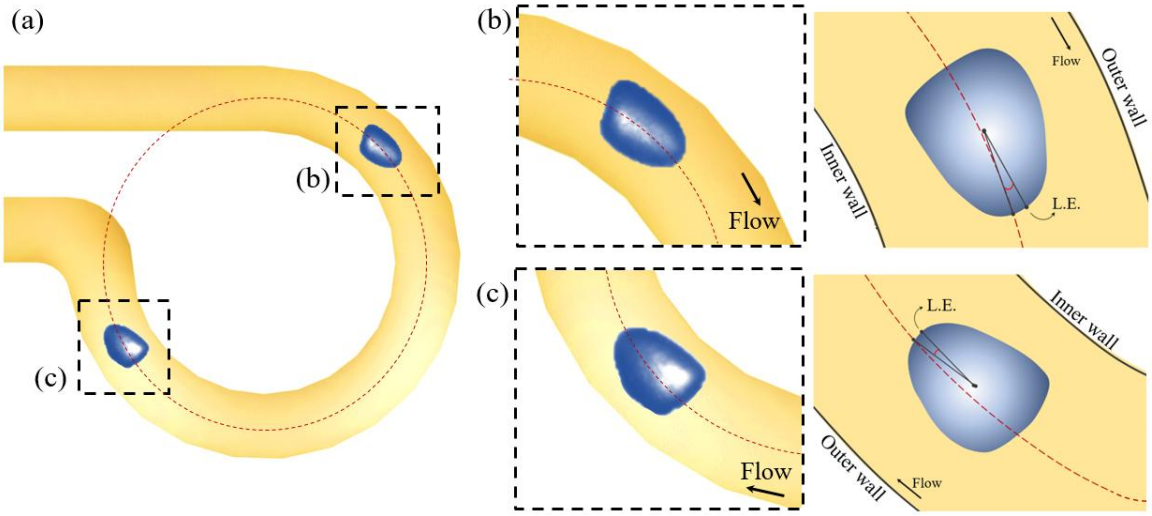

Figure 4-8 Experimental results of a droplet centroid deviation from the centerline with $d_{eq} = 450$, $Re = 5$, Ca =1.4 (a) in Channel B with an indication of the location of the centroid regarding the centerline at two angular positions of (b) $\theta = 45°$ and (c) $\theta = 210°$.

4.5.2. The effect of Reynolds number

To investigate the effect of the Reynolds number of the continuous phase on the three properties of the droplets, i.e., deformation index, lateral migration, and tangential velocity, droplets in three different Reynolds numbers of 3.5, 5, and 7 have been studied. Tangential velocity, u_θ / U_∞ non dimensionalized for each case based on their respective U_∞under the effect of channel Reynolds

number, Re is represented in Figure 4-9 for Channel A and Channel B. In this graph, droplet equivalent diameter, $d_{eq} = 450\mu m$ is constant and capillary number is increasing in proportion to Reynolds number in the range of $1.3 \leq Ca \leq 2.6$ due to the changes in the continuous phase velocity while other parameters are held constant. Figure 4-9(a) shows the tangential velocity of the droplets for Channel A. It can be seen from this figure that increasing the Reynolds number, Re leads to increasing the nondimensional tangential velocity of the droplets. It implies that increasing the velocity reduces the droplet velocity lag when following the main flow stream. Figure 4-9(b) shows the same trend as Channel A in Figure 4-9(a), where with increasing the Reynolds number, Re the nondimensional tangential velocity of the droplet increases for all cases.

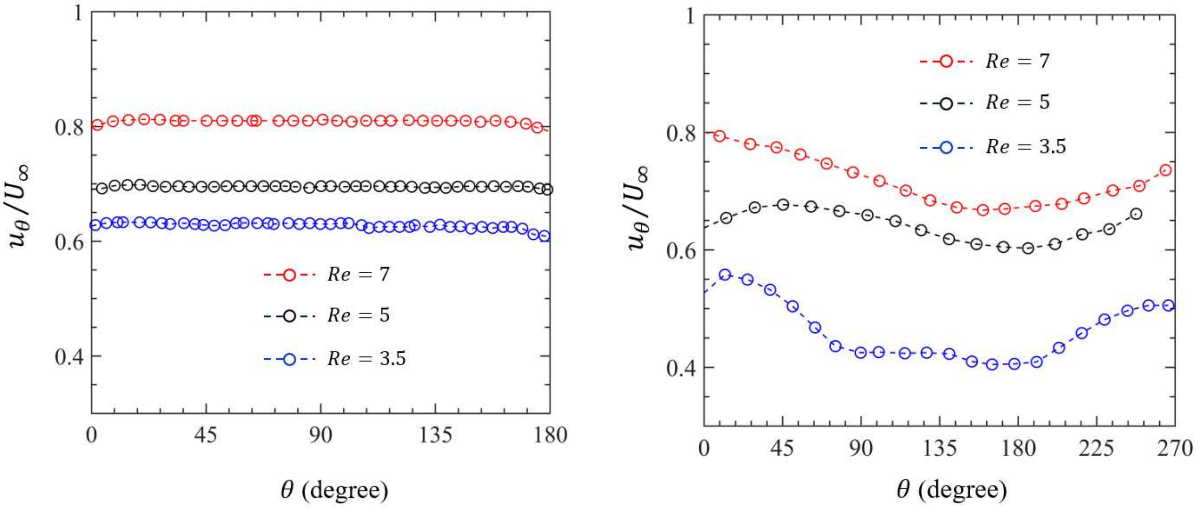

(a) (b)

Figure 4-9 Nondimensional tangential velocity of droplets, u_θ/U_∞ as a function of Reynolds number, Re against angular position, θ. Data is represented for $d_{eq} = 450$ μm (a) in Channel A with a 180° curved section, and (b) in Channel B with a 270° curved section.

The deformation index of different cases with a range of Reynolds number, $3.5 < Re < 7$ against angular position, θ is shown in Figure 4-10. The variation in the deformation index, DI for Channel A is represented in Figure 4-10(a). It can be seen in this figure that changes in the DI for

all cases are less than 3%. This means that in Channel A, the Reynolds number, Re does not have a noticeable impact on the droplet deformation. Figure 4-10(b) shows the deformation index, DI for Channel B against the angular position, θ. Similar to the observations in Channel A, changes in Reynolds number does not have a significant impact on the deformation of the droplets.

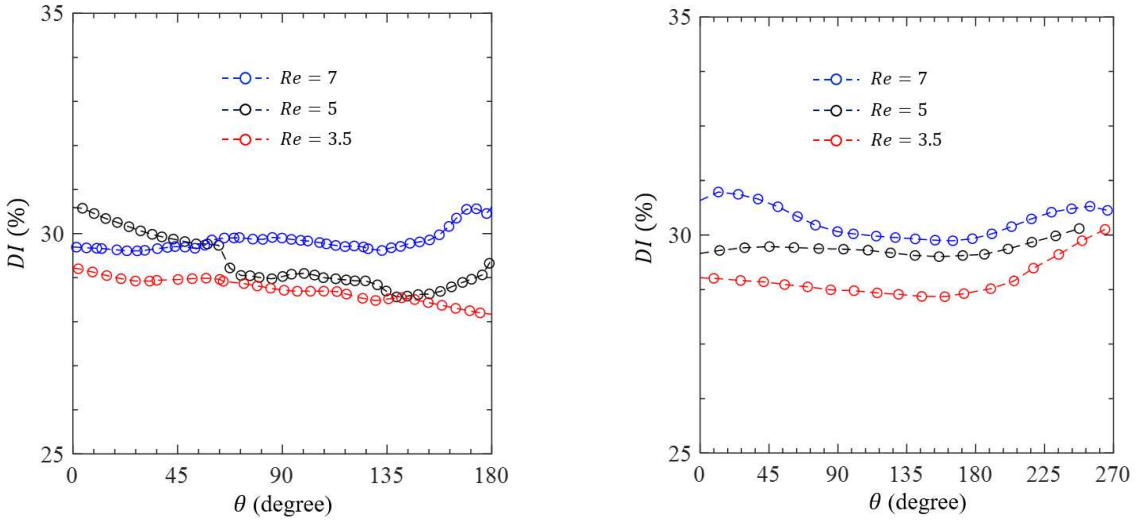

Figure 4-10 Deformation index, DI as a of function Reynolds number, Re against angular position, θ. Data is represented for $d_{eq} = 450$, (a) in Channel A with a 180° curved section, and (b) in Channel B with a 270° curved section.

Figure 4-11 shows the nondimensionalized radial position, $r_d - r_c/w$ of different cases with $3.5 \leq Re \leq 7$ against the angular position, θ. It can be seen in Figure 4-11(a) that for all cases the value of the radial position is overlapping at each angular position. It indicates that the radial position is changing independently from the Reynolds number, Re. The trajectory of the droplets also shows a migration towards the inner wall where the highest deviation is at $\theta \approx 20°$. Moving forward into the curved region, the droplets shift towards the outer half of the channel and move close to the channel centerline. Figure 4-11(b) for Channel B represents almost the same independence with respect to the Reynolds number, Re. In this plot the maximum deviation of trajectory between these cases is 2.5% of the channel width, w. The trajectory of the droplets in

Channel B starts nearer to the centerline in the outer half and remains close to the centerline of the channel.

These results of the droplet lateral migration contrast with the behavior of a looping droplet in a toroidal (donut-shape) channel. For Reynolds number, $Re < 2$, the droplet migrates towards the inner half and for $Re \geq 2$ droplets deviate towards the outer half [40]. This difference in the behavior of the droplets could stem from the geometric configuration of the curved channels which has a straight section at the entrance. In contrast, torus-shape channels lack a straight path before the curved section, causing the droplet passes through the channel multiple times. This repetitive movement enables flow properties to evolve and stabilize, potentially accounting for the differences observed.

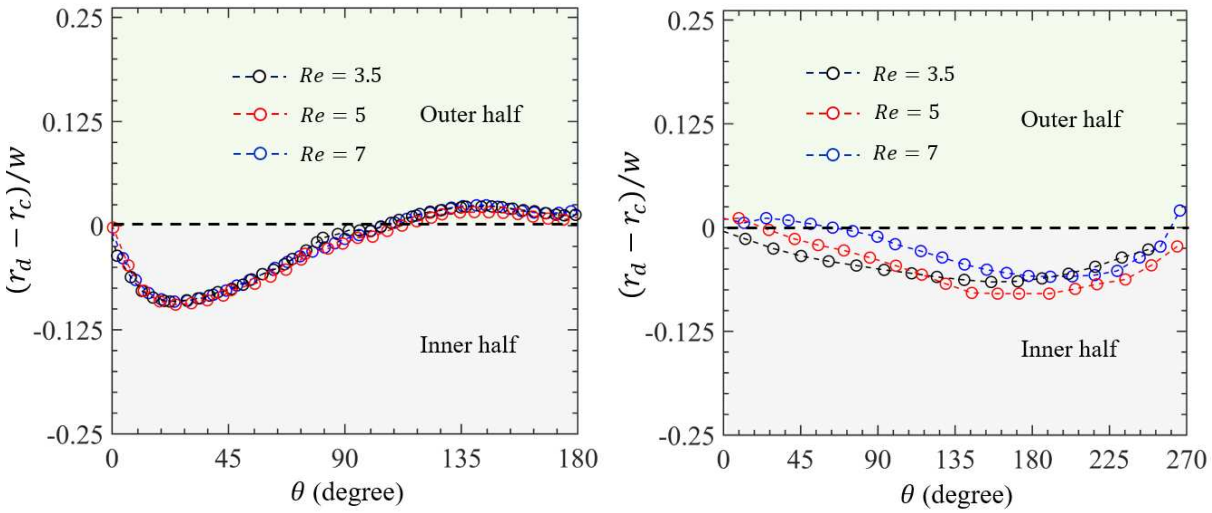

(a) (b)

Figure 4-11 Lateral migration as a function Reynolds number, Re against angular position, θ. Data is represented for $d_{eq} = 450$ (a) in Channel A with a 180° curved section, and (b) in Channel B with a 270° curved section.

4.5.3. The effect of surface tension

In addition to the deformability of the droplets, surface tension can influence properties such as the lateral migration and tangential velocity [40]. This subsection examines the influence of surface tension on these parameters. The surface tension of the dispersed phase is changed by altering the mixture concentration in this phase. Increasing the surface tension leads to a proportional decrease in droplet capillary number. Every other parameter is kept similar while the surface tension is decreasing with increasing capillary number.

The surface tension effect on the nondimensional droplet tangential velocity, u_θ/U_∞ is represented in Figure 4-12 for both Channel A and Channel B against the angular position, θ of the droplet. Here, Re and d_{eq} are held constant for all cases where capillary number is varying between $1.4 \leq Ca \leq 3.2$. For Channel A in Figure 4-12(a), across all cases, the tangential velocity of the droplet increases with increasing the capillary number, Ca. This trend suggests a positive correlation between the droplet deformability and its delay in following the mainstream of the channel. Figure 4-12(b) shows a similar trend as in Figure 4-12(a), where with increasing the capillary number, Ca the droplet tangential velocity increases. For both channels, droplet tangential velocity increases at the entrance of the curved section of the channel, $\theta > 0°$. For Channel A, the velocity reduces after crossing the halfway point of the curved section, $\theta = 90°$, reaching to its minimum to the exit of the curve section, at $\theta = 180°$. For Channel B, velocity asymptotes around $\theta = 90°$ and remains steady until the exit of the channel at $\theta = 270°$. Despite the relatively minor fluctuations in tangential velocity along the channels with maximum variation of $\sim 14\%$, the effect of the capillary number, which signifies deformability, was significant. This implies that the deformation of the droplets slightly changes in a way to allow it to reach a higher velocity.

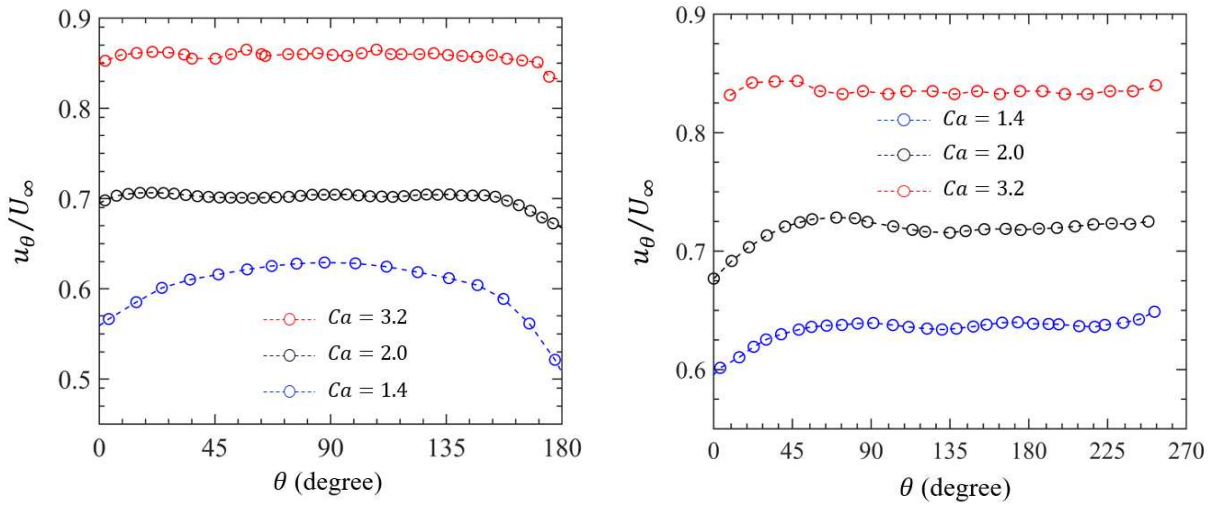

Figure 4-12 The tangential velocity as a function Capillary number, Ca against angular position, θ. Data is represented for $d_{eq} = 450$ µm, and $Re = 5$, (a) in Channel A with a 180° curved section, and (b) channel B with a 270° curved section.

The deformation index, DI for a range of capillary numbers $1.4 < Ca < 3.2$ is plotted against the angular position, θ in Figure 4-13. For this case Reynolds number, $Re = 5$ and the droplet equivalent diameter, $d_{eq} = 450$ µm are constant. Figure 4-13(a) shows the deformation index, DI in Channel A. It can be seen that increasing the capillary number, Ca increases the deformation index, DI. For each case, deformation increases at the entrance of the curve. Figure 4-13(b) shows the same cases for channel B. With increasing the capillary number, Ca deformation index, DI also increases. By comparing the deformation between Channel A and B, it can be seen that the average deformation along the channel is slightly higher for Channel A. It is worth noting that, in Channel B near to the exit of the curved section of the channel, $\theta = 270°$, the deformation index, DI increases locally. This could arise from the sharp 90° curvature at the junction between the curvature section and the straight channel which has been highlighted in Figure 4-13(b).

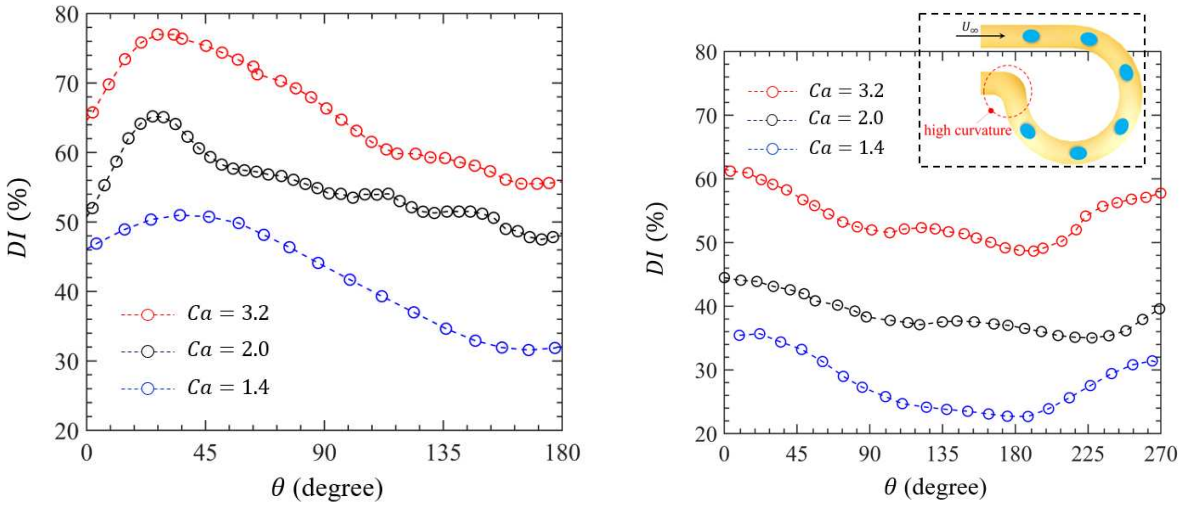

(a) (b)

Figure 4-13 Deformation index as a function of capillary number, Ca against angular position, θ. Data is represented for $d_{eq} = 450\mu m$, $Re = 5$, (a) in Channel A with a 180° curved section, and (b) in Channel B with a 270° curved section.

The trajectory of droplets in different cases with $1.4 \leq Ca \leq 3.2$ is plotted against the angular position, θ in Figure 4-14. In this figure Reynolds number, $Re = 5$ and droplet equivalent diameter, $d_{eq} = 450$ µm and remain constant. In Figure 4-14(a), for higher capillary numbers, Ca a deviation from the channel centerline occurs near to the entrance of the channel and towards the outer wall. For all cases decreasing the capillary number, Ca leads to a shift to the inner half and towards the inner wall. Trajectories for all droplets eventually converge and come together at $\theta \approx 180°$. Figure 4-14(b) shows the trajectory of droplets having the same capillary number cases for Channel B. It can be seen that for a high capillary number of $Ca = 3.2$, the droplet enters the curved channel from the outer half similar to the observation in Channel A but this time it is closer to the centerline of the channel. Across all cases in Channel B, droplets shift to the inner half and towards the inner wall. All trajectories in this channel are shown to converge at $\theta \approx 198°$.

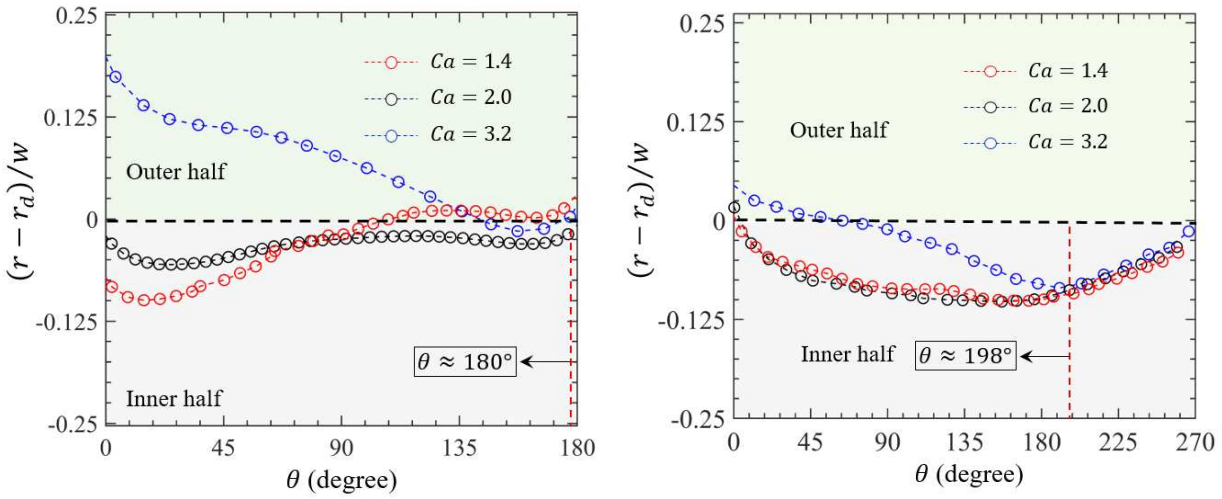

(a) (b)

Figure 4-14 Lateral migration as a function of capillary number, Ca against angular position, θ. Data is represented for $d_{eq} = 450$, $Re = 5$, (a) in Channel A with a 180° curved section, and (b) in Channel B with a 270° curved section.

4.6 Conclusion

This chapter presents an experimental investigation into the deformation and trajectory of deformable droplets in curved microchannels to evaluate the mechanical response of cell-mimicking entities in inertial flow conditions. Two microchannel geometries with 180° and 270° curved sections were used to analyze the effect of curvature, Reynolds number, droplet size, and surface tension on droplet behavior. The continuous and dispersed phases were selected to be immiscible and to differ in physical properties, better approximating real biofluid conditions.

Across the range of Reynolds numbers studied ($3.5 \leq \mathrm{Re} \leq 7$), droplet deformation and lateral migration remained largely unaffected, indicating a weak sensitivity to changes in inertial forces within the tested regime. Despite increases in flow rate and corresponding capillary number, no significant breakup or excessive deformation was observed, and droplets maintained structural

integrity throughout their trajectories. The surface tension and droplet size were found to influence droplet deformation through capillary number, which also impacted tangential velocity.

A key finding is the consistent convergence of droplet trajectories across a wide range of conditions in both channel geometries. This behavior suggests that even under moderate inertial conditions and varying capillary numbers, droplets maintain predictable migration paths, which is essential for reliable particle or cell sorting in microfluidic applications. Additionally, increased curvature length in the 270° geometry altered migration and deformation trends slightly, but without introducing instability or breakup.

These results confirm that deformable droplets used here as surrogates for bio cell clusters remain structurally stable under the flow conditions used for Dean vortex formation in curved microchannels. Therefore, the modified inlet geometry proposed in this thesis can be safely implemented without inducing structural damage or erratic behavior in biological particles. This validation supports the transition to testing the modified spiral micro-hydrocyclone configuration, as it confirms that the flow conditions required to induce Dean vortices do not compromise the integrity of deformable cell-like materials.

References

[1] F. Del Ben, M. Turetta, G. Celetti, A. Piruska, M. Bulfoni, D. Cesselli, W.T.S. Huck, G. Scoles, A Method for Detecting Circulating Tumor Cells Based on the Measurement of Single-Cell Metabolism in Droplet-Based Microfluidics, Angew. Chemie 128 (2016) 8723–8726. https://doi.org/10.1002/ange.201602328.

[2] S. Juul, C.J.F. Nielsen, R. Labouriau, A. Roy, C. Tesauro, P.W. Jensen, C. Harmsen, E.L. Kristoffersen, Y.L. Chiu, R. Frohlich, P. Fiorani, J. Cox-Singh, D. Tordrup, J. Koch, A.L. Bienvenu, A. Desideri, S. Picot, E. Petersen, K.W. Leong, Y.P. Ho, M. Stougaard, B.R. Knudsen, Droplet microfluidics platform for highly sensitive and quantitative detection of malaria-causing plasmodium parasites based on enzyme activity measurement, ACS Nano 6 (2012) 10676–10683. https://doi.org/10.1021/nn3038594.

[3] J.H. Tsui, W. Lee, S.H. Pun, J. Kim, D.H. Kim, Microfluidics-assisted in vitro drug screening and carrier production, Adv. Drug Deliv. Rev. 65 (2013) 1575–1588. https://doi.org/10.1016/j.addr.2013.07.004.

[4] F. He, M.J. Zhang, W. Wang, Q.W. Cai, Y.Y. Su, Z. Liu, Y. Faraj, X.J. Ju, R. Xie, L.Y. Chu, Designable Polymeric Microparticles from Droplet Microfluidics for Controlled Drug Release, Adv. Mater. Technol. 4 (2019) 1–23. https://doi.org/10.1002/admt.201800687.

[5] R. Seemann, M. Brinkmann, T. Pfohl, S. Herminghaus, Droplet based microfluidics, Reports Prog. Phys. 75 (2012). https://doi.org/10.1088/0034-4885/75/1/016601.

[6] S. Mashaghi, A. Abbaspourrad, D.A. Weitz, A.M. van Oijen, Droplet microfluidics: A tool for biology, chemistry and nanotechnology, TrAC - Trends Anal. Chem. 82 (2016) 118–125. https://doi.org/10.1016/j.trac.2016.05.019.

[7] T.S. Kaminski, P. Garstecki, Controlled droplet microfluidic systems for multistep chemical and biological assays, Chem. Soc. Rev. 46 (2017) 6210–6226. https://doi.org/10.1039/c5cs00717h.

[8] K. Schroen, C. Berton-Carabin, D. Renard, M. Marquis, A. Boire, R. Cochereau, C. Amine, S. Marze, Droplet microfluidics for food and nutrition applications, Micromachines 12 (2021). https://doi.org/10.3390/mi12080863.

[9] H. Amini, W. Lee, D. Di Carlo, Inertial microfluidic physics, Lab Chip 14 (2014) 2739–2761. https://doi.org/10.1039/c4lc00128a.

[10] L. Shang, Y. Cheng, Y. Zhao, Emerging Droplet Microfluidics, Chem. Rev. 117 (2017) 7964–8040. https://doi.org/10.1021/acs.chemrev.6b00848.

[11] S. Marsousi, J. Karimi-Sabet, M.A. Moosavian, Y. Amini, Liquid-liquid extraction of calcium using ionic liquids in spiral microfluidics, Chem. Eng. J. 356 (2019) 492–505. https://doi.org/10.1016/j.cej.2018.09.030.

[12] M. Rafeie, S. Hosseinzadeh, R.A. Taylor, M.E. Warkiani, New insights into the physics of inertial microfluidics in curved microchannels. I. Relaxing the fixed inflection point assumption, Biomicrofluidics 13 (2019) 1–15. https://doi.org/10.1063/1.5109004.

[13] C. Chen, Y. Zhao, J. Wang, P. Zhu, Y. Tian, M. Xu, L. Wang, X. Huang, Passive mixing inside microdroplets, Micromachines 9 (2018) 1–16. https://doi.org/10.3390/mi9040160.

[14] J. Zhang, S. Yan, D. Yuan, G. Alici, N.T. Nguyen, M. Ebrahimi Warkiani, W. Li, Fundamentals and applications of inertial microfluidics: A review, Lab Chip 16 (2016) 10–34. https://doi.org/10.1039/c5lc01159k.

[15] M. Hein, M. Moskopp, R. Seemann, Flow field induced particle accumulation inside droplets in rectangular channels, Lab Chip 15 (2015) 2879–2886. https://doi.org/10.1039/c5lc00420a.

[16] S. Ma, J.M. Sherwood, W.T.S. Huck, S. Balabani, On the flow topology inside droplets moving in rectangular microchannels, Lab Chip 14 (2014) 3611–3620. https://doi.org/10.1039/c4lc00671b.

[17] E. Ghazimirsaeed, M. Madadelahi, M. Dizani, A. Shamloo, Secondary Flows, Mixing, and Chemical Reaction Analysis of Droplet-Based Flow inside Serpentine Microchannels with Di ff erent Cross Sections, 37 (2021) 5118–5130. https://doi.org/10.1021/acs.langmuir.0c03662.

[18] M.P. Boruah, A. Sarker, P.R. Randive, S. Pati, K.C. Sahu, Tuning of regimes during two-phase flow through a cross-junction, Phys. Fluids 33 (2021). https://doi.org/10.1063/5.0071743.

[19] S. Ansari, D.S. Nobes, The effect of three-phase contact line pinning during the passage of an isolated bubble through a confining pore, Phys. Fluids 33 (2021). https://doi.org/10.1063/5.0050801.

[20] P. Hadikhani, S.M.H. Hashemi, G. Balestra, L. Zhu, M.A. Modestino, F. Gallaire, D. Psaltis, Inertial manipulation of bubbles in rectangular microfluidic channels, Lab Chip 18 (2018) 1035–1046. https://doi.org/10.1039/c7lc01283g.

[21] T. Alkayyali, T. Cameron, B. Haltli, R.G. Kerr, A. Ahmadi, Microfluidic and cross-linking methods for encapsulation of living cells and bacteria - A review, Anal. Chim. Acta 1053 (2019) 1–21. https://doi.org/10.1016/j.aca.2018.12.056.

[22] S. Guido, V. Preziosi, Droplet deformation under confined Poiseuille flow, Adv. Colloid Interface Sci. 161 (2010) 89–101. https://doi.org/10.1016/j.cis.2010.04.005.

[23] S. Kuriakose, P. Dimitrakopoulos, Deformation of an elastic capsule in a rectangular microfluidic channel, Soft Matter 9 (2013) 4284–4296. https://doi.org/10.1039/c3sm27683j.

[24] A.K. Nema, M.K. Tripathi, K.C. Sahu, Migration of a viscoelastic drop in a ratchet microchannel, J. Nonnewton. Fluid Mech. 307 (2022). https://doi.org/10.1016/j.jnnfm.2022.104870.

[25] H. Konda, M. Kumar Tripathi, K.C. Sahu, Bubble Motion in a Converging-Diverging Channel, J. Fluids Eng. Trans. ASME 138 (2016) 1–6. https://doi.org/10.1115/1.4032296.

[26] S. Ebrahimi, P. Balogh, P. Bagchi, Motion of a capsule in a curved tube, J. Fluid Mech. 908 (2020). https://doi.org/10.1017/jfm.2020.831.

[27] W.R. Dean, LXXII. The stream-line motion of fluid in a curved pipe (Second paper) , London, Edinburgh, Dublin Philos. Mag. J. Sci. 5 (1928) 673–695. https://doi.org/10.1080/14786440408564513.

[28] L. Zhu, L. Brandt, The motion of a deforming capsule through a corner, J. Fluid Mech. 770 (2015) 374–397. https://doi.org/10.1017/jfm.2015.157.

[29] E. Häner, M. Heil, A. Juel, Deformation and sorting of capsules in a T-junction, J. Fluid Mech. 885 (2019). https://doi.org/10.1017/jfm.2019.979.

[30] A. Karimi, S. Yazdi, A.M. Ardekani, Hydrodynamic mechanisms of cell and particle trapping in microfluidics, Biomicrofluidics 7 (2013) 1–23. https://doi.org/10.1063/1.4799787.

[31] S. Nix, Y. Imai, T. Ishikawa, Lateral migration of a capsule in a parabolic flow, J. Biomech. 49 (2016) 2249–2254. https://doi.org/10.1016/j.jbiomech.2015.11.038.

[32] A. Nait-Ouhra, A. Guckenberger, A. Farutin, H. Ez-Zahraouy, A. Benyoussef, S. Gekle, C. Misbah, Lateral vesicle migration in a bounded shear flow: Viscosity contrast leads to off-centered solutions, Phys. Rev. Fluids 3 (2018) 1–16. https://doi.org/10.1103/PhysRevFluids.3.123601.

[33] D. Di Carlo, Inertial microfluidics, Lab Chip 9 (2009) 3038–3046. https://doi.org/10.1039/b912547g.

[34] M.G. Lee, S. Choi, H.J. Kim, H.K. Lim, J.H. Kim, N. Huh, J.K. Park, Inertial blood plasma separation in a contraction-expansion array microchannel, Appl. Phys. Lett. 98 (2011) 2009–2012. https://doi.org/10.1063/1.3601745.

[35] J. Zhou, I. Papautsky, Fundamentals of inertial focusing in microchannels, Lab Chip 13 (2013) 1121–1132. https://doi.org/10.1039/c2lc41248a.

[36] R.S. Srivastava, D.J. McConalogue, Motion of a fluid in a curved tube, Proc. R. Soc. London. Ser. A. Math. Phys. Sci. 307 (1968) 37–53. https://doi.org/10.1098/rspa.1968.0173.

[37] W.R. Dean, The stream-line motion of fluid in a curved pipe, London, Edinburgh, Dublin Philos. Mag. J. Sci. 5 (1928) 673–695. https://doi.org/10.1080/14786440408564513.

[38] N. Nivedita, P. Ligrani, I. Papautsky, Dean flow dynamics in low-aspect ratio spiral microchannels, Sci. Rep. 7 (2017) 1–10. https://doi.org/10.1038/srep44072.

[39] D. Di Carlo, D. Irimia, R.G. Tompkins, M. Toner, Continuous inertial focusing, ordering, and separation of particles in microchannels, Proc. Natl. Acad. Sci. U. S. A. 104 (2007) 18892–18897. https://doi.org/10.1073/pnas.0704958104.

[40] S. Ebrahimi, P. Bagchi, Inertial and non-inertial focusing of a deformable capsule in a curved microchannel, J. Fluid Mech. 929 (2021) 1–38. https://doi.org/10.1017/jfm.2021.868.

[41] A. Lashkaripour, C. Rodriguez, N. Mehdipour, R. Mardian, D. McIntyre, Machine learning enables design automation of microfluidic flow-focusing droplet generation, Nat. Commun. 12 (2021). https://doi.org/10.1038/s41467-020-20284-z.

[42] S. Razavi Bazaz, A. Mashhadian, A. Ehsani, S.C. Saha, T. Krüger, M. Ebrahimi Warkiani, Computational inertial microfluidics: a review, Lab Chip 20 (2020) 1023–1048. https://doi.org/10.1039/c9lc01022j.

Chapter 5: Simultaneous Circulating Tumor Cells (CTCs) Tracking and Flow Field Characterization

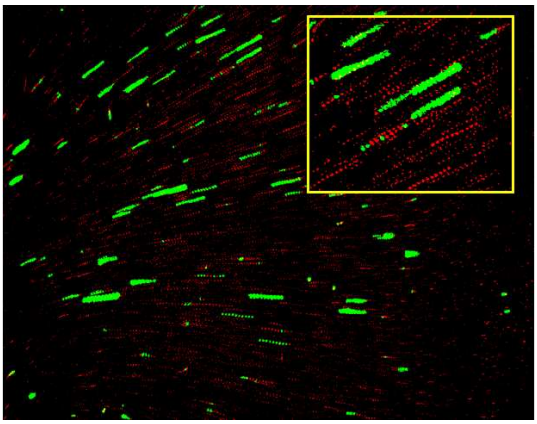

Graphical Abstract: Streaklines of color-coded Cell cluster and particles

This chapter focused on developing an integrated optical measurement system to perform simultaneous flow field and particle tracking measurements inside a micro-hydrocyclone designed for CTC separation. Two experimental conditions were investigated: first, a single-phase flow measurement where the internal velocity field was quantified using particle image velocimetry (PIV); and second, a two-phase flow condition where CTCs were introduced into the working fluid This is the first experimental study of its kind to directly measure and report the internal flow field of a micro-hydrocyclone, evaluating it under both single-phase and two-phase conditions.

This chapter is based on the following paper:

Saffar, Yeganeh, Marianna Kulka, David S. Nobes, and Reza Sabbagh. "Simultaneous circulating tumor cells (CTCs) tracking and flow field characterization through integrated single camera imaging in a micro-hydrocyclone." *Chemical Engineering Journal* (2025): 165681.

5.1 Introduction

Particle separation in microfluidics play an important role in various applications such as biomedicine [1], environmental monitoring [2,3], and phase separation [4]. Numerous traditional methods for particle separation including membrane filtration, dielectrophoretic, and centrifugation, are widely used across different applications [5]. However, these techniques are limited in several ways that can include clogging, high operational cost, long processing time, and the potential loss of cell viability in bio-applications. A miniaturized hydrocyclone has been recently introduced as an innovative solution to address these challenges [6][7]. This high throughput device demonstrated the ability to effectively overcome issues related to clogging and can handle a higher concentration of particles, and operate with lower energy input and operational cost [8].

A hydrocyclone geometry consists of a cylindrical body and a conical section, with one inlet and two outlets as shown in Figure 5-1(a). The flow and particle mixtures enter the device tangentially through the inlet, and two swirling flow regions are developed inside the device as shown in Figure 5-1(a). Smaller particles are carried by the inner swirling flow and exit through the overflow, whereas larger particles are directed into the outer swirling flow and exit through the underflow [9][10]. 2D Axial velocity field is an important parameter in characterizing the flow organization in a hydrocyclone. When examining the axial velocity field, a portion of the flow is directed upward to the overflow, while another part moves downward towards the underflow (spigot) as illustrated in Figure 5-1(b) [11][12]. The boundary between the two regions with zero axial/vertical velocity is known as the locus of zero vertical velocity (LZVV) [13]. Particles inside the LZVV follow the flow to the overflow, while particles outside this boundary are carried to the

underflow [13]. Therefore, investigating the LZVV is one of important flow organization properties in identifying the device performance [13].

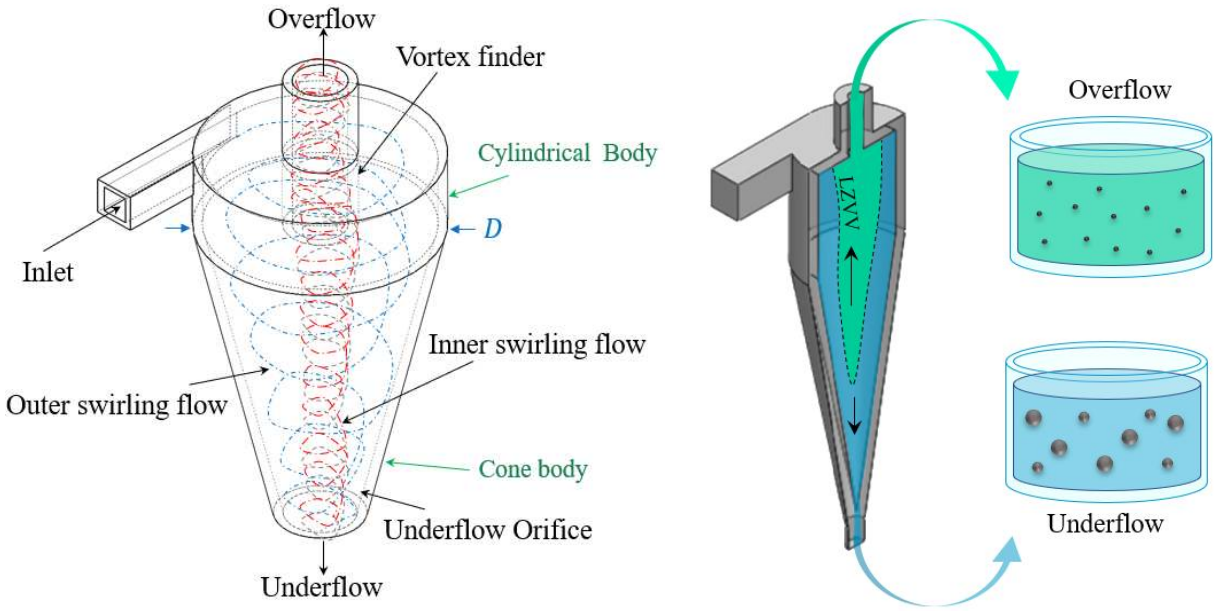

Figure 5-1. A schematic of the micro-hydrocyclone and resultant flow field. (b) A schematic of the particle separation based on the locus of zero vertical velocity (LZVV).

Miniaturized hydrocyclones can be divided in two different categories of mini-hydrocyclone and micro-hydrocyclone depending on the characteristic diameter of the body of the hydrocyclone depicted in Figure 5-1(a) as D. Considering this characteristics, hydrocyclones in the range of $10\ \text{mm} \leq D < 100\ \text{mm}$ are usually known as mini-hydrocyclone and hydrocyclones in the range of $D < 10\ \text{mm}$ are usually known as micro-hydrocyclone[7][14]. Mini-hydrocyclones have been investigated for potential applications in yeast separation during alcoholic fermentation [15], assessing chlorination levels in water, removing micro-particles from lubricant oils [16], separating microplastics from water [17], and isolating mammalian cells [18]. In the last decade, the investigation of micro-hydrocyclones has developed as a new research area, driven by advancements in microfabrication [19]. The differences in the flow dynamics of these device

categories are yet to be investigated. The ability to manufacture complex micro-scale geometries using techniques such as 3D printing and micromachining has made the fabrication of these devices feasible, leading to growth in the studies investigating the application of the micro-hydrocyclones mainly focused on cell and particle separation [19]. Yet, there are limited number of works investigated the application of the micro-hydrocyclone in these fields.

Particle-liquid separation in a 350 μm micro-hydrocyclone [20], demonstrated that flow conditions and particle size significantly influence separation efficiency. Using polystyrene microbeads suspended in PBS as the feed, [20] examined how inlet velocity affects the separation of particles with a cut size of 1 μm, showing that optimizing flow conditions is important for efficient removal of fine particles. He *et al.* [18] studied a 10 mm micro-hydrocyclone for removing 10 μm microplastics (MPs) and found that adjusting the vortex finder and spigot diameters impacted flow distribution, influencing the trade-off between concentration ratio and recovery. Their results suggest that increasing the spigot diameter and decreasing the vortex finder diameter enhance microplastics removal by altering the radial and axial velocity distributions inside the device. Microplastic separation was further improved [21] in a 10 mm micro-hydrocyclone through introducing an aluminum-based flocculant, which increased removal efficiency by 14% for microplastics between 5–20 μm, with a primary focus on 10 μm MPs. Their findings highlight the role of chemical additives in enhancing separation while emphasizing the importance of flow rate optimization for maintaining performance.

Mesenchymal stem cells (MSCs) were separated from microcarrier particles (MCs) [7] using a 3 mm-diameter micro-hydrocyclone and it was demonstrated that adjusting flow conditions can significantly influence separation performance. Their findings showed that increasing the flow rate improved separation efficiency, but excessive flow could impact cell viability, although the overall

reduction remained minimal. While a qualitative visualization of general swirling motion was provided using florescent particles, no qualitative velocity fields and cell trajectory analysis was reported in this study. Building on the previous work, a two-step hydrocyclone system for high-density retention of Chinese Hamster Ovary (CHO) cells was applied, using a similar 3 mm-diameter device [8]. They found that higher flow rates enhance separation but can also introduce mechanical stress that affects cell integrity. Additionally, their study indicated that separation performance remains stable under moderate cell concentrations but declines when the cell density becomes too high. CHO cell viability was further investigated in a 10 mm-diameter hydrocyclone [22], examining cone angles of 6°, 8°, and 10°, and inlet velocities ranging from 4 to 7.5 m/s. Their findings revealed that increasing the cone angle or inlet velocity raises shear stress, which in turn compromises cell viability, with the highest cone angle causing the most significant viability loss.

These results emphasize the need for careful optimization of micro-hydrocyclones in cell separation applications. Design modifications that enhance separation efficiency may also introduce mechanical forces that can damage cells. Such modifications require a thorough understanding of flow dynamics, cell phenomena, and their interactions within the device.

Circulating tumor cells (CTCs) offer critical insights into cancer prognosis and treatment [23]. CTCs circulate in the bloodstream or the lymphatics and during specific conditions, they can extravasate and become seeds for growth of new tumors in a process called metastasis [18]. The lifespan of CTCs in the vasculature is dependent upon their interaction with non-tumor cells such as platelets and neutrophils through adhesion interactions that inhibit their apoptosis [24]. Human glioblastoma is a highly aggressive and malignant brain cancer where approximately 0.4-2% of patients develop metastases outside the central nervous system due to CTC migration. CTCs can be detected throughout disease progression, where the CTCs are comprised of about 2 to 23 cells

[25]. Sampling of circulating CTCs can be a novel diagnostic and early detection tool but to examine these CTC accurately, it is essential to preserve their 3D structures and cell-to-cell relationships. Existing CTC isolation methods use microfluidics and centrifugation which often break apart CTC clusters, destroying their 3D configurations. Convenient and specific methods for CTC detection continue to limit CTC research [13]. Preserving these clusters during separation is essential, as they provide a more accurate analysis of tumor behavior and enable more reliable predictions about how tumors will respond to treatment [23]. Micro-hydrocyclones are gaining attention as a potential method for isolating CTCs due to their high throughput capabilities and the possibility of preserving cell cluster integrity.

Development of microfluidic applications has led to the design and employment of complex devices with complex internal flow organization. Predicting or enhancing the performance of such devices requires an understanding of its internal flow organization [26]. Optical measurement techniques such as particle image velocimetry (PIV) and particle tracking velocimetry (PTV) can be employed to investigate flow transfer in micromixers, particle sorting or separation devices, and to distinguish both the effective and non-effective flow structures forming within a device [27]. The fundamental investigation of flow in microchannels or simple devices has been studied extensively using micro-PIV (μPIV) [27] for flow in spiral particle separators [28], serpentine micromixers [29] and droplet generators[30]. However, in many of these microfluidic applications the flow interacts with other components such as cells, particles, and droplets resulting in a multiphase flow environment [31].

Although PIV and PTV have been used as a solution to measure the velocity of the continuous phase and dispersed phase organization in macro-scale flows, the real time investigation of the interaction of such components and flow organization can be challenging in microdevices [32].

Despite using imaging approaches in velocimetry of the flow within many microfluidic devices [33], experimental investigation of the whole velocity field of micro-hydrocyclones appears to not have been carried out. The flow within micro-hydrocyclone devices has been investigated only in limited numerical works [22]. PIV, however, has been employed in a couple of studies to investigate flow behavior on a larger scale i.e. mini-hydrocyclones, largely focused devices larger than 10 mm and primarily addressed single-phase fluid dynamics [34][35]. In many cases, only line-based velocity profiles were reported, with comprehensive flow maps derived from numerical simulations rather than experimental measurements [35]. Furthermore, these studies have not considered the simultaneous study on the behavior of biological particulates such as circulating tumor cells (CTCs). Such numerical works are in fact limited only to single-phase flow and does not address the influence of the second phase on the flow organization. Therefore, the influence of the second phase on the flow in micro-hydrocyclones remains unclear and to the best knowledge of the authors has not been investigated neither numerically nor experimentally.

Micro-hydrocyclones, typically defined as hydrocyclone devices with characteristic dimensions on the order of $D < 10\,\mathrm{mm}$ [7], were first introduced late 1990s [36]. In their pioneering work, Harrison and Cilliers demonstrated that micro-hydrocyclones are capable of effectively separating particles. Using particles of two distinct sizes, 22μm and 6μm, they showed that larger particles ($D = 22\,\mu\mathrm{m}$) predominantly exited through the underflow, while smaller particles ($D = 6\mu\mathrm{m}$) were collected from the overflow [36]. Building upon this concept, Medronho *et al.* explored the application of micro-hydrocyclone for biological cell separation. In their numerical study, cells with a size distribution centered around 12 μm were introduced into the device, and separation of target cell type BHK-21 mammalian cells was achieved with an efficiency of 90% [37]. While the fundamental principles of macro-scale hydrocyclones are well

established, the physics governing micro-hydrocyclone operation may differ due to scaling effects and microfluidic phenomena [39]. Several studies have attempted to characterize the internal flow field in micro-hydrocyclones through numerical simulations, with some identifying key similarities and differences compared to their macro-scale counterparts [18][40][37]. However, there are only a few numerical investigations focused on particle or bio-cell separation, and experimental visualizations of the internal flow field remain extremely limited. The few available attempts at experimental flow visualization have provided useful preliminary insights but generally lack spatial resolution, quantitative detail, and comprehensive flow characterization. As such, much of the current understanding of micro-hydrocyclone flow physics remains reliant on numerical models.

Given the relatively recent emergence of micro-hydrocyclone applications, numerous open questions remain regarding their underlying flow physics and separation mechanisms. For instance, are the current numerical simulations, often based on single-phase assumptions, valid representations of inherently multiphase micro-hydrocyclone flows? How do multiphase effects alter the separation dynamics, and to what extent do single-phase models fail to capture this complexity? Furthermore, most simulations explore only a narrow range of operating conditions and flow regimes. A systematic classification of flow regimes in micro-hydrocyclones, and a better understanding of the transition criteria between them, are currently lacking. Moreover, there is a clear absence of comprehensive experimental studies that could validate numerical predictions and provide direct insights into the internal flow structures and particle trajectories. Addressing these gaps is essential to establish the reliability of simulation tools, optimize micro-hydrocyclone design, and unlock their full potential in applications ranging from particle sorting to biomedical diagnostics.

In this work, a single-camera imaging system, combined with a custom-developed image processing scheme, was designed to visualize and quantify the velocity field of a two-phase flow inside a micro-hydrocyclone. The system was applied to study a continuous water phase seeded with tracer particles, along with a dispersed phase consisting of circulating tumor clusters (CTCs). To achieve simultaneous characterization of both phases, the imaging data was processed to isolate CTC images from the background seeded flow. Particle image velocimetry (PIV) was applied to determine the velocity field of the continuous phase, while a dedicated particle tracking velocimetry (PTV) scheme was developed to track and quantify the motion of individual CTCs. This experimental framework was used to investigate the influence of suspended CTCs on the underlying flow field by performing experiments under two distinct conditions: single-phase flow (water only) and two-phase flow (water with CTCs).

The experiments were conducted at three different Reynolds numbers (Re = 150, 300, and 700), covering distinct flow regimes within the micro-hydrocyclone, namely laminar, transitional, and statistically steady. Beyond studying the bulk flow behavior, the second objective was to characterize the transport dynamics of CTCs and compare their motion with the background flow field. Importantly, this is the first experimental study of its kind to directly measure and report the internal flow field of a micro-hydrocyclone, evaluating it under both single-phase and two-phase conditions.

5.2 Device fabrication

The geometric characteristics of the designed and manufactured micro-hydrocyclone is listed in Table 5-1. The micro-hydrocyclone was designed with a single inlet configuration with the diameter of $D = 5$ mm as shown in Figure 5-2(a). The designed micro-hydrocyclone had a height of 17 mm, inlet dimensions of 1.7 mm × 1.3 mm, outlet diameters of 1.7 mm (at the top) and 1 mm (at the bottom) as listed in Table 5-1. Fabrication of the transparent micro-hydrocyclone involved a multi-step process that combined 3D printing, laser cutting, and silicone casting as illustrated in Figure 5-2(b) to achieve a functional and optically accessible device.

The casting core for the micro-hydrocyclone was 3D printed using a high-resolution SLA 3D printer (Form 3, Formlabs Inc.) with a layer thickness of 10 μm to ensure fine detail and dimensional accuracy. Following the 3D printing, the walls of a cube mold were fabricated from acrylic sheet using a laser cutter for precision. The cube was designed to encase the hydrocyclone, provide structural support for the silicone casting process and provide orthogonal optical access for improved clarity. To enhance the optical properties of the hydrocyclone and ensure the silicone would not adhere to the printed surfaces, the printed hydrocyclone was coated with a resin spray. This coating provided a glossy finish and created a barrier that rendered the surface impermeable to silicone.

The silicone body of the micro-hydrocyclone was prepared by pouring a specially formulated silicone (Solaris^{TM}, Smooth-On Inc.) over the printed hydrocyclone core. The silicone was chosen for its transparency and its refractive index allowing effective optical access. To facilitate curing, the assembled mold was placed in an oven at 60 °C for a specified duration, ensuring complete drying and curing of the silicone. The flexibility of silicone material allowed

for easy removal without damaging the hydrocyclone structure. Uncured silicone was utilized to adhere a slab of silicone over the top of the hydrocyclone, effectively sealing the device. Precision-engineered metal hypodermic tubes with varying diameters were integrated as inlet and outlet connections. These hypodermic tubes were inserted into the silicone slab, creating access points for fluid flow. Silicone tubing was then connected to the hypodermic tubes to facilitate the movement of fluid through the hydrocyclone. The final assembly produced a transparent micro-hydrocyclone with a complex geometry suitable for optical measurement techniques, enabling detailed observation of particles and cell dynamics within the device. The device's internal cavity scale is shown in Figure 5-2(b).

Table 5-1 Dimensions of the micro-hydrocyclone device designed and fabricated.

Parameter	D	L	d_u	d_o	a	b
Value (mm)	5	17	1	1.7	1.3	1.7

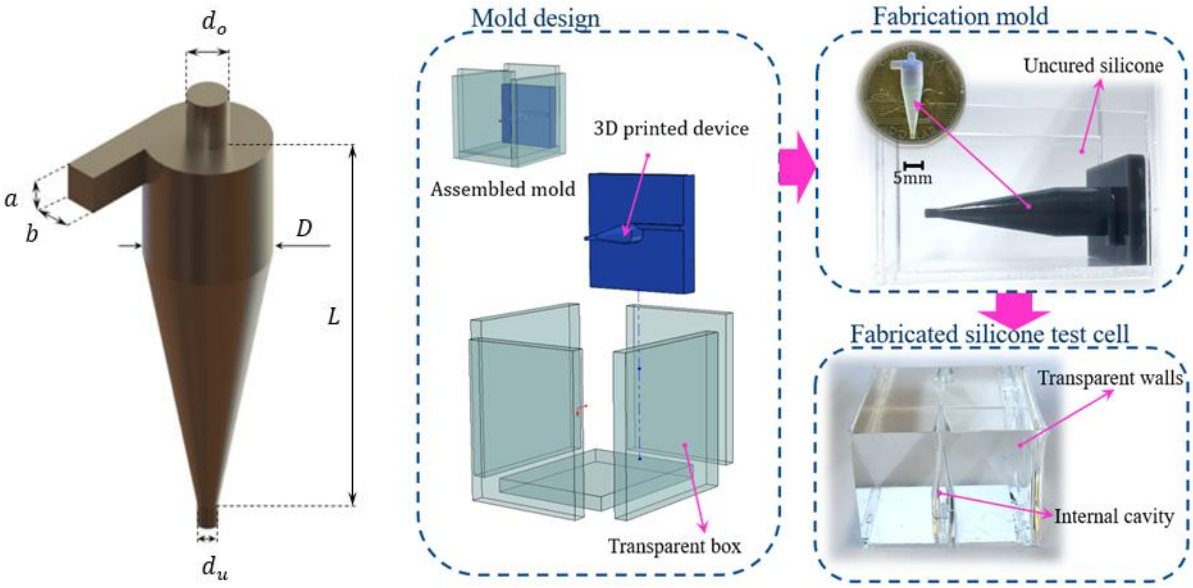

(a) (b)

Figure 5-2 (a) Schematic of the micro-hydrocyclone, showing the critical dimensions. (b) Fabrication process of the micro-hydrocyclone process including mold design, mold fabrication, silicon test cell fabrication. The last image (bottom right) shows the device's internal cavity scale.

Although silicone is a flexible material, the casting was designed with thick walls surrounding the internal cavity to reduce the potential for deformation under flow. The combination of this geometric stiffness and the inherent material stiffness of the selected silicone formulation serves to minimize wall compliance effects.

To evaluate any residual deformation, changes in channel geometry were quantified by analyzing intensity profiles across the channel width using fluorescence images acquired at various Reynolds numbers (Re = 0, 150, 300, and 700). Effective diameters were estimated using the standard deviation of these profiles and plotted accordingly shown in Figure 5-3. The resulting measurements showed variations of approximately 1–5% with respect to the baseline diameter, indicating limited wall movement. Considering the magnitude of these changes and the flow conditions investigated, such deformation did not noticeably impact the measured flow fields.

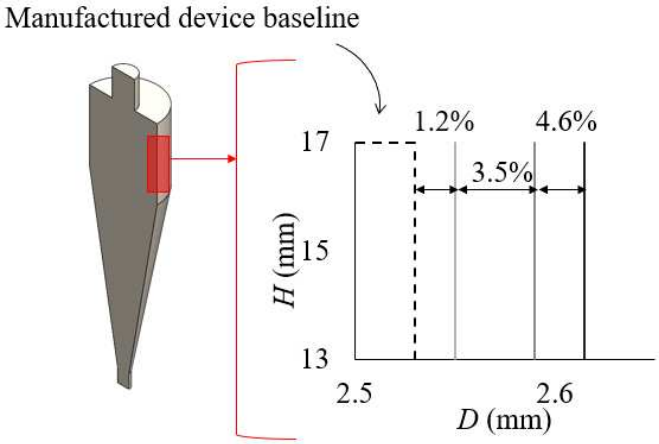

D (mm)	Expansion %	Ideal Re
5.06	1.2	0
5.1	2	150
5.18	3.6	300
5.23	4.6	700

Figure 5-3 Variation of the silicon cavity diameter as a result of increasing Reynolds number.

5.3 Experimental setup

An annotated image of the experimental setup used for flow imaging is shown in Figure 5-4. Components of the setup are also listed in Figure 5-4. Hollow glass 18 μm seeding particles and the fluorescent stained CTCs were used in the experiment. A 532 nm CW laser was employed to illuminate both seeding particles and the fluorescent stained CTCs. A high-speed camera (Phantom VEO 710, AMETEK Inc.) was also used to capture images of the flow. The frame rate of the camera was set from 1000 fps up to 7000 fps depending on the flow rate of the fluid system. A high precision syringe pump (PHD 2000, Harvard Apparatus Inc.) was employed to drive the flow at the desired flow rate into the micro-hydrocyclone.

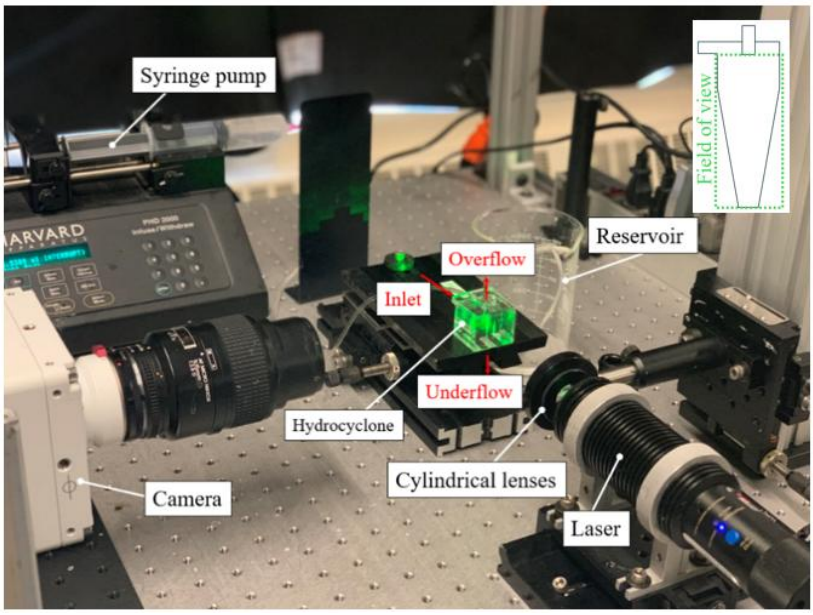

Figure 5-4 Photo of the experimental setup used for applying µPIV and µPTV for measuring the velocity of the flow and CTCs.

Table 5-2 Experimental setup components and specifications.

Component	Model	Manufacturer
Syringe pump	PHD 2000	Harvard Apparatus Inc.
Laser	532 nm / 2 W	Laserglow Technologies
Camera	Phantom VEO 710	AMETEK Inc.
Camera lens	Nikon AF Micro-NIKKOR 60 mm f/28D	Nikon

Refractive index matching is essential when applying optical flow measurement techniques such as PIV and PTV, especially in flow cells with complex or curved geometries [41][42][11]. By matching the refractive indices of the working fluid and the fluid cell, distortions and reflections at material interfaces are minimized. This clarity is important for tracking and measurement of particle displacement and velocity, as it removes aberrations that could compromise data integrity.

In this work, a 50.5% carbamide with water solution was used to achieve a refractive index $RI = 1.4118$ matching between the working fluid and the micro-hydrocyclone device. It is worth noting that this solution maintained a dynamic viscosity of 1.905 mPa·s. Other parameters considered for the experiments including the size of the PIV seeding particles and cell clusters are listed in Table 5-3.

Table 5-3 Experimental parameters considered for the experiment.

Parameter	**Specifications**
Inlet hydraulic diameter	1.5 mm
Tracing particles	18 μm monodisperse neutrally buoyant
Cell clusters	100-400 μm
Liquid phase	50.5% carbamide with water solution

In most cases, bio-cells are transparent by nature and typically unrecognizable by an optical system. Different kinds of dyes can be used to overcome this limitation and stain a cell based on the targeting cellular structure or component [43] . One of the common approaches used is to apply a florescent dye such as Nile Red to make the cell traceable in the existence of laser light. In this work, CTCs were stained using a Nile Red fluorescent dye with the maximum absorption of ~ 520 nm and the maximum emission spectra at ~ 580 nm [44]. Hence, as illustrated in the schematic in Figure 5-5, the flow includes two sets of particles, 18 μm monodisperse neutrally buoyant seeding particles to track the continuous phase, and fluorescent CTCs with a diameter in the range of 100 μm to 400 μm. In this work, the concentration of the CTCs in the working fluid at the inlet was kept at $\xi = 10^2$ cell/ml.

All the parameters and specifications of the experiment are listed in Table 5-3. The experiments were conducted in two scenarios. In Case 1, the flow was studied with only tracer particles introduced to establish the flow without CTCs. In Case 2, both tracer particles and cell clusters were added to the flow. This allowed investigation of two aspects: first, the tracer particles' role in revealing the flow characteristics in the presence of CTCs, and second, the behavior of the cell clusters themselves under these conditions.

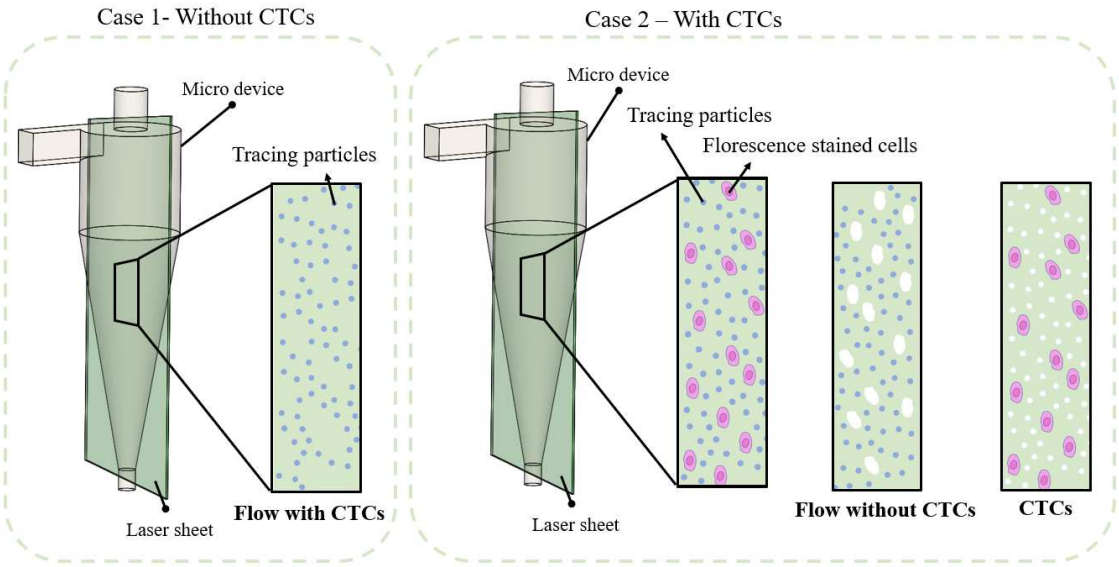

Figure 5-5 Schematic of the micro-hydrocyclone with the mid-plane including fluorescent CTCs and seeding particles.

5.4 Morphological segmentation

The custom image segmentation algorithm shown in Figure 5-6 was designed to differentiate and separate cells and tracer particles based on their size differences and generate two sets of data sets for particle and cell tracking. As a first step, the raw data from the single camera was preprocessed with noise reduction filters. For each individual frame all regions were scanned, and particle images located and categorized based on their shape and size. Regions marked as cells were erased from the raw data and transferred to a new data set utilizing a background image with the same geometry. As a result, two separate images of the flow were generated, one of the CTCs and the other of the tracer particles.

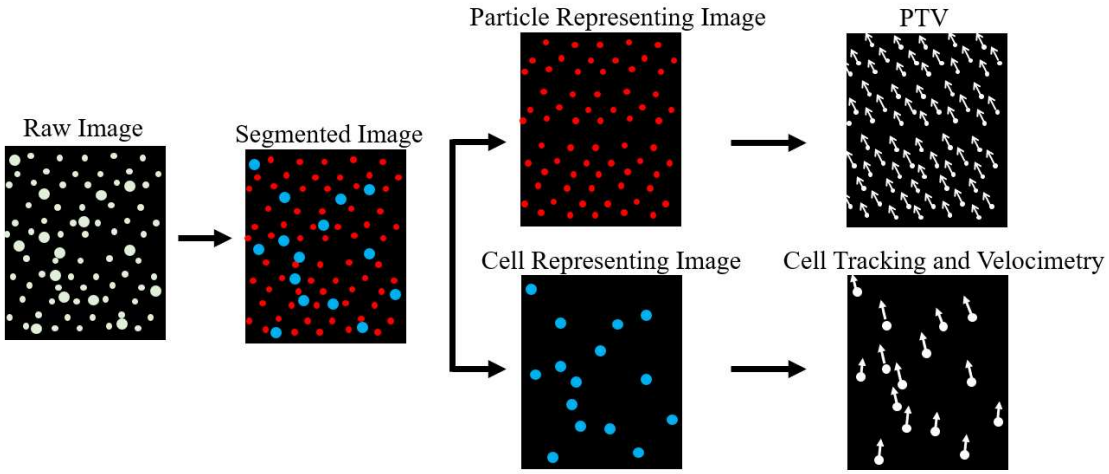

Figure 5-6 Schematic of image segmentation used to separate CTCs (blue dots) from seeding particles (red dots) for apllying µPIV and µPTV velocimetry.

Following this step, each image was post processed and prepared for tracking algorithm implementation. For the image of the seeding particles, µPIV was applied using commercial software (DaVis 8.4 LaVision GmbH.) to estimate the velocity of the continuous phase. For the time series of images of the CTCs, a µPTV algorithm was developed to detect each individual

CTC and follow its motion in order to measure its velocity. Figure 5-6 schematically illustrates all steps toward obtaining the velocity vectors for cells and tracer particles.

5.5 Median filtering and subtraction (MFS)

To test the performance of the image segmentation approach, a set of synthetic images were generated to test the algorithm. The median filtering and subtraction (MFS) technique, originally proposed by [32], was implemented in this study to isolate tracer particles from larger clusters in the synthetic two-phase flow images. This approach relies on distinct particle size properties, treating smaller particles as noise and removing them via a two-dimensional (2D) median filter. Following this initial filtering, the remaining image primarily contains the dispersed phase, represented by larger clusters. This processed image can then be used for PTV in sparse distributions.

The choice of a median filter kernel size was critical to achieve effective phase separation. In 2D median filtering, each pixel is assigned the median value of its surrounding pixels within a specified kernel. A larger kernel, typically between 5 and 7 pixels, effectively removed small tracer particles while preserving larger clusters, corroborating the findings of [32]. However, this kernel size slightly blurred the remaining particles, which did not interfere with the PTV analysis as positional accuracy was maintained. To recover the continuous phase, size-based filtering was applied instead of a subtraction step, as it allowed for a clear separation without artifacts from subtraction.

A smaller kernel size of 3 pixels was used to retain tracer particles with minimal impact on larger clusters to further refine the images. This two-step filtering, along with size-based thresholding, achieved reliable phase separation tailored to the synthetic images. Although no

subtraction was applied, size thresholding alone successfully distinguished tracer particles from clusters, resulting in distributions within the expected tracer range of 8–12 pixels, allowing accurate analysis of the continuous and dispersed phases.

A significant advantage of this approach was its computational efficiency. Median filtering is widely available in image processing software (MATLAB, The MathWorks Inc.), and the processing time is primarily dependent on image size, rather than particle density. For example, a 1024×1024-pixel image can be processed within seconds, making MFS suitable for processing a large stack of data. This refined implementation of MFS provides an effective method for isolating phase-separated flow features, serving as a valuable tool for fluid mechanics research focused on precise continuous and dispersed-phase measurements in multiphase flows.

5.6 Evaluation of synthetic images

The MFS approach was validated using synthetic images with known particles and cluster sizes. The evaluation of the separation performance of tracer particles and cell clusters was conducted using a detailed analysis of detected size distributions. A set of 100 synthetic images was analyzed as shown in Figure 5-7(a). Each image had a resolution of 512×512 pixels, containing 500 tracer particles of 3-5pixel diameter, distributed randomly to mimic fluid flow tracers. Additionally, 50 cell clusters were inserted into the image, with diameters randomly varying between 15-30 pixels, creating diverse cluster sizes. A noise level of 0.02 added a realistic background effect by introducing a fraction of white noise pixels. The output comprised of 100 images, for an accurate evaluation of the segmentation approach.

Probability density functions (PDFs) were generated for both the actual and detected particle and cell cluster sizes to assess the accuracy of the detection algorithms as shown in Figure 5-7(b)

and Figure 5-7(c). The size distributions indicate a high degree of correspondence between the actual and detected cluster sizes, which is also shown by overlapping peaks in their respective PDFs. Small discrepancies in tracer particle detection suggest challenges in isolating smaller particles within the noisy environment simulated in the synthetic images. The application of refined morphological filtering and size thresholding techniques enabled more accurate separation, particularly for the distinct size ranges of tracer particles between 8–12 pixels and cell clusters between 20–30 pixels.

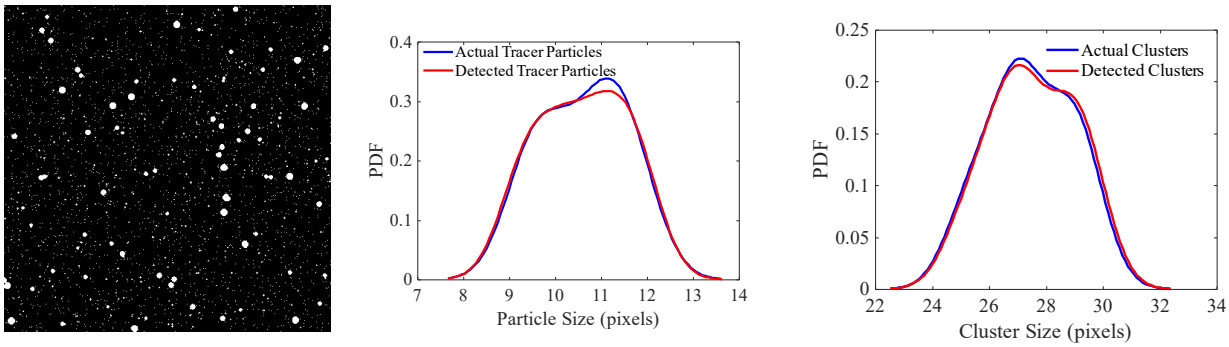

(a) (b) (c)

Figure 5-7 (a) An example synthetic image generated with a variation of large particle sizes for MFS method validation; (b) PDF for synthetic tracer particle detection and; (c) PDF plots for synthetic cell clusters detection.

5.7 Tracer particle and cell tracking velocimetry

Fluorescent staining and cell tracking in microfluidic devices provides a vast range of information for cell analysis. Labeling the cellular components facilitates the real-time observation and cell behavior for tracking in sorting and separation micro-devices [45]. This method can be used for various cell types, including CTCs investigating their migration, deformation, and interaction behavior [46]. As a result, tracking cells using fluorescent staining in microfluidic devices can be an effective method for investigating cell dynamics.

An experimentally collected image sample is represented in Figure 5-8(a) for highlighting the detection of particles including both seeding particles and CTCs is depicted. In this figure, the green particles represent the detected CTCs and the red particles indicate the seeding particles. Figure 5-8(b) highlights the random motion of both seeding particles over several time-resolved images and the motion of the CTCs is visualized by the streaklines for every individual particle. Figure 5-8(c) and (d) indicate the seeding particles and the CTCs in separate images, respectively. outlines the settings used for particle image velocimetry processing. The image set of seeding particles can be used to calculate the flow velocity vectors using a multi-pass PIV scheme with the minimum interrogation window size of 32×32 pixels. The velocity of each individual CTC was calculated using a PTV scheme. This scheme was developed to use the streakline of each cell. The velocity of each individual cell was calculated based on the average displacement of the CTC between two frames. A complete flow chart of the method is presented in Figure 5-9 showcasing the procedure of cell and particle separation to validation and vector calculations.

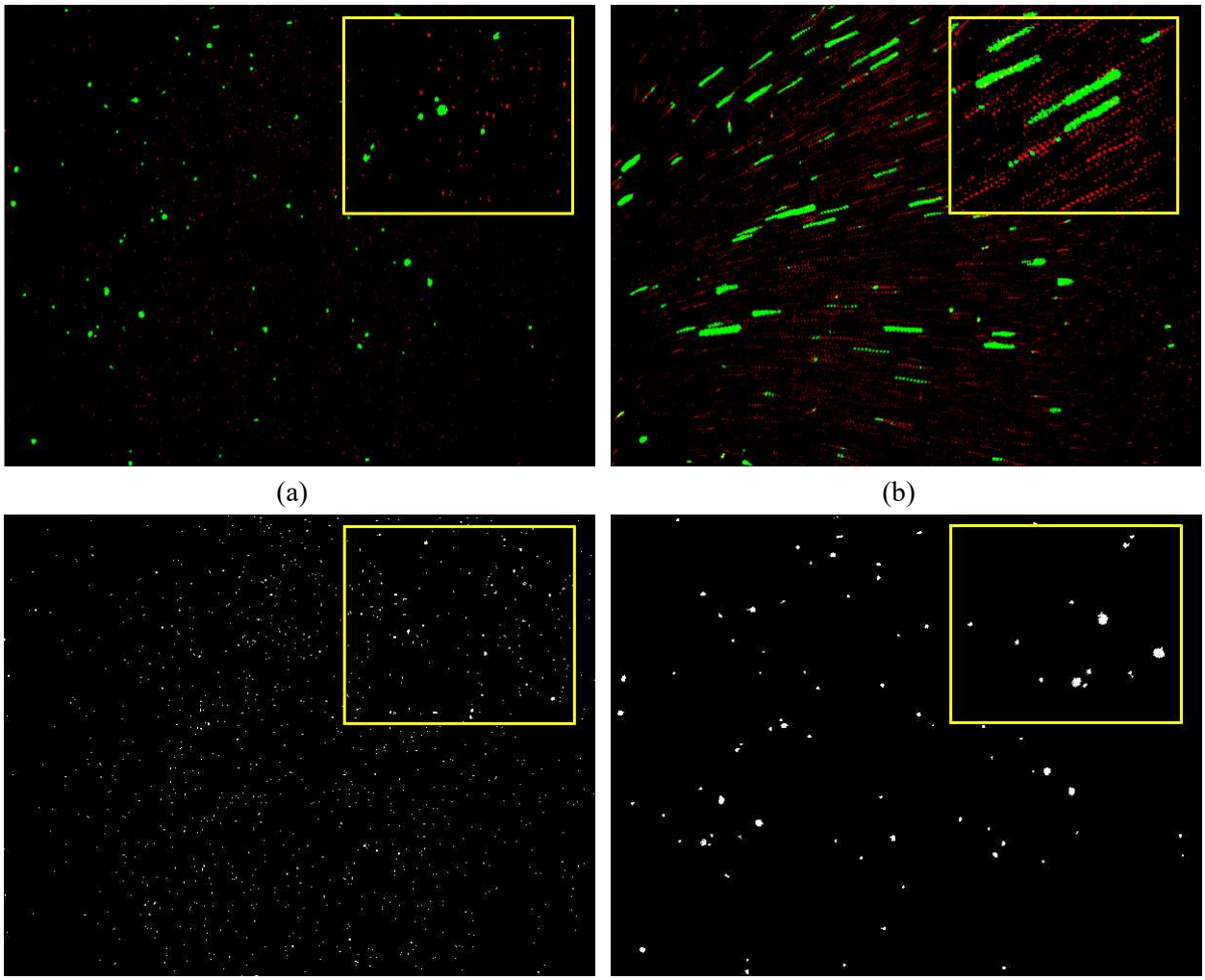

(a) (b)

(c) (d)

Figure 5-8 (a) The detected seeding particles and CTCs coloured in red and green, respectively. (b) Indicates the displacement of the seeding particles and CTCs visualized by streakline of each particle. (c) shows the seperated image of the seeding particles and (d) shows the seperated image of the CTCs.

Table 5-4 Particle image velocimetry settings.

Instrument	Parameters	Set value
Laser sheet	Laser	2 W
	Emission wavelength	532 nm
High frame rate camera	Image resolution	1024 pixels × 768 pixels
	Field of view	20 mm × 10 mm
	Acquisition mood	Continuous mode
	Frame rate	1000-10000 f/s
	Interrogation window size	32 pixels × 32 pixels
	Interrogation window overlaps	50%

The visualization of the flow organization and quantifying the characteristics of the micro-hydrocyclone is important due to two reasons. First, this is the first time that the flow field of a micro-hydrocyclone was visualized and quantified experimentally. Hence the results can be used to identify the physical characteristics of the flow within this device providing important information for numerical studies. Secondly, the comparison between the flow without CTCs and flow with CTCs reveals the influence of the CTCs on the flow field which can be used to identify if the flow simulations or experiments with flow without CTCs can be attributed to the two-phase flow with CTCs which is essential for development of the device. Furthermore, the velocity measurement of the CTCs indicates the behavior of the CTCs in comparison to the fluid flow which is another parameter for further development of this device.

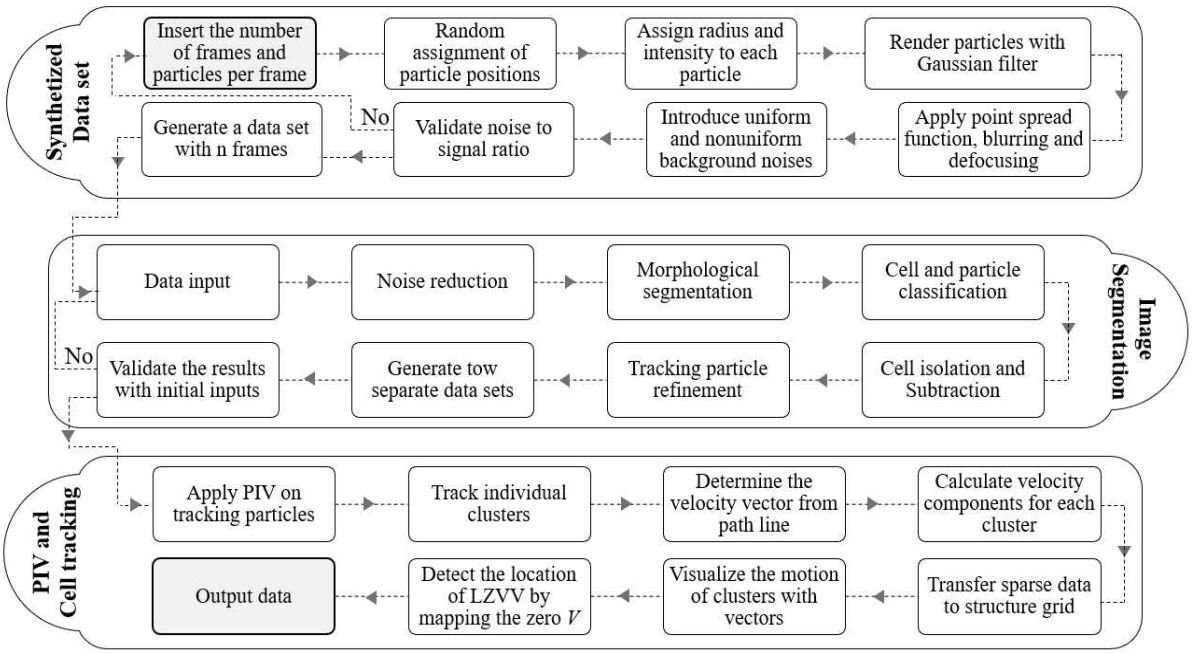

Figure 5-9 Flow chart of the tracking method in 3 different steps for generating synthetized data set, Image segmentation and flow and cell tracking.

5.8 Flow field characteristics

This section presents an analysis of the primary dimensionless numbers characterizing the flow behavior within the hydrocyclone system. Particular Reynolds number is utilized to analyze the overall flow regime. Stokes number is employed to assess the inertial response of both tracing particles and cell clusters within the flow field. These dimensionless parameters are discussed to provide deeper understanding of the system characteristics as shown in Table 5-5.

A common method to calculate the Reynolds number (Re) in hydrocyclones is to calculate the inlet Reynolds number based on the inlet hydraulic diameter, as:

$$Re_i = \frac{\rho V d_i}{\mu}$$

where ρ is the fluid density, V is the characteristic velocity, d_i is the inlet diameter of the hydrocyclone, and μ is the dynamic viscosity of the fluid [38]. In this work, three different Reynolds numbers have been investigated. Each Reynolds number represents a specific regime of the flow i.e., laminar, unsteady, and statistically steady regimes [38].

Calculating the Stokes number (Stk) provides an understanding of the particle and cell dynamics within the flow and the effect of tracing particles on the flow field and is defined as:

$$Stk = \frac{\tau_p V}{L}$$

where L is the characteristic length scale, V is the characteristics velocity which is the inlet velocity and τ_p is the particle relaxation time calculated as:

$$\tau_p = \frac{\rho_p d_p^2}{18\mu}$$

where ρ_p is the density and d_p is the diameter of the particle. For tracing particles used for PIV, the Stokes number is significantly small i.e. $Stk \ll 1$ for all three regimes. This criterion is usually used to show that the tracing particles follow the flow [47]. However, for CTC clusters, it can be seen that the Stokes number is varying significantly in a range from O(10^{-2}) to O(10) due to the variation of the size of the clusters and the flow regime. This shows that CTC clusters might have different dynamics from the seeding particles and the flow field.

Table 5-5 Flow characteristics for experimental cases.

Re_i	U (m/s)	Particles Stokes Number	CTC cluster Stokes Number	
		d_p =18 μm	d_p =100 μm	d_p =400 μm
150	0.168	2.79×10^{-3}	0.0862	1.38
300	0.335	5.58×10^{-3}	0.1726	2.76
700	0.782	1.30×10^{-2}	0.4021	6.44

5.9 Results and discussion

Based on the developed method two sets of experiments were conducted. The first, used just the working fluid with seeding particles denoted as the flow without CTCs. For the second, the working fluid with seeding particles and CTC particles is denoted as the flow with CTCs. To investigate the influence of the CTC on the flow organization three Reynolds numbers of $Re = 150, 300$ and 700 were investigated. Here, Reynolds number is defined as $Re = u_i d_i/\nu$ where u_i is velocity of the inlet based on the mean flow field, d_i is the hydraulic diameter of the inlet, and ν represents the kinematic viscosity of the working fluid. These conditions based on this definition of *Re* were selected to cover the laminar, unsteady, and statistically steady regimes, respectively of the micro-hydrocyclone [38].

5.9.1. Influence of CTCs on flow organization

The time averaged streamlines with a normalized velocity magnitude, $V^* = V/V_{\max\,(Re_i)}$, overlaid on the midplane of the micro-hydrocyclone is shown in Figure 5-11(a-c) shows the flow without CTCs where only tracing particles are added to the working fluid. Figure 5-11(d-f) represents the flow organization with the existence of cell clusters in the device in addition to the tracing particles i.e. the flow with CTCs. For each of the above scenarios, three cases with different Reynolds numbers represent the flow organization at various operational phases of the device.

At $Re = 150$, the laminar flow regime is shown in Figure 5-11(a), a large vortex appears on the midplane of the device. It can also be seen that a low flow rate stream is formed towards the vortex finder resulting in a low separation efficiency. An increase in the Reynolds number to $Re = 300$ leads to the transition regime and generation of multiple unstable vortices as shown in Figure 5-11(b). At this Re, flow passes through both outlets, however, the number and size of vortices constantly changes with time. At a higher Reynolds number, $Re = 700,$ the statistically steady regime is shown in Figure 5-11(c) and two stable vortices are generated at the mid-height of the device. The location of the maximum velocity, $V^* = V/V_{\max}$ is altered from the spigot to two locations closer to the center of the micro-hydrocyclone and stretched towards both outlets. It indicates an increase in the flow rate passing through the vortex finder at this Re which hypothetically can improve the performance of the device.

The influence of the CTCs on the fluid flow can be observed by comparing the result of the flow field in Figure 5-11(a-c) with Figure 5-11(d-f). As can be observed, for the lowest Reynolds number, $Re = 150$ the flow organization and velocity magnitude are almost the same. This shows that at this Reynolds number, CTCs have no influence on the flow field of the micro-hydrocyclone. For the unsteady regime at $Re = 300$, although the velocity field and flow organization are very similar to the flow without CTCs, there are some irregularities in the number and size of the vortices. Although, this can be attributed to the influence of the CTCs on the flow, the physics of the flow, which is unsteady, makes it difficult to characterize whether this difference is due to the effect of CTCs or it is the nature of the flow. For the highest Reynolds number, $Re = 700$, Figure 5-10(a) shows the instantaneous spatial average of the velocity fluctuating around a mean value of ~0.156 (red), with a deviation of about ±0.007, as indicated by the RMS line (yellow). This indicates that while the mean is stable, there is consistent small-scale temporal variation. The

cumulative average shown in Figure 5-10(b) initially fluctuates but gradually stabilizes and converges to the temporal average (red line). This indicates that the fluctuations are centered around a consistent mean and the system has reached a statistically steady state[38]. This regime can be seen in Figure 5-11(f), in comparison to the base flow, Figure 5-11(c), the flow organization appears to be the same. However, as is highlighted in both figures, the location of the core vortex has moved upward toward the vortex finder. Based on these observations for the three Reynolds numbers, it can be inferred that the existence of the CTCs in the flow field does not have a significant effect on the mean flow organization. It is worth noting that the concentration of the CTCs in the flow field might affect this conclusion.

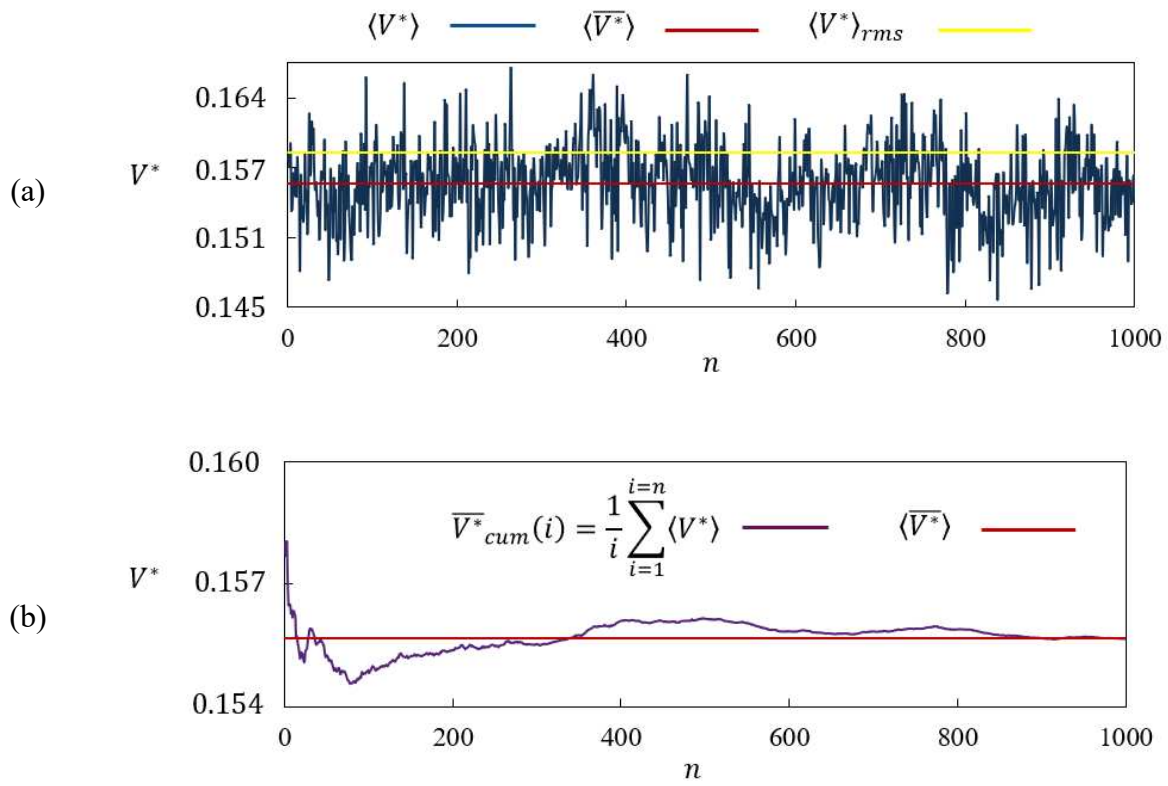

Figure 5-10 (a) Spatially and (b) cumulative averaged velocity magnitude in $Re = 700$ indicating the state of the flow converging toward the cumulative average value.

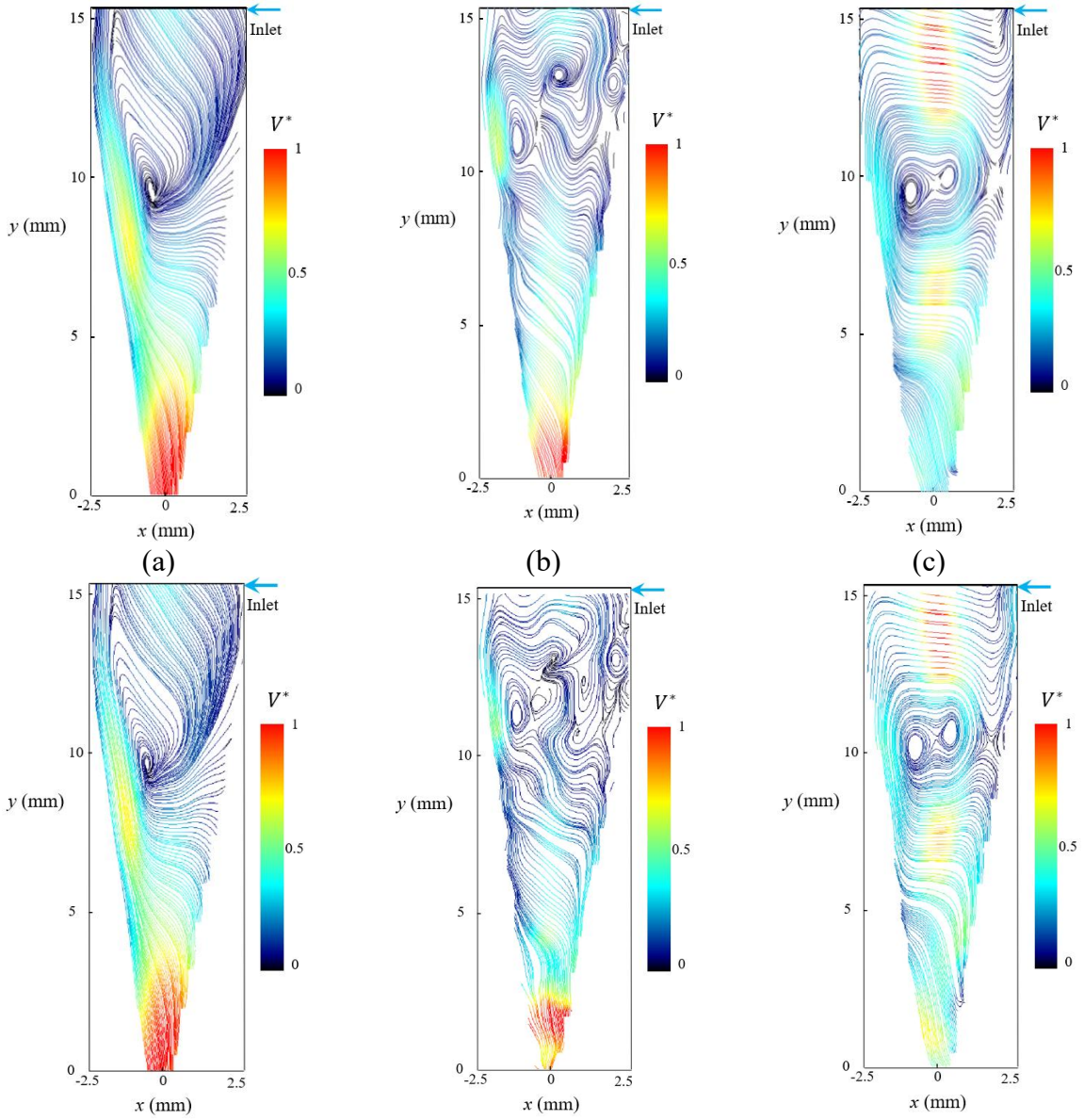

Figure 5-11 Streamlines and normalized velocity magnitude averaged on the midplane of the device for flow without CTCs in (a) $Re = 150$, (b) $Re = 300$, (c) $Re = 700$, and flow with CTCs in (d) $Re = 150$, (e) $Re = 300$, and (f) $Re = 700$.

To investigate the vertical motion of the flow which is essential in determination of the performance of the device, axial velocity, U_a is mapped onto the midplane of the micro-hydrocyclone as shown in Figure 5-12. This figure reveals both the upward and downward flow motion toward the outlets. This map also visualizes the location of the LZVV, where $U_a^* = 0$

highlighting the boundary between the upward and downward motion. Figure 5-12 shows the normalized axial velocity on the midplane of the device, U_a^* where $U_a^* = U_a/|U_{a,max}|$, for both the flow without CTCs Figure 5-12(a-c) and the flow with CTCs Figure 5-12(d-f).

For $Re = 150$ the LZVV region is clearly identifiable, outlined by a blacked dashed line as shown in Figure 5-12(a). Within this region a subtle upward flow motion is visible moving towards the vortex finder and the overflow. The maximum axial velocity magnitude can be located near the spigot (underflow outlet), indicating that the majority of the flow is draining from the underflow. Increasing the Reynolds number to $Re = 300$ into the unsteady regime, the LZVV is unsteady due to the unsteady nature of the velocity field. Consequently, the region appears broken into pieces as shown in Figure 5-12(b). Despite these fluctuations, the upward flow motion through the vortex finder persists. However, it may directly affect the separation performance of the device. At the higher Reynolds number of $Re = 700$ the axial velocity map shown in Figure 5-12(c) represents an elongated and expanded LZVV, indicating a noticeable change in the flow pattern. The upward flow motion towards the vortex finder is notably strong, suggesting that a significant portion of the flow is passing through the vortex finder. Such a motion increases the potential for high-performance separation.

Introducing the CTC clusters to the flow induces changes in the shape of the LZVV compared to the flow without CTCs. At a lower Reynolds number, $Re = 150$ it leads to a slight sharpening of the bottom tip of the region as shown in Figure 5-12(d). However, the amount of changes in this regime is negligible. For the unsteady regime at $Re = 300$, a noticeable change can be observed in the shape of the LZVV. As can be seen in Figure 5-12(e) a bridge is formed in between the two detected areas of the region. This change however, is expected to be mostly related to the unstable nature of the flow structure rather than the influence of the cell clusters. At the higher Reynolds

number of $Re = 700$, the LZVV becomes slightly narrower and extends slightly further along the axis as shown in Figure 5-12(e). Yet, representing the same characteristics which highlights a negligible influence of the CTCs on the LZVV.

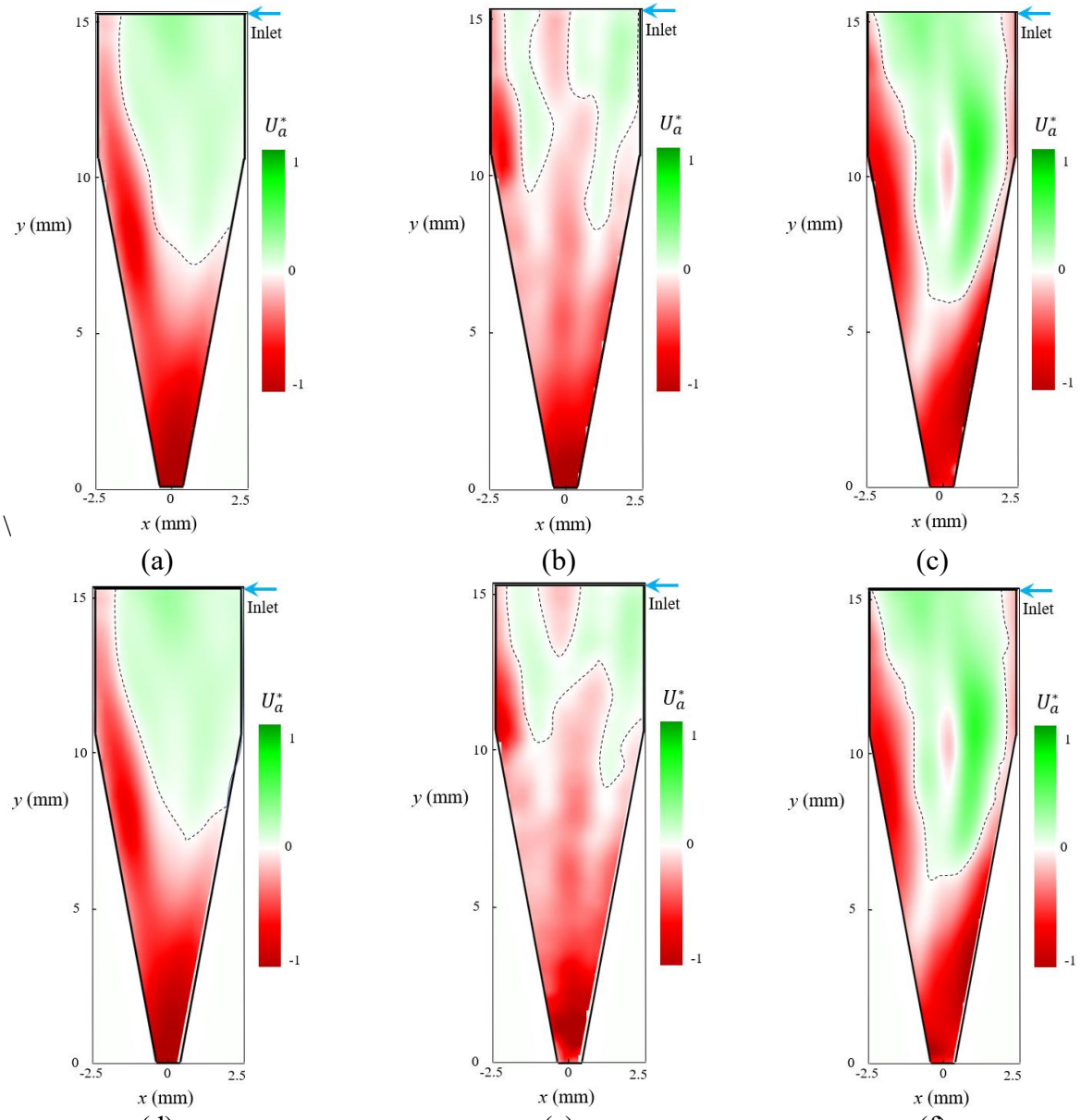

Figure 5-12 Axial velocity and LZVV on the midplane of the device for base flow in (a) $Re = 150$, (b) $Re = 300$, (c) $Re = 700$, and flow with CTCs in (d) $Re = 150$, (e) $Re = 300$, (f) $Re = 700$.

Figure 5-13 shows the changes in the LZVV characteristics across different Reynolds numbers and flow conditions (with and without CTC clusters) in a micro-hydrocyclone. This figure provides a visual comparison of the LZVV contours at representative Reynolds numbers. The results show that as the Reynolds number increases, the LZVV undergoes distinct regime transitions. In $Re = 150$, the LZVV is stable and compact, with minor differences between the flows with and without CTCs, indicating minimal influence of CTC clusters on the vortex structure for the laminar flow regime. As the Reynolds number reaches $Re = 300$, the LZVV width and length vary, particularly in the "flow with cell" case, indicating that the presence of CTCs intensifies flow instabilities as the flow transitions toward turbulence. It is worth noting that in micro-hydrocyclones, the statistically steady regime has been shown to occur for $Re > 400$ (Zhu *et al.* 2012). This is due to the complexity of the geometry of this system in which multiple length scales can be defined within quite a large range. Yet, it is common to define the Reynolds number based on the hydraulic diameter of the entrance channel [38]. The contours in Figure 5-13 for $Re = 300$ display more changes in the shape of LZVV in the flow with CTCs compared to the flow without CTCs. $Re = 700$, corresponding to fully statistically steady flow, the LZVV stabilizes again but becomes narrower and more elongated. Notably, for $Re = 700$, the LZVV with CTCs is slightly elevated compared to the flow without CTCs, indicating that the presence of cells continues to influence vortex positioning even for statistically steady conditions.

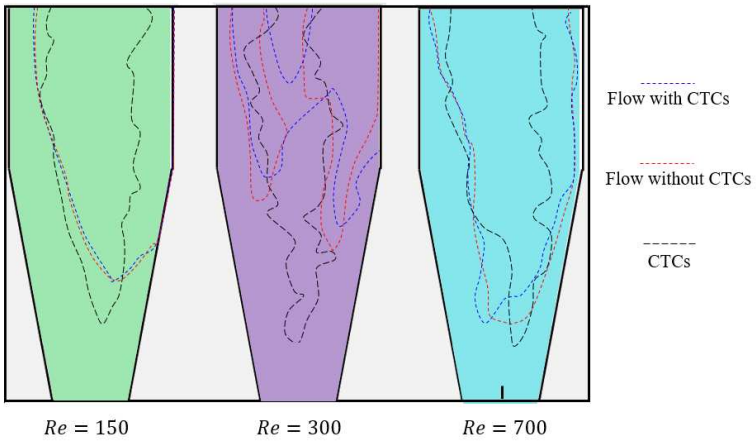

Figure 5-13 Comparison of the changes in the shape of LZVV for 3 different phases between flow without CTCs, flow with CTCs flow and CTCs on the midplane of a micro-hydrocyclone.

To investigate the unsteady flow at $Re = 300$, and also to have a deeper understanding of the flow structure and the influence of CTCs, a PDF of axial velocity is plotted in Figure 5-14 providing a statistical representation of the axial velocity on the midplane in the flow without CTCs and flow with CTCs cases for all conditions. For $Re = 150$ shown in Figure 5-14(a), the PDF of the flow without CTCs shows a sharp peak around $U_a/(U_a)_{max} = -0.2$, indicating that the majority of the fluid elements have similar velocities.

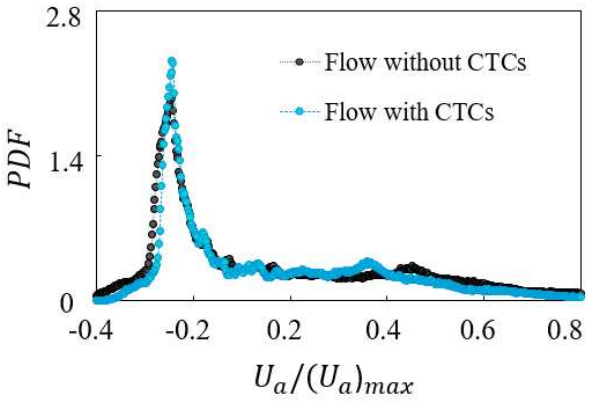

(a)

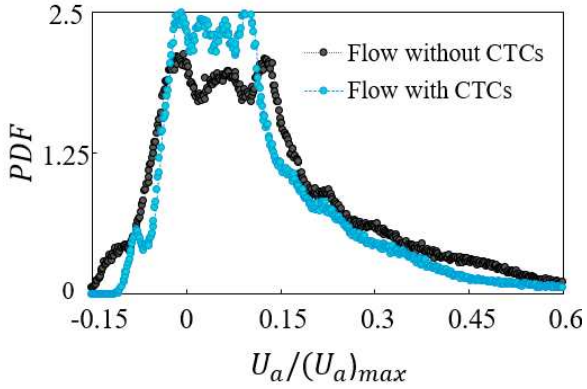

(b)

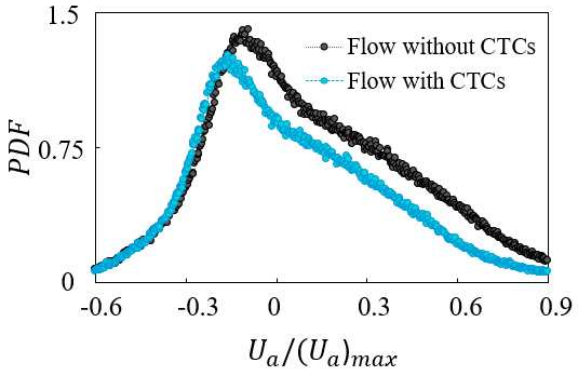

(c)

Figure 5-14 Probability density function of axial velocity for (a) $Re = 150$ (b) $Re = 300$ (c) $Re = 700$.

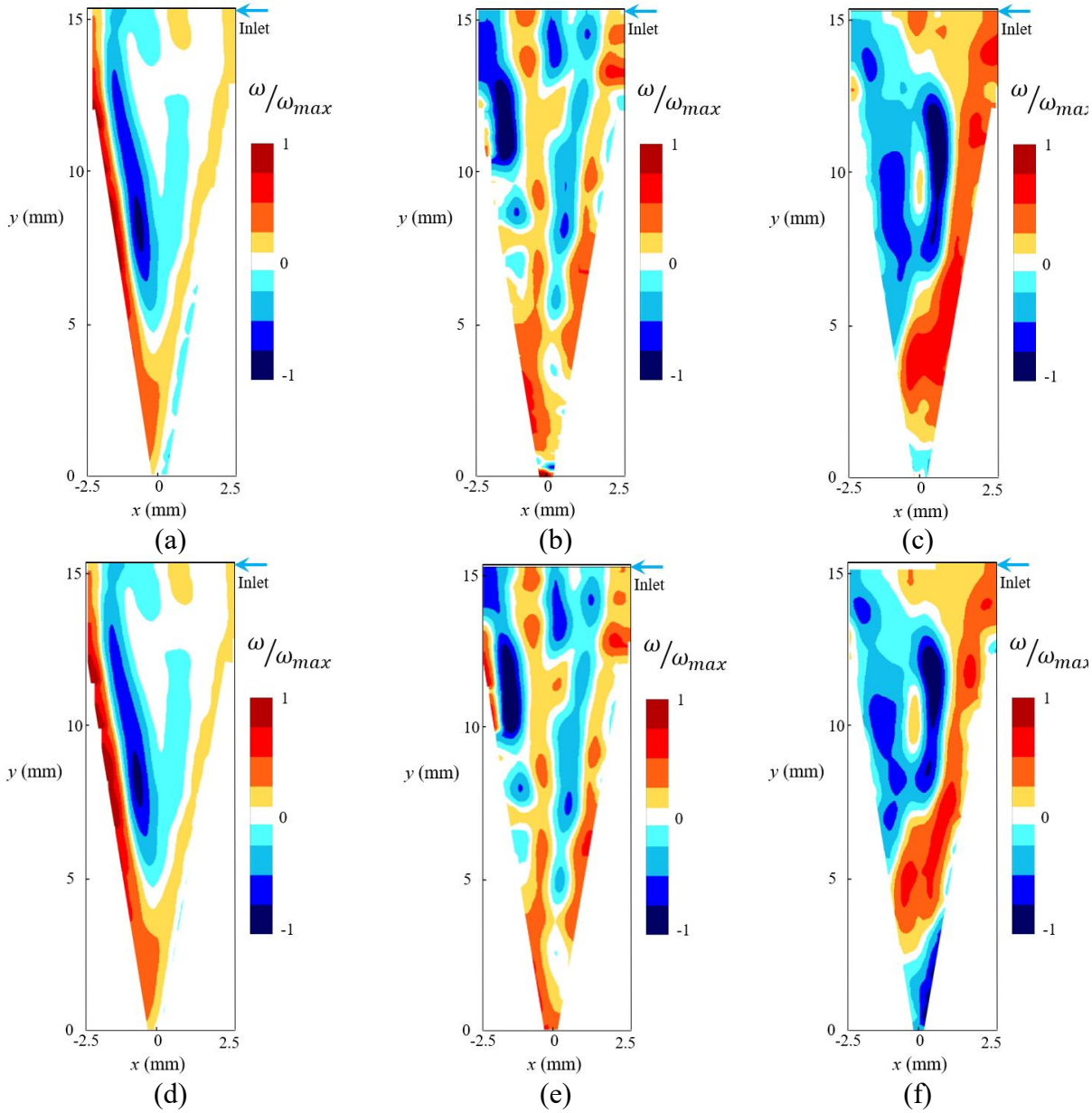

Figure 5-15 Normalized vorticity on the midplane of the device for flow without CTCs in (a) $Re = 150$ (b) $Re = 300$ (c) $Re = 700$and flow with CTCs in (d) $Re = 150$ (e) $Re = 300$ (f) $Re = 700$.

The flow with CTCs shows a slightly broader distribution, indicating that the presence of cells introduces minor deviations in axial velocity though the overall impact is negligible. For the unsteady regime at $Re = 300$ shown in Figure 5-14(b) the flow without CTCs PDF broadens. The majority of velocities are moved to $U_a/(U_a)_{max} = 0.15$ and there is a greater spread in the

distribution. The flow with CTCs shows a general increase in the velocity field. Figure 5-14(c) shows the PDF for $Re = 700$ where the softer peak reflects the highly variable nature of the flow. The majority of the velocities are centered around $U_a/(U_a)_{max} = -0.2$. The flow with CTCs shows a reduction in the number of velocity vectors with positive value. However, the overall layout is still similar to the flow without CTCs.

An ensemble average normalized vorticity field, ω/ω_{max} for the three Reynolds numbers cases for both the flow without CTCs and flow with CTCs is shown in Figure 5-15. As can be observed from Figure 5-15(a), although the vorticity field near the LZVV region indicates a circulating flow in this region, it does not effectively highlight or distinguish areas with upward and downward flow. This is important in unsteady conditions such as for $Re = 300$, indicated in Figure 5-15(b) and (e). Regarding the comparison between the flow without CTCs condition, Figure 5-15 (a)-(c) with the flow with CTCs, it can be seen that except for the unsteady cases shown in Figure 5-15(b) and (e) the other two cases appear rather similar for both tracer particles and flow with CTCs. The difference in the unsteady cases can be attributed to the flow regime instead of the influence of the CTCs on the flow field. Based on the results represented for the variation of the velocity field and the characteristics of the LZVV for the three investigated Reynolds numbers, it can be concluded that for this specific concentration of the CTCs i.e. $\xi = 10^2$ cell/ml, influence of the CTCs on the physics of the flow is negligible.

5.9.2. The motion of the CTCs

Although the influence of the CTCs on the flow dynamics is negligible, it is important to investigate the motion of the CTCs in the flow field and compare it with the flow motion itself. It is worth noting that the density of the cells is almost the same as that of the working fluid i.e.

water, yet the size of the clusters can be as large as 400 μm or ~10% of the micro-hydrocyclone diameter which can influence the motion of the CTCs. Hence, using PTV, the cells are tracked and the motion has been investigated and compared with the flow without CTCs field.

The velocity of the tracked cell clusters within the micro-hydrocyclone is depicted in Figure 5-16 (a) to (c). The velocity vectors shown here are the accumulated velocity of the CTCs captured from 500 frames. The dispersed accumulated velocity vectors are interpolated onto a structured grid with the size of 16×16 pixels and the results are shown in Figure 5-16. In this figure, the highlighted pink regions depict the detected LZVV based on the vertical motion of the CTCs. For $Re = 150$, the upward and downward motion of the cell clusters can be observed. Comparing the results of the velocity vectors of the CTCs with the continuous phase velocity field, it can be seen that the upward motion is within the vortex area. For the two other Reynolds numbers, the downward motion of the CTCs can be clearly observed. However, the upward motion of the CTCs is influenced by a significant motion of them in the x-direction which is due to the increase in the inlet velocity leading to an increase in radial momentum. However, for $Re = 700$, it can be seen that the upward motion of clusters is within the LZVV. For $Re = 300$, however, the upward motion of the CTCs is dominated in a larger region in comparison with the detected LZVV from the flow field of both flow without CTCs and flow with CTCs. This is probably due to the unsteady behavior of the flow field and the different representation of the results since the CTCs velocity field represents the accumulated velocity rather than the ensemble average velocity field.

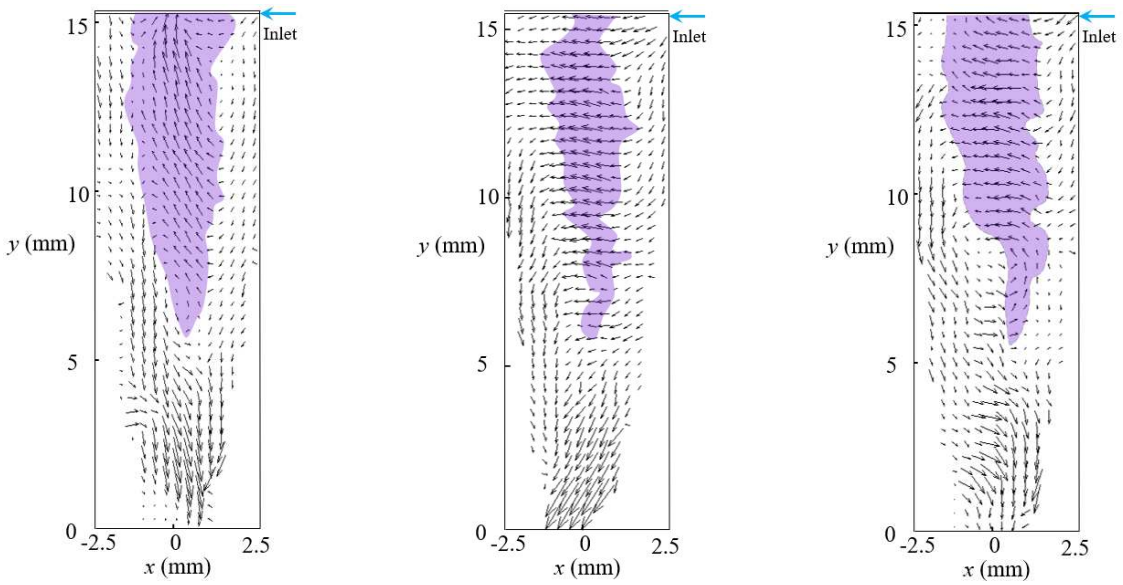

Figure 5-16 Velocity vectors of the cell clusters on the midplane of the device in (a)$Re = 150$ (b) $Re = 300$ (c) $Re = 700$. Pink areas highlight the LZVV detected based on the vertical motion of the CTCs.

Figure 5-17 shows the normalized axial velocity profiles, $U_a/(U_a)_{max}$ along the vertical axis (centerline) of the micro-hydrocyclone for the three Reynolds numbers. Here, the axial velocity, U_a is normalized by the maximum axial velocity on the midplane, $(U_a)_{max}$. Given the orientation of the coordinate system of measurement shown in Figure 5-17(a), a positive axial velocity indicates an upward flow to the outlet. This figure compares three cases: the flow without CTCs, flow with CTCs and the motion of the CTCs. Figure 5-17(b) shows the axial velocity profile along the centerline for $Re = 150$. The profile indicates a similar trend for both flow without CTCs and flow with CTCs. The maximum magnitude of the axial velocity occurs as the flow enters the spigot into the underflow. Additionally, it is evident that the axial velocity sharply increases after reversing direction at $y/L = 0.43$. However, for CTCs the change in the direction occurs near $y/L = 0.6$. The steep change in the axial velocity near the center may indicate that the CTCs are being drawn down rapidly toward the underflow. Despite the flow field, the velocity of the CTCs reduces near $y/L = 0.85$, which is close to the spigot in the underflow. This sudden drop in the

velocity near the outlet indicates accumulation of the CTCs near the outlet since the length scale of the CTCs, up to 0.4 mm is comparable with the outlet of the underflow, 1 mm.

Figure 5-17(c) shows the velocity profiles for $Re = 300$. For the flow without CTCs case, the axial velocity shows a downward flow motion along the axis. However, with the introduction of cells it can be seen that a small portion of the profile has shifted to the negative range indicating that the LZVV has intersected with the axis. The velocity magnitude of the flow starts to increase significantly after the $y/L = 0.2$ and increases further to a higher rate closer to the spigot. The velocity profile for the CTCs cases however shows a weak downward flow motion along the axis indicating that all the clusters are draining from the underflow with a slower rate since the axial velocity is negative, yet close to zero. This suggests that in this unsteady regime, $Re = 300$, the device cannot be functional i.e. separating cells based on their size, although the axial flow profile appears to have characteristics similar as a functional regime, e.g. $Re = 150$.

Figure 5-17(d) shows the profile for $Re = 700$. For both flow without CTCs and flow with CTCs the direction of the flow changes at $y/L = 0.6$. The axial velocity profile has the same trend as the two other Reynolds numbers. The CTCs axial velocity shows a subtle deviation from the flow similar to what occurs for the two other Reynolds numbers. As can be observed, the CTCs axial velocity magnitude decreases after $y/L = 0.85$ similar to $Re = 150$. Hence it can be inferred that the reduction in the velocity of the CTCs occurs for all three regimes near the spigot where the outlet diameter is comparable in size to the outlet diameter. Interestingly, the change in the axial velocity near the overflow outlet for CTCs is only evident for the first Reynolds number, $Re = 150$. One reason that may explain this is the difference in the geometry of the outlet of the overflow in comparison with the underflow. In the underflow, the geometry converges to a final diameter of 1 mm. However, the change in the geometry occurs suddenly for the overflow.

From the axial velocity profile for the three different Reynolds numbers, it can be seen that the overall CTCs axial velocity is lower than the axial velocity of the flow field. It can also be concluded that while the flow field axial velocity increased by moving through the converging geometry to the spigot, the axial velocity of the CTCs increases up to $y/L = 0.85$, then decreases significantly. Both of these two phenomena could be attributed to the influence of the size of the CTC clusters since their density is close to that of the working fluid, i.e. CTCs are neutrally buoyant.

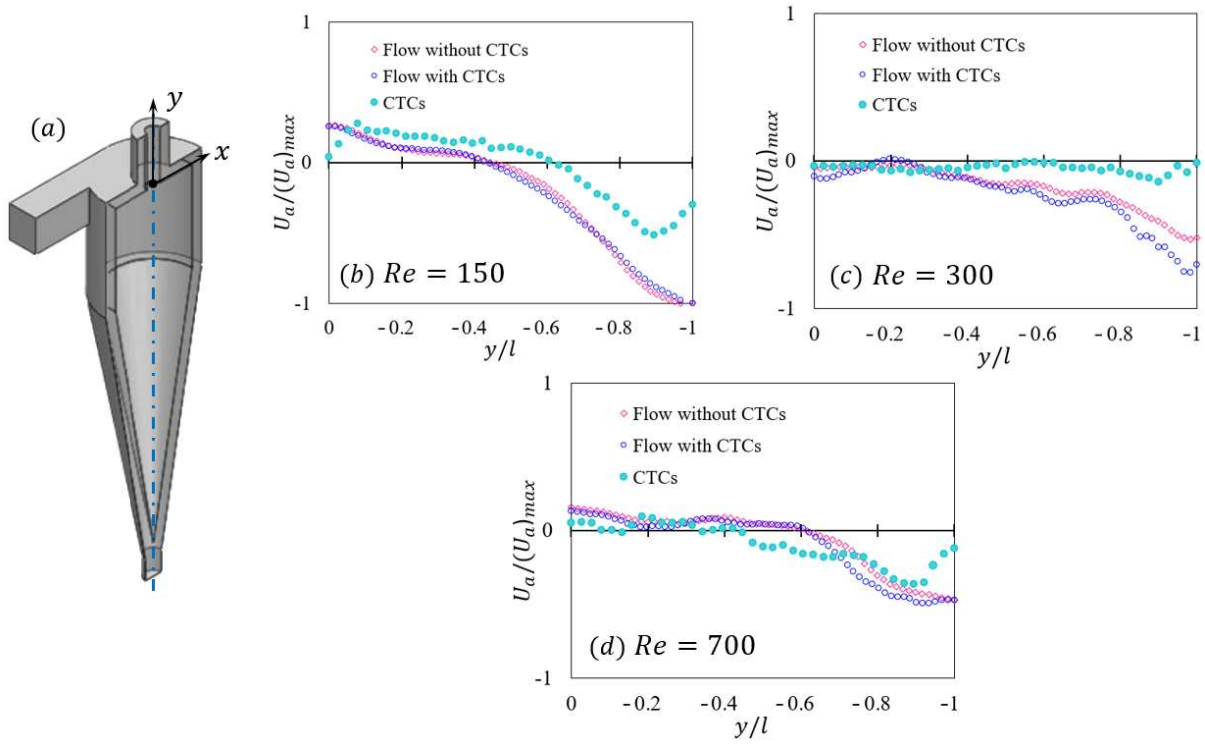

Figure 5-17 axial velocity on the center vs flow rate for flow without CTCs, flow with CTCs and flow with cell clusters.

Figure 5-18 presents the axial velocity profile for the three *Re* cases across three horizontal lines (HL1, HL2, HL3) within the micro-hydrocyclone. At HL1, located in the cylindrical section of the device, a combination of upward and downward flow motion is evident. For $Re = 150$, a non-symmetrical velocity profile is observed, displaying slight variations across the flow cases.

Interestingly, while each flow case exhibits some degree of asymmetry, the profile of the CTCs shows a more symmetrical axial velocity profile compared to the flow without CTCs and flow with CTCs. This tendency toward symmetry in the cell clusters suggests that the clusters contribute to a more even distribution of upward and downward flow motion. For $Re = 300$, however, it can be seen that the axial velocity of the CTCs are close to zero at the center, $x = 0$, and positive at the left and right locations, $x \to D/2$ and $x \to -D/2$. While this behavior is in contrast to a functioning micro-hydrocyclone, similar to the results in Figure 5-18, it suggests that the device is functioning at this regime, $Re = 300$.

At HL2, positioned at the mid-height of the micro-hydrocyclone and for $Re = 150$ both the flow without CTCs and cell induces cases follow a similar profile, with axial velocity values oscillating symmetrically around zero, near the center of the geometry. For the motion of the cell clusters, while following the same general trend, the axial velocity is slightly reduced, particularly near the centerline of the hydrocyclone. This reduction is probably due to the additional drag introduced by the cell clusters. At $Re = 300$, the profiles for both the flow without CTCs and flow with CTCs show more variability across the diameter, with notable fluctuations near the centerline. The CTCs profile follows a similar pattern but exhibit lower velocity values. For the fully statistically steady case at $Re = 700$ the flow without CTCs and flow with CTCs exhibit significant fluctuations, with sharp peaks near the outer edges and noticeable dips toward the centerline. The CTCs profile shows a similar pattern with a less pronounced peak.

At HL3, located closer to the underflow outlet of the micro-hydrocyclone, a general downward flow motion is observed across all three cases. For $Re = 150$ both the flow without CTCs and flow with CTCs cases display a similar trend in axial velocity, maintaining a consistent downward motion across the profile. However, the cell clusters show the same downward trend but with a

slightly reduced axial velocity. For $Re = 300$, a similar pattern was observed, however, the overall axial velocity was lower than what was observed for the $Re = 150$ case. This suggests increased flow resistance as the system transitions toward turbulence. The flow symmetry remains generally intact, but CTCs exhibit slightly reduced velocities again. For the fully statistically steady regime at $Re = 700$, HL3 intersects the tip of the LZVV, capturing a marked decrease in axial velocity at the center, where it approaches zero.

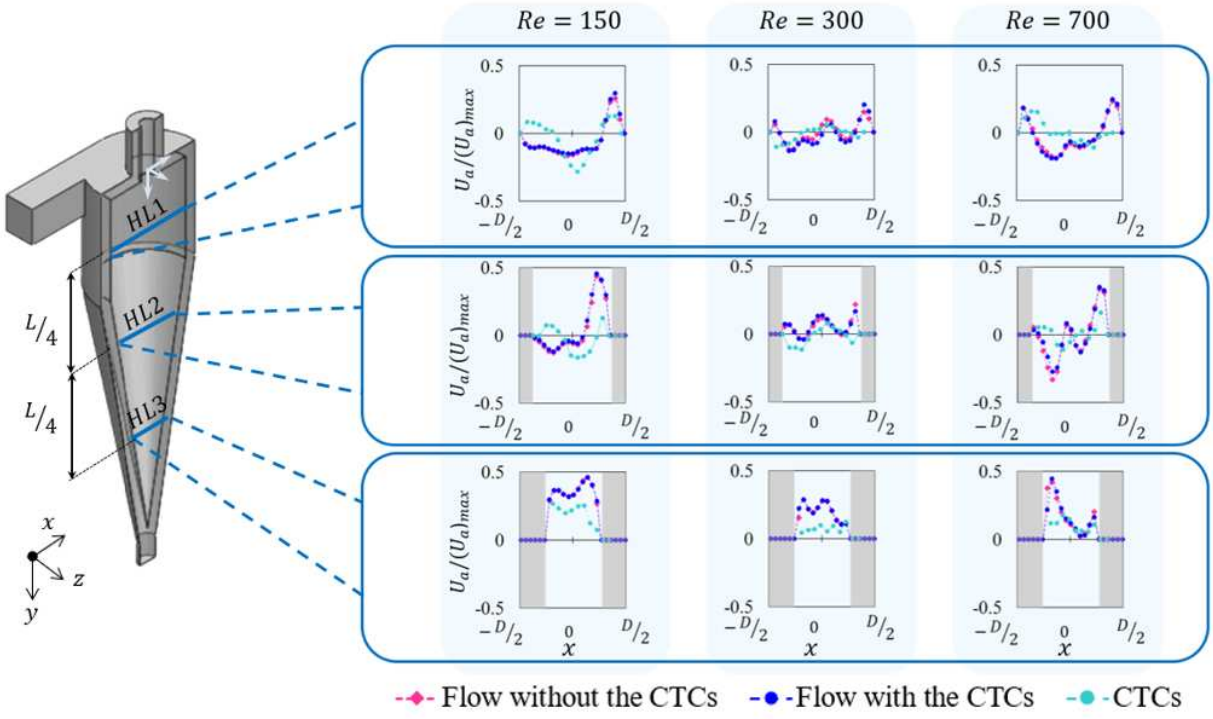

Figure 5-18 Axial velocity at the selected sections across the x-axis for flow without CTCs, flow with CTCs and the CTCs for three flow rates with $Re = 150$, 300, and 700.

To visually demonstrate the separation behavior of circulating tumor cell (CTC) clusters within the micro-hydrocyclone, Figure 5-19 presents microscopic images of samples collected from the mixed inlet, overflow, and underflow outlets. As seen in the inlet sample, a heterogeneous distribution of CTC clusters is introduced into the device. The overflow image, in contrast, reveals mostly small individual cells or cell debris, indicating successful exclusion of larger clusters from

this outlet. The underflow sample distinctly contains larger and more numerous clusters, confirming that the device effectively directs bulkier CTC aggregates toward the underflow path. These visual results qualitatively validate the size-based separation capability of the device and provide insight into its practical application for isolating CTC clusters from a mixed suspension. A detailed quantitative analysis of the device's separation efficiency across various flow conditions and particle types is being prepared for a separate publication.

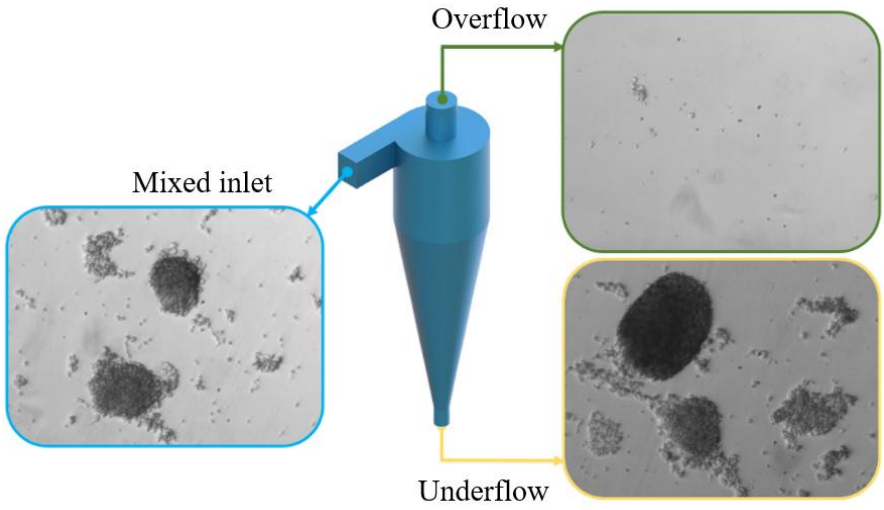

Figure 5-19 Microscopic images of samples taken from the mixed inlet, overflow, and underflow outlets of the micro-hydrocyclone. The inlet shows a mixture of individual cells and cell clusters. The overflow primarily contains small cells or cell fragments, while the underflow is enriched with larger CTC clusters, demonstrating the device's ability to perform size-based separation.

5.10 Conclusion

The separation of CTCs was experimentally investigated in a high throughput microfluidic device i.e. a micro-hydrocyclone. An image processing scheme was developed to image the seeding particles and CTCs. Using this scheme, and using a single camera, PIV was applied to the flow of the micro-hydrocyclone with seeding particles. A PTV scheme was also developed to trace the CTCs and calculate their velocity. The velocity field of the micro-hydrocyclone was

investigated for two cases, first flow without CTCs, and second, the flow with the CTCs. The developed scheme was crucial since it allowed investigation of the influence of the CTCs on the flow field of the micro-hydrocyclone and the velocity of the CTCs as well.

The findings of this study reveal that while the presence of CTCs within the micro-hydrocyclone does induce changes in the flow field, these effects are typically negligible across most operational conditions. This result is important since it shows that within the range of Reynolds numbers studied, single phase experiments and numerical simulations could be conducted to study further the physics of the flow within micro-hydrocyclones which allows optimizing the performance of this system. In the stable laminar regime at low Reynolds numbers the flow organization remains largely unaffected by cell clusters, with only minor alterations observed near the LZVV. As the flow transitions to higher Reynolds numbers, unsteady minor irregularities and flow instabilities become more apparent. However, these disturbances appear to be dominated by the flow perturbations rather than a noticeable influence from the cell clusters.

At higher Reynolds numbers, within the fully statistically steady regime, the presence of CTCs similarly has minimal impact on the overall flow organization. The flow patterns and separation characteristics remain consistent with flow without CTCs single-phase flow, suggesting that the influence of the CTCs in this regime is dominated by the stability of the statistically steady structures. These observations underscore that, while cell clusters introduce some variability in the flow behavior, the primary contributors to flow instabilities, particularly in the unsteady phase, are intrinsic flow dynamics rather than the physical presence of cells. This detailed understanding of CTCs influence on the flow, supports refining separation performance in bio-applications and in general.

It is important to note that the CTCs used in this study had a size on the order of one-fifth of the device inlet diameter, raising initial concerns about their potential to disrupt flow organization within the micro-hydrocyclone. Despite this, the results indicate that the impact of cell clusters on the flow structure is minimal across the tested Reynolds numbers. This finding suggests that single-phase velocity measurements can still provide valid and valuable insights into the flow dynamics within the device, even when CTCs are present. Such single-phase studies can be useful in understanding the flow without CTCs behavior, optimizing device performance, and modifying micro-hydrocyclone designs for various applications, including those in biomedical and environmental fields. By confirming the stability of single-phase investigations, this study supports the broader applicability of micro-hydrocyclones in scenarios where particle influenced flows must be accurately characterized without significant interference from dispersed phases. A concentration of $\xi = 10^2$ cells/mL was selected as it reflects values commonly encountered in practical applications, particularly in clinical and microfluidic studies involving rare cell detection. While the present study focused on a fixed concentration of CTCs which allowed for a clear assessment of individual cell-flow interactions, future work could explore higher concentrations. This would help identify thresholds at which cell-cell interactions or collective effects begin to influence the flow field, providing further insight into behavior under more dense conditions.

References

[1] A. Dalili, E. Samiei, M. Hoorfar, A review of sorting, separation and isolation of cells and microbeads for biomedical applications: microfluidic approaches, Analyst 144 (2019) 87–113. https://doi.org/10.1039/c8an01061g.

[2] I. Maguire, R. O'Kennedy, J. Ducrée, F. Regan, A review of centrifugal microfluidics in environmental monitoring, Anal. Methods 10 (2018) 1497–1515. https://doi.org/10.1039/c8ay00361k.

[3] R. Pol, F. Céspedes, D. Gabriel, M. Baeza, Microfluidic lab-on-a-chip platforms for environmental monitoring, TrAC - Trends Anal. Chem. 95 (2017) 62–68. https://doi.org/10.1016/j.trac.2017.08.001.

[4] R. Nasiri, A. Shamloo, S. Ahadian, L. Amirifar, J. Akbari, M.J. Goudie, K.J. Lee, N. Ashammakhi, M.R. Dokmeci, D. Di Carlo, A. Khademhosseini, Microfluidic-Based Approaches in Targeted Cell/Particle Separation Based on Physical Properties: Fundamentals and Applications, Small 16 (2020). https://doi.org/10.1002/smll.202000171.

[5] P. Sajeesh, A.K. Sen, Particle separation and sorting in microfluidic devices: A review, Microfluid. Nanofluidics 17 (2014) 1–52. https://doi.org/10.1007/s10404-013-1291-9.

[6] Y. Saffar, D.S. Nobes, R. Sabbagh, Integrated Single Camera μPTV And Florescence Imaging For Cell Tracking And Flow Investigation In Centrifugal Microfluidic Devices, Proc. Int. Symp. Appl. Laser Imaging Tech. to Fluid Mech. 21 (2024) 1–10. https://doi.org/10.55037/lxlaser.21st.49.

[7] M.S. Syed, F. Mirakhorli, C. Marquis, R.A. Taylor, M.E. Warkiani, Particle movement and fluid behavior visualization using an optically transparent 3D-printed micro-hydrocyclone, Biomicrofluidics 14 (2020). https://doi.org/10.1063/5.0025391.

[8] M.S. Syed, C. Marquis, R. Taylor, M.E. Warkiani, A two-step microengineered system for high-density cell retention from bioreactors, Sep. Purif. Technol. 254 (2021) 117610. https://doi.org/10.1016/j.seppur.2020.117610.

[9] R. Sabbagh, M.G. Lipsett, C.R. Koch, D.S. Nobes, Hydrocyclone Performance and Energy Consumption Prediction: A Comparison with Other Centrifugal Separators, Sep. Sci. Technol. 50 (2015) 788–801. https://doi.org/10.1080/01496395.2014.978463.

[10] A.F. Concha, A.J.L. Bouso, Fluid Mechanics and Its Applications Fluid Mechanics Fundamentals of Hydrocyclones and Its Applications in the Mining Industry, 2021. http://www.springer.com/series/5980.

[11] R. Sabbagh, D.S. Nobes, Centrifugal separation, Kirk-Othmer Encyclopedia of Chemical Technology, 2018. https://doi.org/10.1201/9780203752494-9.

[12] R. Sabbagh, M.G. Lipsett, C.R. Koch, D.S. Nobes, An experimental investigation on hydrocyclone underflow pumping, Powder Technol. 305 (2017) 99–108. https://doi.org/10.1016/j.powtec.2016.09.045.

[13] Z. Zhao, H. Wang, C. Xie, Y. Wei, J. Xue, X. Xiao, B. Liu, Hydrocyclone separation performance influenced by feeding solid concentration and correcting separation size, (n.d.). https://doi.org/10.1007/s00231-020-02940-8/Published.

[14] L.M. Tavares, L.L.G. Souza, J.R.B. Lima, M. V. Possa, Modeling classification in small-diameter hydrocyclones under variable rheological conditions, Miner. Eng. 15 (2002) 613–622. https://doi.org/10.1016/S0892-6875(02)00085-7.

[15] I.C. Bicalho, J.L. Mognon, J. Shimoyama, C.H. Ataíde, C.R. Duarte, Separation of yeast from alcoholic fermentation in small hydrocyclones, Sep. Purif. Technol. 87 (2012) 62–70. https://doi.org/10.1016/j.seppur.2011.11.023.

[16] T. Zhang, J. Li, A. Wei, J. Huang, S. Li, J. Huan, F. Wang, H. Wang, Ultra-clean separation of micro-particles in lubricant oil based on short-flow control of mini-hydrocyclone, Sep. Purif. Technol. 304 (2023) 122370. https://doi.org/10.1016/j.seppur.2022.122370.

[17] L. Liu, Y. Sun, Z. Kleinmeyer, G. Habil, Q. Yang, L. Zhao, D. Rosso, Microplastics separation using stainless steel mini-hydrocyclones fabricated with additive manufacturing, Sci. Total Environ. 840 (2022) 156697. https://doi.org/10.1016/j.scitotenv.2022.156697.

[18] L. He, L. Ji, Y. He, Y. Liu, S. Chen, K. Chu, S. Kuang, Experimental and numerical analysis of Chinese hamster ovary cell viability loss in mini-hydrocyclones, Sep. Purif. Technol. 295 (2022). https://doi.org/10.1016/j.seppur.2022.121203.

[19] Y. Fan, J. Li, Q. Wei, Z. Xiong, Y. Ji, H. Ma, B. Liu, Y. Huang, W. Lv, H. Wang, Study on the law of turbulent flow and self-rotation and revolution of particles in micro-hydrocyclone, Powder Technol. 415 (2023) 118200. https://doi.org/10.1016/j.powtec.2022.118200.

[20] P. Bhardwaj, P. Bagdi, A.K. Sen, Microfluidic device based on a micro-hydrocyclone for particle-liquid separation, Lab Chip 11 (2011) 4012–4021. https://doi.org/10.1039/c1lc20606k.

[21] Z. Liu, Z. Lu, C. Zhang, H. Lang, X. Zhai, Zhongmin Liu, * Zezhao Lu, Chengwei Zhang, Heng Lang, and Xin Zhai, (2023). https://doi.org/10.1021/acs.langmuir.2c03448.

[22] L. He, L. Ji, X. Sun, S. Chen, S. Kuang, Investigation of mini-hydrocyclone performance in removing small-size microplastics, Particuology 71 (2022) 1–10. https://doi.org/10.1016/j.partic.2022.01.011.

[23] S.H. Au, J. Edd, A.E. Stoddard, K.H.K. Wong, F. Fachin, S. Maheswaran, D.A. Haber, S.L. Stott, R. Kapur, M. Toner, Microfluidic isolation of circulating tumor cell clusters by size and asymmetry, Sci. Rep. 7 (2017). https://doi.org/10.1038/s41598-017-01150-3.

[24] Z.S. Sayed, M.G. Khattap, M.A. Madkour, N.S. Yasen, H.A. Elbary, R.A. Elsayed, D.A. Abdelkawy, A.H.S. Wadan, I. Omar, M.H. Nafady, Circulating tumor cells clusters and their role in Breast cancer metastasis; a review of literature, Discov. Oncol. 15 (2024). https://doi.org/10.1007/s12672-024-00949-7.

[25] I. Krol, F. Castro-Giner, M. Maurer, S. Gkountela, B.M. Szczerba, R. Scherrer, N. Coleman, S. Carreira, F. Bachmann, S. Anderson, M. Engelhardt, H. Lane, T.R. Jeffry Evans, R.

Plummer, R. Kristeleit, J. Lopez, N. Aceto, Detection of circulating tumour cell clusters in human glioblastoma, Br. J. Cancer 119 (2018) 487–491. https://doi.org/10.1038/s41416-018-0186-7.

[26] A.A. Mouza, C.M. Patsa, F. Schönfeld, Mixing performance of a chaotic micro-mixer, Chem. Eng. Res. Des. 86 (2008) 1128–1134. https://doi.org/10.1016/j.cherd.2008.04.009.

[27] F.G. Ergin, B.B. Watz, N.F. Gade-Nielsen, A review of planar PIV systems and image processing tools for lab-on-chip microfluidics, Sensors (Switzerland) 18 (2018) 1–23. https://doi.org/10.3390/s18093090.

[28] N. Nivedita, P. Ligrani, I. Papautsky, Dean flow dynamics in low-aspect ratio spiral microchannels, Sci. Rep. 7 (2017) 1–10. https://doi.org/10.1038/srep44072.

[29] M. Nimafar, V. Viktorov, M. Martinelli, Experimental Investigation of Split and Recombination Micromixer in Confront with Basic T- and O- type Micromixers, Int. J. Mech. Appl. 2 (2012) 61–69. https://doi.org/10.5923/j.mechanics.20120205.02.

[30] K.I. Belousov, N.A. Filatov, I. V. Kukhtevich, V. Kantsler, A.A. Evstrapov, A.S. Bukatin, An asymmetric flow-focusing droplet generator promotes rapid mixing of reagents, Sci. Rep. 11 (2021). https://doi.org/10.1038/s41598-021-88174-y.

[31] Y. Saffar, S. Kashanj, D.S. Nobes, R. Sabbagh, The Physics and Manipulation of Dean Vortices in Single- and Two-Phase Flow in Curved Microchannels : A Review, Micromachines 14 (2023) 2202.

[32] K.T. Kiger, C. Pan, PIV Technique for the Simultaneous Measurement of Dilute Two-Phase Flows, J. Fluids Eng. (2000) 811–818. http://asmedigitalcollection.asme.org/fluidsengineering/article-pdf/122/4/811/5615298/811_1.pdf.

[33] F.G. Ergin, B.B. Watz, N.F. Gade-Nielsen, A review of planar PIV systems and image processing tools for lab-on-chip microfluidics, Sensors (Switzerland) 18 (2018). https://doi.org/10.3390/s18093090.

[34] F. He, H. Wang, J. Wang, S. Li, Y. Fan, X. Xu, Experimental study of mini-hydrocyclones with different vortex finder depths using Particle Imaging Velocimetry, Sep. Purif. Technol. 236 (2020) 116296. https://doi.org/10.1016/j.seppur.2019.116296.

[35] Y. Fan, J. Wang, Z. Bai, J. Wang, H. Wang, Experimental investigation of various inlet section angles in mini-hydrocyclones using particle imaging velocimetry, Sep. Purif. Technol. 149 (2015) 156–164. https://doi.org/10.1016/j.seppur.2015.04.047.

[36] S.T.L. Harrison5, J.J. Cillierst, THE USE OF MINI-HYDROCYCLONES FOR DIFFERENTIAL SEPARATIONS WITHIN MINERAL SLURRJES SUBJECTED TO BIOLEACHING, Mitwrrrls Eng. IO (1997) 529–535.

[37] R.A. Medronho, J. Schuetze, W.D. Deckwer, Numerical simulation of hydrocyclones for cell separation, Lat. Am. Appl. Res. 35 (2005) 1–8.

[38] G. Zhu, J.L. Liow, A. Neely, Computational study of the flow characteristics and separation efficiency in a mini-hydrocyclone, Chem. Eng. Res. Des. 90 (2012) 2135–2147. https://doi.org/10.1016/j.cherd.2012.05.020.

[39] J.Y. Han, B. Krasniqi, J. Kim, M. Keckley, D.L. DeVoe, Miniaturization of Hydrocyclones by High-Resolution 3D Printing for Rapid Microparticle Separation, Adv. Mater. Technol. 5 (2020) 1–11. https://doi.org/10.1002/admt.201901105.

[40] C.A. Petty, S.M. Parks, Flow structures within miniature hydrocyclones, Miner. Eng. 17 (2004) 615–624. https://doi.org/10.1016/j.mineng.2004.01.020.

[41] R. Sabbagh, S. Ansari, D.S. Nobes, An imaging approach for in-situ measurement of refractive index of a porous medium, Opt. Lasers Eng. 134 (2020). https://doi.org/10.1016/j.optlaseng.2020.106175.

[42] Y.K. Agrawal, R. Sabbagh, S. Sanders, D.S. Nobes, Measuring the refractive index, density, viscosity, pH, and surface tension of potassium thiocyanate (KSCN) solutions for refractive index matching in flow experiments, J. Chem. Eng. Data 63 (2018) 1275–1285.

[43] P. Greenspan, E.P. Mayer, S.D. Fowler, Nile Red" A Selective Fluorescent Stain for Intracellular Lipid Droplets, 1985. http://rupress.org/jcb/article-pdf/100/3/965/1457917/965.pdf.

[44] G.S. Alemán-Nava, S.P. Cuellar-Bermudez, M. Cuaresma, R. Bosma, K. Muylaert, B.E. Ritmann, R. Parra, How to us Nile Red, a selective fluorescent stain for microalgal neutral lipids, J. Microbiol. Methods 128 (2016) 74–79. https://doi.org/10.1016/j.mimet.2016.07.011.

[45] P.K. Horan, M.J. Melnicoff, B.D. Jensen, S.E. Slezak, Chapter 42 Fluorescent Cell Labeling for in Vivo and in Vitro Cell Tracking, Methods Cell Biol. 33 (1990) 469–490. https://doi.org/10.1016/S0091-679X(08)60547-6.

[46] Y. Guo, L. Su, J. Wu, D. Zhang, X. Zhang, G. Zhang, T. Li, J. Wang, C. Liu, Assessment of the green florescence protein labeling method for tracking implanted mesenchymal stem cells, Cytotechnology 64 (2012) 391–401. https://doi.org/10.1007/s10616-011-9417-y.

[47] M. Raffel, C.E. Willert, F. Scarano, C.J. Kähler, S.T. Wereley, J. Kompenhans, Particle Image Velocimetry: A Practical Guide, Part. Image Velocim. A Pract. Guid. (2018) 1–32. https://doi.org/10.1007/978-3-319-68852-7_1.

Chapter 6: Flow Organization and Measurement within the Micro-hydrocyclone

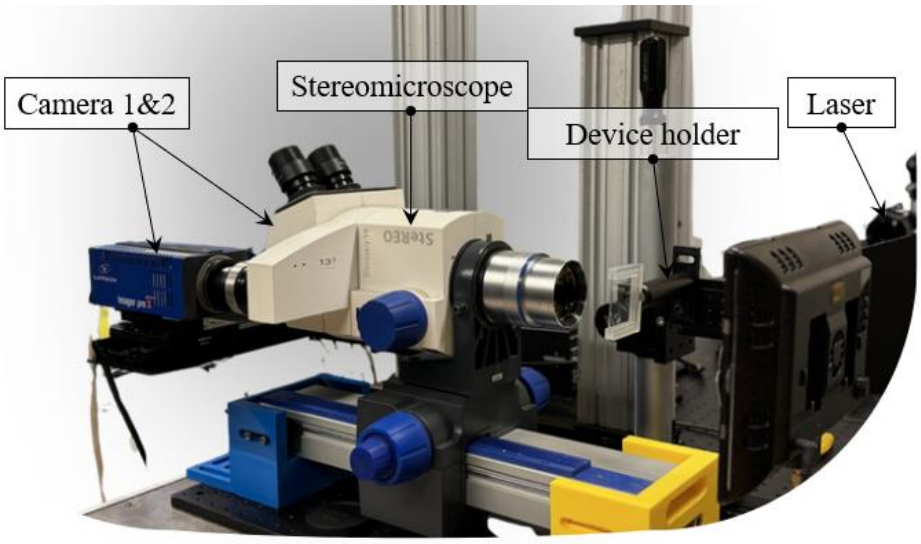

Graphical Abstract: Stereo microscopy setup used for the 2D3C experiment

This study presents the first implementation of stereoscopic micro-particle image velocimetry (Stereo μPIV) in a micro-hydrocyclone to resolve all three velocity components on the midplane. Two inlet geometries straight and spiral were investigated across Reynolds numbers from 100 to 600. The Locus of Zero Vertical Velocity (LZVV) was used to identify the axial transition between downward and upward flow, with the spiral inlet showing larger and more elevated recirculation zones.

6.1 Introduction

Microfluidic devices have become essential in various fields, including biological and biomedical diagnostics, chemical analysis, and environmental monitoring. These devices enable precise control over small volumes of fluids, allowing for high-throughput screening, chemical reactions, and particle manipulation [1]. The need to understand and control flow behavior in these systems is critical, especially for applications such as particle separation, DNA analysis, and drug delivery.

Passive separation devices in microfluidics exploit channel geometry, flow characteristics, or intrinsic fluid properties to achieve separation without external energy input. These devices include geometry-based splitters (T-junction splitters, Y-junction channels, H-shaped diffusion channels) [1], inertial microfluidic structures (spiral microchannels, curved or serpentine channels, expansion–contraction arrays) [2], and deterministic lateral displacement (DLD) devices (micropillar arrays) [3]. These systems provide robust and continuous separation, making them highly suitable for biological, chemical, and environmental applications.

Inertial Microfluidics devices including Dean flow-based inertial microfluidic systems represent an important class of passive separation devices. By introducing curvature into microchannel geometries, Dean vortices are generated perpendicular to the main flow direction. Devices such as Dean Flow Fractionation (DFF) systems exploit these secondary flows to focus or separate particles based on size and deformability [4][5]. These systems have been employed for cell sorting, blood component separation, and enrichment of rare cells, illustrating the potential of harnessing inertial effects for high-throughput, label-free separations [5].

Additional passive separation approaches involve filtration and sieving structures [4], capillarity and interfacial tension devices [5], gravity and buoyancy-based separators [6], and centrifugal flow devices [7]. Among these, micro-hydrocyclones, a centrifugal flow device utilizing centrifugal forces to separate particles based on their size and density, have gained significant attention not only for their passive separation capabilities but also for being a high-throughput device with no moving part, [2][3].

Microfluidic hydrocyclones miniaturize the operational principles of macroscale hydrocyclones, generating strong swirling flows. Due to their enclosed geometry and high curvature, micro-hydrocyclones sustain complex three-dimensional flow patterns, including strong out-of-plane components, helical vortices, and asymmetric core structures as shown in Figure 6-1(a). These features are fundamental to their operation but remain difficult to capture, particularly at the microscale [6].

Quantifying three-component velocity fields is essential for understanding vortex asymmetry, flow instabilities, and transport barriers such as the Locus of Zero Vertical Velocity (LZVV) represented in Figure 6-1(b), a flow feature known to influence macro-hydrocyclone's behavior but previously unquantified in microfluidic analogues [8]. Despite the rapid advancement of microfluidic separation technologies, the experimental characterization of three-dimensional (3D) velocity fields in inertial microflows remains limited. This limitation stems from the sophisticated and costly techniques required to experimentally resolve three-dimensional velocity fields. Traditional planar micro-PIV techniques provide valuable insight into in-plane velocity distributions but are inherently constrained in resolving out-of-plane motion, which is critical in swirling and vertical systems [7].

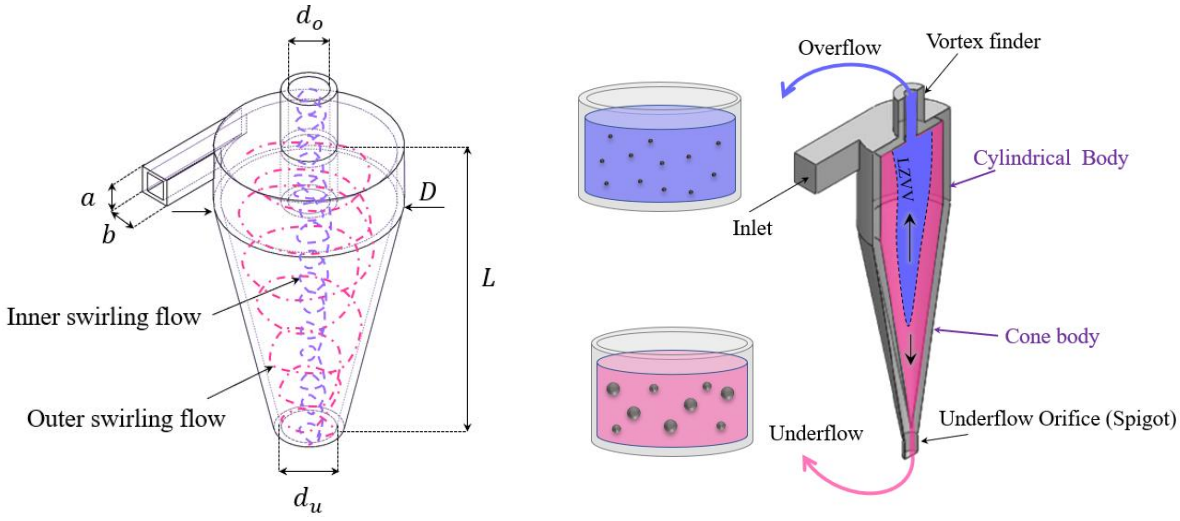

(a) (b)

Figure 6-1 (a) A schematic of the micro-hydrocyclone and inner flow structure (b) A schematic of the particle separation based on the locus of zero vertical velocity (LZVV).

Several approaches have been developed to extend flow measurements into three dimensions in microfluidics. Techniques based on defocused particle imaging, such as depth-from-defocus [9][10] and point spread function fitting [11][12] have enabled depth localization of tracer particles (particles that are added to the main flow stream to track the flow behavior), but often require large particles, sparse seeding, and high illumination power. Holographic micro-PIV methods [13][14] provide volumetric access but involve complex optical setups and are often limited in spatial resolution. Confocal and astigmatic imaging approaches have demonstrated success in obtaining 3D2C flow fields [12][15], however, their inherently limited acquisition rates restrict their application primarily to slow or steady flows.

Stereoscopic micro-PIV (stereo-μPIV) offers a promising alternative by enabling simultaneous capture of all three velocity components within a plane using dual perspectives and a calibration procedure. Initial demonstrations by Bown *et al.* [16] employed stereomicroscopy to measure flows over backward-facing steps, highlighting the feasibility of stereo-PIV at the microscale. Klank *et al.* [17] introduced a translation-based stereo-PIV method, limited to steady flows due to

sequential imaging. More recent studies have applied stereo-PIV to laminar flows in T-mixers and rectangular channels, often relying on external calibration targets and simplified optical models [18]. However, these efforts have primarily focused on low Reynolds number regimes and have not addressed flows with strong out-of-plane components or rotational symmetry as such those observed in micro-hydrocyclones [18].

Stereoscopic micro-PIV extends conventional planar PIV techniques by enabling the measurement of all three components of the velocity vector within a two-dimensional plane [19]. This is accomplished using two cameras positioned at carefully defined angles relative to the optical axis, viewing the same region of the flow from different perspectives. The angled views create a measurable disparity in how tracer particles appear in each camera's frame and this disparity contains depth information [20]. By resolving this disparity, it becomes possible to extract the out-of-plane velocity component, allowing for the reconstruction of 2D three-component flow fields (2D3C) even though measurements are restricted to a single illuminated plane. Each camera captures a pair of double frame images, and a standard PIV correlation algorithm is used to determine particle displacements in its own coordinate system. The output consists of two sets of 2D displacement vectors, one per camera that describe how particle patterns have moved between frames. These two perspectives are not directly comparable due to their different viewing angles. Therefore, a calibration procedure is performed in advance to determine how image-plane displacements in each camera correspond to real-world spatial displacements [21]. Using this mapping, the paired 2D vectors are transformed and combined to reconstruct the actual three-component vector at each point within the measurement plane. Conceptually, this is similar to triangulation, the same point viewed from two known angles allows its 3D location or, in this case, velocity vector to be resolved.

The integration of stereo-μPIV in microfluidic devices operating under complex conditions remains rare, primarily due to the experimental challenges associated with alignment, calibration, and imaging depth in confined geometries. As a result, there exists a significant gap in the literature regarding experimental quantification of three-dimensional velocity fields in inertial microflows, particularly in devices with curved geometries and swirling motion. This gap limits the ability to validate numerical models, optimize device designs, and fully understand transport and separation phenomena in such systems.

In this work, stereoscopic micro-PIV is implemented for the first time in a micro-hydrocyclone to quantify all three components of velocity within the midplane of the device. The system is calibrated using a self-referencing method adapted to the enclosed geometry, eliminating the need for external calibration targets. By comparing two inlet configurations, spiral and straight, the influence of entrance geometry on vortex symmetry, radial and tangential velocity distributions, and the formation of the Locus of Zero Vertical Velocity (LZVV) is investigated.

6.2 Experimental setup

6.3.1. Test cell fabrication

Two single-inlet micro-hydrocyclones were fabricated with a main body diameter of 5 mm and a total height of 17 mm, as presented in Figure 6-2. The inlet cross-section measured 1.7 mm by 1.3 mm, while the outlet diameters were 1.7 mm at the top and 1 mm at the bottom, as listed in Table 6-1 and shown in Figure 6-2. To produce a transparent and functional device suitable for optical access, a multi-stage fabrication approach is employed and shown in Figure 6-3, integrating high-resolution 3D printing, precision laser cutting, and silicone casting. The internal core is printed using an SLA 3D printer (Form 3, Formlabs Inc.) at a layer thickness of 10 μm to capture

fine geometrical details. A supporting mold structure is assembled from laser-cut acrylic sheets in a cubic configuration, designed both to house the hydrocyclone during casting and to maintain optical clarity by offering orthogonal viewing access. Prior to casting, the printed part is coated with a resin spray, which provides a glossy finish and creates a non-stick surface to prevent silicone adhesion.

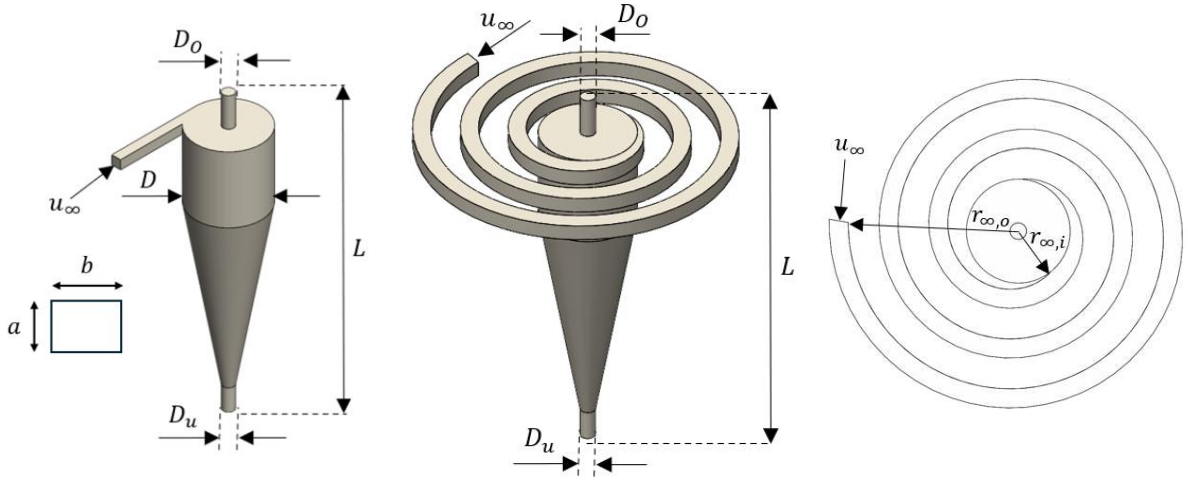

(a) (b) (c)

Figure 6-2 (a) basic and (b) modified hydrocyclone device geometry (c) spiral inlet geometry of the modified device.

Table 6-1 Dimensions of the micro-hydrocyclone device designed and fabricated.

Parameter	D	L	d_u	d_o	a	b
Value (mm)	5	17	1	1.7	1.3	1.7

To form the transparent body of the hydrocyclone, a specialized silicone (Solaris™, Smooth-On Inc.) is poured over the printed core. This silicone is chosen for its optical properties, including transparency and a suitable refractive index for imaging applications. The mold is thermally cured at 60 °C to ensure complete cross-linking of the silicone. After curing, the elasticity of the silicone allows the core to be removed without damage to the internal structure. A silicone slab is sealed

onto the device using uncured silicone to fully enclose the system. Metal hypodermic tubes of selected diameters are integrated into the top slab to form inlet and outlet connections and external silicone tubing is attached to enable fluid delivery. The completed device provides clear optical access to its internal flow geometry, making it the smallest micro-hydrocyclone to this day suitable and used for detailed flow visualization and analysis of particle or cell behavior, as shown in Figure 6-3.

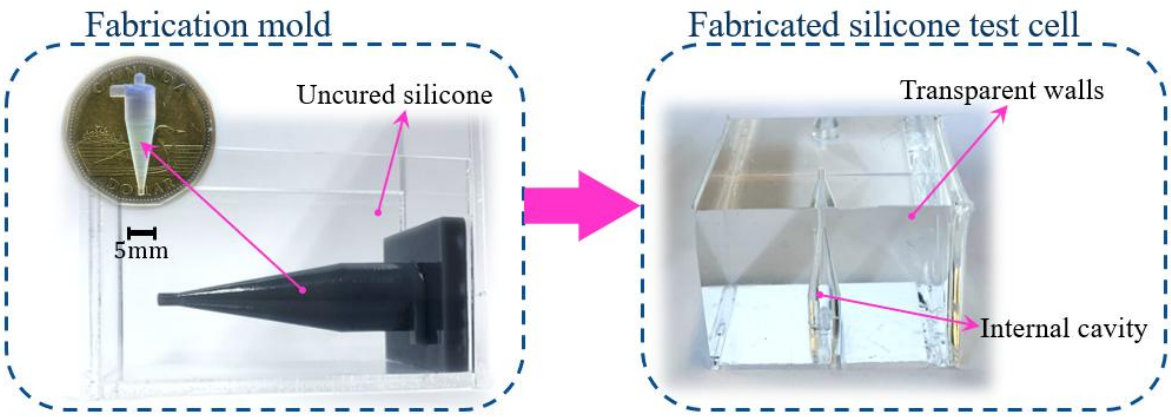

Figure 6-3 Fabrication process of the micro-hydrocyclone including mold design, mold fabrication, silicon test cell fabrication and device's internal cavity scale.

6.3.2. Fluid system

Accurate optical flow measurements, such as those obtained through Particle Image Velocimetry (PIV) and Particle Tracking Velocimetry (PTV), rely heavily on refractive index matching particularly when working with microfluidic devices that include curved or non-uniform geometries [32][33]. Refractive index mismatch between the fluid and test cell material can introduce distortions and reflections at boundaries, degrading image quality and compromising the precision of particle tracking. To address this, a 50.5% (w/w) solution of carbamide in water is prepared, yielding a refractive index of 1.4118 to closely match that of the silicone structure. This eliminated optical aberrations at the fluid–solid interface and allows for clear visualization within

the device. The selected solution also exhibits a dynamic viscosity of 1.905 mPa·s, supporting controlled flow conditions. For flow control, a high-precision syringe pump (PHD 2000, Harvard Apparatus Inc.) is used to deliver fluid at a stable and consistent rate through the inlet, providing well-defined and repeatable flow conditions essential for quantitative analysis.

6.3.3. Optical system

Velocity measurements are conducted using a stereoscopic micro-PIV (Stereo-μPIV) system configured to resolve all three velocity components within a single midplane of the flow domain (2D3C). As illustrated in Figure 6-4, the system is built around a Zeiss V8 stereomicroscope, with two double-frame cameras (LaVision GmBh) positioned at oblique angles to the optical axis via the microscope ports. This stereoscopic arrangement enables depth-resolved velocity reconstruction within the imaging plane.

Flow illumination is provided by a dual-pulsed Nd:YAG laser (532 nm), synchronized with the camera triggering through an onboard unit to control the inter-frame time delay with microsecond precision. A thin laser sheet intersects the midplane of the microfluidic channel, exciting 2 μm size fluorescent tracer particles that are neutrally buoyant in the working fluid. Obtained data is processed using commercial software (DaVis V8, LaVision GmbH).

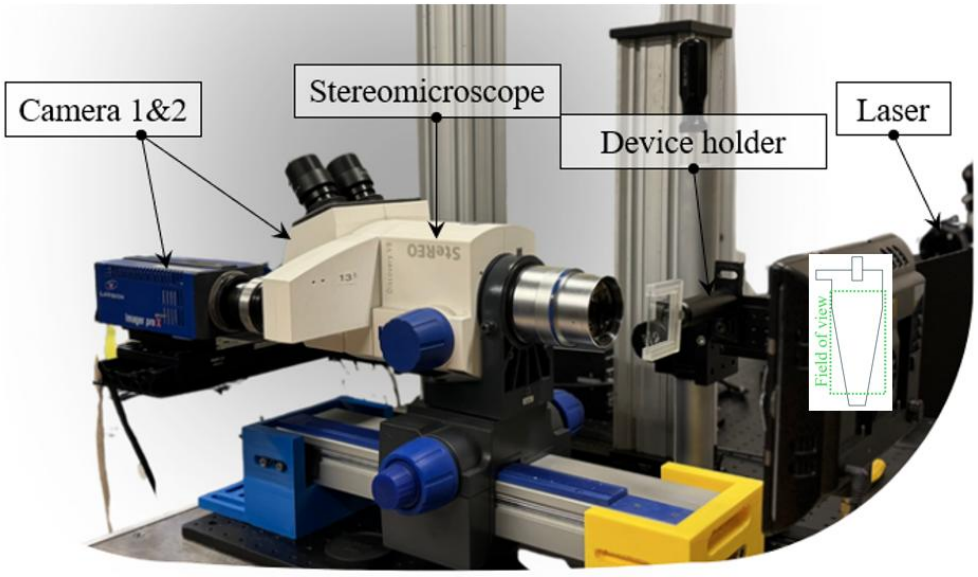

Figure 6-4 Photo of the experimental setup used for applying μPIV and μPTV for measuring the velocity of the flow and CTCs.

Temporal synchronization between the two stereo cameras is achieved using a hardware-based timing controller (LaVision Programmable Timing Unit) that provided precise trigger signals to both cameras and the pulsed laser source. The cameras are operated in double-frame mode with inter-frame times carefully adjusted to match the expected particle displacement and minimize motion blur. A master trigger signal generated by the timing unit initiates simultaneous image acquisition and laser pulse emission, ensuring that both camera exposures are tightly synchronized with the illumination pulses. Hardware connections are established using shielded BNC cables to minimize electronic noise and signal delays. Additionally, synchronization accuracy is verified by imaging static calibration targets and analyzing frame-to-frame displacements, confirming negligible temporal misalignment. This precise synchronization is essential for accurate stereo particle displacement measurements, especially given the small spatial scales and high-speed flow characteristics of micro-hydrocyclone operation.

6.3 Results and discussion

Samples of non-dimensionalized axial velocity fields on the midplane of the micro-hydrocyclone are presented in Figure 6-5 for both inlet geometries across different Reynolds numbers. The axial velocity has been normalized using average inlet velocity. In Figure 6-5(a-c), corresponding to the straight inlet configuration at $Re = 100$, 300, and 600 , where $Re = \rho V d_i/\mu$ and ρ is the fluid density, V is the characteristic velocity, d_i is the hydraulic inlet diameter of the micro-hydrocyclone and μ is the dynamic viscosity of the fluid, no significant upward flow is observed at lower Reynolds numbers. However, as the flow rate increases, an upward-moving region develops near the center and gradually expands toward the top of the device. By $Re = 600$, this upward motion becomes more prominent, indicating the development of a central reverse flow.

Figure 6-5(d-f) shows the results for the modified inlet geometry. Even at $Re = 100$, a distinct upward axial flow appears, extending to approximately 30 % of the device height. With increasing the Reynolds number, the upward flow region intensifies and expands vertically. This recirculation appears more developed and spatially symmetric compared to the straight inlet case. The axial velocity values shown are non-dimensionalized using the average inlet velocity for each respective case, enabling consistent comparison across flow conditions and geometries. Comparing the axial velocity between the two geometrical inlet cases i.e. straight inlet versus modified inlet, it can be concluded that the axial velocity develops further at lower Reynolds numbers in the modified inlet geometry.

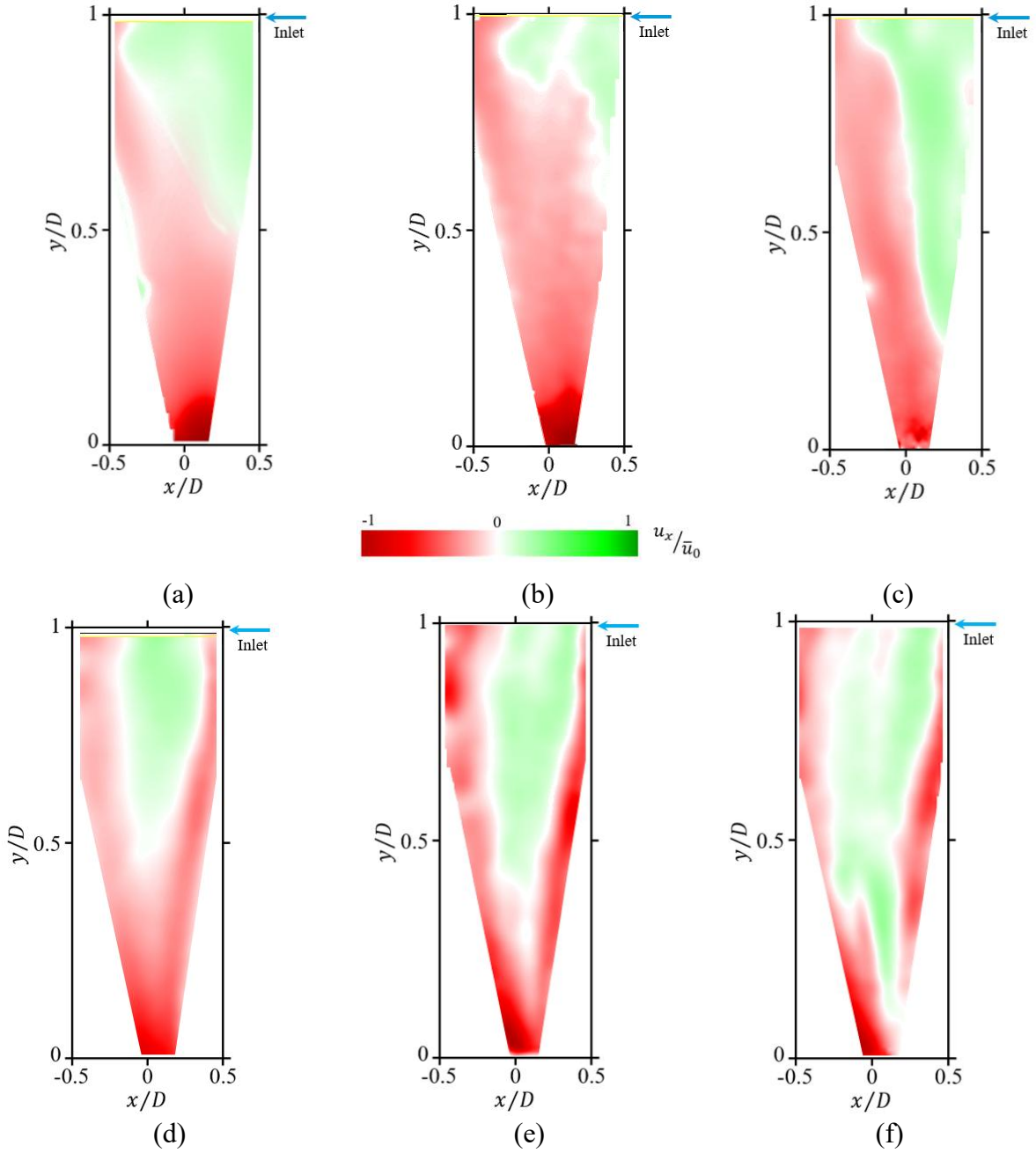

Figure 6-5 Axial velocity on the midplane of the device normalized by average inlet velocity . Flow having a straight inlet shown in (a) $Re = 150$, (b) $Re = 300$, (c) $Re = 600$, and flow having a spiral inlet shown in (d) $Re = 150$, (e) $Re = 300$, and (f) $Re = 600$.

As depicted in the schematic of the flow field in Figure 6-1(a), the flow contains a major swirling flow which can be shown by measurement of the out-of-plane velocity component, in the z-direction. Figure 6-6 shows the non-dimensionalized out-of-plane (tangential) velocity

component on the midplane of the micro-hydrocyclone for both inlet geometries across three Reynolds numbers. The velocity fields are non-dimensionalized using the average inlet velocity in each case to enable consistent comparison across conditions. In the straight inlet configuration i.e. Figure 6-6(a-c), the flow at $Re = 100$ exhibits weak and disorganized tangential motion. This results in substantial dampening of swirling structures, particularly in the lower region of the device. As the Reynolds number increases, the strength of the tangential flow improves, and the dampening becomes restricted to areas near the spigot. By $Re = 600$, a well-developed swirling motion can be observed, extending throughout the length of the device. In contrast, the spiral inlet configuration i.e. Figure 6-6(d-f) produces a strong and coherent swirling flow even at lower Reynolds numbers. The tangential motion spans the full height of the device and further intensifies with increasing Reynolds number. Notably, at higher Reynolds numbers, counter-rotating regions emerge near the cylindrical wall, indicating the formation of localized shear layers and secondary vortex structures.

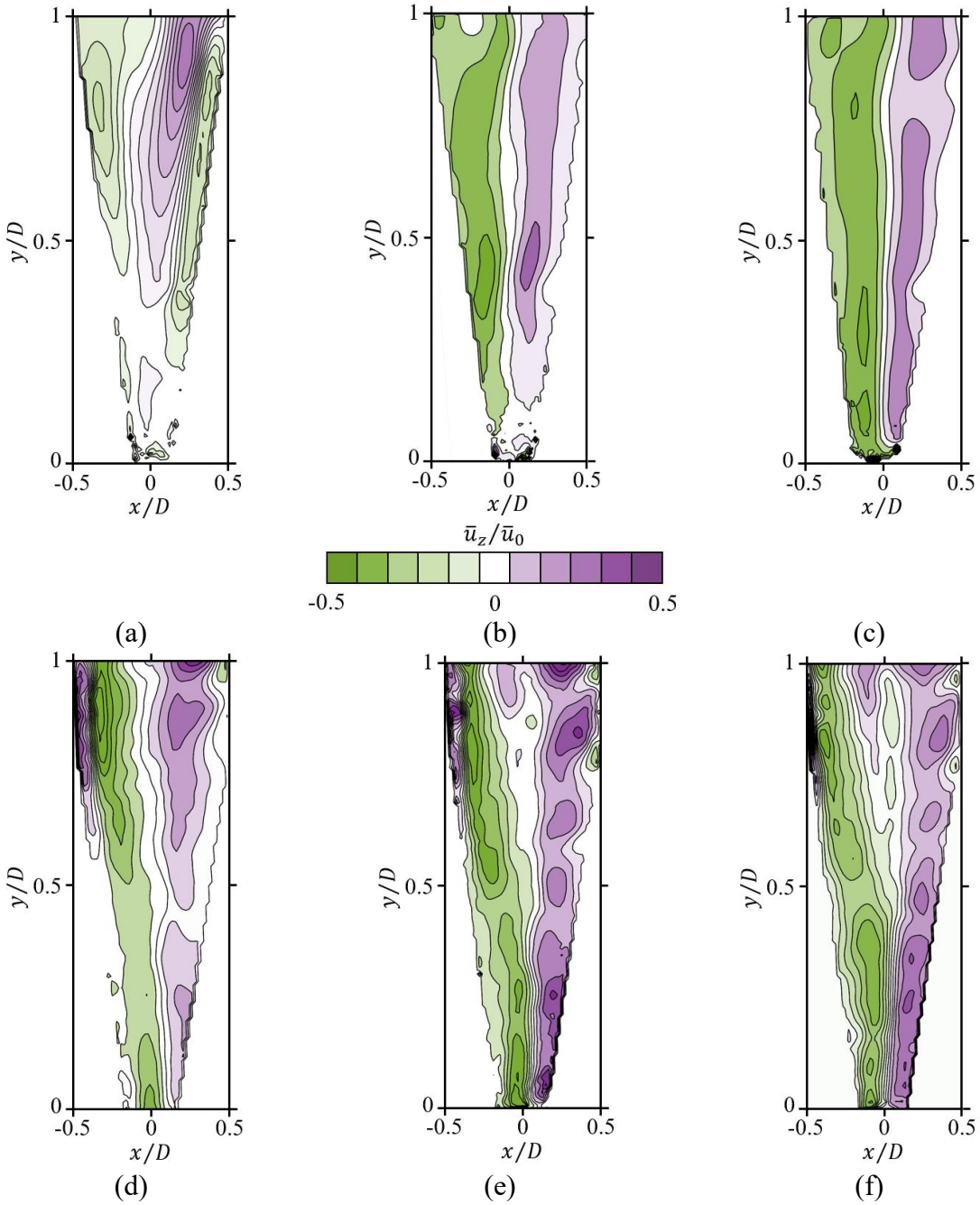

Figure 6-6 Out of plane velocity on the midplane of the device with a straight inlet in (a) $Re = 150$, (b) $Re = 300$, (c) $Re = 600$, and with a spiral inlet in (d) $Re = 150$, (e) $Re = 300$, and (f) $Re = 600$.

The non-dimensionalized in-plane velocity magnitude (composed of axial and radial velocity components) fields are compared in Figure 6-7 for the straight inlet and spiral inlet configurations at increasing Reynolds numbers. In each case, the in-plane velocity magnitude is normalized by

the average inlet velocity to enable consistent comparison across cases. The straight inlet configuration shown in Figure 6-7(a-c) shows a relatively confined high-velocity core region near the bottom of the device at $Re = 100$, with weak radial penetration and limited expansion in the upper portion of the flow. As the Reynolds number increases, the velocity magnitude near the centerline becomes more pronounced and the region of elevated in-plane motion extends upward, particularly in the central and near-spigot regions. At $Re = 600$, a vertically elongated core forms along the axis, but the velocity field remains mostly symmetric and lacks evidence of strong radial deflection or complex secondary flow structures.

In contrast, the spiral inlet configuration Figure 6-7(d-f) exhibits markedly different behavior. Even at $Re = 100$, the in-plane velocity field is concentrated near the lower wall and exhibits signs of radial deviation, consistent with the introduction of angular momentum from the inlet. As the Reynolds number increases, these features intensify. At $Re = 300$, the high-velocity region becomes more asymmetric and begins to spread upward and outward, interacting with the surrounding slower-moving fluid. This evolution suggests enhanced momentum transfer and the onset of secondary flow structures not observed in the standard inlet configuration.

By $Re = 600$, the in-plane velocity field becomes significantly more complex, showing multiple high velocity zones and strong gradients. The flow is no longer axisymmetric; instead, it reveals signatures of multi-scale structure and radial shear layers, particularly near the wall. The asymmetric penetration of velocity from the spiral inlet promotes enhanced mixing and suggests the onset of more complex secondary motion, including localized vortex stretching and redistribution of momentum.

Comparatively, the spiral inlet consistently produces a broader and more structured in-plane velocity field than the straight inlet. This indicates stronger momentum transfer across the cross-

section and enhanced radial flow components. The presence of multiple high velocity regions and increased asymmetry at high Reynolds numbers point to the intensified convective transport and potentially higher shear-induced gradients within the device. These flow features are essential for separation efficiency in micro-hydrocyclone applications, as they influence the centrifugal field distribution and the migration of particles or cells. The contrast between these two inlet designs underscores the critical role of inlet geometry in shaping flow development and highlights the potential of tailored inlet configurations to actively manipulate flow topology for targeted microfluidic performance.

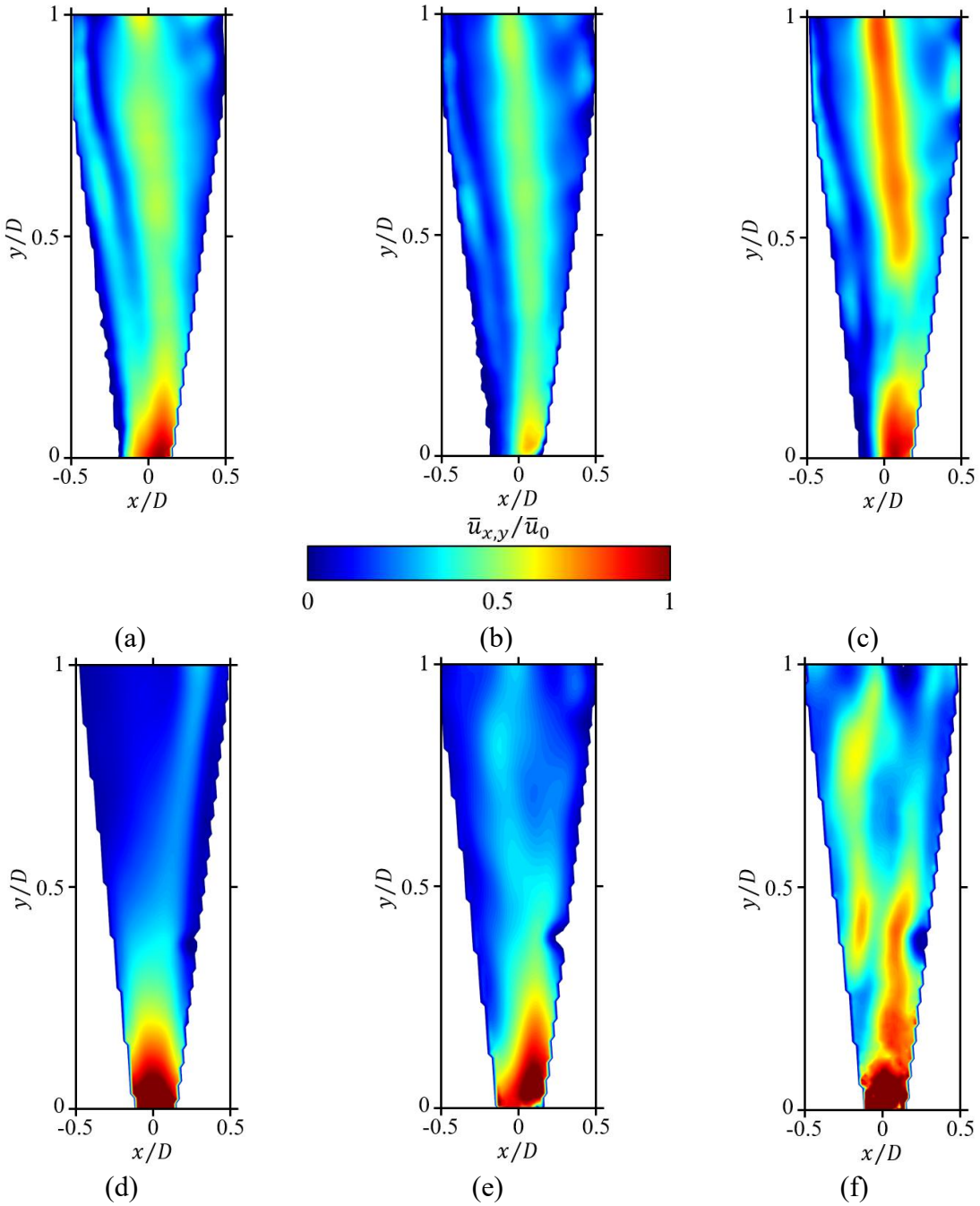

Figure 6-7 In plane velocity magnitude on the midplane of the device with a straight inlet in (a) $Re = 150$, (b) $Re = 300$, (c) $Re = 600$, and with a spiral inlet (d) $Re = 150$, (e) $Re = 300$, and (f) $Re = 600$.

In the axial velocity fields, the straight inlet geometry in Figure 6-5(a-c) shows a consistently strong downward core flow along the centerline, with a relatively smooth gradient from the inlet to the spigot. At low a Reynolds number of $Re = 150$, the flow remains largely axisymmetric and unidirectional, with minimal upward motion. As the Reynolds number increases, a localized upward axial motion emerges near the upper portion of the device, most notably at $Re = 600$, indicating the development of a central recirculation or reverse flow zone. In contrast, the spiral inlet geometry Figure 6-5(d-f) exhibits an earlier onset and greater vertical extent of upward axial velocity. Even at $Re = 150$, there is a visible upward motion occupying nearly one-third of the device height, which expands significantly at higher Reynolds numbers. This suggests that the spiral inlet promotes enhanced flow recirculation and vertical momentum redistribution along the device axis.

The out-of-plane velocity fields in Figure 6-6 highlight the rotational nature of the flow and reflect the swirl intensity within the device. In the straight inlet case Figure 6-6(d-f), the tangential velocity at $Re = 150$ is weak and disorganized, especially near the base of the hydrocyclone, where swirl is expected to be strongest. With increasing Reynolds number, the swirl becomes more coherent and vertically extended, but its peak strength remains centered around the spigot region. At $Re = 600$, the out-of-plane velocity exhibits a more continuous swirling structure, though still with asymmetries and weak regions near the top. In comparison, the spiral inlet (bottom row) generates a strong, well-structured tangential velocity field throughout the entire height of the device from the lowest Reynolds number. The spiral-induced swirl intensifies with increasing Re, and exhibits smoother gradients and higher spatial coverage. Additionally, signs of local counter-rotation near the walls at higher Re suggest secondary flow formation or boundary-layer interaction effects that are absent or muted in the straight inlet case.

The in-plane velocity magnitudes further reinforce these differences in flow structure. In the straight inlet configuration, high-velocity regions are concentrated near the lower core and expand modestly upward with increasing Re, retaining axial symmetry and limited radial complexity. Conversely, the spiral inlet introduces significant asymmetry and radial spreading even at low Reynolds numbers. By $Re = 600$, the in-plane velocity fields reveal multiple zones of elevated velocity and sharper gradients, indicative of complex interactions between swirling core flow and wall-bounded layers. This distribution suggests stronger convective mixing and more distributed shear, both of which can have critical implications for separation efficiency and particle transport within the device.

A comparative assessment of the Locus of Zero Vertical Velocity (LZVV) on the midplane of the micro-hydrocyclone for both the spiral and straight inlet configurations at three Reynolds numbers is presented in Figure 6-8. The LZVV represents the set of spatial points where the axial (vertical) velocity component is zero, effectively delineating the boundary between downward and upward flow. The shape and position of the LZVV are directly influenced by the strength and structure of the internal vortex and the development of recirculating flow zones. Colored contours mark the LZVV region for $Re = 100$ (purple), $Re = 300$ (green), and $Re = 600$ (pink) in Figure 6-8(a).

For the straight inlet configuration shown in Figure 6-8 the LZVV remains more confined across all Reynolds numbers. At lower flow rates, the boundary is narrow and located near the vortex finder. Although some upward flow emerges at higher Reynolds numbers, its extent remains limited, and the LZVV rises only modestly. Even at $Re = 600$, the LZVV does not reach as high or spread as widely as in the spiral inlet case. This suggests that in the straight inlet geometry,

vortex breakdown and recirculating structures are weaker and more localized, consistent with the more laminar and symmetric axial velocity fields observed earlier.

In the spiral inlet geometry, the LZVV shifts upward and expands both vertically and laterally with increasing Reynolds number. At $Re = 100$, the LZVV is limited to the lower half of the device, indicating that upward flow is initially weak and localized. As the Reynolds number increases, the region of upward axial motion becomes more pronounced, and the LZVV boundary rises along the device axis. By $Re = 600$, the LZVV reaches nearly the full height of the hydrocyclone and displays a broader, more asymmetric shape. This reflects a well-developed central recirculation structure driven by enhanced tangential motion and radial pressure gradients introduced by the spiral inlet.

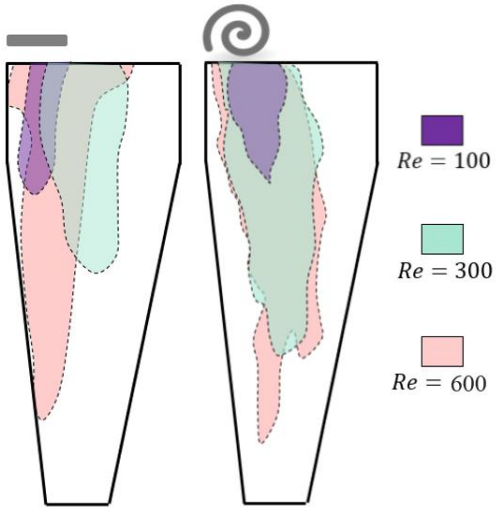

Figure 6-8 Comparison of the changes in the shape of LZVV for 3 different regimes between flow basic and modified device on the midplane of a micro-hydrocyclone.

Figure 6-9 presents the normalized horizontal velocity profiles extracted along the midline at $y = L/2$ of the micro-hydrocyclone, comparing the tangential, U_x and radial velocity, U_z components for the spiral inlet Figure 6-9(a) and (b) and straight inlet Figure 6-9(c) and (d)

configurations at Reynolds numbers of 100, 300, and 600. All velocity components are normalized by the respective average inlet velocity at $Re = 600$ to enable consistent comparison.

In the straight inlet configuration, the tangential velocity profiles shown in Figure 6-9(a) reveal substantially weaker swirl compared to the spiral case. The antisymmetric structure is preserved, but the amplitude is significantly lower, especially at $Re = 100$ where the profile remains nearly flat. As Reynolds number increases, the profile steepens and the two opposing peaks become more distinct. This supports previous observations that the straight inlet generates a less intense and more axisymmetric vortex structure. The radial velocity profiles represented in Figure 6-9(b) also remain negative flat across the entire width, again suggesting that the vortex center is not aligned with the measurement plane. However, the straight inlet produces smoother and more gradual gradients, lacking the sharper features seen in the spiral case, which may indicate weaker radial shear and less pronounced secondary motion.

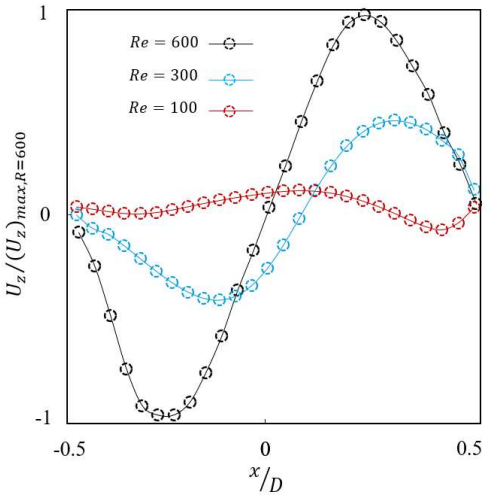

(a)

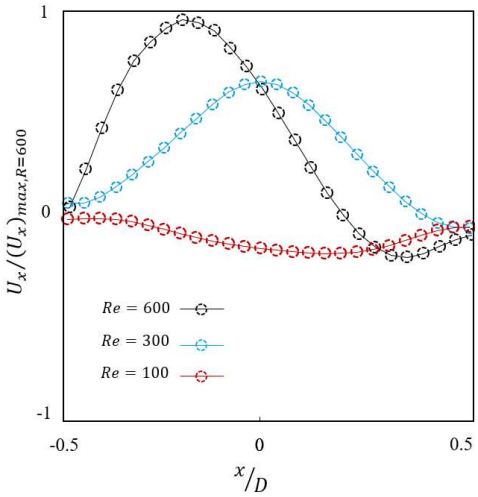

(b)

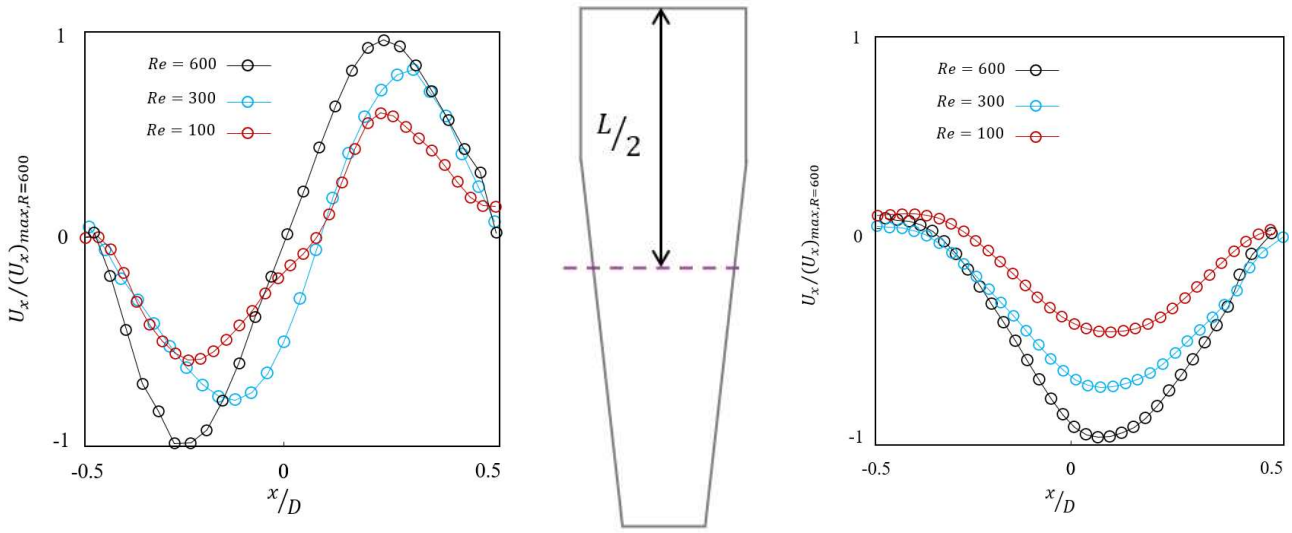

(c) (d)

Figure 6-9 Comparison of the changes in the in and out of plain velocity for 3 different phases on the midline of the micro-hydrocyclone between (a,b) modified device and (c,d) basic device

In the spiral inlet configuration, the tangential velocity profiles in Figure 6-9(c) exhibit a clear antisymmetric structure about the centerline with the magnitude and gradient of the profiles increasing significantly with Reynolds number. At $Re = 600$, the profile displays two well-defined peaks of opposite sign, indicating a strong and coherent swirling motion across the midplane. The inflection point near the center suggests the presence of a well-developed vortex core. At lower Reynolds numbers, the profile remains qualitatively similar but with reduced intensity and sharper confinement near the centerline. In contrast, the radial velocity component in Figure 6-9(d) shows a consistently negative distribution across the domain, particularly at higher Reynolds numbers. This unidirectional trend is a consequence of the vortex core being laterally offset from the measurement plane, as seen in the earlier velocity contour plots. As a result, the midplane captures only one side of the radially inward flow, explaining the absence of symmetry in the u_x component.

Overall, these horizontal velocity profiles confirm the stronger swirling motion and more complex flow structure induced by the spiral inlet. The tangential component exhibits both higher magnitude and clearer asymmetry, while the radial component reveals more substantial inflow toward the vortex core. In both inlet geometries, the asymmetry in the radial component likely arises from the off-center position of the vortex core with respect to the measurement plane. These observations are consistent with the full-field velocity data and further emphasize the role of inlet geometry in dictating the generation, positioning, and intensity of internal vortex structures.

6.4 Conclusion

This chapter presents stereoscopic micro-PIV measurement in a micro-hydrocyclone, enabling measurement of full three-component of velocity on the midplane of a microscale swirling flow. The experimental methodology provides detailed insight into the internal flow structure that would not be accessible through conventional planar velocimetry. By simultaneously resolving the axial, radial, and tangential velocity components, the measurements reveal the spatial development of vortex structures, flow asymmetries, and regions of flow reversal.

Comparison of two micro-hydrocyclones with a straight or spiral inlet geometry demonstrates the substantial influence of inlet-induced swirl on the evolution of the internal flow. The spiral inlet was shown to promote earlier and more extensive upward axial flow, stronger and more coherent tangential motion, and greater radial velocity gradients, especially at higher Reynolds numbers. Analysis of the Locus of Zero Vertical Velocity (LZVV) further confirmed the expansion and migration of recirculation zones in the spiral configuration, quantitatively linking flow structure to device geometry. Additionally, velocity profile analysis along the midplane highlights off-axis vortex positioning and underscores the importance of full three-component measurements in characterizing such confined swirling flows.

These findings not only demonstrate the feasibility and utility of stereoscopic micro-PIV for resolving complex three-dimensional flow fields in microscale devices but also highlight the strong coupling between inlet design and internal vortex dynamics. By quantifying flow structures previously inaccessible through conventional methods, this work provides a framework for tailoring micro-hydrocyclone performance through geometric optimization. More broadly, the methodology and insights presented here can be extended to other microscale swirling flows where

precise control of flow topology is critical, such as particle separation, mixing, and biochemical processing.

References

[1] A. Dalili, E. Samiei, M. Hoorfar, A review of sorting, separation and isolation of cells and microbeads for biomedical applications: microfluidic approaches, Analyst 144 (2019) 87–113. https://doi.org/10.1039/c8an01061g.

[2] I. Maguire, R. O'Kennedy, J. Ducrée, F. Regan, A review of centrifugal microfluidics in environmental monitoring, Anal. Methods 10 (2018) 1497–1515. https://doi.org/10.1039/c8ay00361k.

[3] R. Pol, F. Céspedes, D. Gabriel, M. Baeza, Microfluidic lab-on-a-chip platforms for environmental monitoring, TrAC - Trends Anal. Chem. 95 (2017) 62–68. https://doi.org/10.1016/j.trac.2017.08.001.

[4] R. Nasiri, A. Shamloo, S. Ahadian, L. Amirifar, J. Akbari, M.J. Goudie, K.J. Lee, N. Ashammakhi, M.R. Dokmeci, D. Di Carlo, A. Khademhosseini, Microfluidic-Based Approaches in Targeted Cell/Particle Separation Based on Physical Properties: Fundamentals and Applications, Small 16 (2020). https://doi.org/10.1002/smll.202000171.

[5] P. Sajeesh, A.K. Sen, Particle separation and sorting in microfluidic devices: A review, Microfluid. Nanofluidics 17 (2014) 1–52. https://doi.org/10.1007/s10404-013-1291-9.

[6] Y. Saffar, D.S. Nobes, R. Sabbagh, Integrated Single Camera μPTV And Florescence Imaging For Cell Tracking And Flow Investigation In Centrifugal Microfluidic Devices, Proc. Int. Symp. Appl. Laser Imaging Tech. to Fluid Mech. 21 (2024) 1–10. https://doi.org/10.55037/lxlaser.21st.49.

[7] M.S. Syed, F. Mirakhorli, C. Marquis, R.A. Taylor, M.E. Warkiani, Particle movement and fluid behavior visualization using an optically transparent 3D-printed micro-hydrocyclone, Biomicrofluidics 14 (2020). https://doi.org/10.1063/5.0025391.

[8] M.S. Syed, C. Marquis, R. Taylor, M.E. Warkiani, A two-step microengineered system for high-density cell retention from bioreactors, Sep. Purif. Technol. 254 (2021) 117610. https://doi.org/10.1016/j.seppur.2020.117610.

[9] R. Sabbagh, M.G. Lipsett, C.R. Koch, D.S. Nobes, Hydrocyclone Performance and Energy Consumption Prediction: A Comparison with Other Centrifugal Separators, Sep. Sci. Technol. 50 (2015) 788–801. https://doi.org/10.1080/01496395.2014.978463.

[10] A.F. Concha, A.J.L. Bouso, Fluid Mechanics and Its Applications Fluid Mechanics Fundamentals of Hydrocyclones and Its Applications in the Mining Industry, 2021. http://www.springer.com/series/5980.

[11] R. Sabbagh, D.S. Nobes, Centrifugal separation, Kirk-Othmer Encyclopedia of Chemical Technology, 2018. https://doi.org/10.1201/9780203752494-9.

[12] R. Sabbagh, M.G. Lipsett, C.R. Koch, D.S. Nobes, An experimental investigation on hydrocyclone underflow pumping, Powder Technol. 305 (2017) 99–108. https://doi.org/10.1016/j.powtec.2016.09.045.

[13] Z. Zhao, H. Wang, C. Xie, Y. Wei, J. Xue, X. Xiao, B. Liu, Hydrocyclone separation performance influenced by feeding solid concentration and correcting separation size, (n.d.). https://doi.org/10.1007/s00231-020-02940-8/Published.

[14] L.M. Tavares, L.L.G. Souza, J.R.B. Lima, M. V. Possa, Modeling classification in small-diameter hydrocyclones under variable rheological conditions, Miner. Eng. 15 (2002) 613–622. https://doi.org/10.1016/S0892-6875(02)00085-7.

[15] I.C. Bicalho, J.L. Mognon, J. Shimoyama, C.H. Ataíde, C.R. Duarte, Separation of yeast from alcoholic fermentation in small hydrocyclones, Sep. Purif. Technol. 87 (2012) 62–70. https://doi.org/10.1016/j.seppur.2011.11.023.

[16] T. Zhang, J. Li, A. Wei, J. Huang, S. Li, J. Huan, F. Wang, H. Wang, Ultra-clean separation of micro-particles in lubricant oil based on short-flow control of mini-hydrocyclone, Sep. Purif. Technol. 304 (2023) 122370. https://doi.org/10.1016/j.seppur.2022.122370.

[17] L. Liu, Y. Sun, Z. Kleinmeyer, G. Habil, Q. Yang, L. Zhao, D. Rosso, Microplastics separation using stainless steel mini-hydrocyclones fabricated with additive manufacturing, Sci. Total Environ. 840 (2022) 156697. https://doi.org/10.1016/j.scitotenv.2022.156697.

[18] L. He, L. Ji, Y. He, Y. Liu, S. Chen, K. Chu, S. Kuang, Experimental and numerical analysis of Chinese hamster ovary cell viability loss in mini-hydrocyclones, Sep. Purif. Technol. 295 (2022). https://doi.org/10.1016/j.seppur.2022.121203.

[19] Y. Fan, J. Li, Q. Wei, Z. Xiong, Y. Ji, H. Ma, B. Liu, Y. Huang, W. Lv, H. Wang, Study on the law of turbulent flow and self-rotation and revolution of particles in micro-hydrocyclone, Powder Technol. 415 (2023) 118200. https://doi.org/10.1016/j.powtec.2022.118200.

[20] P. Bhardwaj, P. Bagdi, A.K. Sen, Microfluidic device based on a micro-hydrocyclone for particle-liquid separation, Lab Chip 11 (2011) 4012–4021. https://doi.org/10.1039/c1lc20606k.

[21] Z. Liu, Z. Lu, C. Zhang, H. Lang, X. Zhai, Zhongmin Liu, * Zezhao Lu, Chengwei Zhang, Heng Lang, and Xin Zhai, (2023). https://doi.org/10.1021/acs.langmuir.2c03448.

[22] L. He, L. Ji, X. Sun, S. Chen, S. Kuang, Investigation of mini-hydrocyclone performance in removing small-size microplastics, Particuology 71 (2022) 1–10. https://doi.org/10.1016/j.partic.2022.01.011.

[23] S.H. Au, J. Edd, A.E. Stoddard, K.H.K. Wong, F. Fachin, S. Maheswaran, D.A. Haber, S.L. Stott, R. Kapur, M. Toner, Microfluidic isolation of circulating tumor cell clusters by size and asymmetry, Sci. Rep. 7 (2017). https://doi.org/10.1038/s41598-017-01150-3.

[24] Z.S. Sayed, M.G. Khattap, M.A. Madkour, N.S. Yasen, H.A. Elbary, R.A. Elsayed, D.A. Abdelkawy, A.H.S. Wadan, I. Omar, M.H. Nafady, Circulating tumor cells clusters and their role in Breast cancer metastasis; a review of literature, Discov. Oncol. 15 (2024). https://doi.org/10.1007/s12672-024-00949-7.

[25] I. Krol, F. Castro-Giner, M. Maurer, S. Gkountela, B.M. Szczerba, R. Scherrer, N. Coleman, S. Carreira, F. Bachmann, S. Anderson, M. Engelhardt, H. Lane, T.R. Jeffry Evans, R.

Plummer, R. Kristeleit, J. Lopez, N. Aceto, Detection of circulating tumour cell clusters in human glioblastoma, Br. J. Cancer 119 (2018) 487–491. https://doi.org/10.1038/s41416-018-0186-7.

[26] A.A. Mouza, C.M. Patsa, F. Schönfeld, Mixing performance of a chaotic micro-mixer, Chem. Eng. Res. Des. 86 (2008) 1128–1134. https://doi.org/10.1016/j.cherd.2008.04.009.

[27] F.G. Ergin, B.B. Watz, N.F. Gade-Nielsen, A review of planar PIV systems and image processing tools for lab-on-chip microfluidics, Sensors (Switzerland) 18 (2018) 1–23. https://doi.org/10.3390/s18093090.

[28] N. Nivedita, P. Ligrani, I. Papautsky, Dean flow dynamics in low-aspect ratio spiral microchannels, Sci. Rep. 7 (2017) 1–10. https://doi.org/10.1038/srep44072.

[29] M. Nimafar, V. Viktorov, M. Martinelli, Experimental Investigation of Split and Recombination Micromixer in Confront with Basic T- and O- type Micromixers, Int. J. Mech. Appl. 2 (2012) 61–69. https://doi.org/10.5923/j.mechanics.20120205.02.

[30] K.I. Belousov, N.A. Filatov, I. V. Kukhtevich, V. Kantsler, A.A. Evstrapov, A.S. Bukatin, An asymmetric flow-focusing droplet generator promotes rapid mixing of reagents, Sci. Rep. 11 (2021). https://doi.org/10.1038/s41598-021-88174-y.

[31] Y. Saffar, S. Kashanj, D.S. Nobes, R. Sabbagh, The Physics and Manipulation of Dean Vortices in Single- and Two-Phase Flow in Curved Microchannels : A Review, Micromachines 14 (2023) 2202.

[32] K.T. Kiger, C. Pan, PIV Technique for the Simultaneous Measurement of Dilute Two-Phase Flows, J. Fluids Eng. (2000) 811–818. http://asmedigitalcollection.asme.org/fluidsengineering/article-pdf/122/4/811/5615298/811_1.pdf.

[33] F.G. Ergin, B.B. Watz, N.F. Gade-Nielsen, A review of planar PIV systems and image processing tools for lab-on-chip microfluidics, Sensors (Switzerland) 18 (2018). https://doi.org/10.3390/s18093090.

[34] F. He, H. Wang, J. Wang, S. Li, Y. Fan, X. Xu, Experimental study of mini-hydrocyclones with different vortex finder depths using Particle Imaging Velocimetry, Sep. Purif. Technol. 236 (2020) 116296. https://doi.org/10.1016/j.seppur.2019.116296.

[35] Y. Fan, J. Wang, Z. Bai, J. Wang, H. Wang, Experimental investigation of various inlet section angles in mini-hydrocyclones using particle imaging velocimetry, Sep. Purif. Technol. 149 (2015) 156–164. https://doi.org/10.1016/j.seppur.2015.04.047.

[36] S.T.L. Harrison5, J.J. Cillierst, THE USE OF MINI-HYDROCYCLONES FOR DIFFERENTIAL SEPARATIONS WITHIN MINERAL SLURRJES SUBJECTED TO BIOLEACHING, Mitwrrrls Eng. IO (1997) 529–535.

[37] R.A. Medronho, J. Schuetze, W.D. Deckwer, Numerical simulation of hydrocyclones for cell separation, Lat. Am. Appl. Res. 35 (2005) 1–8.

[38] G. Zhu, J.L. Liow, A. Neely, Computational study of the flow characteristics and separation efficiency in a mini-hydrocyclone, Chem. Eng. Res. Des. 90 (2012) 2135–2147. https://doi.org/10.1016/j.cherd.2012.05.020.

[39] J.Y. Han, B. Krasniqi, J. Kim, M. Keckley, D.L. DeVoe, Miniaturization of Hydrocyclones by High-Resolution 3D Printing for Rapid Microparticle Separation, Adv. Mater. Technol. 5 (2020) 1–11. https://doi.org/10.1002/admt.201901105.

[40] C.A. Petty, S.M. Parks, Flow structures within miniature hydrocyclones, Miner. Eng. 17 (2004) 615–624. https://doi.org/10.1016/j.mineng.2004.01.020.

[41] R. Sabbagh, S. Ansari, D.S. Nobes, An imaging approach for in-situ measurement of refractive index of a porous medium, Opt. Lasers Eng. 134 (2020). https://doi.org/10.1016/j.optlaseng.2020.106175.

[42] Y.K. Agrawal, R. Sabbagh, S. Sanders, D.S. Nobes, Measuring the refractive index, density, viscosity, pH, and surface tension of potassium thiocyanate (KSCN) solutions for refractive index matching in flow experiments, J. Chem. Eng. Data 63 (2018) 1275–1285.

[43] P. Greenspan, E.P. Mayer, S.D. Fowler, Nile Red" A Selective Fluorescent Stain for Intracellular Lipid Droplets, 1985. http://rupress.org/jcb/article-pdf/100/3/965/1457917/965.pdf.

[44] G.S. Alemán-Nava, S.P. Cuellar-Bermudez, M. Cuaresma, R. Bosma, K. Muylaert, B.E. Ritmann, R. Parra, How to us Nile Red, a selective fluorescent stain for microalgal neutral lipids, J. Microbiol. Methods 128 (2016) 74–79. https://doi.org/10.1016/j.mimet.2016.07.011.

[45] P.K. Horan, M.J. Melnicoff, B.D. Jensen, S.E. Slezak, Chapter 42 Fluorescent Cell Labeling for in Vivo and in Vitro Cell Tracking, Methods Cell Biol. 33 (1990) 469–490. https://doi.org/10.1016/S0091-679X(08)60547-6.

[46] Y. Guo, L. Su, J. Wu, D. Zhang, X. Zhang, G. Zhang, T. Li, J. Wang, C. Liu, Assessment of the green florescence protein labeling method for tracking implanted mesenchymal stem cells, Cytotechnology 64 (2012) 391–401. https://doi.org/10.1007/s10616-011-9417-y.

[47] M. Raffel, C.E. Willert, F. Scarano, C.J. Kähler, S.T. Wereley, J. Kompenhans, Particle Image Velocimetry: A Practical Guide, Part. Image Velocim. A Pract. Guid. (2018) 1–32. https://doi.org/10.1007/978-3-319-68852-7_1.

Chapter 7: Evaluation of the Separation Performance of Micro-hydrocyclone with a Spiral Inlet

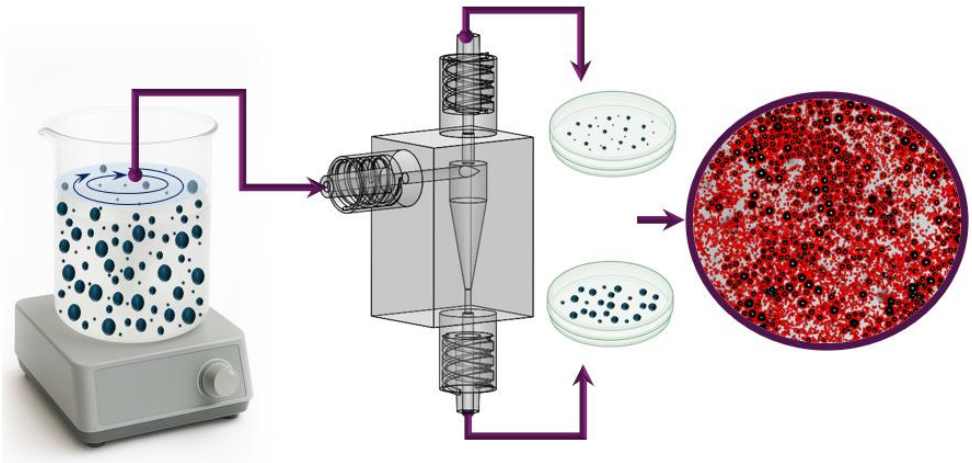

Graphical Abstract: Schematic of the separation and sampling process with a micro-hydrocyclone

This chapter investigates the performance of a micro-hydrocyclone and elucidates the influence of inlet geometry modifications on the separation of circulating tumor cells (CTCs). Separation efficiency was quantified using both rigid microparticles and fragile tumor cell clusters across a broad range of Reynolds numbers. The modified micro-hydrocyclone exhibited superior performance at low flow rates, achieving high recovery while preserving the structural integrity of cell clusters. In contrast, the conventional design demonstrated enhanced efficiency at elevated flow rates but induced substantial cluster disruption, thereby limiting its suitability for biomedical applications requiring preservation of cellular architecture.

7.1 Introduction

Micro-hydrocyclones (micro-HC), miniaturized derivatives of conventional hydrocyclones, have recently attracted attention for biological and biomedical applications, particularly for label-free cell and particle separation. Their operation relies on tangentially introduced flow to generate a swirling motion, which produces centrifugal forces that direct larger particles toward the outer wall and smaller particles toward the central vortex [1]. The separated fractions are discharged through distinct underflow and overflow outlets. These devices retain key advantages of their macroscale counterparts, including compactness, absence of moving parts, and ease of integration into microfluidic platforms, while enabling precise control and scalability suitable for emerging applications such as rare cell isolation and diagnostic sample preparation.

The miniaturization of hydrocyclones into microfluidic platforms enables their unique advantage in biomedical and analytical applications where precise and high-throughput handling of sample volumes is required. Micro-hydrocyclones facilitate passive, label-free separation, making them particularly attractive for size-based sorting of cells, beads, or biomolecules in lab-on-a-chip systems [3]. However, the microscale operation introduces fundamental changes in fluid behavior which is yet to be fully understood. As a result, the design and performance of micro-hydrocyclones must be carefully tailored to the low Reynolds number regime characteristic of microfluidic flows [4].

A limited number of studies have evaluated micro and mini hydrocyclones performance in separating microplastics [5], offshore solid-liquid mixtures [6], swirl focusing for cells and suspended cell cultures [3]. These studies have examined the impact of factors such as feed concentration, inlet velocity, and hydrocyclone geometry on separation efficiency and pressure

distribution. Some have incorporated computational fluid dynamics (CFD) to analyze internal flow structures and derive corrections for separation size [6] while others have explored removal of fine particles to improve classification at the micro-scale [5]. Optically transparent micro-hydrocyclones have also been fabricated to enable in-situ flow visualization and particle trajectory tracking [4]. However, the total number of experimental reports focused on true miniaturized hydrocyclones remains limited, and performance data under biologically relevant conditions are still sparse.

In parallel, passive microfluidic systems utilizing Dean flow have shown significant potential for continuous and size-selective separation [7]. Dean vortices form as secondary flow in curved microchannels and apply lateral drag forces on suspended particles [8], [9]. This inertial focusing mechanism is size-dependent and allows for separation without external fields or complex instrumentation [10]. Spiral microchannels, in particular, have been adopted in multiple designs to increase throughput while maintaining the benefits of inertial migration [11]. Although Dean-based systems have been applied to various biological targets, including mammalian cells and microalgae, their scalability and efficiency can be constrained by flow rate and concentration limits [12]. At high cell densities, reduced focusing performance emerges as a significant limitation. As a result, these Dean-based systems have mostly been deployed as downstream modules rather than as standalone units for high-throughput bioprocessing.

Despite initial progress, there remains a clear gap in the extensive evaluation and optimization of micro-hydrocyclones for biological applications, particularly for cases where particle or cell integrity must be preserved. Most available studies focus on rigid synthetic particles or simple suspensions, while few address the specific challenges posed by fragile, deformable biological clusters such as multicellular aggregates [4]. Moreover, although several studies have

demonstrated efficient separation at high Reynolds numbers, a comprehensive quantitative framework investigating hydrodynamic conditions, device design, and biological performance metrics remains absent [13], [14]. Widespread adoption of micro-hydrocyclones in biomedical or cell-based manufacturing workflows will require strategies to minimize shear-induced damage, a deeper understanding of the deformation mechanics of biological targets that reconcile high separation efficiency with preservation of cellular integrity.

This work presents a comprehensive experimental investigation of the separation efficiency of a modified micro-hydrocyclone using both synthetic particles and fluorescently labeled cell clusters. To ensure consistent spatial sampling, a motorized traverse system is developed to automate imaging of petri dish samples under a microscope. A custom image analysis framework was implemented to process large volumes of microscopy data, enabling frame-by-frame quantification of particle size and abundance in the overflow and underflow streams. The results were used to evaluate key performance metrics, including recovery to underflow and separation selectivity, across a range of flow rates and sample conditions. This integrated approach provides a comprehensive assessment of the novel microfluidic device performance and highlights its potential for high-throughput bioseparation in microfluidic applications.

7.2 Experimental setup

The experimental setup used to evaluate the separation performance of the micro-hydrocyclone for both microparticles and fluorescently stained cell clusters is shown in Figure 7-1. For the particle separation experiments, a Masterflex L/S peristaltic pump (Model 7523-80, Cole-Parmer, USA) was used to drive the suspension through the system. A pulse dampener (Cole-Parmer, spherical, PTFE-lined) was installed downstream of the pump to attenuate flow pulsations

typically associated with peristaltic pumping and to ensure a stable inlet profile. The particle suspension was continuously stirred using a magnetic stirrer (Thermo Scientific Cimarec I-Series) to maintain homogeneity and prevent sedimentation during sampling. The flow was directed into the hydrocyclone via the tangential inlet, generating a strong swirling motion that enabled centrifugal separation of particles by size and density. Two outlets, corresponding to the overflow and underflow, allowed the collection of the separated fractions for downstream analysis.

For experiments involved the cell separation, in order to prevent structural deformation of clusters, a syringe pump (Model PHD Ultra 70-3007, Harvard Apparatus USA) was used to deliver the sample at a precisely controlled volumetric flow rate. The cell suspension was also stirred continuously using a magnetic stirrer to prevent settling and ensure uniformity of cell distribution in the inlet.

The same micro-hydrocyclone design was used for both types of experiments (particle separation and cell separation) to allow direct performance comparison. Following separation, the underflow and overflow samples were collected in separate sterile petri dishes. These samples were subsequently analyzed using microscopy-based image processing routines to quantify particle or cell cluster concentration, enabling calculation of separation efficiency and breakup of the cell clusters to smaller clusters or single cells.

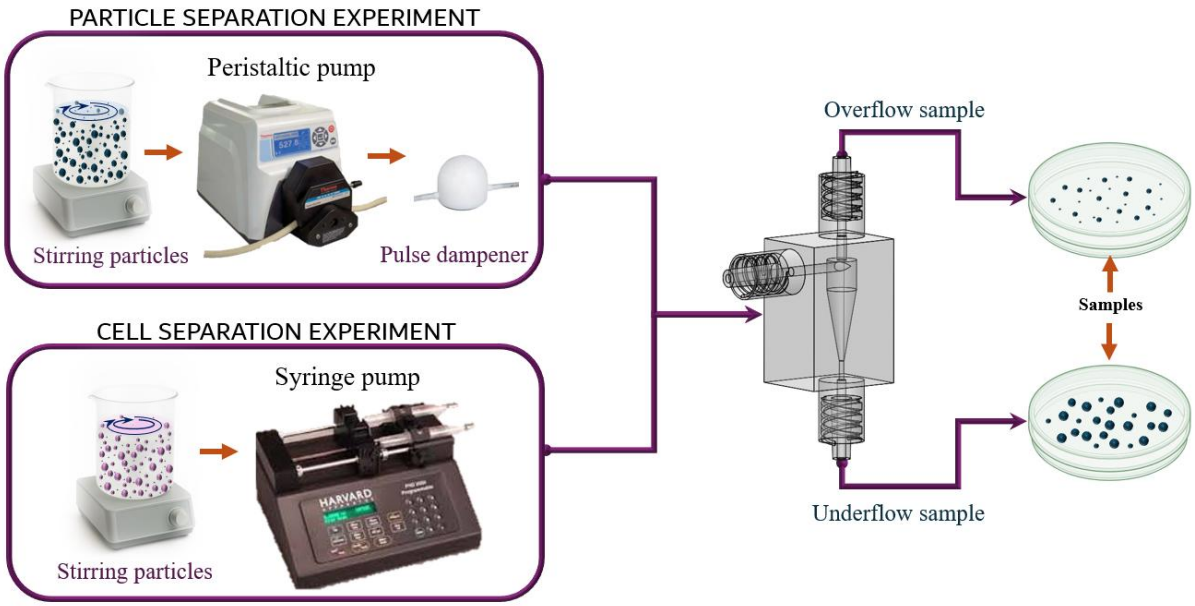

Figure 7-1 Schematic of the experimental setup used for evaluating separation performance of the micro-hydrocyclone.

To enable high-throughput and spatially consistent imaging of 45 collected samples, petri dishes containing overflow and underflow fractions were placed under a microscope equipped with a motorized traverse system. The traverse was programmed to move the sample in discrete steps, allowing the microscope to scan the entire area of interest across multiple fields of view. This approach ensured thorough coverage and minimized sampling bias across different regions of the dish.

To ensure the accuracy of size-based particle and cell detection across the field of view, a pixel-to-physical calibration was first conducted using a micro-scale circular calibration target. As shown in Figure 7-2(a), the diameters of multiple circles on a microfluidic target across the field of view were detected and quantified. Considering that the circles are of identical true size on the target, the consistency of measured diameters serves as an indicator of optical fidelity and uniform resolution. The observed diameter variations remained below a single pixel, confirming that the

optical system introduces negligible distortion, blur, or scaling error across the frame. This uniformity validates the reliability of subsequent image-based measurements, ensuring that particle sizing remains consistent regardless of position within the field.

In addition to optical calibration, the motion of the camera-traverse system was evaluated to ensure precise spatial mapping of the sample surface. Step-wise motion was performed in both horizontal and vertical directions, capturing images before and after each step. As shown in Figure 7-2(b) and (c), circle centers were detected in each frame, and the two images were overlaid to compute the pixel-wise displacement. This comparison enabled quantification of actual movement per step, providing a basis for calibrating the motion-to-image registration. The deviations in center positions between steps were consistently below one pixel, highlighting the high precision of the motion control system and confirming that the imaging covered the sample surface with sub-pixel accuracy and minimal overlap error. These results form the basis for constructing reliable maps of the entire sample during automated scanning and analysis.

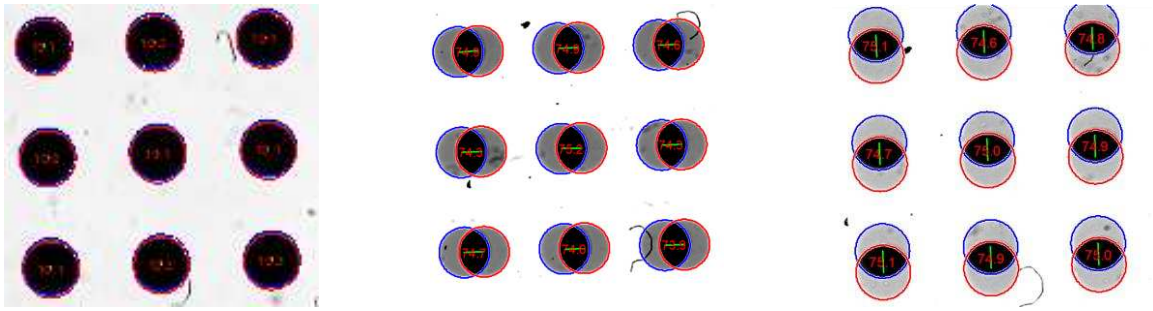

(a) (b) (c)

Figure 7-2 Detected circles before and after motion (a) pixel-to-physical scaling using a micro scale calibration target. (b) right to left, up and down (c) motion step size calibration.

7.3 Image segmentation and binarization method

Quantitative evaluation of separation efficiency in micro-hydrocyclone systems requires accurate measurement of particle or cell counts in the overflow and underflow samples. In this study, about 10,000 microscopy images were captured from multiple sampling events at each outlet to ensure statistical relevance. Given the high number of frames acquired per condition, a reliable and automated image analysis approach was necessary to ensure consistency and reproducibility across all datasets. The initial stage of image analysis involved the segmentation of particles or cell clusters from the background in grayscale microscopy images. The accuracy of segmentation directly affected all subsequent measurements, including particle count, size distribution, and recovery calculation. Inadequate segmentation, arising from poor contrast, background variability, or noise, could compromise the reliability of performance metrics, particularly in size-selective separation experiments.

Threshold-based binarization is a standard technique for differentiating foreground objects from the background in grayscale images [5]. However, global thresholding methods often underperform when applied to images, exhibiting non-uniform illumination and subtle contrast variations [4]. To overcome these limitations, adaptive binarization methods were employed, enabling localized threshold adjustment and improved object detection under diverse imaging conditions. Figure 7-3 presents a comparison of binarization techniques used for segmenting particles and cell clusters in microscopy images obtained from the separation experiments. The raw grayscale images shown in Figure 7-3 (a) exhibit non-uniform background intensity and low-contrast features, which complicate threshold-based segmentation. Figure 7-3 (b) shows different global binarization methods fail to consistently isolate relevant objects. High thresholds eliminate

dimmer features (left image), while low thresholds result in background noise being misclassified as foreground (right image).

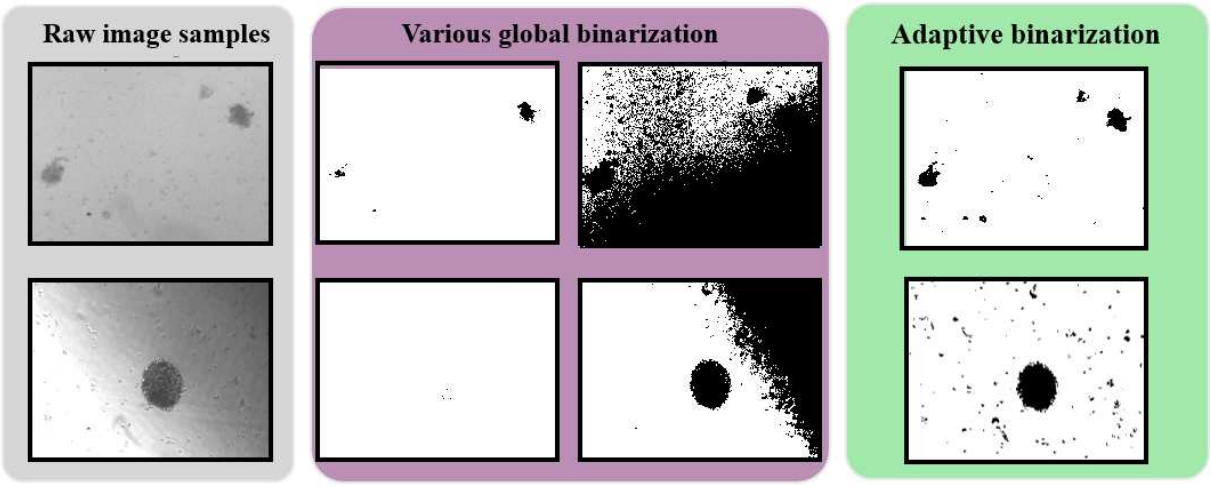

(a) (b) (c)

Figure 7-3 Comparison of binarization methods for segmenting particles and cell clusters in microscopy images: (a) raw grayscale images from underflow and overflow samples, (b) results of global thresholding, with both high and low thresholds showing inconsistent segmentation due to background variations and uneven illumination, (c) adaptive binarization, yielding improved object detection through locally adjusted thresholding.

The green panel in Figure 7-3 (c) displays the outcome of adaptive binarization, which applies a locally varying threshold across the image. This approach improves segmentation by accounting for spatial intensity variations, resulting in sharper object boundaries and more accurate discrimination of particles from the background. Consequently, adaptive binarization was selected for all image processing steps in the efficiency analysis to ensure robust detection and reliable quantification.

To ensure the particle detection approach reliably, Figure 7-4 summarizes the frame-by-frame analysis of particle size and count in both the overflow (a, b) and underflow (c, d) sample sets. In Figure 7-4 (a) and (c), the red curves represent the average particle detected in each individual

frame, while the black line shows the cumulative average diameter calculated across all frames processed up to that point. This cumulative curve smooths out local fluctuations caused by transient variations in particle size distribution.

The frame-by-frame average reflects instantaneous changes in particle size within a small sample volume, which may be sensitive to spatial or temporal inhomogeneities in the flow. In contrast, the cumulative average progressively incorporates a larger number of detected particles, providing a more robust and statistically stable estimate of the overall size distribution. This comparison is critical for assessing temporal convergence and ensuring that a sufficient number of frames has been processed to yield a representative average, free from local anomalies.

Figure 7-4 (b) and (d) show the corresponding number of detected particles per frame, providing insight into sample concentration and the consistency of particle detection throughout the image sequence. Figure 7-4 (a, b) correspond to the overflow, which generally contains smaller particles and a higher abundance per frame, while the Figure 7-4 (c, d) represent the underflow, characterized by a relatively larger average particle size and lower particle count. The frame-wise fluctuations observed in both diameter and count reflect inherent variations in particle distribution and image quality. Together, these plots help confirm the statistical reliability of the measurement and validate that the detected sample is large enough for performance evaluation.

Figure 7-4 (e) and (f) display representative segmentation results from different frames, illustrating the effectiveness of the detection method across a range of sample conditions. These examples include particles of varying sizes, from large isolated objects to smaller particles in close proximity or near overlap. Representative segmentation results confirm that the detection approach reliably resolves particles across a wide range of sizes and spatial configurations, including closely spaced or partially overlapping objects. These findings validate the robustness of the image

analysis pipeline and support its application for automated, high-throughput quantification of separation efficiency.

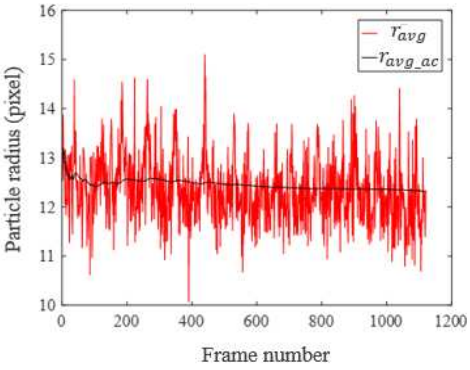

(a)

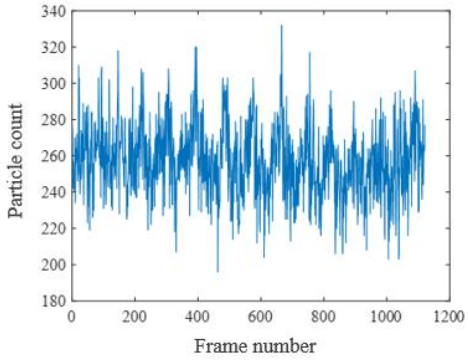

(b)

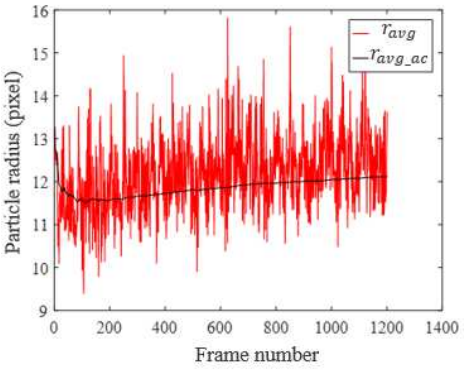

(c)

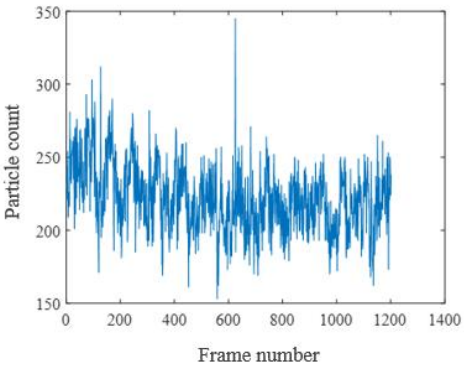

(d)

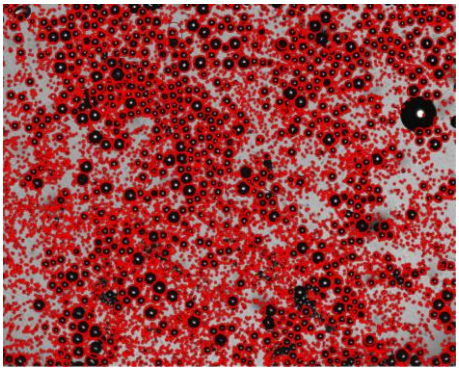

(e)

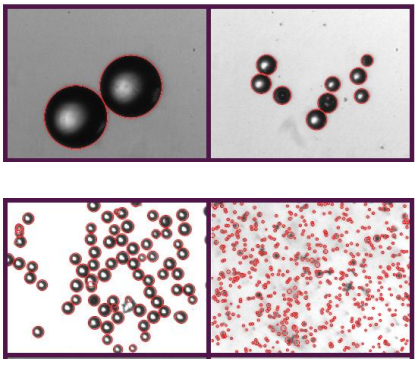

(f)

Figure 7-4 (a) Average of detected particle radius per frame and (b) particle count per frame for overflow samples. (c) Average of detected particle radius per frame and (d) particle count per

frame for underflow samples. Red curves represent the average particle diameter detected in each individual frame, and the black line shows the cumulative average diameter across all frames processed up to that point. (e) particle detection precision in a super dense sample with overlapping particles as a worse case scenario, (f) Particle detection across different sample size and densities and background noises circled in red,

7.4 Results and Discussion

7.4.1. Particle separation performance

With particles reliably detected through automated image analysis, the separation performance of the microhydrocyclone can be quantitatively assessed. Here, we compare the performance of the standard and modified designs across a range of operating conditions, evaluating their ability to separate both synthetic particles and circulating tumor cell (CTC) clusters. The analysis focuses on key performance metrics including grade efficiency, and size selectivity while examining how device geometry and flow conditions influence separation outcomes. This combined evaluation provides insight into the trade-offs between maximizing efficiency and preserving the integrity of fragile biological targets.

Grade efficiency is an important factor in microhydrocyclone performance evaluation and is defined as the ratio of particles of a specific size in the underflow to those in the feed. Figure 7-5 compares the grade efficiency, ε_G, of the basic and the modified hydrocyclone device for rigid particles across a range of inlet Reynolds numbers: $Re = 150, 300, 450$, and 600 where $Re = \rho V d_i / \mu$ and ρ is the fluid density, V is the characteristic velocity, d_i is the hydraulic inlet diameter of the micro-hydrocyclone and μ is the dynamic viscosity of the fluid. In each plot, ε_G is shown as a function of particle diameter d_p, representing the fraction of particles of a given size recovered

in the underflow. Figure 7-5 (a) displays results for the basic configuration, where Figure 7-5 (b) presents the modified design. The diagrams on the right-hand side of each plot illustrate the 3D geometry of the corresponding device.

The basic hydrocyclone in Figure 7-5 (a) demonstrates a progressive improvement in grade efficiency with increasing Reynolds number. At $Re = 150$, the curve rises gradually and remains below 0.7. Insufficient driving forces fail to direct an adequate fraction of particles (particularly the finer ones) towards the underflow, resulting in substantial escape to the overflow and limiting separation grade efficiency to below 70%. At $Re = 600$, efficiency exceeds 0.9 for particles larger than 150 μm. This indicates that higher flow rates significantly enhance the separation of larger particles.

In contrast, the modified device shown in Figure 7-5 (b) performs best at the lowest Reynolds number, with $Re = 150$ achieving nearly complete recovery for large particles. As the Reynolds number of the system increases, however, the efficiency of the modified device decreases slightly or remains flat, particularly at or beyond $Re = 450$. This trend suggests that the modified geometry provides superior control at low flow rates but may become less effective under higher Reynolds number conditions.

These results highlight a fundamental distinction in how each geometry responds to varying flow conditions. The basic design benefits from increased Reynolds number, improving its ability to direct larger particles to the underflow. The modified design, however, appears optimized for low-Reynolds operation, these findings underscore the need to tailor hydrocyclone designs not only to specific particle properties but also to the intended operational Reynolds number.

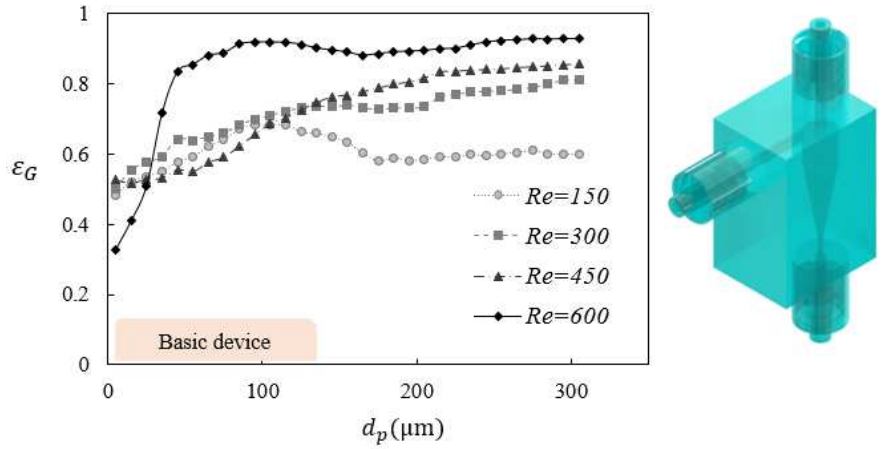

(a)

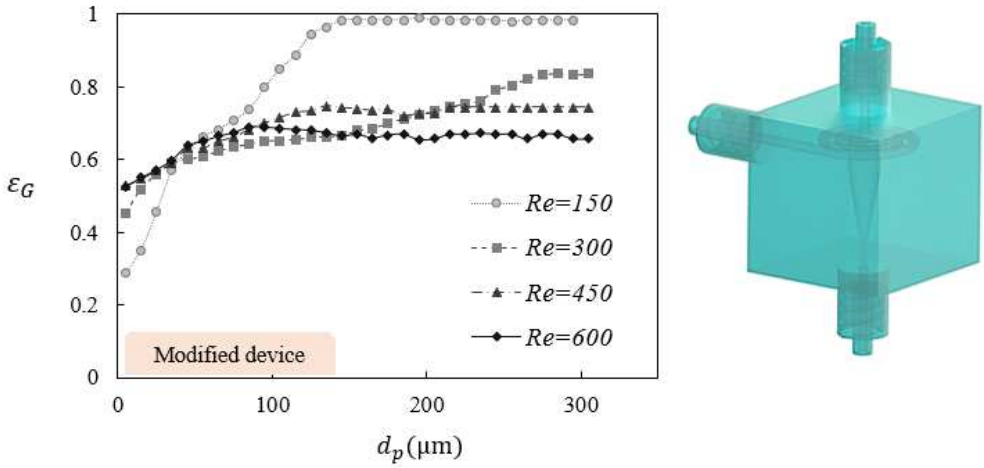

(b)

Figure 7-5 Grade efficiency curves for rigid particles in (a) basic and (b) modified hydrocyclone designs at four Reynolds numbers, showing size-dependent recovery to the underflow. 3D schematics of each device are shown alongside their respective plots.

Figure 7-6 presents a comparative analysis of the grade efficiency, ε_G, for rigid particles processed through basic and modified hydrocyclone devices across four Reynolds numbers: 150, 300, 450, and 600. Each plot corresponds to one Reynolds number and shows the variation of ε_G with particle diameter d_p, enabling size-resolved assessment of underflow recovery. The plots

offer insight into how the flow regime and internal geometry influence particle separation performance, particularly in terms of separation sharpness and maximum achievable recovery.

At $Re = 150$ (Figure 7-6 a), the modified hydrocyclone exhibits substantially better separation performance than the basic design. The grade efficiency increases steeply with particle size and reaches near-complete recovery ($\varepsilon_G \approx 1$) for particles above ~150 µm. In contrast, the basic device shows a more gradual slope and a lower limit, indicating reduced selectivity and lower maximum recovery. However, as the flow rate increases to $Re = 300$ (Figure 7-6 b), the performance gap narrows. Both devices achieve comparable efficiencies across the size range, with the basic hydrocyclone slightly outperforming the modified one for particles above ~200 µm.

At $Re = 450$ and 600 (Figure 7-6 c and d), the basic hydrocyclone clearly outperforms the modified configuration. Grade efficiency in the basic device continues to improve with Reynolds number, achieving ε_G values above 0.9 for particles larger than ~200 µm. In contrast, the modified hydrocyclone shows limited improvement with increasing the flow rate and reaches a limit around $\varepsilon_G \approx$ 0.7. Conversely, the basic geometry becomes more effective as inertial forces dominate, enhancing particle segregation. This comparative trend reinforces the importance of matching hydrocyclone design to both the physical properties of the particles and the intended flow regime to achieve optimal separation efficiency.

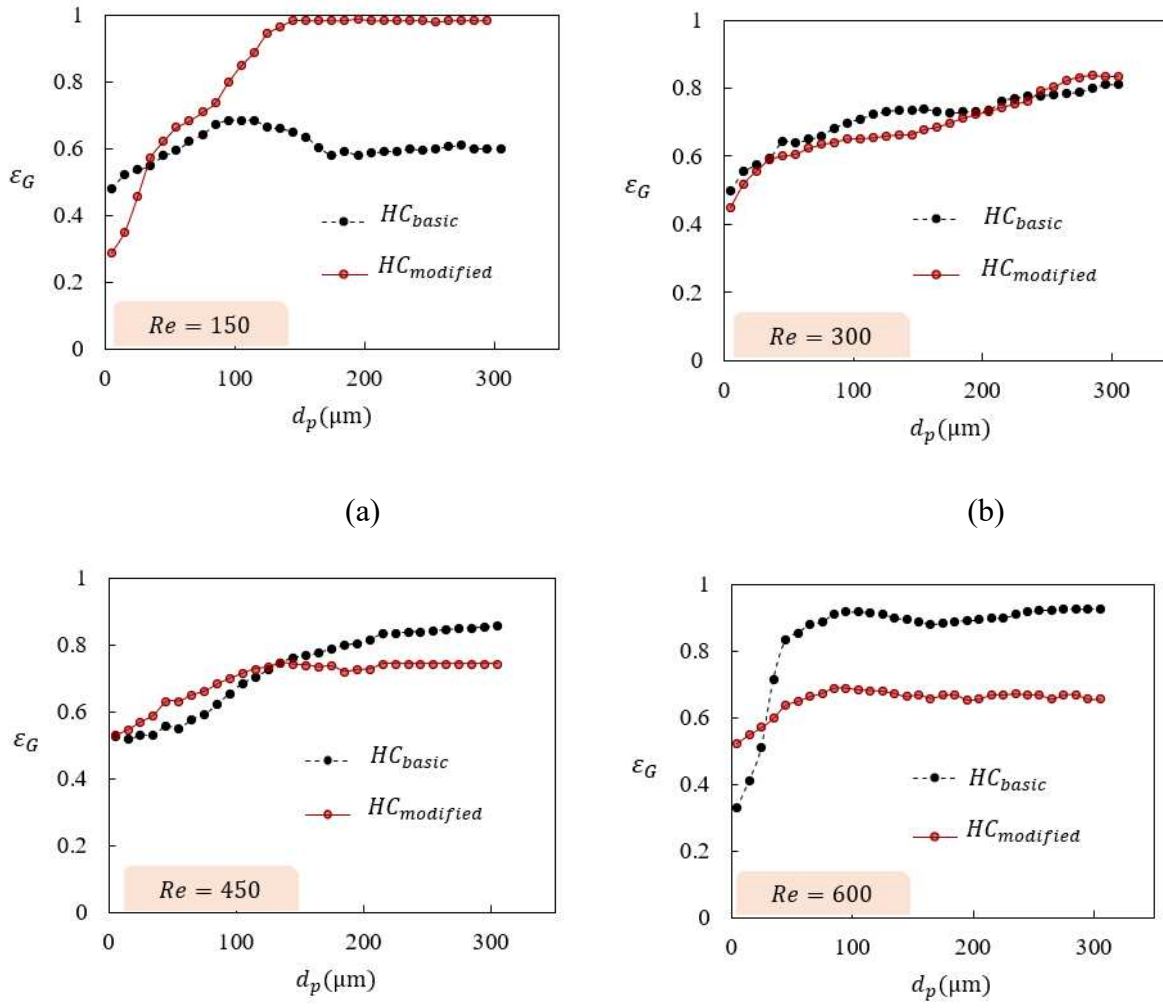

Figure 7-6 Grade efficiency curves for rigid particles in basic and modified hydrocyclone designs at four Reynolds numbers (a) 150, (b) 300, (c) 450, (d) 600, showing the effect of flow rate on size-dependent recovery performance.

7.4.1. CTC separation performance

To emphasize the biological relevance of separation performance, we extended the evaluation beyond synthetic rigid particles to include biologically derived targets. Malignant glioma (U-87 MG) cells were cultured into spheroid structures and chemically fixed with 5% formalin and used as model circulating tumor cell (CTC) clusters. Such clusters represent clinically important entities

in cancer biology, as their detection and analysis are central to understanding metastatic potential and guiding therapeutic decision-making. Unlike rigid particles, CTC clusters exhibit deformability, heterogeneous morphology, and potential for fragmentation, all of which influence their hydrodynamic response. Assessing how these biological features interact with device design and flow conditions provides critical insight into the feasibility of using micro-hydrocyclones for biomedical applications, where both separation efficiency and preservation of cluster integrity are paramount.

Comparing grade efficiency curves at equivalent Reynolds numbers for both particle types enables isolation of the influence of mechanical properties on separation dynamics. This comparison also allows for an investigation in terms of the breakage rate of the cluster in the separation process. This rate is an important metric in biobased applications as any change in the size of separated clusters would cause a misleading diagnosis or conclusion.

Figure 7-7 presents grade efficiency, ε_G, curves for CTC clusters processed through two hydrocyclone designs, a basic configuration (a) and a modified design (b) under three flow conditions corresponding to Reynolds numbers of 150, 300, and 600. The recovery of clusters to the underflow is plotted against the equivalent diameter of clusters, d_p, providing a size-resolved evaluation of separation performance. The figure includes 3D schematics of each device to illustrate the respective geometries. This dataset complements earlier experiments conducted with rigid particles, allowing for direct comparison of how particle deformability and flow regime influence separation behavior in microfluidic hydrocyclone.

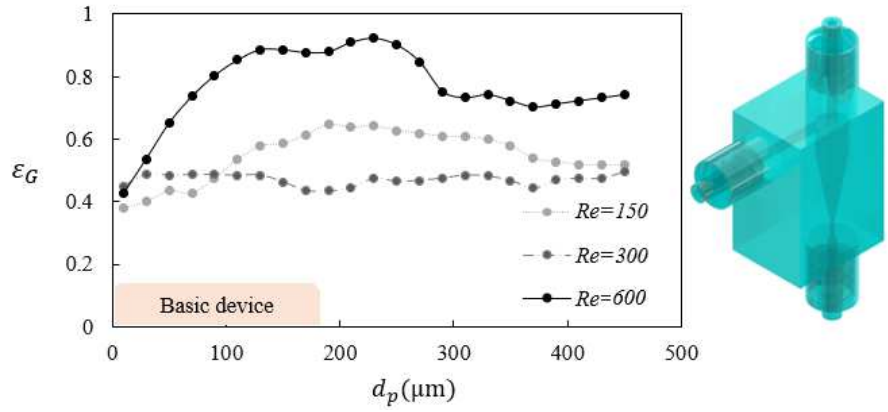

(a)

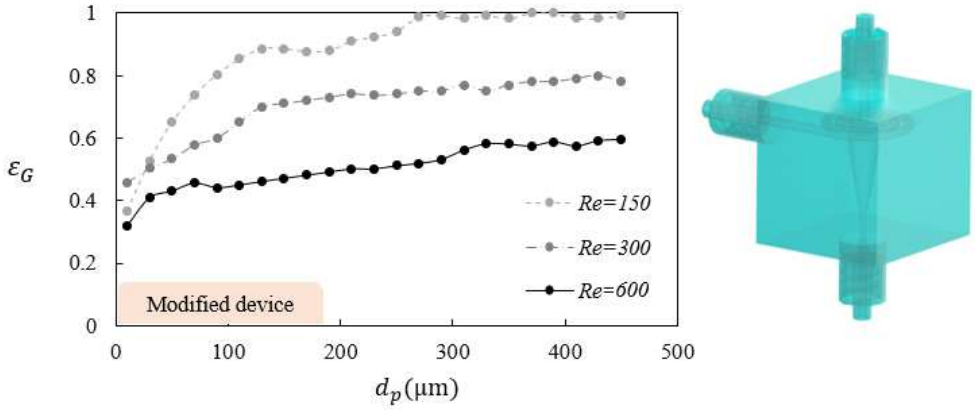

(b)

Figure 7-7 Grade efficiency curves for circulating tumor cell clusters in basic (a) and modified (b) micro-hydrocyclone designs at three Reynolds numbers, highlighting size-dependent recovery performance. Device geometries are shown alongside each plot for reference.

Compared to rigid particles, CTC clusters pose a greater separation challenge. Their deformability, potential for partial breakup, and variability in morphology likely reduce the effectiveness of the inertial and centrifugal separation mechanisms, particularly at higher Reynolds numbers where flow instabilities amplify mechanical stress and may exacerbate cluster disruption. Notably, the modified hydrocyclone, which achieved near-complete recovery of rigid particles at $Re = 150$, performs similarly for CTC clusters only under that same condition, reinforcing its

suitability for gentle, size-selective separation. The basic design, although less effective at low Re, exhibits more robust behavior at higher flow rates for both particle types.

Figure 7-8 presents grade efficiency curves for the CTC clusters processed through basic and modified hydrocyclone configurations. Grade efficiency, ε_G, is plotted as a function of cluster equivalent diameter, d_p, capturing the proportion of clusters of each size directed to the underflow. The analysis is performed at three different Reynolds numbers, Re = 150, 300 and 600, to evaluate the effect of flow rate on separation performance. CTC cluster diameters span from below 50 μm to approximately 500 μm, encompassing the full range of cluster sizes encountered within the experimental system. The figure allows for a direct comparison of the two geometries under equivalent flow conditions, enabling assessment of their effectiveness in size-based separation across operational regimes.

At Re = 150, the modified hydrocyclone in Figure 7-8(a) demonstrates a significantly higher grade efficiency across the entire particle size range. The ε_G for modified hydrocyclone increases steeply with particle size and reaches values near unity for clusters above ~250 μm, indicating highly effective capture of large aggregates. In contrast, the basic hydrocyclone exhibits only moderate efficiency with a flatter response, plateauing around 0.6. A similar trend is observed in Figure 7-8(b) at Re = 300, where the modified hydrocyclone consistently outperforms the basic hydrocyclone, though the difference in efficiency becomes somewhat narrower. For both devices, the increase in Reynolds number improves separation for smaller clusters. The modified design continues to show sharper size discrimination, suggesting better performance in separating biologically relevant cluster sizes under moderate flow conditions.

At Re = 600, the performance trend is reversed as shown in Figure 7-8(c). The basic micro-hydrocyclone achieves higher grade efficiencies than the modified design, particularly for particles after 200– µm, where ε_G exceeds 0.9. The modified hydrocyclone configuration, however, exhibits a flattened efficiency curve with no significant improvement across the size range and a maximum ε_G below 0.5. The basic design appears more robust under high-Reynolds number conditions. These results emphasize that hydrocyclone geometry must be matched to the operating regime to maintain effective and selective separation of fragile, deformable biological clusters such as CTC aggregates.

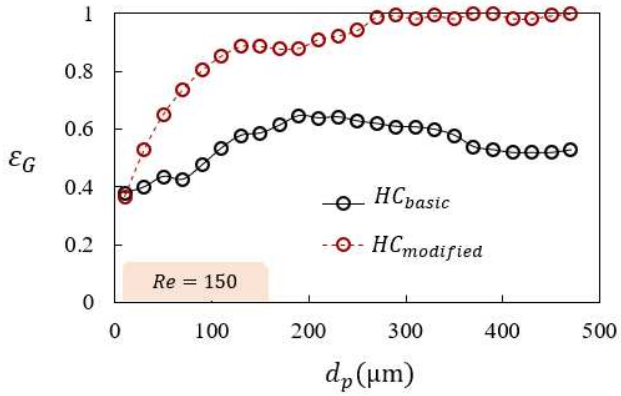

(a)

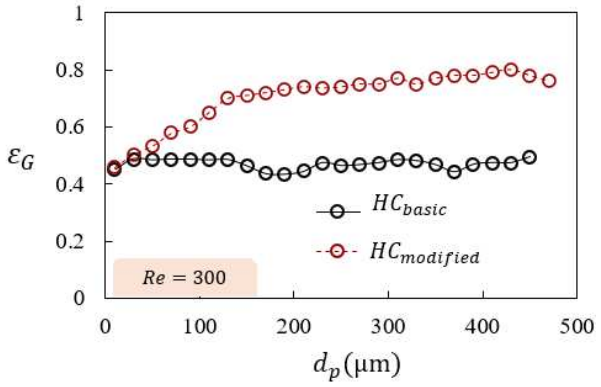

(b)

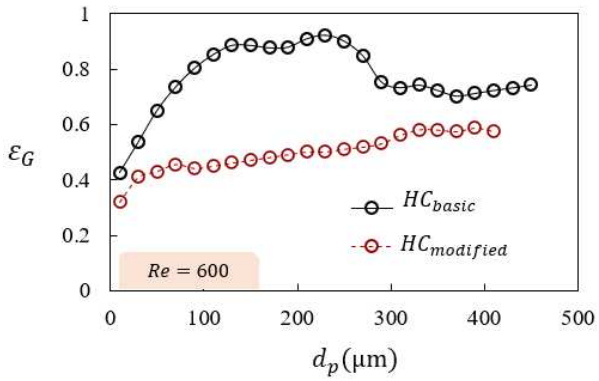

(c)

Figure 7-8 Grade efficiency curves of basic and modified hydrocyclone designs for circulating tumor cell clusters at three Reynolds numbers ($Re = 150, 300, 600$), showing separation performance as a function of particle diameter.

In contrast to rigid particle results, both devices exhibit overall lower grade efficiencies for CTC clusters across all Reynolds numbers which might be related to the density differences between actual cell clusters and particles which emphasizes the important of cell performance validations. The modified device shows a steady increase in ε_G with particle size and achieves the highest performance at $Re = 150$, where recovery exceeds 90% for clusters larger than 200 μm. As Reynolds number increases, efficiency decreases, particularly at $Re = 600$, where ε_G remains below 0.7 across the full-size range. The basic device exhibits a different trend: performance improves with Reynolds number, reaching a peak around 0.85 at $Re = 600$ for intermediate-sized clusters (~200 μm), though the curve flattens and drops for both smaller and larger diameters. These observations suggest that while the modified geometry performs optimally at low flow rates, the basic design becomes more effective under higher inertial conditions, even for deformable biological clusters.

7.4.1. Evaluating the Integrity of Separated Clusters

Separation technologies that rely on high shear or strong inertial forces risk inducing cluster fragmentation, potentially biasing downstream analyses. To assess whether the modified micro-hydrocyclone geometry mitigates this risk, we examined size distributions of CTC clusters in the separated fractions and compared them with input distributions. These measurements provide insight into the relationship between flow structure and cluster breakage, offering a direct evaluation of the device's suitability for bioseparation.

The plots in Figure 7-9 present the normalized particle size distribution, expressed as a percentage of total count, for CTC clusters at the inlet and outlet of both the basic (left column) and modified (right column) micro-hydrocyclone designs, evaluated at Reynolds numbers of 150, 300, and 600. The *x*-axis represents particle diameter, d_{p}, while the *y*-axis indicates the percentage of clusters abundance in each size bin relative to the entire sample. Insets are included in each plot to magnify the low-frequency population of larger clusters, providing a clearer view of their size distribution. Across all flow conditions, in the basic device the inlet distributions contain a broad range of cluster sizes, with a noticeable presence of large clusters (>100 μm), particularly at $Re = 600$. These large clusters are critical to separate intact for diagnostic and prognostic applications. In the modified device however, the inlet and outlet distributions remain largely similar at lower Reynolds number corresponding to the device highest performance operating window.

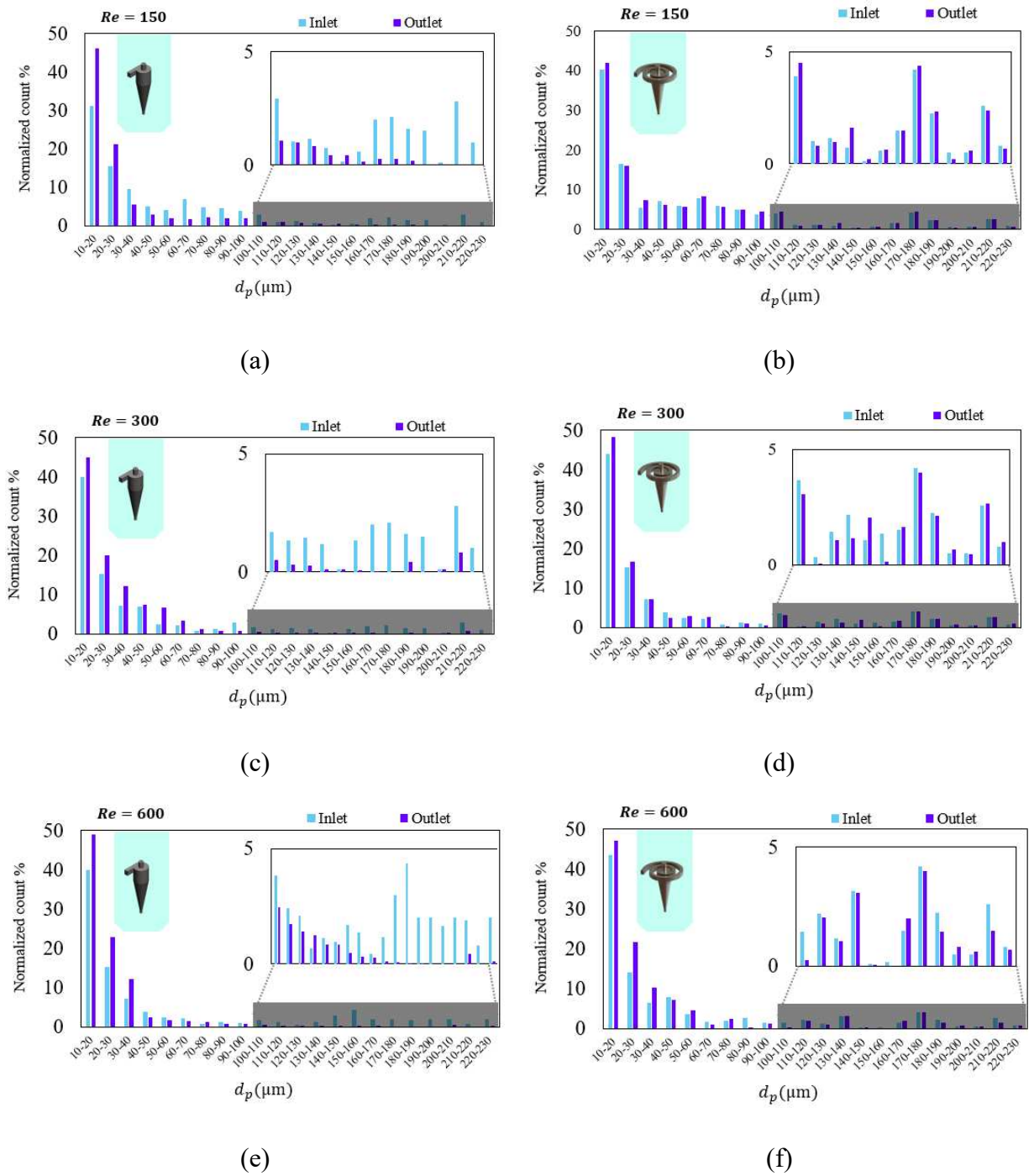

Figure 7-9 Normalized count percentage of circulating tumor cell clusters at the inlet and outlet of basic (left column) and modified (right column) hydrocyclone designs at three Reynolds numbers 150, 300, and 600. Insets highlight the presence and preservation of larger clusters.

A key observation is the pronounced difference in outlet distributions between the two device designs. In the basic hydrocyclone in Figure 7-9 (a, c, e), the outlet samples exhibit a clear

depletion of large clusters and a corresponding increase in smaller fragments. This indicates that exposure to the flow structures within the device induces cluster fragmentation, breaking larger cell aggregates into smaller constituents. This fragmentation compromises the reliability of downstream analyses aimed at identifying or quantifying CTC clusters. In contrast, the modified device plots in Figure 7-9 (b, d, f) maintains the integrity of the original size distribution, including the presence of large clusters at the outlet across all tested Reynolds numbers. This preservation of cluster size strongly suggests that the modified geometry reduces the flow structure responsible for cell breakage. Addressing this issue in the basic design is essential, as the therapeutic and diagnostic utility of CTC cluster detection relies on their physical integrity at the point of collection.

The results demonstrate, for the first time, that microhydrocyclone geometry can be engineered to preserve the structural integrity of circulating tumor cell (CTC) clusters during inertial separation. While conventional high-shear designs caused significant fragmentation, depleting large clusters and producing smaller fragments that could bias diagnostic and prognostic analyses, the modified configuration maintained the original cluster size distribution across all tested flow conditions. By demonstrating that shear-sensitive biological targets can be effectively separated without compromising their structural integrity, this work highlights the potential of tailored micro-hydrodynamic design for size-selective bioseparation, offering a novel approach for translational cancer diagnostics and cell-based research.

7.5 Conclusion

This study provides a comprehensive evaluation of basic and modified micro-hydrocyclone geometries across a range of Reynolds numbers to assess their suitability for particle and cell cluster separation. For rigid particles, the basic device demonstrated increasing grade efficiency with higher Reynolds numbers, achieving recovery rates exceeding 90% for particles larger than 200 μm at $Re = 600$. The modified hydrocyclone, in contrast, exhibited optimal performance at low Reynolds numbers, particularly $Re = 150$, where it effectively recovered large particles with sharp separation profiles. These findings suggest that the basic design is more responsive to inertial enhancement of separation, while the modified configuration offers better control in low-flow, laminar regimes.

When tested with biologically relevant CTC clusters, however, the performance dynamics shifted significantly. While the basic hydrocyclone maintained high grade efficiency values at elevated Reynolds numbers, a detailed comparison of inlet and outlet particle size distributions revealed a critical limitation: substantial fragmentation of large clusters occurred within the basic device at $Re = 300$ and above. This mechanical disruption compromises the diagnostic reliability of CTC separation by altering the native size distribution and potentially eliminating clinically significant aggregates. In contrast, the modified hydrocyclone consistently preserved cluster integrity across all flow conditions, maintaining large cluster populations even at moderate Reynolds numbers.

These results underscore the importance of evaluating not only separation efficiency but also the physical integrity of biological targets during processing. Although the basic hydrocyclone may appear favorable based on traditional performance metrics at high flow rates, its inability to

preserve fragile clusters renders it unsuitable for CTC separation or similar biomedical applications. The modified device, despite lower efficiency at higher *Re*, provides a more biologically appropriate platform by minimizing mechanical stress and enabling gentle, size-selective recovery. Therefore, for applications requiring the preservation of structurally sensitive materials such as CTC aggregates, the modified micro-hydrocyclone operated at low Reynolds numbers offers a more effective and reliable solution.

Moreover, this study establishes a direct link between micro-hydrodynamic design and the preservation of biologically relevant structures during cell separation. By demonstrating that a modified microhydrocyclone can maintain circulating tumor cell (CTC) clusters intact across a range of flow conditions, the work addresses a critical limitation of conventional inertial separation systems that often compromise sample integrity. Preserving cluster size is essential not only for accurate enumeration and morphological characterization but also for maintaining clinically relevant features associated with metastatic potential and therapeutic response. This approach provides a new pathway for integrating high-throughput, label-free separation into diagnostic and research workflows without sacrificing the fidelity of fragile biological targets. This capability provides a novel avenue for translational cancer diagnostics and cell-based research, where preserving the structural and functional integrity of fragile biological targets is paramount.

References

[1] R. Sabbagh and David. S. Nobes, *Centrifugal separation*. Kirk-Othmer Encyclopedia of Chemical Technology, 2018. doi: 10.1201/9780203752494-9.

[2] R. Sabbagh, M. G. Lipsett, C. R. Koch, and D. S. Nobes, "An experimental investigation on hydrocyclone underflow pumping," *Powder Technol*, vol. 305, pp. 99–108, Jan. 2017, doi: 10.1016/j.powtec.2016.09.045.

[3] M. S. Syed, C. Marquis, R. Taylor, and M. E. Warkiani, "A two-step microengineered system for high-density cell retention from bioreactors," *Sep Purif Technol*, vol. 254, no. August 2020, p. 117610, 2021, doi: 10.1016/j.seppur.2020.117610.

[4] M. S. Syed, F. Mirakhorli, C. Marquis, R. A. Taylor, and M. E. Warkiani, "Particle movement and fluid behavior visualization using an optically transparent 3D-printed micro-hydrocyclone," *Biomicrofluidics*, vol. 14, no. 6, 2020, doi: 10.1063/5.0025391.

[5] Y. Liu *et al.*, "Mini-hydrocyclone performance enhancement in removing small-size microplastics using flocculants," *Journal of Water Process Engineering*, vol. 53, no. April, 2023, doi: 10.1016/j.jwpe.2023.103755.

[6] Z. Zhao *et al.*, "Hydrocyclone separation performance influenced by feeding solid concentration and correcting separation size", doi: 10.1007/s00231-020-02940-8/Published.

[7] Z. Wu, M. Zhao, Z. Liu, L. Shi, T. Li, and T. Zhou, "Microalgae separation using spiral inertial microchannel," *Microfluid Nanofluidics*, vol. 27, no. 3, pp. 1–13, 2023, doi: 10.1007/s10404-023-02630-x.

[8] A. Nikdoost and P. Rezai, "Dean flow velocity of viscoelastic fluids in curved microchannels," *AIP Adv*, vol. 10, no. 8, 2020, doi: 10.1063/5.0019021.

[9] D. Di Carlo, "Inertial microfluidics," *Lab Chip*, vol. 9, no. 21, pp. 3038–3046, 2009, doi: 10.1039/b912547g.

[10] A. A. S. Bhagat, S. S. Kuntaegowdanahalli, and I. Papautsky, "Continuous particle separation in spiral microchannels using dean flows and differential migration," *Lab Chip*, vol. 8, no. 11, pp. 1906–1914, 2008, doi: 10.1039/b807107a.

[11] X. Wei *et al.*, "A Spiral-Helix (3D) Tubing Array That Ensures Ultrahigh-Throughput Single-Cell Sampling," *Anal Chem*, vol. 91, no. 24, pp. 15826–15832, 2019, doi: 10.1021/acs.analchem.9b04122.

[12] A. A. S. Bhagat, H. Bow, H. W. Hou, S. J. Tan, J. Han, and C. T. Lim, "Microfluidics for cell separation," *Med Biol Eng Comput*, vol. 48, no. 10, pp. 999–1014, 2010, doi: 10.1007/s11517-010-0611-4.

[13] Y. Fan, J. Wang, Z. Bai, J. Wang, and H. Wang, "Experimental investigation of various inlet section angles in mini-hydrocyclones using particle imaging velocimetry," *Sep Purif Technol*, vol. 149, pp. 156–164, 2015, doi: 10.1016/j.seppur.2015.04.047.

[14] L. He *et al.*, “Experimental and numerical analysis of Chinese hamster ovary cell viability loss in mini-hydrocyclones,” *Sep Purif Technol*, vol. 295, no. February, 2022, doi: 10.1016/j.seppur.2022.121203.

Chapter 8: Conclusion and future work

The goal of this research is to experimentally investigate and modify micro-hydrocyclone flow structures to enable high-throughput, biologically compatible separation, with particular focus on inlet geometry modifications that induce Dean vortices for improved performance in biomedical applications.

Although micro-hydrocyclones offer a promising solution for high-throughput particles and cell separation, their internal flow physics and performance behavior at microscale remain poorly characterized in the literature, especially under biologically relevant flow conditions. To address this gap, the study was structured to systematically analyze and quantify (1) the formation and role of Dean vortices in curved microchannels, (2) the impact of inlet geometry on flow organization in micro-hydrocyclones, and (3) the implications of these flow structures on separation performance for both synthetic particles and biological cell clusters.

A unified and physically consistent definition of the Dean number was proposed and benchmarked against numerous inconsistent formulations in the literature. This definition, rooted in microscale flow regimes, enables more consistent evaluation of vortex thresholds and allows broader design generalization for microfluidic devices with curved geometries.

Experimental evidence of Dean vortex formation in curved channels was obtained using three-dimensional scanning PIV and two-phase flow visualizations. It was confirmed that Dean vortices form under microfluidic conditions and directly influence the deformation and trajectory of suspended droplets. These observations were used to inform the design of a spiral inlet geometry for micro-hydrocyclones.

Planar and stereoscopic particle image velocimetry (PIV) were employed to visualize and quantify the three-component velocity field within the device under single-phase and multiphase flow configurations. Key flow features, such as the Locus of Zero Vertical Velocity (LZVV), were resolved and used to characterize the swirl strength and symmetry of the internal flow. The spiral inlet configuration demonstrated enhanced flow symmetry, more defined vortex cores, and a stable LZVV across the flow domain compared to the conventional design.

The performance of the modified and baseline devices was compared through automated image-based particle analysis. Dedicated software was developed to handle detection, classification, and statistical characterization of particle and cluster sizes. Grade efficiency curves were generated for rigid particles and for biologically relevant circulating tumor cell (CTC) clusters across a range of Reynolds numbers. The modified micro-hydrocyclone consistently exhibited improved recovery of target-sized particles to the underflow, particularly in the intermediate size range.

Importantly, experiments with cell clusters confirmed that the spiral-induced Dean flow improved size-based separation while minimizing fragmentation, demonstrating the potential for gentle yet effective bioseparation. The LZVV remained more stable in the presence of CTCs under Dean-induced conditions, and cell cluster trajectories aligned closely with those of the desired particle populations.

This work provides one of the first comprehensive experimental investigations into the combined effects of Dean flow manipulation and biological multiphase separation within a micro-hydrocyclone. It also introduces an integrated diagnostic framework that combines PIV, fluorescence imaging, and computational post-processing for simultaneous flow and particle analysis. The research results provide a novel avenue for translational cancer diagnostics and

cell-based research, where preserving the structural and functional integrity of fragile biological targets is paramount.

Future work

Building on the findings of this study, several directions are proposed for future investigations:

- **Parametric Optimization of Spiral Inlet Geometry**: Further optimization of the spiral geometry (e.g., number of turns, pitch, and radius) could enhance control over Dean vortex strength. Parametric sweeps supported by CFD or experimental Design of Experiments (DoE) would help quantify the trade-offs between pressure drop, mixing intensity, and separation resolution.
- **Active Flow Control**: While this work focused on passive geometric induction of Dean vortices, active control strategies such as acoustic excitation or pulsed inlet flows could be explored to dynamically manipulate the internal vortex field and target specific particle populations.
- **Bio-applicability Testing with Diverse Cell Types**: Future studies should explore the applicability of this system for other biological targets, such as blood components, stem cells, or microplastic contaminants in environmental samples. Compatibility with a broader range of suspending media and particle properties will enhance device relevance.
- **Parallelization for Throughput Scaling**: The feasibility of multiplexing several micro-hydrocyclones on a single chip should be explored. This would enable high-throughput operation suitable for clinical or industrial workflows, while preserving the enhanced performance characteristics demonstrated in this study.

Overall, this research lays the groundwork for a new class of high-performance, low-shear microfluidic separation systems that exploit tailored flow manipulation via Dean vortex engineering. The methodologies and insights developed here have broad implications for the design of next-generation lab-on-chip systems for biomedical, environmental, and industrial applications.

Appendix 1: Droplet detection image processing scheme

This appendix provides the source codes developed and used throughout the experimental and analytical portions of this thesis. The first set of codes includes a synthetic image generator designed to simulate images containing both cells and PIV seeding particles. These synthetic datasets were used to validate the detection and tracking algorithms presented in Chapter 5. The second set is the image processing scheme for separating cells from PIV particles in experimental images, also discussed in Chapter 5. Finally, the third set of codes focuses on analyzing experimental images of cells and particles in the micro-hydrocyclone to extract key separation parameters such as separation efficiency investigated and presented in Chapter 7.

Detection correction

In order to track the droplet in multiple frames, it is important to account for any changes in the location of the channel itself due the movements regarding the channel reinstallation in the process of conducting the experiment. To achieve this a correlation analysis as shown in equation (1) is performed between each raw image and the background to identify any shifts in the channel position. In equation (1), r is the correlation coefficient that shows the displacement of the origin between the raw and background images. A and B are two matrices representing raw and the background images. $\bar{A}$ and $\bar{B}$ are the mean values of the images A and B, respectively. Subscripts m and n are the pixel location in horizontal and vertical directions, respectively.

$$r = \frac{\sum_m \sum_n (A_{mn} - \bar{A})(B_{mn} - \bar{B})}{\sqrt{(\sum_m \sum_n (A_{mn} - \bar{A})^2)(\sum_m \sum_n (B_{mn} - \bar{B})^2)}} \quad (1)$$

Upon the correlation analysis, the displacement of the origin is obtained that is shown in Figure S1(a) from one frame of each series of raw images and the base background image, (Figure

S1(b)). This displacement is utilized as a correction vector which can be applied to eliminate the error of the droplet location. The flow chart of the applied algorithm for this purpose is represented in Figure S1(c). Essentially, this correlation vector serves as a tool to adjust for any shifts in the channel's position between frames, allowing for a more accurate tracking of the droplet's location within the channel over time.

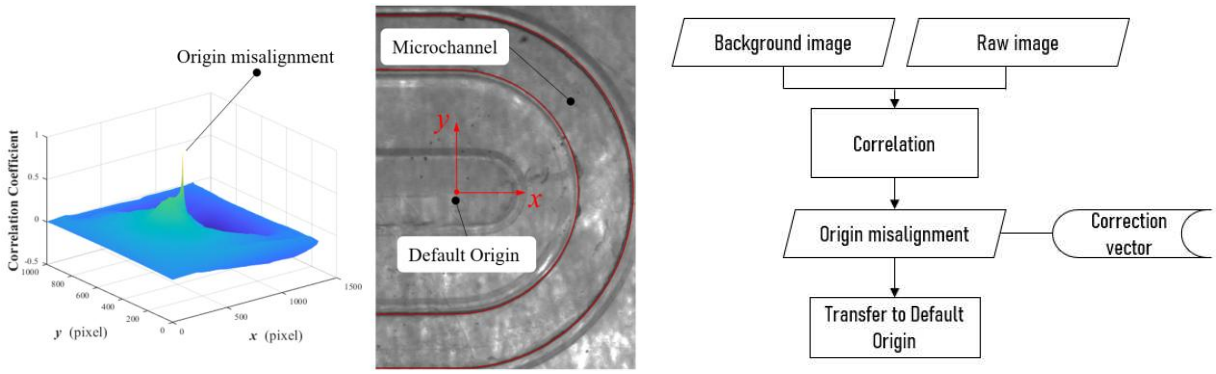

(a) (b) (c)

Figure S1. (a) Detected default origin and a sample correlation correction vector calculation, (b) location of the origin on the default background (c) Channel detection and origin alignment process flowchart.

Droplet detection

Image processing scheme flowchart is shown in Figure S2.

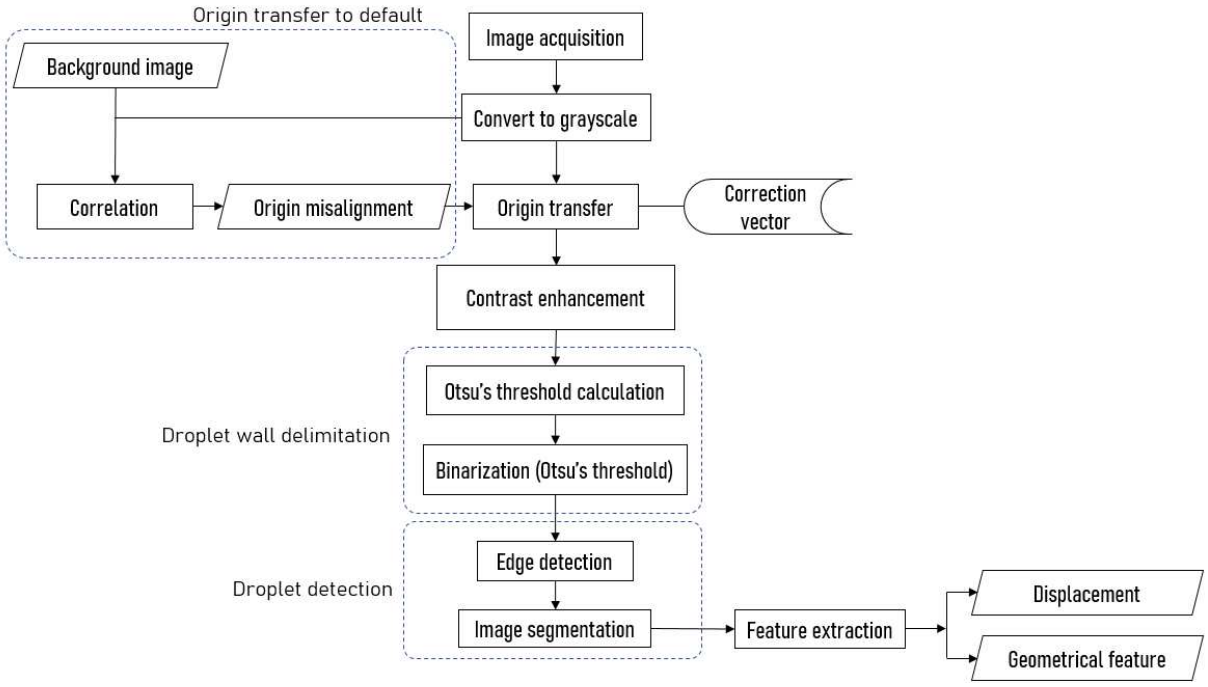

Figure S2. Droplet detection processing flowchart.

Figure S3(a) shows the image intensity histogram and the raw image. Implementing the intensity stretching enhancement results in the intensity histogram shown in Figure S3(b). This technique is used to amplify the dark regions of an image and increase the contrast between the droplet and its surroundings. By enhancing the contrast in the image, it becomes easier to delineate the droplet walls and accurately track its movement within the channel.

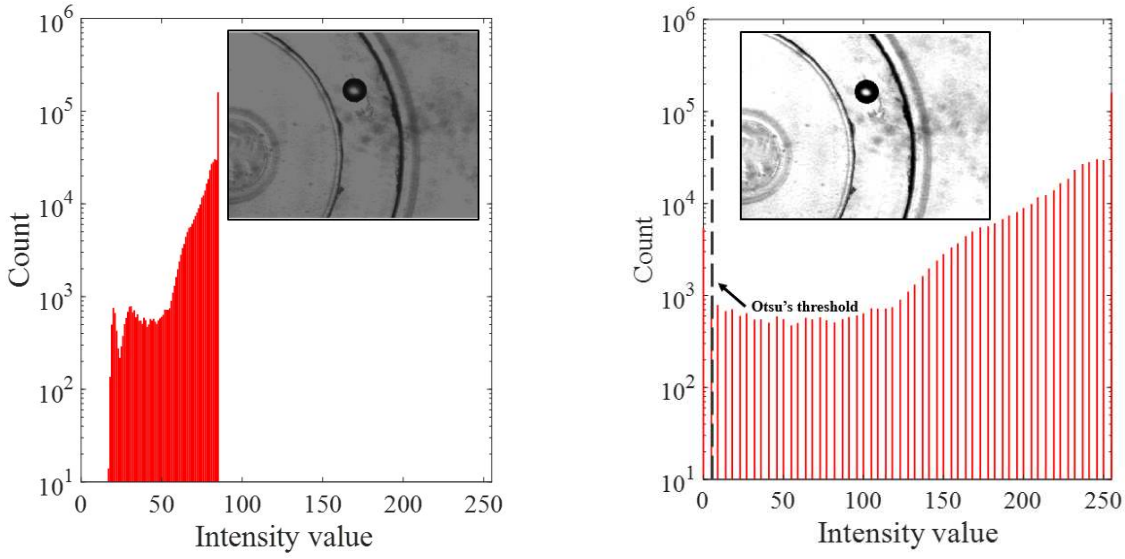

(a) (b)

Figure S3. (a) Raw image intensity histogram, (b) contrast enhanced image and stretched histogram.

Once the image intensity has been enhanced, Otsu's threshold [1] calculation can be applied to binarize the image. By determining this threshold value, the droplet walls can be clearly delineated as shown in Figure S4(a)with the extra background residuals and inverted without the residuals, which allows for better discrimination between the droplet and its surrounding environment and a precise edge detection. The edges of droplets were detected using an edge detection algorithm. The algorithm identifies and highlights the boundaries between regions of different intensities as shown in Figure S4(b) with red boundaries.

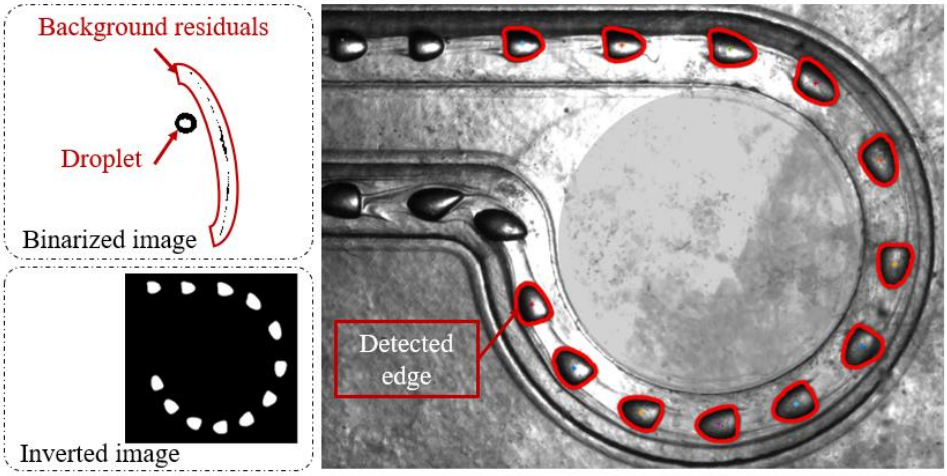

(a) (b)

Figure S4. (a) Eliminating residuals from binarized image using the Otsu's threshold and inverting the image, (b) detected droplet boundaries mapped on the raw image.

Feature extraction

Detecting the droplet boundary and inner region and boundary provides the opportunity to investigate droplet properties. The centroid of a droplet can be expressed as (x_c, y_c) with respect to the origin mapped to the center of the curved channel. The projected area centroid is the weighted average position of all the pixels in the inner region, where the weights are given by their respective densities or mass per unit area [2]. It can be calculated using equation (2),(3), where m is the total mass of the shape, and dA represents an infinitesimal area element [2].

$$x_c = \frac{1}{m}\iint x\, f(x,y)dA \tag{2}$$

$$y_c = \frac{1}{m}\iint y\, f(x,y)dA \tag{3}$$

To calculate the area of a segmented region in an image, a labeling algorithm is applied to group the connected pixels in the binary image together. The Euler characteristic [3], which defines

the relationship between the number of edges, holes and vertices of an object, is then utilized to determine the number of pixels within the region. The Euler characteristic is given by the equation $P - E + H = 1$, where P is the number of boundary pixels, E is the number of edges, and H is the number of holes. By rearranging the equation to solve for P, the projected area of the region can be calculated as $P = E - H + 1$. This approach provides a precise and reliable measurement of the region's projected area, particularly for irregular or complex shapes [3].

References

[1] N. Otsu, "A threshold selection method from gray-level histograms," IEEE Trans. on Systems, Man and Cybernetics, vol. 9, no. 1, pp. 62–66, 1996.

[2] G. Bashein and Paul R. Detmer, "Centroid of a polygon," Graphics gems IV, 1994, pp. 3-6.

[3] S. Mondal and J. Mukherjee, "Image Similarity Measurement using Region Props, Color and Texture: An Approach," International Journal of Computer Applications, vol. 121, no. 22, pp. 23–26, 2015, doi: 10.5120/21833-5092.

Appendix 2: Hydrocyclone performance analysis

This appendix demonstrates the image processing methodology developed to detect and track droplets within a microchannel during experimental investigations discussed in chapter 4. Due to potential shifts in the channel position caused by reinstallation or handling, an initial correction step is performed to align all image frames to a common reference. This correction is achieved using a correlation-based algorithm that identifies and compensates for positional displacements between raw images and background reference. Following alignment, a series of image enhancement and segmentation steps including contrast stretching, thresholding using Otsu's method, and edge detection are applied to isolate the droplet boundaries. Finally, feature extraction techniques are employed to determine key droplet properties such as centroid location and projected area, enabling detailed quantitative analysis of droplet motion and deformation over time.

Synthetic image generator code

```
% Parameters
imageSize = [512, 512];  % Size of the image (pixels)
numParticles = 300;       % Number of tracer particles
numClusters = 20;         % Number of cell clusters
particleDiameter = 5;    % Diameter of tracer particles (pixels)
clusterDiameterRange = [20, 30];  % Range for cell cluster diameters (pixels)
noiseLevel = 0.02;        % Noise level (0 to 1, fraction of white pixels)
numImages = 10;           % Number of images to generate
allParticleDiameters = [];  % Accumulate particle diameters for analysis
allDetectedDiameters = [];  % Accumulate detected diameters for analysis

% Function to convert area to diameter
areaToDiameter = @(area) 2 * sqrt(area / pi);

% Loop to generate multiple images
for imgNum = 1:numImages
    % Create a blank black image
    syntheticImage = zeros(imageSize);

    % Function to draw a circle on the image
    drawCircle = @(img, x, y, r) insertShape(img, 'FilledCircle', [x, y, r], ...
        'Color', 'white', 'Opacity', 1, 'SmoothEdges', false);

    % Add tracer particles (small circles)
    for i = 1:numParticles
```

```
            x = randi([1, imageSize(2)]);  % Random x-coordinate
            y = randi([1, imageSize(1)]);  % Random y-coordinate
            r = particleDiameter / 2;  % Radius of particle
            syntheticImage = drawCircle(syntheticImage, x, y, r);
        end

        % Add cell clusters (larger circles)
        for i = 1:numClusters
            x = randi([1, imageSize(2)]);
            y = randi([1, imageSize(1)]);
            r = randi(clusterDiameterRange) / 2;
            syntheticImage = drawCircle(syntheticImage, x, y, r);
        end

        % Convert to binary image (logical array)
        syntheticImage = im2bw(syntheticImage, 0.5);

        % Add noise
        noise = rand(imageSize) < noiseLevel;
        syntheticImage = syntheticImage | noise;

        % Apply median filter with smaller window to preserve small particles
        filterSize = 2;  % Smaller filter size to preserve small particles
        filteredImage = medfilt2(syntheticImage, [filterSize, filterSize]);

        % Use a very small structuring element for morphological opening
        se = strel('disk', 1);   % Smaller structuring element for less aggressive
separation
        filteredImage = imopen(filteredImage, se);

        % Label connected components (particles)
        connectedComponents = bwconncomp(syntheticImage);
        particleAreas = cellfun(@numel, connectedComponents.PixelIdxList);
        particleDiameters = arrayfun(areaToDiameter, particleAreas);

        % Only consider particles within the tracer particle range
        particleDiameters = particleDiameters(particleDiameters >= 8 & particleDiameters
<= 12);
        allParticleDiameters = [allParticleDiameters; particleDiameters(:)];

        % Label detected large particles for clusters
        largeComponents = bwconncomp(filteredImage);
        detectedAreas = cellfun(@numel, largeComponents.PixelIdxList);
        detectedDiameters = arrayfun(areaToDiameter, detectedAreas);

        % Only consider detected particles within tracer size range
        detectedDiameters = detectedDiameters(detectedDiameters >= 8 & detectedDiameters
<= 12);
        allDetectedDiameters = [allDetectedDiameters; detectedDiameters(:)];
    end

    % Generate PDFs for particle sizes (Tracer Particles)
    figure;
    hold on;
    [fActualParticles, xiActualParticles] = ksdensity(allParticleDiameters);
    plot(xiActualParticles, fActualParticles, 'b', 'LineWidth', 2, 'DisplayName',
'Actual Tracer Particles');

    [fDetectedParticles, xiDetectedParticles] = ksdensity(allDetectedDiameters);
    plot(xiDetectedParticles, fDetectedParticles, 'r', 'LineWidth', 2, 'DisplayName',
'Detected Tracer Particles');

    xlabel('Particle Size (pixels)');
```

```
    ylabel('Probability Density');
    title('PDF Comparison of Tracer Particle Sizes');
    legend('show');
    grid on;
    hold off;

    % Separate cell clusters from tracer particles using size threshold
    clusterThreshold = mean(clusterDiameterRange); % Threshold for clusters

    % Kernel density estimation for large clusters (actual vs detected)
    figure;
    hold on;
    [fActualClusters, xiActualClusters] = ksdensity(actualClusterDiameters);
    plot(xiActualClusters, fActualClusters, 'b', 'LineWidth', 2, 'DisplayName', 'Actual
Clusters');

    [fDetectedClusters, xiDetectedClusters] = ksdensity(detectedClusterDiameters);
    plot(xiDetectedClusters, fDetectedClusters, 'r', 'LineWidth', 2, 'DisplayName',
'Detected Clusters');

    xlabel('Cluster Size (pixels)');
    ylabel('Probability Density');
    title('PDF Comparison of Cell Cluster Sizes');
    legend('show');
    grid on;
    hold off;
```

Cell particle separator

This MATLAB-based code was developed to segment and separate biological cell clusters (such as circulating tumor cells) from tracer particles in PIV images acquired during simultaneous flow field and cell tracking experiments. The algorithm uses morphological and intensity-based criteria to distinguish between larger cell clusters and smaller spherical tracer particles. It then generates two separate outputs, one containing only the cell clusters and another containing only the tracer particles. Which can be independently analyzed. This tool was a key part of the integrated μPTV and fluorescence imaging workflow used to visualize both flow structures and biological samples within the micro-hydrocyclone.

```
    % Define the input directory for raw images
    Dir_Raw                                                                    =
'C:\Users\ysaffar\Documents\Yeganeh\PHD\publications\Confrences\2024\2024_Lisbon\1-
micro HC\3- data\data 1\24053_1_153\';

    % Create directory for saving separated images if needed
    outputDir = 'output';
    if ~exist(outputDir, 'dir')
        mkdir(outputDir)
    end

    % Load or save raw images into a cell array
    F_Name = fullfile(outputDir, 'Test_im.mat');
    if ~isfile(F_Name)
        Fol_Raw = dir(fullfile(Dir_Raw, '*.jpg'));
        for i = 1:length(Fol_Raw)
            Name_Raw{i,1} = Fol_Raw(i).name;
            Test_im{i,1} = imread(fullfile(Dir_Raw, Name_Raw{i}));
        end
        save(F_Name, 'Test_im');
    else
        load(F_Name, 'Test_im');
    end

    % Initialize variables
    frames = cell(1, length(Test_im));
    frames_colord = cell(1, length(Test_im));
    frames_largedots = cell(1, length(Test_im));
    propsinfo = cell(1, length(Test_im));

    % Process each image in the sequence
    for i = 1:length(Test_im)
        Im2 = Test_im{i};
        Im = imbinarize(Im2);
        binaryImage = Im;
```

```
        % Label the connected components and separate small and large dots
        [labeledImage, numComponents] = bwlabel(binaryImage);
        props = regionprops(labeledImage, 'Area', 'PixelIdxList');
        smallDotsImage = false(size(binaryImage));
        largeDotsImage = false(size(binaryImage));

        % Separate components based on size
        for k = 1:numComponents
            if props(k).Area > 10
                largeDotsImage(labeledImage == k) = true;
            else
                smallDotsImage(labeledImage == k) = true;
            end
        end

        % Save the segmented images for small and large dots
        imwrite(uint8(smallDotsImage)         *         255,         fullfile(outputDir,
sprintf('small_dots_image_%03d.png', i)));
        imwrite(uint8(largeDotsImage)         *         255,         fullfile(outputDir,
sprintf('large_dots_image_%03d.png', i)));

        % Create a colored image to visualize small (blue) and large (green) particles
        coloredImage = repmat(uint8(binaryImage) * 255, [1, 1, 3]);
        for k = 1:numComponents
            if props(k).Area > 10
                coloredImage(props(k).PixelIdxList) = 0;  % Green for large
                coloredImage(props(k).PixelIdxList + numel(binaryImage)) = 255;
            else
                coloredImage(props(k).PixelIdxList) = 255;  % Blue for small
            end
        end

        % Save the colored image
        imwrite(coloredImage,   fullfile(outputDir,   sprintf('colored_image_%03d.png',
i)));

        % Store frames and properties for analysis
        frames{i} = coloredImage;
        frames_colord{i} = coloredImage;
        frames_largedots{i} = largeDotsImage;
        propsinfo{i} = props;
    end

    % Accumulate and save images of small and large dots over n frames
    n = 10;  % Adjust the number of frames as needed
    accumulatedSmall = false(size(frames_largedots{1}));
    accumulatedLarge = false(size(frames_largedots{1}));
    for i = 1:n
        accumulatedSmall = accumulatedSmall | frames{i};
        accumulatedLarge = accumulatedLarge | frames_largedots{i};
    end

    imwrite(uint8(accumulatedSmall)         *         255,         fullfile(outputDir,
'accumulated_small_dots.png'));
    imwrite(uint8(accumulatedLarge)         *         255,         fullfile(outputDir,
'accumulated_large_dots.png'));

    disp('Processed images and accumulated images saved successfully.');

    % Initialize an array to store particle sizes from all frames
    all_particle_sizes = [];

    % Loop through the properties and accumulate particle sizes (areas)
```

```
for i = 1:length(propsinfo)
    for k = 1:length(propsinfo{i})
        all_particle_sizes = [all_particle_sizes; propsinfo{i}(k).Area];
    end
end

% Define a separation point (e.g., 10 as used in the previous segmentation logic)
separation_point = 10;

% Plot the PDF of the particle size distribution
figure;
histogram(all_particle_sizes, 'Normalization', 'pdf', 'EdgeColor', 'none');
hold on;

% Overlay a dashed line at the separation point
yLimits = ylim; % Get the current y-axis limits
plot([separation_point separation_point], yLimits, '--r', 'LineWidth', 1.5);

% Labeling the plot
xlabel('Particle Size');
ylabel('Probability Density Function (PDF)');
title('Particle Size Distribution');
legend('Particle Size PDF', 'Separation Threshold');

hold off;

% Initialize an array to store particle sizes from all frames
all_particle_sizes = [];

% Loop through the properties and accumulate particle sizes (areas)
for i = 1:length(propsinfo)
    for k = 1:length(propsinfo{i})
        all_particle_sizes = [all_particle_sizes; propsinfo{i}(k).Area];
    end
end

% Initialize an array to store particle sizes from all frames
all_particle_sizes = [];

% Loop through the properties and accumulate particle sizes (areas)
for i = 1:length(propsinfo)
    for k = 1:length(propsinfo{i})
        particle_size = propsinfo{i}(k).Area;
        % Only include particles with size >= 3
        if particle_size >= 3
            all_particle_sizes = [all_particle_sizes; particle_size];
        end
    end
end
%%%%%%%%%%%%%%%%%%%%%%%%%%%%
% Filter out particles smaller than 3 in size
filtered_sizes = all_particle_sizes(all_particle_sizes >= 3);

% PDF Plot of Particle Size Distribution
figure;
histogram(filtered_sizes, 'Normalization', 'pdf', 'EdgeColor', 'none');
hold on;

% Overlay a dashed line at the separation point
yLimits = ylim;
plot([separation_point separation_point], yLimits, '--r', 'LineWidth', 1.5);

% Labeling and formatting the plot
```

```
    xlabel('Particle Size', 'FontName', 'Times New Roman', 'FontSize', 14);
    ylabel('Probability Density Function (PDF)', 'FontName', 'Times New Roman',
'FontSize', 14);
    title('Particle Size Distribution', 'FontName', 'Times New Roman', 'FontSize', 14);
    legend('Particle Size PDF', 'Separation Threshold');
    set(gca, 'FontName', 'Times New Roman', 'FontSize', 14);
    hold off;

    % Histogram Plot of Particle Counts by Size
    figure;
    histogram(filtered_sizes, 'EdgeColor', 'none');
    hold on;

    % Overlay a dashed line at the separation point
    yLimits = ylim;
    plot([separation_point separation_point], yLimits, '--r', 'LineWidth', 1.5);
    % Labeling and formatting the plot
    xlabel('Particle Size', 'FontName', 'Times New Roman', 'FontSize', 14);
    ylabel('Number of Particles', 'FontName', 'Times New Roman', 'FontSize', 14);
    title('Number of Particles by Size', 'FontName', 'Times New Roman', 'FontSize', 14);
    legend('Particle Count', 'Separation Threshold');
    set(gca, 'FontName', 'Times New Roman', 'FontSize', 14);
    hold off;
    %%%%%%%%_____________________________
    % Define small and large particle groups based on separation_point
    small_particle_sizes = all_particle_sizes(all_particle_sizes >= 3 &
all_particle_sizes < separation_point);
    large_particle_sizes = all_particle_sizes(all_particle_sizes >= separation_point);

    % Plotting number distribution for small particles
    figure;
    histogram(small_particle_sizes, 'EdgeColor', 'none');
    hold on;

    % Labeling and formatting the plot
    xlabel('Particle Size', 'FontName', 'Times New Roman', 'FontSize', 14);
    ylabel('Number of Small Particles', 'FontName', 'Times New Roman', 'FontSize', 14);
    title('Number of Small Particles by Size', 'FontName', 'Times New Roman', 'FontSize',
14);
    set(gca, 'FontName', 'Times New Roman', 'FontSize', 14);
    hold off;

    % Plotting number distribution for large particles
    figure;
    histogram(large_particle_sizes, 'EdgeColor', 'none');
    hold on;

    % Labeling and formatting the plot
    xlabel('Particle Size', 'FontName', 'Times New Roman', 'FontSize', 14);
    ylabel('Number of Large Particles', 'FontName', 'Times New Roman', 'FontSize', 14);
    title('Number of Large Particles by Size', 'FontName', 'Times New Roman', 'FontSize',
14);
    set(gca, 'FontName', 'Times New Roman', 'FontSize', 14);
    hold off;

    %%%%_________________________

    % Define small and large particle groups based on separation_point
    small_particle_sizes = all_particle_sizes(all_particle_sizes >= 3 &
all_particle_sizes < separation_point);
    large_particle_sizes = all_particle_sizes(all_particle_sizes >= separation_point);

    % Plotting the PDF curve for small particles
```

```
    figure;
    ksdensity(small_particle_sizes);  % Kernel density estimate for smooth curve
    hold on;

    % Labeling and formatting the plot
    xlabel('Particle Size', 'FontName', 'Times New Roman', 'FontSize', 14);
    ylabel('Probability Density Function (PDF)', 'FontName', 'Times New Roman',
'FontSize', 14);
    title('PDF of Small Particle Sizes', 'FontName', 'Times New Roman', 'FontSize', 14);
    set(gca, 'FontName', 'Times New Roman', 'FontSize', 14);
    hold off;

    % Plotting the PDF curve for large particles
    figure;
    ksdensity(large_particle_sizes);  % Kernel density estimate for smooth curve
    hold on;

    % Labeling and formatting the plot
    xlabel('Particle Size', 'FontName', 'Times New Roman', 'FontSize', 14);
    ylabel('Probability Density Function (PDF)', 'FontName', 'Times New Roman',
'FontSize', 14);
    title('PDF of Large Particle Sizes', 'FontName', 'Times New Roman', 'FontSize', 14);
    set(gca, 'FontName', 'Times New Roman', 'FontSize', 14);
    hold off;

    figure;
    ksdensity(filtered_sizes);  % Kernel density estimate for smooth curve
    hold on;

    % Labeling and formatting the plot
    xlabel('Particle Size', 'FontName', 'Times New Roman', 'FontSize', 14);
    ylabel('Probability Density Function (PDF)', 'FontName', 'Times New Roman',
'FontSize', 14);
    title('PDF of all Particle Sizes', 'FontName', 'Times New Roman', 'FontSize', 14);
    set(gca, 'FontName', 'Times New Roman', 'FontSize', 14);
    hold off;
```

Microsep$_{TM}$ particle size distribution analysis software

Microsep is a MATLAB-based software developed for the high-throughput analysis of microfluidic separation experiments, particularly involving micro-hydrocyclones. The tool performs automated image processing to detect and segment particles or cell clusters, extract size distributions, and quantify separation efficiency across different outlet streams. It includes features for adaptive binarization, object classification, and performance curve generation (e.g., grade efficiency curves).

```
classdef Microsep < matlab.apps.AppBase

% Properties that correspond to app components
properties (Access = public)
UIFigure matlab.ui.Figure
Toolbar matlab.ui.container.Toolbar
PushTool matlab.ui.container.toolbar.PushTool
TabGroup2 matlab.ui.container.TabGroup
IntroTab matlab.ui.container.Tab
Label_2 matlab.ui.control.Label
Label matlab.ui.control.Label
Image matlab.ui.control.Image
DataanalysisTab matlab.ui.container.Tab
InletPanel matlab.ui.container.Panel
UIAxes5 matlab.ui.control.UIAxes
UIAxes6 matlab.ui.control.UIAxes
UnderflowPanel matlab.ui.container.Panel
UIAxes3 matlab.ui.control.UIAxes
UIAxes4 matlab.ui.control.UIAxes
OverflowPanel matlab.ui.container.Panel
UIAxes matlab.ui.control.UIAxes
UIAxes2 matlab.ui.control.UIAxes
SeparationanalysisTab matlab.ui.container.Tab
LargeparticlesPanel matlab.ui.container.Panel
UIAxes9 matlab.ui.control.UIAxes
UIAxes10 matlab.ui.control.UIAxes
AllparticlesPanel matlab.ui.container.Panel
UIAxes7 matlab.ui.control.UIAxes
UIAxes8 matlab.ui.control.UIAxes
LCSeparationanalysisTab matlab.ui.container.Tab
LargeparticlesPanel_2 matlab.ui.container.Panel
UIAxes13 matlab.ui.control.UIAxes
UIAxes14 matlab.ui.control.UIAxes
AllparticlesPanel_2 matlab.ui.container.Panel
UIAxes11 matlab.ui.control.UIAxes
UIAxes12 matlab.ui.control.UIAxes
ImageprocessingTab matlab.ui.container.Tab
Label_3 matlab.ui.control.Label
maximagenumber matlab.ui.control.TextArea
Switch matlab.ui.control.Switch
ShowButton matlab.ui.control.Button
```

```
DataseriesDropDown matlab.ui.control.DropDown
DataseriesDropDownLabel matlab.ui.control.Label
ChooseanimageLabel matlab.ui.control.Label
EditField matlab.ui.control.NumericEditField
UIAxes20 matlab.ui.control.UIAxes
ExportTab matlab.ui.container.Tab
ExportfiguresPanel matlab.ui.container.Panel
FigurenameDropDown matlab.ui.control.DropDown
FigurenameDropDownLabel matlab.ui.control.Label
DatasetButtonGroup_2 matlab.ui.container.ButtonGroup
SmallParticlesButton matlab.ui.control.RadioButton
LargeParticlesButton matlab.ui.control.RadioButton
TextArea_2 matlab.ui.control.TextArea
SelecttheexportinglocationLabel_2 matlab.ui.control.Label
BrowseButton_2 matlab.ui.control.Button
ExportdataPanel matlab.ui.container.Panel
DatasetButtonGroup matlab.ui.container.ButtonGroup
UnderflowButton matlab.ui.control.RadioButton
OverflowButton matlab.ui.control.RadioButton
InletButton matlab.ui.control.RadioButton
TextArea matlab.ui.control.TextArea
SelecttheexportinglocationLabel matlab.ui.control.Label
BrowseButton matlab.ui.control.Button
Lastmodificationwinter2024Label matlab.ui.control.Label
DesignedbyYeganehSaffarLabel matlab.ui.control.Label
MicrosepV10Label matlab.ui.control.Label
TabGroup matlab.ui.container.TabGroup
OpenTab matlab.ui.container.Tab
InletF matlab.ui.control.EditField
UnderflowF matlab.ui.control.EditField
OverflowF matlab.ui.control.EditField
SelectinletfolderButton matlab.ui.control.Button
SelectunderflowfolderButton matlab.ui.control.Button
SelectoverflowfolderButton matlab.ui.control.Button
HelpTab matlab.ui.container.Tab
PleasepressHelpforapplicationtutorialLabel matlab.ui.control.Label
HelpButton matlab.ui.control.Button
ControlPanel matlab.ui.container.Panel
StartdetectionButton matlab.ui.control.Button
StartProcessButton matlab.ui.control.Button
ImporteddatainformationTextArea matlab.ui.control.TextArea
ImporteddatainformationTextAreaLabel matlab.ui.control.Label
SizethresholdEditField matlab.ui.control.EditField
SizethresholdEditFieldLabel matlab.ui.control.Label
ScalefactorEditField matlab.ui.control.EditField
ScalefactorEditFieldLabel matlab.ui.control.Label
AnalysisPanel matlab.ui.container.Panel
AnalysisprogressTextArea matlab.ui.control.TextArea
AnalysisprogressTextAreaLabel matlab.ui.control.Label
end

properties (Access = private)
imagenumbers; % To get the number of images loaded by the user
filenameof; % To get filenames of the images
pathnameof; % To get the pathname of th loaded images % Description
filenameuf; % To get filenames of the images
pathnameuf; % To get the pathname of th loaded images % Description
filenamein; % To get filenames of the images
pathnamein; % To get the pathname of th loaded images % Description
image_count;
info;
test_im1;
test_im2;
```

```
    test_im3;
    Fol_Raw2;
    L1_of;
    L2_of;
    L1_uf;
    L2_uf;
    radius_uf;
    center_uf;
    Paticle_num_frame_uf;
    radius_of;
    center_of;
    Paticle_num_frame_of;
    data_name = 'test1';
    data_name2 = 'test2';
    inputename_of = 'overflow';
    inputename_uf = 'underflow';
    inputename_in = ' inlet'; % Description
    radius_in;
    center_in;
    Paticle_num_frame_in;
    L1_in ;
    L2_in ; % Description
    allData_of;
    allData_uf;
    allData_inlet;
    Image_processed;
    rawImage; % Description
    largeData_of;
    largeData_uf;
    largeData_inlet; % Description
    end
    methods (Access = private)

    function [L1,L2,centers,radii,Paticle_num_1frame] = detection(app,Im22,i,Pixtoreal)

    Im2 = medfilt2(Im22);

    % figure('name','filtered image');
    % imshow(Im2)
    Im = imbinarize( Im2, 'adaptive','ForegroundPolarity','dark','Sensitivity',0.5);
    % Im = imbinarize( Im2);
    % figure('name','Binarized image');
    % imshow(Im)
    II1 = ~Im; % invert image for circle detection
    II = imfill(II1,'holes' );

    stats                                                                    =
regionprops('table',II,'Centroid','MajorAxisLength','MinorAxisLength','Area');
    centers = stats.Centroid;
    area = stats.Area;
    L1 = stats.MajorAxisLength .* Pixtoreal;
    L2 = stats.MinorAxisLength .*Pixtoreal;
    diameters = mean([stats.MajorAxisLength stats.MinorAxisLength],2);
    % radii = diameters/2;
    radii = sqrt (area./3.14).*Pixtoreal;
    offdata = find (500<radii);
    radii (offdata ) = radii (offdata )/1000*50;

    % figure('name','Detected particles on raw image');
    % imshow(Im2)

    Paticle_num_1frame = size (radii,1);
```

```
app.AnalysisprogressTextArea.Value ='Detection execution is completed'
end
%---------------------------------------------------
function [] = datainfo(app,Paticle_num_frame,radius,inputename,size1,A1,A2)


plot(A1,Paticle_num_frame);
title(A1,['Particle count per frame for',num2str(inputename)]);
xlabel(A1,'Farame number')
ylabel(A1,'Particle count ')


max_size = max(max(Paticle_num_frame));
Radius_data = zeros( max_size, size(Paticle_num_frame,2));
for i = 1:size1
Radius_data(1:Paticle_num_frame(i),i) = radius {i};
%%%%% calculate average and pdf

end

%%% calculate the D avg for 1-i photos

for i = 1:size1
%%% accumulatove avg
D_sums(i) = sum (sum(Radius_data(:,1:i)));
D_bar(i) = D_sums(i)/(sum (Paticle_num_frame (1:i)));

%%% normal avg
D_avg(i) = sum(Radius_data(:,i))/Paticle_num_frame (i);
end

% figure('name','Particle accumulative avg vs avg ');


plot (A2,D_avg,'r') ;
hold(A2,'on')
plot (A2,D_bar,'k') ;

% title(['Particle average for',num2str(inputename)]);
xlabel(A2,'Farame number');
ylabel(A2,'Particle diameter average');
legend (A2,'D_ avg','D_ bar');
end
%---------------------------------------------------
function [big_matrix,allData] = dataplots(app,radius_of,inputename,A1,A2)

% check to see if input is a single matrix or a cell
tf = iscell(radius_of);
if tf == 1
allData = vertcat(radius_of{:});
big_matrix = vertcat(radius_of{:});
else
allData = radius_of;
big_matrix = radius_of;
end

% Number of points for the smooth curve
numPoints = 100;

% Plot the overall normalized PDF as a smooth curve
figure;

[f, x] = ksdensity(allData, 'NumPoints', numPoints);
```

```
    plot(x, f,'k', 'LineWidth', 2);
    title(['Overall Smooth PDF for All particles in ',num2str(inputename)]);
    xlabel('Values');
    ylabel('Probability Density');

    % % Create the full file path
    % fullFilePath = fullfile(Dir_Raw, [data_name, '.mat'])

    % big_matrix = vertcat(radius_of{:});
    d_max = max(big_matrix);

    for k = 1:d_max
    count_smaller(k) = sum(big_matrix < k);
    end
    figure('name','cumulative distribution ');
    plot (count_smaller(1:end),'r', 'LineWidth', 2)
    title('Cumulative distribution');
    xlabel('particle size');
    ylabel('count');

    app.AnalysisprogressTextArea.Value ='data plots execution is completed'

    end

    function                    [allData_of,allData_uf,allData_inlet]                    =
dataplots_allcases(app,radius_of,inputename_of...
    ,radius_uf,inputename_uf,radius_in,A1,A2,A3,A4)


    % check to see if input is a single matrix or a cell
    tf = iscell(radius_of);
    if tf == 1
    allData_of = vertcat(radius_of{:});
    else
    allData_of = radius_of;
    end

    tf = iscell(radius_uf);
    if tf == 1
    allData_uf = vertcat(radius_uf{:});
    else
    allData_uf = radius_uf;
    end

    tf = iscell(radius_in);
    if tf == 1
    allData_inlet = vertcat(radius_in{:});
    else
    allData_inlet = radius_in;
    end
    % allData_inlet = vertcat(allData_of,allData_uf);


    % Number of points for the smooth curve
    numPoints = 100;

    % Plot the overall normalized PDF as a smooth curve

    [f_of, x_of] = ksdensity(allData_of, 'NumPoints', numPoints);
    [f_uf, x_uf] = ksdensity(allData_uf, 'NumPoints', numPoints);
    [f_in, x_in] = ksdensity(allData_inlet, 'NumPoints', numPoints);
    figure;
    plot(x_of, f_of,'b-', 'LineWidth', 2);
```

```
hold on
plot(x_uf, f_uf,'r-.', 'LineWidth', 2);
hold on
plot(x_in, f_in,'k', 'LineWidth', 2);
title('Particle count per frame ');
title('Overall Smooth PDF for All particles ');
xlabel('Values');
ylabel('Probability Density');
legend ([num2str(inputename_of)],[num2str(inputename_uf)],'inlet')
figure;
plot(A1,x_of, f_of,'b-', 'LineWidth', 2);
hold on
plot(A1,x_uf, f_uf,'r-.', 'LineWidth', 2);
hold on
plot(A1,x_in, f_in,'k', 'LineWidth', 2);
title(A1,'Overall Smooth PDF for All particles ');
xlabel(A1,'Values');
ylabel(A1,'Probability Density');
legend (A1,[num2str(inputename_of)],[num2str(inputename_uf)],'inlet')
d_max_of = max(allData_of);
d_max_uf = max(allData_uf);
d_max_in = max(allData_inlet);
for k = 1:d_max_of
count_smaller_of1(k) = sum(allData_of < k);
end
for k = 1:d_max_uf
count_smaller_uf1(k) = sum(allData_uf < k);
end
for k = 1:d_max_in
count_smaller_in1(k) = sum(allData_inlet < k);
end
count_smaller_of = count_smaller_of1./size (allData_inlet,1);
count_smaller_uf = count_smaller_uf1./size (allData_inlet,1);
count_smaller_in = count_smaller_in1./size (allData_inlet,1);
figure('name','cumulative distribution ');
plot (A2,count_smaller_of(1:end),'r', 'LineWidth', 2)
hold(A2,'on')
plot (A2,count_smaller_uf(1:end),'b', 'LineWidth', 2)
hold(A2,'on')
plot (A2,count_smaller_in(1:end),'k', 'LineWidth', 2)
title(A2,'Cumulative distribution');
xlabel(A2,'particle size ($\mu$m)');
ylabel(A2,'Count');
legend (A2,[num2str(inputename_of)],[num2str(inputename_uf)],'inlet')
figure('name','Over flow large particles');
histogram(allData_of ,20)
figure('name','Nomalized Over flow large particles');
histogram(allData_of ,'Normalization','pdf')
figure('name','Under flow large particles');
histogram(allData_uf ,20)
h.FaceColor = [0 0.5 0.5];
figure('name','Nomalized Under flow large particles');
histogram(allData_uf ,'Normalization','pdf')
figure('name','Inlet large particles');
histogram(allData_inlet ,20)
h.FaceColor = [0 0.5 0.5];
figure('name','Nomalized Inlet large particles');
histogram(allData_inlet ,'Normalization','pdf')
figure('name','Over flow large particles');
histogram(A3,allData_inlet ,20)
hold(A3,'on')
histogram(A3,allData_uf ,20)
hold(A3,'on')
```

```
    histogram(A3,allData_of ,20)
    axis(A3,'tight');
    legend (A3,'Inlet', 'Underflow', 'Overflow')
    figure('name','Nomalized large particles');
    histogram(A4,allData_of ,'Normalization','pdf')
    hold(A4,'on')
    histogram(A4,allData_uf ,'Normalization','pdf')
    hold(A4,'on')
    histogram(A4,allData_inlet ,'Normalization','pdf')
    legend (A4,'overflow','Inlet', 'Underflow')
    axis(A4,'tight');
    figure ('name','uni ke mikham');
    plot (count_smaller_of(1:end),'r', 'LineWidth', 2)
    hold on
    plot (count_smaller_uf(1:end),'b', 'LineWidth', 2)
    hold on
    plot (count_smaller_in(1:end),'k', 'LineWidth', 2)
    title('Cumulative distribution');
    xlabel('particle size ($\mu$m)');
    ylabel('Count');
    legend ([num2str(inputename_of)],[num2str(inputename_uf)],'inlet')
    figure('name','Over flow large particles');
    histogram(allData_of ,20)
    figure('name','Nomalized Over flow large particles');
    histogram(allData_of ,'Normalization','pdf')
    figure('name','Under flow large particles');
    histogram(allData_uf ,20)
    h.FaceColor = [0 0.5 0.5];
    figure('name','Nomalized Under flow large particles');
    histogram(allData_uf ,'Normalization','pdf')
    figure('name','Inlet large particles');
    histogram(allData_inlet ,20)
    h.FaceColor = [0 0.5 0.5];
    figure('name','Nomalized Inlet large particles');
    histogram(allData_inlet ,'Normalization','pdf')
    figure('name','Over flow large particles');
    histogram(allData_inlet ,20)
    hold on
    histogram(allData_uf ,20)
    hold on
    histogram(allData_of ,20)
    legend ('Inlet', 'Underflow', 'Overflow')
    figure('name','Nomalized large particles');
    histogram(allData_of ,'Normalization','pdf')
    hold on
    histogram(allData_uf ,'Normalization','pdf')
    hold on
    histogram(allData_inlet ,'Normalization','pdf')
    legend ('overflow','Inlet', 'Underflow')
    app.AnalysisprogressTextArea.Value ='data plots for device is completed'
    end
    end

    % Callbacks that handle component events
    methods (Access = private)

    % Button pushed function: SelectoverflowfolderButton
    function SelectoverflowfolderButtonPushed(app, event)
    [app.filenameof,                          app.pathnameof]                          =
uigetfile({'*.jpg;*.jpeg;*.bmp;*.tif;*.png;*.gif','All Image Files';...
    '*.*','All Files' },'Pick a file', ...
    'MultiSelect', 'on'); % Open the file browser
    % initial mask (consider one pixel on the top left as the selected
```

```
    % mask area at the first)
    app.OverflowF.Value = app.pathnameof; % Display the filenames in text box
    app.image_count (1) = size(app.filenameof,2);

    for i = 1 : size(app.filenameof, 2)

    Name_Raw2 = app.filenameof';
    app.test_im1{i} = imread( [app.pathnameof, Name_Raw2{i}] ) ;
    end
    app.AnalysisprogressTextArea.Value = ' Importing overflow data is completed'
    end

    % Value changed function: OverflowF
    function OverflowFValueChanged(app, event)
    % value = app.OverflowF.Value;
    % value = app.pathname.Value;
    end

    % Button pushed function: SelectunderflowfolderButton
    function SelectunderflowfolderButtonPushed(app, event)
    [app.filenameuf,                          app.pathnameuf]                          =
uigetfile({'*.jpg;*.jpeg;*.bmp;*.tif;*.png;*.gif','All Image Files';...
    '*.*','All Files' },'Pick a file', ...
    'MultiSelect', 'on'); % Open the file browser
    % initial mask (consider one pixel on the top left as the selected
    % mask area at the first)
    app.UnderflowF.Value = app.pathnameuf; % Display the filenames in text box
    app.image_count (2) = size(app.filenameuf,2);

    for i = 1 : size(app.filenameuf, 2)

    Name_Raw2 = app.filenameuf';
    app.test_im2{i,1} = imread( [app.pathnameuf, Name_Raw2{i}] ) ;
    end
    app.AnalysisprogressTextArea.Value = ' Importing under flow data is completed'
    end

    % Button pushed function: SelectinletfolderButton
    function SelectinletfolderButtonPushed(app, event)
    [app.filenamein,                          app.pathnamein]                          =
uigetfile({'*.jpg;*.jpeg;*.bmp;*.tif;*.png;*.gif','All Image Files';...
    '*.*','All Files' },'Pick a file', ...
    'MultiSelect', 'on'); % Open the file browser
    % initial mask (consider one pixel on the top left as the selected
    % mask area at the first)
    app.InletF.Value = app.pathnamein; % Display the filenames in text box
    app.image_count (3) = size(app.filenamein,2);
    app.info = {sprintf('Number of overflow images : %d', app.image_count(1)); ...
    sprintf('Number of underflow images : %d', app.image_count(2));...
    sprintf('Number of inlet images : %d', app.image_count(3))}; % to make the image
information text for textbox
    app.ImporteddatainformationTextArea.Value = app.info; % Display info in the textbox
    for i = 1 : size(app.filenamein, 2)

    Name_Raw2 = app.filenamein';
    app.test_im3{i,1} = imread( [app.pathnamein, Name_Raw2{i}] ) ;
    end
    app.AnalysisprogressTextArea.Value = ' Importing inlet data is completed'
    end

    % Value changed function: ImporteddatainformationTextArea
    function ImporteddatainformationTextAreaValueChanged(app, event)
    % value = app.ImporteddatainformationTextArea.Value;
```

```
    end

    % Value changed function: AnalysisprogressTextArea
    function AnalysisprogressTextAreaValueChanged(app, event)
    % value = app.AnalysisprogressTextArea.Value;
    end

    % Button pushed function: StartProcessButton
    function StartProcessButtonPushed(app, event)

    [app.allData_of,app.allData_uf,app.allData_inlet]                                    =
dataplots_allcases(app,app.radius_of,app.inputename_of...
    ,app.radius_uf,app.inputename_uf,app.radius_in,app.UIAxes7,app.UIAxes8,app.UIAxes9
,app.UIAxes10)
    treshold = str2num(app.SizethresholdEditField.Value);
    largedata_of = any(app.allData_of > treshold,2);
    new_matrix2_of = app.allData_of(largedata_of, :);
    new_matrix2_of1 = new_matrix2_of';
    %                     [big_matrix_larg_of,allData_large_of]                          =
dataplots(app,new_matrix2_of1,Dir_Raw,app.data_name,app.inputename_of);
    largedata_uf = any(app.allData_uf > treshold ,2);
    new_matrix2_uf = app.allData_uf(largedata_uf, :);
    new_matrix2_uf1 = new_matrix2_uf';
    %                     [big_matrix_larg_uf,allData_large_uf]                          =
dataplots(new_matrix2_uf1,Dir_Raw,data_name,inputename_uf);
    largedata_in = any(app.allData_inlet > treshold,2);
    new_matrix2_in = app.allData_inlet(largedata_in, :);
    new_matrix2_in1 = new_matrix2_in';


    [app.largeData_of,app.largeData_uf,app.largeData_inlet]                              =
dataplots_allcases(app,new_matrix2_of1,app.inputename_of...
    ,new_matrix2_uf1,app.inputename_uf,new_matrix2_in1,app.UIAxes11,app.UIAxes12,app.U
IAxes13,app.UIAxes14)
    end

    % Button pushed function: StartdetectionButton
    function StartdetectionButtonPushed(app, event)
    class(app.test_im2)
    for i = 1:size(app.filenameof,2)

    Im22 = app.test_im1{i}; % read the image

    [L1o,L2o,center,radius_frame_o,Paticle_num_1frame]                                   =
detection(app,Im22,i,app.ScalefactorEditField.Value);

    app.radius_of {i} = radius_frame_o;
    app.center_of{i} = center;
    app.Paticle_num_frame_of(i) = Paticle_num_1frame;
    app.L1_of {i} = L1o;
    app.L2_of {i} = L2o;

    end
    for k = 1:size(app.filenameuf,2)

    Im33 = app.test_im2{k}; % read the image
    [L1u,L2u,center,radius_frame_u,Paticle_num_1frame_u]                                 =
detection(app,Im33,k,app.ScalefactorEditField.Value); % detect cell
    app.radius_uf {k} = radius_frame_u;
    app.center_uf{k} = center;
    app.Paticle_num_frame_uf(k) = Paticle_num_1frame_u;
    app.L1_uf {k} = L1u;
    app.L2_uf {k} = L2u;
```

```
    end
    for j = 1:size(app.filenamein,2)
    class(app.test_im3)
    size(app.filenamein)
    size(app.test_im3)
    Im44 = app.test_im3{j}; % read the image

    [L1in,L2in,center,radius_frame_in,Paticle_num_1frame]                                =
detection(app,Im44,j,app.ScalefactorEditField.Value);

    app.radius_in {j} = radius_frame_in;
    app.center_in{j} = center;
    app.Paticle_num_frame_in(j) = Paticle_num_1frame;
    app.L1_in {j} = L1in;
    app.L2_in {j} = L2in;

    end
    app.AnalysisprogressTextArea.Value = ' image detection finished '

    datainfo(app,app.Paticle_num_frame_of,app.radius_of,app.inputename_of,size(app.fil
enameof, 2),app.UIAxes,app.UIAxes2)
    datainfo(app,app.Paticle_num_frame_uf,app.radius_uf,app.inputename_uf,size(app.fil
enameuf, 2),app.UIAxes3,app.UIAxes4)
    datainfo(app,app.Paticle_num_frame_in,app.radius_in,app.inputename_in,size(app.fil
enamein, 2),app.UIAxes5,app.UIAxes6)
    app.AnalysisprogressTextArea.Value = ' data info plot completed '
    end

    % Value changed function: ScalefactorEditField
    function ScalefactorEditFieldValueChanged(app, event)
    value = app.ScalefactorEditField.Value;
    end

    % Value changed function: DataseriesDropDown
    function DataseriesDropDownValueChanged(app, event)
    value = app.DataseriesDropDown.Value;
    % Choose the data set based on the selected value
    if strcmp(app.DataseriesDropDown.Value, 'Overflow')
    app.maximagenumber.Value = num2str(app.image_count(1));
    elseif strcmp(app.DataseriesDropDown.Value, 'Underflow')
    app.maximagenumber.Value = num2str(app.image_count(2));
    elseif strcmp(app.DataseriesDropDown.Value, 'Inlet')
    app.maximagenumber.Value = num2str(app.image_count(3));
    end
    %
    % imshow (app.UIAxes20,app.rawImage)
    % title(app.UIAxes20,'raw image');
    %

    % xlabel(UIAxes11,'particle size ($\mu$m)');
    % ylabel(UIAxes11,'Count');

    end

    % Value changed function: EditField
    function EditFieldValueChanged(app, event)
    value = app.EditField.Value;
    end

    % Button pushed function: ShowButton
    function ShowButtonPushed(app, event)
    if strcmp(app.DataseriesDropDown.Value, 'Overflow')
    dataset = app.test_im1;
```

```
    app.maximagenumber.Value = num2str(app.image_count(1));
    elseif strcmp(app.DataseriesDropDown.Value, 'Underflow')
    dataset = app.test_im2;
    app.maximagenumber.Value = num2str(app.image_count(2));
    elseif strcmp(app.DataseriesDropDown.Value, 'Inlet')
    dataset = app.test_im3;
    app.maximagenumber.Value = num2str(app.image_count(3));
    end
    app.rawImage = dataset{app.EditField.Value};
    imagesc(app.rawImage,'Parent',app.UIAxes20);  % display image with user input
settings
    % define display settings for axises
    axis(app.UIAxes20,'tight','equal');
    colormap(app.UIAxes20,gray)

    %
    % imshow (app.UIAxes20,app.Image)
    % title(app.UIAxes20,'raw image');
    Im2 = medfilt2(app.rawImage);
    Im = imbinarize( Im2, 'adaptive','ForegroundPolarity','dark','Sensitivity',0.5);
    II1 = ~Im; % invert image for circle detection
    app.Image_processed = imfill(II1,'holes' );
    end

    % Value changed function: Switch
    function SwitchValueChanged(app, event)
    value = app.Switch.Value;
    if strcmp (value,'raw image')
    % Use the if condition to change the image by changing the toggle
    % button value
    a = 1
    % imshow (app.UIAxes20,app.Image)
    % title(app.UIAxes20,'raw image');
    imagesc(app.rawImage,'Parent',app.UIAxes20);  % display image with user input
settings
    % define display settings for axises
    axis(app.UIAxes20,'tight','equal');
    colormap(app.UIAxes20,gray)

    else
    a = 2
    imagesc(app.Image_processed,'Parent',app.UIAxes20); % display image with user input
settings
    % define display settings for axises
    axis(app.UIAxes20,'tight','equal');
    colormap(app.UIAxes20,gray)
    % imshow (app.UIAxes20,app.Image_processed)
    % title(app.UIAxes20,'processed image');
    end
    end

    % Value changed function: maximagenumber
    function maximagenumberValueChanged(app, event)
    value = app.maximagenumber.Value;
    end

    % Value changed function: SizethresholdEditField
    function SizethresholdEditFieldValueChanged(app, event)
    value = app.SizethresholdEditField.Value;
    end
    end

    % Component initialization
```

```
    methods (Access = private)

    % Create UIFigure and components
    function createComponents(app)

    % Create UIFigure and hide until all components are created
    app.UIFigure = uifigure('Visible', 'off');
    app.UIFigure.Position = [100 100 1386 793];
    app.UIFigure.Name = 'MATLAB App';

    % Create Toolbar
    app.Toolbar = uitoolbar(app.UIFigure);

    % Create PushTool
    app.PushTool = uipushtool(app.Toolbar);

    % Create AnalysisPanel
    app.AnalysisPanel = uipanel(app.UIFigure);
    app.AnalysisPanel.Title = 'Analysis';
    app.AnalysisPanel.BackgroundColor = [0.9412 0.9412 0.9412];
    app.AnalysisPanel.FontWeight = 'bold';
    app.AnalysisPanel.Position = [4 207 569 160];

    % Create AnalysisprogressTextAreaLabel
    app.AnalysisprogressTextAreaLabel = uilabel(app.AnalysisPanel);
    app.AnalysisprogressTextAreaLabel.HorizontalAlignment = 'right';
    app.AnalysisprogressTextAreaLabel.Position = [14 114 100 22];
    app.AnalysisprogressTextAreaLabel.Text = 'Analysis progress';

    % Create AnalysisprogressTextArea
    app.AnalysisprogressTextArea = uitextarea(app.AnalysisPanel);
    app.AnalysisprogressTextArea.ValueChangedFcn        =        createCallbackFcn(app,
@AnalysisprogressTextAreaValueChanged, true);
    app.AnalysisprogressTextArea.Position = [14 9 267 106];

    % Create ControlPanel
    app.ControlPanel = uipanel(app.UIFigure);
    app.ControlPanel.Title = 'Control Panel';
    app.ControlPanel.BackgroundColor = [0.9412 0.9412 0.9412];
    app.ControlPanel.FontWeight = 'bold';
    app.ControlPanel.Position = [4 386 569 207];

    % Create ScalefactorEditFieldLabel
    app.ScalefactorEditFieldLabel = uilabel(app.ControlPanel);
    app.ScalefactorEditFieldLabel.HorizontalAlignment = 'right';
    app.ScalefactorEditFieldLabel.Position = [300 46 69 22];
    app.ScalefactorEditFieldLabel.Text = 'Scale factor';

    % Create ScalefactorEditField
    app.ScalefactorEditField = uieditfield(app.ControlPanel, 'text');
    app.ScalefactorEditField.ValueChangedFcn          =          createCallbackFcn(app,
@ScalefactorEditFieldValueChanged, true);
    app.ScalefactorEditField.HorizontalAlignment = 'center';
    app.ScalefactorEditField.Position = [440 46 49 22];
    app.ScalefactorEditField.Value = '1';

    % Create SizethresholdEditFieldLabel
    app.SizethresholdEditFieldLabel = uilabel(app.ControlPanel);
    app.SizethresholdEditFieldLabel.HorizontalAlignment = 'right';
    app.SizethresholdEditFieldLabel.Position = [300 16 82 22];
    app.SizethresholdEditFieldLabel.Text = 'Size threshold';

    % Create SizethresholdEditField
```

```
    app.SizethresholdEditField = uieditfield(app.ControlPanel, 'text');
    app.SizethresholdEditField.ValueChangedFcn = createCallbackFcn(app,
@SizethresholdEditFieldValueChanged, true);
    app.SizethresholdEditField.HorizontalAlignment = 'center';
    app.SizethresholdEditField.Position = [440 16 50 22];
    app.SizethresholdEditField.Value = '100';

    % Create ImporteddatainformationTextAreaLabel
    app.ImporteddatainformationTextAreaLabel = uilabel(app.ControlPanel);
    app.ImporteddatainformationTextAreaLabel.HorizontalAlignment = 'right';
    app.ImporteddatainformationTextAreaLabel.Position = [17 159 142 22];
    app.ImporteddatainformationTextAreaLabel.Text = 'Imported data information';

    % Create ImporteddatainformationTextArea
    app.ImporteddatainformationTextArea = uitextarea(app.ControlPanel);
    app.ImporteddatainformationTextArea.ValueChangedFcn = createCallbackFcn(app,
@ImporteddatainformationTextAreaValueChanged, true);
    app.ImporteddatainformationTextArea.Position = [17 16 207 144];

    % Create StartProcessButton
    app.StartProcessButton = uibutton(app.ControlPanel, 'push');
    app.StartProcessButton.ButtonPushedFcn = createCallbackFcn(app,
@StartProcessButtonPushed, true);
    app.StartProcessButton.BackgroundColor = [0.9412 0.9412 0.9412];
    app.StartProcessButton.FontWeight = 'bold';
    app.StartProcessButton.Position = [305 84 179 31];
    app.StartProcessButton.Text = 'Start Process';

    % Create StartdetectionButton
    app.StartdetectionButton = uibutton(app.ControlPanel, 'push');
    app.StartdetectionButton.ButtonPushedFcn = createCallbackFcn(app,
@StartdetectionButtonPushed, true);
    app.StartdetectionButton.BackgroundColor = [0.9412 0.9412 0.9412];
    app.StartdetectionButton.FontWeight = 'bold';
    app.StartdetectionButton.Position = [305 120 179 31];
    app.StartdetectionButton.Text = 'Start detection';

    % Create TabGroup
    app.TabGroup = uitabgroup(app.UIFigure);
    app.TabGroup.Position = [2 623 567 171];

    % Create OpenTab
    app.OpenTab = uitab(app.TabGroup);
    app.OpenTab.Title = 'Open';
    app.OpenTab.BackgroundColor = [0.902 0.902 0.902];

    % Create SelectoverflowfolderButton
    app.SelectoverflowfolderButton = uibutton(app.OpenTab, 'push');
    app.SelectoverflowfolderButton.ButtonPushedFcn = createCallbackFcn(app,
@SelectoverflowfolderButtonPushed, true);
    app.SelectoverflowfolderButton.Position = [22 110 146 22];
    app.SelectoverflowfolderButton.Text = 'Select overflow folder';

    % Create SelectunderflowfolderButton
    app.SelectunderflowfolderButton = uibutton(app.OpenTab, 'push');
    app.SelectunderflowfolderButton.ButtonPushedFcn = createCallbackFcn(app,
@SelectunderflowfolderButtonPushed, true);
    app.SelectunderflowfolderButton.Position = [26 63 138 22];
    app.SelectunderflowfolderButton.Text = 'Select underflow folder';

    % Create SelectinletfolderButton
    app.SelectinletfolderButton = uibutton(app.OpenTab, 'push');
```

```
    app.SelectinletfolderButton.ButtonPushedFcn = createCallbackFcn(app,
@SelectinletfolderButtonPushed, true);
    app.SelectinletfolderButton.Position = [22 17 146 22];
    app.SelectinletfolderButton.Text = 'Select inlet folder';

    % Create OverflowF
    app.OverflowF = uieditfield(app.OpenTab, 'text');
    app.OverflowF.ValueChangedFcn = createCallbackFcn(app, @OverflowFValueChanged,
true);
    app.OverflowF.FontSize = 10;
    app.OverflowF.Position = [192 110 359 22];
    app.OverflowF.Value = 'Select the folder - No data selected';

    % Create UnderflowF
    app.UnderflowF = uieditfield(app.OpenTab, 'text');
    app.UnderflowF.FontSize = 10;
    app.UnderflowF.Position = [192 63 359 22];
    app.UnderflowF.Value = 'Select the folder - No data selected';

    % Create InletF
    app.InletF = uieditfield(app.OpenTab, 'text');
    app.InletF.FontSize = 10;
    app.InletF.Position = [192 17 359 22];
    app.InletF.Value = 'Select the folder - No data selected';

    % Create HelpTab
    app.HelpTab = uitab(app.TabGroup);
    app.HelpTab.Title = 'Help';

    % Create HelpButton
    app.HelpButton = uibutton(app.HelpTab, 'push');
    app.HelpButton.Position = [422 95 82 28];
    app.HelpButton.Text = 'Help';

    % Create PleasepressHelpforapplicationtutorialLabel
    app.PleasepressHelpforapplicationtutorialLabel = uilabel(app.HelpTab);
    app.PleasepressHelpforapplicationtutorialLabel.HorizontalAlignment = 'center';
    app.PleasepressHelpforapplicationtutorialLabel.Position = [45 94 352 28];
    app.PleasepressHelpforapplicationtutorialLabel.Text = 'Please press Help for
application tutorial ';

    % Create MicrosepV10Label
    app.MicrosepV10Label = uilabel(app.UIFigure);
    app.MicrosepV10Label.FontColor = [0.651 0.651 0.651];
    app.MicrosepV10Label.Position = [15 11 86 22];
    app.MicrosepV10Label.Text = 'Microsep V 1.0';

    % Create DesignedbyYeganehSaffarLabel
    app.DesignedbyYeganehSaffarLabel = uilabel(app.UIFigure);
    app.DesignedbyYeganehSaffarLabel.FontSize = 10;
    app.DesignedbyYeganehSaffarLabel.FontColor = [0.651 0.651 0.651];
    app.DesignedbyYeganehSaffarLabel.Position = [117 11 138 22];
    app.DesignedbyYeganehSaffarLabel.Text = 'Designed by : Yeganeh Saffar';

    % Create Lastmodificationwinter2024Label
    app.Lastmodificationwinter2024Label = uilabel(app.UIFigure);
    app.Lastmodificationwinter2024Label.FontSize = 10;
    app.Lastmodificationwinter2024Label.FontColor = [0.651 0.651 0.651];
    app.Lastmodificationwinter2024Label.Position = [271 11 141 22];
    app.Lastmodificationwinter2024Label.Text = 'Last modification : winter 2024';

    % Create TabGroup2
    app.TabGroup2 = uitabgroup(app.UIFigure);
```

```
    app.TabGroup2.Position = [618 20 740 750];

    % Create IntroTab
    app.IntroTab = uitab(app.TabGroup2);
    app.IntroTab.Title = 'Intro';

    % Create Image
    app.Image = uiimage(app.IntroTab);
    app.Image.Position = [197 210 367 395];
    app.Image.ImageSource = 'microhydrocyclone2.JPG';

    % Create Label
    app.Label = uilabel(app.IntroTab);
    app.Label.FontWeight = 'bold';
    app.Label.Position = [137 182 524 25];
    app.Label.Text = 'Microsep is designed and developed to analyse the performance of
a micro hyrocyclone. ';

    % Create Label_2
    app.Label_2 = uilabel(app.IntroTab);
    app.Label_2.FontSize = 10;
    app.Label_2.FontColor = [0.502 0.502 0.502];
    app.Label_2.Position = [270 102 211 25];
    app.Label_2.Text = 'For more information please check the help';

    % Create DataanalysisTab
    app.DataanalysisTab = uitab(app.TabGroup2);
    app.DataanalysisTab.Title = 'Data analysis';

    % Create OverflowPanel
    app.OverflowPanel = uipanel(app.DataanalysisTab);
    app.OverflowPanel.Title = 'Overflow';
    app.OverflowPanel.Position = [19 493 694 219];

    % Create UIAxes2
    app.UIAxes2 = uiaxes(app.OverflowPanel);
    xlabel(app.UIAxes2, 'Frame')
    ylabel(app.UIAxes2, 'Diameter (unit)')
    zlabel(app.UIAxes2, 'Z')
    app.UIAxes2.Position = [379 10 300 185];

    % Create UIAxes
    app.UIAxes = uiaxes(app.OverflowPanel);
    xlabel(app.UIAxes, 'Frame')
    ylabel(app.UIAxes, 'Number of cells')
    zlabel(app.UIAxes, 'Z')
    app.UIAxes.Position = [25 10 300 185];

    % Create UnderflowPanel
    app.UnderflowPanel = uipanel(app.DataanalysisTab);
    app.UnderflowPanel.Title = 'Underflow';
    app.UnderflowPanel.Position = [19 258 694 219];

    % Create UIAxes4
    app.UIAxes4 = uiaxes(app.UnderflowPanel);
    xlabel(app.UIAxes4, 'Frame')
    ylabel(app.UIAxes4, 'Diameter (unit)')
    zlabel(app.UIAxes4, 'Z')
    app.UIAxes4.Position = [379 10 300 185];

    % Create UIAxes3
    app.UIAxes3 = uiaxes(app.UnderflowPanel);
    xlabel(app.UIAxes3, 'Frame')
```

```
ylabel(app.UIAxes3, 'Number of cells')
zlabel(app.UIAxes3, 'Z')
app.UIAxes3.Position = [25 10 300 185];

% Create InletPanel
app.InletPanel = uipanel(app.DataanalysisTab);
app.InletPanel.Title = 'Inlet';
app.InletPanel.Position = [19 23 694 219];

% Create UIAxes6
app.UIAxes6 = uiaxes(app.InletPanel);
xlabel(app.UIAxes6, 'Frame')
ylabel(app.UIAxes6, 'Diameter (unit)')
zlabel(app.UIAxes6, 'Z')
app.UIAxes6.Position = [379 10 300 185];

% Create UIAxes5
app.UIAxes5 = uiaxes(app.InletPanel);
xlabel(app.UIAxes5, 'Frame')
ylabel(app.UIAxes5, 'Number of cells')
zlabel(app.UIAxes5, 'Z')
app.UIAxes5.Position = [25 10 300 185];

% Create SeparationanalysisTab
app.SeparationanalysisTab = uitab(app.TabGroup2);
app.SeparationanalysisTab.Title = 'Separation analysis';

% Create AllparticlesPanel
app.AllparticlesPanel = uipanel(app.SeparationanalysisTab);
app.AllparticlesPanel.Title = 'All particles';
app.AllparticlesPanel.Position = [19 366 694 301];

% Create UIAxes8
app.UIAxes8 = uiaxes(app.AllparticlesPanel);
xlabel(app.UIAxes8, 'Frame')
ylabel(app.UIAxes8, 'Diameter (unit)')
zlabel(app.UIAxes8, 'Z')
app.UIAxes8.Position = [379 31 300 246];

% Create UIAxes7
app.UIAxes7 = uiaxes(app.AllparticlesPanel);
xlabel(app.UIAxes7, 'Frame')
ylabel(app.UIAxes7, 'Number of cells')
zlabel(app.UIAxes7, 'Z')
app.UIAxes7.Position = [25 30 300 247];

% Create LargeparticlesPanel
app.LargeparticlesPanel = uipanel(app.SeparationanalysisTab);
app.LargeparticlesPanel.Title = 'Large particles';
app.LargeparticlesPanel.Position = [19 32 694 315];

% Create UIAxes10
app.UIAxes10 = uiaxes(app.LargeparticlesPanel);
xlabel(app.UIAxes10, 'Frame')
ylabel(app.UIAxes10, 'Diameter (unit)')
zlabel(app.UIAxes10, 'Z')
app.UIAxes10.Position = [379 33 300 258];

% Create UIAxes9
app.UIAxes9 = uiaxes(app.LargeparticlesPanel);
xlabel(app.UIAxes9, 'Frame')
ylabel(app.UIAxes9, 'Number of cells')
zlabel(app.UIAxes9, 'Z')
```

```
    app.UIAxes9.Position = [25 32 300 259];

    % Create LCSeparationanalysisTab
    app.LCSeparationanalysisTab = uitab(app.TabGroup2);
    app.LCSeparationanalysisTab.Title = 'LC Separation analysis';

    % Create AllparticlesPanel_2
    app.AllparticlesPanel_2 = uipanel(app.LCSeparationanalysisTab);
    app.AllparticlesPanel_2.Title = 'All particles';
    app.AllparticlesPanel_2.Position = [19 366 694 301];

    % Create UIAxes12
    app.UIAxes12 = uiaxes(app.AllparticlesPanel_2);
    xlabel(app.UIAxes12, 'Frame')
    ylabel(app.UIAxes12, 'Diameter (unit)')
    zlabel(app.UIAxes12, 'Z')
    app.UIAxes12.Position = [379 31 300 246];

    % Create UIAxes11
    app.UIAxes11 = uiaxes(app.AllparticlesPanel_2);
    xlabel(app.UIAxes11, 'Frame')
    ylabel(app.UIAxes11, 'Number of cells')
    zlabel(app.UIAxes11, 'Z')
    app.UIAxes11.Position = [25 30 300 247];

    % Create LargeparticlesPanel_2
    app.LargeparticlesPanel_2 = uipanel(app.LCSeparationanalysisTab);
    app.LargeparticlesPanel_2.Title = 'Large particles';
    app.LargeparticlesPanel_2.Position = [19 32 694 315];

    % Create UIAxes14
    app.UIAxes14 = uiaxes(app.LargeparticlesPanel_2);
    xlabel(app.UIAxes14, 'Frame')
    ylabel(app.UIAxes14, 'Diameter (unit)')
    zlabel(app.UIAxes14, 'Z')
    app.UIAxes14.Position = [379 33 300 258];

    % Create UIAxes13
    app.UIAxes13 = uiaxes(app.LargeparticlesPanel_2);
    xlabel(app.UIAxes13, 'Frame')
    ylabel(app.UIAxes13, 'Number of cells')
    zlabel(app.UIAxes13, 'Z')
    app.UIAxes13.Position = [25 32 300 259];

    % Create ImageprocessingTab
    app.ImageprocessingTab = uitab(app.TabGroup2);
    app.ImageprocessingTab.Title = 'Image processing';

    % Create UIAxes20
    app.UIAxes20 = uiaxes(app.ImageprocessingTab);
    xlabel(app.UIAxes20, 'X')
    ylabel(app.UIAxes20, 'Y')
    zlabel(app.UIAxes20, 'Z')
    app.UIAxes20.Position = [259 316 454 351];

    % Create EditField
    app.EditField = uieditfield(app.ImageprocessingTab, 'numeric');
    app.EditField.ValueChangedFcn   =   createCallbackFcn(app,   @EditFieldValueChanged,
true);
    app.EditField.HorizontalAlignment = 'center';
    app.EditField.Position = [61 525 69 22];
    app.EditField.Value = 1;
```

```
    % Create ChooseanimageLabel
    app.ChooseanimageLabel = uilabel(app.ImageprocessingTab);
    app.ChooseanimageLabel.Position = [86 551 100 22];
    app.ChooseanimageLabel.Text = 'Choose an image';

    % Create DataseriesDropDownLabel
    app.DataseriesDropDownLabel = uilabel(app.ImageprocessingTab);
    app.DataseriesDropDownLabel.HorizontalAlignment = 'right';
    app.DataseriesDropDownLabel.Position = [27 610 70 22];
    app.DataseriesDropDownLabel.Text = 'Data series ';

    % Create DataseriesDropDown
    app.DataseriesDropDown = uidropdown(app.ImageprocessingTab);
    app.DataseriesDropDown.Items = {'Overflow', 'Underflow', 'Inlet', ''};
    app.DataseriesDropDown.ValueChangedFcn           =           createCallbackFcn(app,
@DataseriesDropDownValueChanged, true);
    app.DataseriesDropDown.Position = [112 610 100 22];
    app.DataseriesDropDown.Value = 'Overflow';

    % Create ShowButton
    app.ShowButton = uibutton(app.ImageprocessingTab, 'push');
    app.ShowButton.ButtonPushedFcn = createCallbackFcn(app, @ShowButtonPushed, true);
    app.ShowButton.Position = [76 481 100 22];
    app.ShowButton.Text = 'Show';

    % Create Switch
    app.Switch = uiswitch(app.ImageprocessingTab, 'slider');
    app.Switch.Items = {'raw image', 'Processed'};
    app.Switch.ValueChangedFcn = createCallbackFcn(app, @SwitchValueChanged, true);
    app.Switch.Position = [103 424 45 20];
    app.Switch.Value = 'raw image';

    % Create maximagenumber
    app.maximagenumber = uitextarea(app.ImageprocessingTab);
    app.maximagenumber.ValueChangedFcn            =            createCallbackFcn(app,
@maximagenumberValueChanged, true);
    app.maximagenumber.BackgroundColor = [0.9412 0.9412 0.9412];
    app.maximagenumber.Position = [158 525 50 21];

    % Create Label_3
    app.Label_3 = uilabel(app.ImageprocessingTab);
    app.Label_3.Position = [147 524 12 22];
    app.Label_3.Text = '/';

    % Create ExportTab
    app.ExportTab = uitab(app.TabGroup2);
    app.ExportTab.Title = 'Export';

    % Create ExportdataPanel
    app.ExportdataPanel = uipanel(app.ExportTab);
    app.ExportdataPanel.Title = 'Export data ';
    app.ExportdataPanel.Position = [19 516 678 166];

    % Create BrowseButton
    app.BrowseButton = uibutton(app.ExportdataPanel, 'push');
    app.BrowseButton.Position = [194 58 98 23];
    app.BrowseButton.Text = 'Browse';

    % Create SelecttheexportinglocationLabel
    app.SelecttheexportinglocationLabel = uilabel(app.ExportdataPanel);
    app.SelecttheexportinglocationLabel.Position = [273 87 156 23];
    app.SelecttheexportinglocationLabel.Text = 'Select the exporting location';
```

```
    % Create TextArea
    app.TextArea = uitextarea(app.ExportdataPanel);
    app.TextArea.Position = [298 57 319 25];

    % Create DatasetButtonGroup
    app.DatasetButtonGroup = uibuttongroup(app.ExportdataPanel);
    app.DatasetButtonGroup.Title = 'Data set';
    app.DatasetButtonGroup.Position = [25 22 123 106];

    % Create InletButton
    app.InletButton = uiradiobutton(app.DatasetButtonGroup);
    app.InletButton.Text = 'Inlet';
    app.InletButton.Position = [11 60 58 22];
    app.InletButton.Value = true;

    % Create OverflowButton
    app.OverflowButton = uiradiobutton(app.DatasetButtonGroup);
    app.OverflowButton.Text = 'Overflow';
    app.OverflowButton.Position = [11 38 69 22];

    % Create UnderflowButton
    app.UnderflowButton = uiradiobutton(app.DatasetButtonGroup);
    app.UnderflowButton.Text = 'Underflow';
    app.UnderflowButton.Position = [11 16 76 22];

    % Create ExportfiguresPanel
    app.ExportfiguresPanel = uipanel(app.ExportTab);
    app.ExportfiguresPanel.Title = 'Export figures';
    app.ExportfiguresPanel.Position = [20 283 678 191];

    % Create BrowseButton_2
    app.BrowseButton_2 = uibutton(app.ExportfiguresPanel, 'push');
    app.BrowseButton_2.Position = [204 128 98 23];
    app.BrowseButton_2.Text = 'Browse';

                % Create SelecttheexportinglocationLabel_2
                app.SelecttheexportinglocationLabel_2                                    =
uilabel(app.ExportfiguresPanel);
                app.SelecttheexportinglocationLabel_2.Position = [24 128 156 23];
                app.SelecttheexportinglocationLabel_2.Text  =  'Select  the  exporting
location';

                % Create TextArea_2
                app.TextArea_2 = uitextarea(app.ExportfiguresPanel);
                app.TextArea_2.Position = [327 126 319 25];
                app.TextArea_2.Value = {'None'};

                % Create DatasetButtonGroup_2
                app.DatasetButtonGroup_2 = uibuttongroup(app.ExportfiguresPanel);
                app.DatasetButtonGroup_2.Title = 'Data set';
                app.DatasetButtonGroup_2.Position = [24 33 123 72];

                % Create LargeParticlesButton
                app.LargeParticlesButton = uiradiobutton(app.DatasetButtonGroup_2);
                app.LargeParticlesButton.Text = 'Large Particles';
                app.LargeParticlesButton.Position = [11 26 102 22];
                app.LargeParticlesButton.Value = true;

                % Create SmallParticlesButton
                app.SmallParticlesButton = uiradiobutton(app.DatasetButtonGroup_2);
                app.SmallParticlesButton.Text = 'Small Particles';
                app.SmallParticlesButton.Position = [11 4 101 22];
```

```
% Create FigurenameDropDownLabel
app.FigurenameDropDownLabel = uilabel(app.ExportfiguresPanel);
app.FigurenameDropDownLabel.HorizontalAlignment = 'right';
app.FigurenameDropDownLabel.Position = [238 58 73 22];
app.FigurenameDropDownLabel.Text = 'Figure name';
```

Under flow

This function imports the data from the under flow folder that is chosen in the directory function.

```
function [Test_im2] = UF_importer(Dir_Raw2)

F_Name2 = [ 'info\', 'Test_im2.mat' ] ;
% is the file existing?
ISF2 = isfile( F_Name2 ) ;
if ISF2 == 0
    Fol_Raw2 = dir( fullfile( Dir_Raw2, '*.tiff' ) ) ;
    for i = 1 : size( Fol_Raw2, 1)
        Name_Raw2{i,1} = Fol_Raw2(i).name ;
        Test_im2{i,1} =  imread( [Dir_Raw2, Name_Raw2{i}] ) ;
    end
    % save the raw image file
    save( [ 'info\' 'Test_im2' ] , 'Test_im2' ) ;
else  ISF2 == 1

    % load the raw image file
    load( [ 'info\' 'Test_im2' ] , 'Test_im2' ) ;
end

' Importing execution is completed'
end
```

Overflow

This function imports the data from the over flow folder that is chosen in the directory function.

```
 function [Test_im] = OF_importer(Dir_Raw)

F_Name = [ 'info\', 'Test_im.mat' ] ;
% is the file existing?
ISF = isfile( F_Name ) ;
if ISF == 0
    Fol_Raw = dir( fullfile( Dir_Raw, '*.tiff' ) ) ;
    for i = 1 : size( Fol_Raw, 1)
        Name_Raw{i,1} = Fol_Raw(i).name ;
        Test_im{i,1} =  imread( [Dir_Raw, Name_Raw{i}] ) ;
    end
    % save the raw image file
    save( [ 'info\' 'Test_im' ] , 'Test_im' ) ;
else  ISF == 1

    % load the raw image file
    load( [ 'info\' 'Test_im' ] , 'Test_im' ) ;
end

' Importing execution is completed'
end
```

Detection

This function controls the process of detection implementation.

```
function [L1,L2,centers,radii,Paticle_num_1frame] = detection(Im22,i,Pixtoreal)

Im2 = medfilt2(Im22);

Im = imbinarize( Im2, 'adaptive','ForegroundPolarity','dark','Sensitivity',0.5);
II1 = ~Im; % invert image for circle detection
II = imfill(II1,'holes' );
 figure('name','inverted binarized image');
 imshow(II)
 figure('name','Raw image');
 imshow(Im2)

 figure;
 Subplot 1: Image 1
 subplot(1, 4, 1);
 imshow(Im22);
 title('raw image');

Subplot 2: Image 2
 subplot(1, 4, 2);
 imshow(Im2);
 title('filtered');

 Subplot 3: Image 3
 subplot(1, 4, 3);
 imshow(Im);
 title('binarized');

 Subplot 4: Image 4
 subplot(1, 4, 4);
 imshow(II);
 title('filled inverted');

stats                                                                    =
regionprops('table',II,'Centroid','MajorAxisLength','MinorAxisLength','Area');
centers = stats.Centroid;
area = stats.Area;
L1 = stats.MajorAxisLength .* Pixtoreal;
L2 = stats.MinorAxisLength .*Pixtoreal;
diameters = mean([stats.MajorAxisLength stats.MinorAxisLength],2);
radii = sqrt (area./3.14).*Pixtoreal;
 hold on
 viscircles(centers,radii);
 hold off
 figure('name','Detected particles on raw image');
 imshow(Im2)

Paticle_num_1frame = size (radii,1);

'Detection execution is completed'
end
```

cell analysis

The following code is designed to detect cells and calculate the frame average and cumulative average for the detected items.

```
    % set default fonts
    set(0, 'DefaultAxesFontName', 'Times New Roman');
    set(0, 'DefaultUIControlFontName', 'Times New Roman');
    set(0, 'defaultUitableFontName', 'Times New Roman');
    set(0, 'defaultTextFontName', 'Times New Roman');
    set(0, 'defaultUipanelFontName', 'Times New Roman');
    set(0, 'defaulttextinterpreter','Latex')

    font_size = 14;
    % font_name = 'Times New Roman';
    % set default font size, line width and marker size
    set(0,'DefaultLineLineWidth',1.0);
    set(0,'DefaultLineMarkerSiz',5);
    set(0,'defaultaxesfontsize',font_size);
    set(0,'DefaultAxesFontSize',font_size);
    %-------------------------------------------------------------------------
    %%%% Parameters :

    Pixtoreal = 2.5; % calibration rate

    treshold = 100; % filtration threshold

    data_name = 'test1';
    data_name2 = 'test2';
    inputename_of = 'overflow';
    inputename_uf = 'underflow';

    %%%% data loading
    [Dir_Raw,Dir_Raw2] = filedirectory(); % Dir_Raw = the overflow raw data   Dir_Raw2
= the underflow raw data

    %%%% Import over flow data
    [Test_im] = OF_importer(Dir_Raw);
    %%%% Import under flow data
    [Test_im2] = UF_importer(Dir_Raw2);


    %%%%%% particle detection

    % over flow range
    from_of = 1;
    % to_of = 20;
    to_of = size (Test_im,1);

    % Under flow range
    from_uf = 1;
    % to_uf = 15;
    to_uf = size (Test_im2,1);


    %%% Cell detection ---  the overflow data set
    for i = from_of:to_of
```

```
    Im22 =  Test_im{i}; % read the image
    % [center,radius_frame_o,Paticle_num_1frame] = detection(Im22,i); % detect cell
    [L1o,L2o,center,radius_frame_o,Paticle_num_1frame] = detection(Im22,i,Pixtoreal);

    radius_of {i} = radius_frame_o;
    center_of{i} = center;
    Paticle_num_frame_of(i) = Paticle_num_1frame;
    L1_of {i} = L1o;
    L2_of {i} = L2o;

    end

    %%% Cell detection ---  the undderflow data set
    for k = from_uf:to_uf

    Im33 =  Test_im2{k}; % read the image
    [L1u,L2u,center,radius_frame_u,Paticle_num_1frame_u] = detection(Im33,k,Pixtoreal);
% detect cell
    radius_uf {k} = radius_frame_u;
    center_uf{k} = center;
    Paticle_num_frame_uf(k) = Paticle_num_1frame_u;
    L1_uf {i} = L1u;
    L2_uf {i} = L2u;
    end


    % plot the overall information for each imported data sets
    datainfo(Paticle_num_frame_of,from_of,to_of,radius_of,inputename_of)
    datainfo(Paticle_num_frame_uf,from_uf,to_uf,radius_uf,inputename_uf)

    % plot data analysis for one input data
    [big_matrix,allData] = dataplots(radius_of,Dir_Raw,data_name,inputename_of);
    [big_matrix2,allData2] = dataplots(radius_uf,Dir_Raw2,data_name2,inputename_uf);

    % plot data analysis for all data sets for all particle sizes
    [allData_of,allData_uf,allData_inlet]                                    =
dataplots_allcases(radius_of,Dir_Raw,data_name,inputename_of...
        ,radius_uf,Dir_Raw2,data_name2,inputename_uf);

    % Calculate the statisctics
     Xn(big_matrix);


    % filtration threshold
    largedata_of = any(allData_of  > treshold,2);
    new_matrix2_of = allData_of(largedata_of, :);
    new_matrix2_of1 = new_matrix2_of';
    [big_matrix_larg_of,allData_large_of]                                    =
dataplots(new_matrix2_of1,Dir_Raw,data_name,inputename_of);


    largedata_uf = any(allData_uf  > treshold,2);
    new_matrix2_uf = allData_uf(largedata_uf, :);
    new_matrix2_uf1 = new_matrix2_uf';
    [big_matrix_larg_uf,allData_large_uf]                                    =
dataplots(new_matrix2_uf1,Dir_Raw,data_name,inputename_uf);

    largedata_in = any(allData_inlet  > treshold,2);
    new_matrix2_in = allData_inlet(largedata_in, :);
    new_matrix2_in1 = new_matrix2_in';
    [big_matrix_larg_in,allData_large_in]                                    =
dataplots(new_matrix2_in1,Dir_Raw,data_name,'inlet');
```

```
    [allData_of_L,allData_uf_L,allData_inlet]                                   =
dataplots_allcases(new_matrix2_of,Dir_Raw,data_name,inputename_of...
        ,new_matrix2_uf,Dir_Raw2,data_name2,inputename_uf);
```

Appendix 3: Uncertainty calculations

This appendix demonstrates the uncertainty analysis discussed thesis. It provides a detailed assessment of the measurement uncertainties associated with both velocimetry and particle size measurements. The calculations presented here quantify the potential errors in the experimental data, offering a clearer understanding of the reliability and precision of the results reported in the thesis.

Uncertainty analysis for PIV

The uncertainty of PIV velocity measurements consists of both random and systematic components. Random uncertainty originates from stochastic variability in particle image recording and displacement estimation, including image noise, background fluctuations, finite particle image size, seeding non-uniformity, peak locking, and sub-pixel peak-fitting limitations. These effects appear as scatter in repeated measurements and are commonly quantified by the standard deviation of the measured displacement or velocity obtained from ensembles of statistically equivalent samples. Random uncertainty decreases with sample averaging but cannot be completely eliminated for individual measurements.

Systematic uncertainty represents measurement bias that persists across all samples and therefore does not decrease with averaging. The dominant systematic contributions typically arise from uncertainties in the spatial calibration and mapping procedure, including calibration target alignment errors, mapping fit residuals, lens distortion, refractive-index mismatch across optical windows or interfaces, and small optical misalignments. Additional systematic uncertainty can originate from inaccuracies in the inter-frame timing resulting from camera–laser synchronization

offsets or timing jitter. Calibration uncertainties are generally estimated from repeated calibration procedures and analysis of mapping residuals, while timing uncertainties are taken from device specifications or independent synchronization tests.

The total uncertainty of the velocity measurement is evaluated as a combined standard uncertainty using classical uncertainty propagation applied to the velocity definition.

$$u = M\Delta x/\Delta t \tag{1}$$

where Δx is the measured particle image displacement in pixels, M is the calibration factor converting pixels to physical length (mm per pixel), and Δt is the time delay between the two images used for correlation. Each variable contains an associated uncertainty: $\sigma_{\Delta x}$ for the displacement measurement, which reflects predominantly random contributions from image correlation and peak fitting σ_M for the spatial calibration factor, which represents systematic mapping uncertainty; and $\sigma_{\Delta t}$ for the inter-frame timing, which represents systematic synchronization uncertainty. Applying the law of propagation of uncertainty yields:

$$\sigma_u^2 = \left(\frac{\partial u}{\partial \Delta x}\sigma_{\Delta x}^2\right)^2 + \left(\frac{\partial u}{\partial M}\sigma_M^2\right)^2 + \left(\frac{\partial u}{\partial \Delta t}\sigma_{\Delta t}^2\right)^2 \tag{2}$$

For $u = M\Delta x/\Delta t$, the partial derivatives are:

$$\frac{\partial u}{\partial \Delta x} = \frac{M}{\Delta t}, \frac{\partial u}{\partial M} = \frac{\Delta x}{\Delta t}, \frac{\partial u}{\partial \Delta t} = -\frac{M\Delta x}{\Delta t^2} = -\frac{u}{\Delta t} \tag{3}$$

so that the propagated velocity uncertainty becomes:

$$\sigma_u^2 = \left(\frac{M}{\Delta t}\sigma_{\Delta x}^2\right)^2 + \left(\frac{\Delta x}{\Delta t}\sigma_M^2\right)^2 + \left(\frac{u}{\Delta t}\sigma_{\Delta t}^2\right)^2 \tag{4}$$

In the present measurements, spatially averaged velocity magnitudes of $0.04\ \mathrm{m/s}$, $0.14\ \mathrm{m/s}$, and of $0.23\ \mathrm{m/s}$ were obtained for Reynolds numbers of 150, 300, and 700, respectively. The spatial calibration yielded a magnification factor of $M = 1.875 \times 10^{-6}\ \mathrm{m/pixel}$. The inter frame time was $\Delta t = 500\ \mu\mathrm{s}$, $\Delta t = 250\ \mu\mathrm{s}$, and $\Delta t = 125\ \mu\mathrm{s}$, for Reynolds numbers of 150, 300, and 700, respectively. For the uncertainty estimation, a representative displacement uncertainty of $\sigma_{\Delta x} = 0.10$ pixel was assumed based on the performance of the cross correlation and sub pixel peak fitting, together with a calibration uncertainty of 2 percent, $\sigma_M = 0.02$ obtained from the regression of the calibration target images, and a timing uncertainty of $\sigma_{\Delta t} = 10$ ns associated with camera–laser synchronization. The combined standard uncertainty of the spatially averaged velocity for each case was evaluated by propagating these uncertainties through the relation in equation (1).

Using the mean displacements implied by the measured velocities and the corresponding Δt values, the resulting uncertainties in the spatial mean velocity are approximately $8.8 \times 10^{-4}\ \mathrm{m/s}$, $2.9 \times 10^{-3}\ \mathrm{m/s}$, and $4.8 \times 10^{-3}\ \mathrm{m/s}$ for Reynolds numbers of 150, 300, and 700, respectively. These values correspond to relative uncertainties of about $2.2\ \%$, $2.1\ \%$,, and $2.1\ \%$. The uncertainty level is therefore nearly constant in relative terms over the range of Reynolds numbers considered, with the total uncertainty dominated by the combined effect of displacement estimation and spatial calibration, while timing uncertainty remains negligible.

Uncertainty analysis for particle size measurements

The particle sizing method employed in this study determines individual particle diameters from microscopic images by detecting particle boundaries and fitting a circular model, assuming spherical particle geometry. The fitted diameter is obtained in pixel units and subsequently converted to a physical length scale using a calibration factor obtained from a calibration target. The physical particle diameter is therefore given by:

$$D = M d_{pix} \tag{8}$$

where d_{pix} is the particle diameter measured in pixels and M is the spatial calibration coefficient (mm per pixel).

The total measurement uncertainty consists of both random and systematic components. The random uncertainty is associated primarily with the determination of the particle boundary and circle fitting. Its sources include image noise, background non-uniformity, thresholding and segmentation variability, finite pixel resolution affecting edge localization, slight out-of-focus blur, and deviations of particle shape from perfect sphericity. This uncertainty is represented by the standard uncertainty of the fitted diameter in pixels, denoted as σ_d, which can be estimated from repeated measurements of the same particle or from the statistical distribution of radial residuals obtained during the circle-fitting procedure.

Systematic uncertainty is dominated by the spatial calibration process and affects the conversion from pixels to physical units. Its sources include uncertainties in the known spacing of the calibration target, imperfections in target positioning and alignment, lens distortion or uncorrected optical mapping errors, and potential small discrepancies between the calibration

plane and the particle imaging plane. These effects lead to an uncertainty in the calibration coefficient M, denoted as σ_M , which is quantified from the regression error of the calibration fit combined with manufacturer tolerance of the calibration target.

The combined standard uncertainty of an individual diameter measurement is obtained through classical propagation of uncertainties applied to the measurement model $D = Md_{pix}$.

$$\sigma_D^2 = \left(\frac{\partial D}{\partial d_{pix}}\sigma_d\right)^2 + \left(\frac{\partial D}{\partial M}\sigma_M\right)^2 = (M\sigma_d)^2 + \left(d_{pix}\sigma_M\right)^2 \quad (9)$$

The first term represents the contribution of random uncertainty associated with image processing and circle fitting, while the second term represents the systematic contribution arising from the spatial calibration.

In the present study, detected particle diameters span a range from approximately 10 μm to 300 μm. The spatial calibration yielded a conversion coefficient of $M = 2.5$ μm/pixel. Using a displacement uncertainty associated with boundary detection and circle fitting of $\sigma_d = 0.5$ pixel, estimated from repeated processing of identical particle images, and a calibration uncertainty of $\sigma_M = 0.05$, corresponding to a relative calibration uncertainty of approximately 2 percent, the combined standard uncertainty of the diameter measurement was computed from:

$$\sigma_D = \sqrt{(M\sigma_d)^2 + \left(d_{pix}\sigma_M\right)^2} \quad (9)$$

For the smallest resolvable particles in this study, $D = 10$ μm, corresponding to $d_{pix} = 4$ pixels the resulting absolute uncertainty is approximately $\sigma_d = 1.3$ μm, which corresponds to a relative uncertainty of about 13 %. For the largest detected particles, $D = 300$ μm, he combined

uncertainty increases to $\sigma_d = 6.4$ μm. while the relative uncertainty decreases to approximately 2.1 %. These results indicate that sizing uncertainty is dominated by image-scale resolution and fitting uncertainty for small particles, whereas calibration uncertainty governs performance for larger particles.